

ABSTRACT

Title of Document: STRAINING ENGINEERING OF
GRAPHENE AND GRAPHENE-BASED
NANOSTRUCTURES

Shuze Zhu, Doctor of Philosophy, 2015

Directed By: Associate Professor Teng Li,
Department of Mechanical Engineering

Graphene has emerged as an extraordinary material with its capability to accommodate an array of remarkable electronic, mechanical and chemical properties. Extra-large surface-to-volume ratio renders graphene a highly flexible morphology, giving rise to intriguing observations such as ripples, wrinkles and folds as well as the potential to transform into other novel carbon nanostructures. Ultra-thin, mechanically tough, electrically conductive graphene films promise to enable a wealth of possible applications ranging from hydrogen storage scaffolds, electronic transistors, to bottom-up material designs.

Enthusiasm for graphene-based applications aside, there are still significant challenges to their realization, largely due to the difficulty of precisely controlling the graphene properties. Controlling the graphene morphology over large areas is crucial in enabling future graphene-based applications and material design. This dissertation aims to shed lights on potential mechanisms to actively manipulate the graphene morphology and

properties and therefore enable the material design principle that delivers desirable mechanical and electronic functionalities of graphene and its derivatives.

STRAIN ENGINEERING OF GRAPHENE AND GRAPHENE-BASED
NANOSTRUCTURES

By

Shuze Zhu

Dissertation submitted to the Faculty of the Graduate School of the
University of Maryland, College Park, in partial fulfillment
of the requirements for the degree of
Doctor of Philosophy
2015

Advisory Committee:

Associate Professor Peter Chung

Professor Abhijit Dasgupta

Assistant Professor Liangbing Hu

Associate Professor Teng Li, Chair/Advisor

Associate Professor Chunsheng Wang, Dean's Representative

© Copyright by
Shuze Zhu
2015

Acknowledgements

I acknowledge Dr. Teng Li, my advisor, for his invaluable time and constant dedication to my research projects. I also acknowledge all excellent collaborative researches done by our experimental collaborators. Experimental results and analysis in Section 4.1.1 are mainly obtained by Dr. Joseph Stroschio's group at National Institute of Standards and Technology. Experimental results in Section 5.2.1 and Section 5.2.2 are mainly obtained by Dr. Liangbing Hu's group in the Department of Material Science at the University of Maryland.

Table of Contents

Acknowledgements.....	ii
Table of Contents.....	iii
List of Tables.....	iv
List of Figures.....	v
Chapter 1: Introduction.....	1
1.1. Background and motivation.....	1
1.1.1. Superior material properties of graphene.....	3
1.1.2. Morphologic properties of graphene.....	5
1.1.3. Unconventional graphene nanostructures and their potential applications.....	6
1.2. Scope and goals of this dissertation research.....	12
Chapter 2: Programmable wrinkling morphology of graphene.....	14
2.1. Morphology of a graphene bilayer intercalated by nanoparticles.....	15
2.2. Wrinkle formation in graphene on substrate-supported nanoparticles.....	21
2.3. Chapter summary.....	34
Chapter 3: Functionalization enabled unconventional carbon nanostructures.....	35
3.1. Hydrogenation enabled scrolling of graphene.....	35
3.2. Hydrogenation assisted graphene origami and its application.....	51
3.3. Chapter summary.....	80
Chapter 4: Strain engineering of graphene: Pseudomagnetic field.....	82
4.1. Electromechanics of graphene drumhead – generating pseudomagnetic field.....	82
4.1.1. Quantum dot in suspended graphene without physical barriers.....	83
4.1.2. Understand the formation of quantum dot: A molecular dynamics study.....	92
4.1.3. Design quantum dot device: A coarse-grained study.....	99
4.1.4. Concluding remarks.....	115
4.2. Programmable extreme pseudomagnetic fields in graphene – finding the right shape.....	117
4.3. Chapter summary.....	141
Chapter 5: Strain engineering of compliance, stretchability, strength, toughness in graphene-based nanostructures.....	143
5.1. Extremely compliant and highly stretchable patterned graphene.....	143
5.2. Incorporating cellulose: Attaining stronger and tougher materials.....	155
5.2.1. Anomalous scaling law of strength and toughness of cellulose nanopaper.....	156
5.2.2. Hybridizing cellulose and graphene oxide toward strong and tough fibers.....	175
5.3. Chapter summary.....	192
Chapter 6: Conclusions and Outlook.....	194
6.1. Summary and concluding remarks.....	194
6.2. Outlook and future work.....	197
Bibliography.....	199

List of Tables

Table 5.1. CG parameters used in simulations

Table 5.2. Mechanical properties for paper made from cellulose fibers with different diameters

List of Figures

Figure 1.1. Carbon family members are derived from graphene (1).

Figure 1.2. Structure of carbon nanoscroll (39). (A) End view. (B) Perspective view.

Figure 1.3. Structure of graphane (52). The carbon atoms are shown in gray and the hydrogen atoms in white.

Figure 1.4. A growth mechanism and experimental image for graphene quantum dot (GQD) (58). (A) Schematic showing that the majority of C_{60} molecules adsorb on the terrace, and these decompose to produce carbon clusters with restricted mobility. (B) Schematic showing that temperature-dependent growth of GQDs with different equilibrium shape from the aggregation of the surface diffused carbon clusters. (C) STM image for hexagonal equilibrium shaped GQDs produced from C_{60} derived carbon clusters.

Figure 1.5. Schematic of fabrication of a graphene nanomesh (59).

Figure 1.6. Scheme of the fabrication of large-scale graphene nanomesh (64).

Figure 1.7. GO as the cross-linker in a PAM/GO nanocomposite hydrogel (71).

Figure 2.1. Wrinkles in graphene on rigid substrate (72, 73). (A) Left: AFM top view of sidewall ribbons showing their long-range order. Right: Perspective AFM view of 18-nm-deep graphitized trenches. (B) Left: A wrinkle is created by applying a uniaxial in-plane compression on substrate-supported graphene sheet. The compressive strain is related to the size ratio of wrinkle height to width. Right: Energy gap for different size ratios.

Figure 2.2. Wrinkles in graphene on stretchable substrate (74, 75). (A) Crumpled graphene after the release of pre-biaxial-strain in substrate. The wettability and resistance of such crumpled surface can be tuned by further applying tensile strain. (B) Rippled graphene nanoribbons after the release of pre-uniaxial-strain in substrate. The resistance of such rippled graphene device can be modulated by applied strain.

Figure 2.3. The morphology of graphene intercalated by a single Si NP of various diameters, d_{NP} . For visual clarity, the top panel shows the top graphene layer and the bottom one shows the Si NP and the bottom graphene layer (only the portion near the Si NP is shown). Note the ridged morphology formation as d_{NP} increases.

Figure 2.4. (A-E) The morphologic evolution of the Si NP-graphene system over simulation time. For visual clarity, only the bottom graphene layer and the Si NPs are shown. When the distance between the two Si NPs is sufficiently large (here $d_{NP} = 5nm$, and $S = 37nm$), the two Si NPs remain dispersed and are wrapped individually by the graphene bilayer. The intercalated graphene morphology near each Si NP is similar to that shown in Fig. 2.3. (F-J) When the distance between the two Si NPs is below a critical value (here $d_{NP} = 5nm$, and $S = 25nm$), the two Si NPs evolve to come closer and eventually bundle together.

Figure 2.5. A phase diagram of the morphologic evolution of the Si NP-graphene system in the space of NP distance and diameter. “+” denote the MD simulation cases in which Si NPs remain dispersed and “×” denote those in which Si NPs evolve to bundle together. A critical dispersion

distance of the Si NPs, S_{cr} , can be determined, which has an approximately linear dependence on d_{NP} .

Figure 2.6. **(A)** Schematics of graphene covering a substrate with dispersed NPs (not to scale). **(B)** Atomic force microscopy image of the wrinkled morphology of a monolayer graphene covering a SiO₂ substrate with dispersed SiO₂ NPs. The atomic force microscopy image is reprinted from Ref. (38), under the terms of the Creative Commons Attribution 3.0 License. Three representative types of wrinkling morphology (highlighted by red circles) can be observed: (1) wrinkling of graphene on isolated NP; (2) wrinkling of graphene bridging two neighboring NPs; (3) wrinkling of graphene on quasi-isolated NPs.

Figure 2.7. A schematic of a flat graphene monolayer on a substrate with a separation distance of h .

Figure 2.8. **(A)** MD simulation model. Inset shows the cross-section view of the initial configuration. Periodical boundary condition (PBC) is applied in y direction, so that the length of the simulation box along the PBC direction represents the NP dispersion distance S . **(B)** The typical equilibrium morphology of graphene on a small and isolated NP on the substrate. **(C-E)** Variation of wrinkling morphology of graphene on an isolated NP with increasing size.

Figure 2.9. Wrinkling morphology of graphene on NPs with relatively small dispersion distance. For visual guidance, two periodical images are combined along the PBC direction. For $d_{NP} = 2$ nm: **(A)** The two NP-intercalated graphene domes remain isolated when dispersion distance $S = 25$ nm. **(B)** A tunneling wrinkle forms between two NPs, when $S = 21$ nm. For $d_{NP} = 6$ nm: **(C)** Two long tipped wrinkles run in parallel between neighboring NPs and terminate in the middle with a short overlap but their tips remain distinct from each other (inset) when $S = 110$ nm. **(D)** When $S = 100$ nm, a tunneling wrinkle forms between two neighboring NPs.

Figure 2.10. A diagram of the wrinkling instability of graphene morphology on substrate-supported NPs in the space of NP dispersion distance and diameter.

Figure 2.11. A mechanism revealed by MD simulations to produce tunable and reversible wrinkles for graphene on stretchable substrate. PBC is applied along loading direction.

Figure 3.1. **(A)** Side view (top) and top view (bottom) of the equilibrium shape of a graphene nanoribbon (green) with one row of hydrogenation (red) on the same side along an armchair line. The graphene folds along the hydrogenation line to about 160°. **(B)** Two rows of hydrogenation along neighboring armchair lines on the same side result in further folding of the graphene nanoribbon to about 135°. **(C)** One row of hydrogenation along a zigzag line on the same side result in folding of the graphene nanoribbon to about 130°. **(D)** Two rows of hydrogenation along neighboring zigzag lines on the same side result in further folding of the graphene nanoribbon to about 100°.

Figure 3.2. **(A)** Simulation model of a graphene of a length L and a width W that is single-sided hydrogenated at one end in a length of L_h . Inset shows the detailed lattice structure of the hydrogenated region. **(B)** Energy minimized structure of the model.

Figure 3.3. Three types of scrolling behavior of partially single-sided hydrogenated graphene. Here $L=W=12$ nm. When $L_h/W=0.3$, the graphene can only scroll up partially, as shown in sequential snapshots of the graphene morphology at **(A)** 1ps, **(B)** 5ps, **(C)** 28ps and **(D)** 47ps, respectively. When $L_h/W=0.4$, the graphene can completely scroll up into a CNS, as shown in

sequential snapshots of the graphene morphology at **(F)** 1ps, **(G)** 9ps, **(H)** 13ps and **(I)** 50ps, respectively. When $L_h/W=0.8$, the graphene scrolls into an irregular nanostructure, as shown in sequential snapshots of the graphene morphology at **(K)** 1ps, **(L)** 3ps, **(M)** 13ps and **(N)** 52ps, respectively. **(E)**, **(J)** and **(O)** plots the evolution of the system potential energy as simulation time for the above three cases, respectively.

Figure 3.4. The equilibrium morphology of a square-shaped graphene of a wide range of size (from 6 nm to 21 nm) with various sizes of hydrogenated area (i.e., L_h/W ranges from 0.2 to 0.8).

Figure 3.5. A diagram of the three types of scrolling behavior of partially single-sided hydrogenated graphene in the parametric space spanned by L_h/W and W .

Figure 3.6. **(A-D)** Morphologic evolution of a partially single-sided hydrogenated graphene nanoribbon ($L=21\text{nm}$, $L_h=8.4\text{nm}$ and $W=12\text{nm}$), which ends up as an irregular nanostructure. **(E-H)** Morphologic evolution of a graphene nanoribbon ($L=21\text{nm}$, $L_h=8.4\text{nm}$ and $W=21\text{nm}$), which fully rolls up into a stable CNS. **(I-L)** Morphologic evolution of a graphene nanoribbon ($L=21\text{nm}$, $L_h=6.3\text{nm}$ and $W=21\text{nm}$), which can only partially roll up the hydrogenated portion (highlighted in red). Perspective views from the side in **(K)** and **(L)** reveal that the partial CNS tends to bend toward its outer edge that separates the hydrogenated and pristine portions of the graphene.

Figure 3.7. The evolution of the system potential energy of a 12 nm by 30 nm partially single-sided hydrogenated graphene as a function of simulation time. The hydrogenation enabled scrolling causes continuous decrease in the potential energy, leading to a complete CNS that remains stable at 300K.

Figure 3.8. Top view and side view of graphene structures folded to an angle due to single-sided hydrogenation along various lines at equilibrium. **(A)** one-line and **(B)** two-line hydrogenation are introduced along zigzag direction of graphene lattice, respectively. **(C)-(E)**: one-line, two-line, and three-line hydrogenation are introduced along arm-chair direction of graphene lattice, respectively. The bottom row plots the variation of the folding angle at 300K over time, which is shown to be minimum, indicating robust stability of the folded substructure.

Figure 3.9. **(A)** Double-cross shaped graphene flake to achieve HAGO-enabled hexahedral graphene nanocage. Insets show the hydrogenation lines, which demarcate the graphene flake into nine regions (labeled by numbers). **(B)** Energy-minimized structure by conjugate gradient (CG) and steepest descent algorithm. **(C)** Further energy minimization towards the formation of a graphene nanocage.

Figure 3.10. **(A)** Under an external electric field parallel to the plane of a graphene bilayer, point dipoles of the same direction as the electric field form in the graphene bilayer. **(B)** Schematics of in-plane sliding (left and middle panels) and out-of-plane separation (right panel) of the graphene bilayer. **(C)** As the two graphene layers slide off each other in the plane, the normalized dipole-dipole interaction energy decreases as the total surface area of the bilayer (e.g., $2(L+dL)W$ or $2L(W+dW)$) increases. **(D)** Similarly, as the two graphene layers separate out-of-plane, such an energy also decreases as the separation distance increases.

Figure 3.11. Controlled opening and closing of graphene nanocage via tuning effective inter-wall adhesion. $\lambda_{CC}=1$: without applied electric field, nanocage is closed; $\lambda_{CC}=0.12$: under an applied electric field, inter-wall adhesion decreases, leading to the opening of the nanocage

under thermal fluctuation. The simulation is done in the NVT ensemble at 300K.

Figure 3.12. **(A-D)**: Controlled opening and closing of a graphene nanocage immersed in a C_{60} reservoir can enable the uptake of C_{60} molecules by the nanocage. **(E-H)**: After the cargo-loaded nanocage is transported to the destination, the stored C_{60} molecule can be released by the electric field induced opening of the nanocage. **(I-L)** Release of a silicon nanoparticle from a graphene nanocage under the same mechanism.

Figure 3.13. **(A)** Patterned graphene is suitably hydrogenated to form a graphene nanocage of large size. **(B)** Morphology after initial energy minimization. **(C-F)** Electric field assisted formation of large size graphene nanocage. **(G)** Evolution of potential energy from **(B)** to **(F)**, indicating that the electric field can help prevent the graphene nanostructure trapped in unwanted metastable state **(C)** and facilitate the formation of the final nanocage **(F)**, a thermodynamically stable state.

Figure 3.14. **(A)** High density hydrogen storage in HAGO-enabled graphene nanocage, with a weighted percentage of 9.7%, beyond the US DOE ultimate goal of 7.5% for hydrogen storage. For visual clarity, only half of the nanocage is shown. **(B)** Weighted percentage of hydrogen storage in HAGO-enabled graphene nanocage as a function of the side length of a cubic graphene nanocage, for four different hydrogen volume densities inside the nanocage. Dashed lines denote US DOE ultimate goal and year 2017 goal on hydrogen storage density.

Figure 3.15. **(A)** Complete single-sided hydrogenation pattern, with 184 hydrogen atoms, as in Fig. 3.9. For visual clarity, only hydrogen atoms are shown. **(B)** A randomly generated defective hydrogenation pattern, which contains 128 hydrogen atoms (i.e., the perfection rate is 69.6%). **(C)** Double-cross shaped graphene flake with the defective hydrogenation pattern of **(B)**. **(D)** Energy-minimized structure in **(C)** by conjugate gradient and steepest descent algorithm. **(E)** Further energy minimization towards the formation of a graphene nanocage.

Figure 3.16. **(A)** Randomly generated defective hydrogenation pattern with 164 hydrogen atoms (perfection rate 89.2%) and its resulting graphene nanocage. **(B)** Randomly generated defective hydrogenation pattern with 144 hydrogen atoms (perfection rate 78.3%) and its resulting graphene nanocage. **(C)** Comparison of the energy evolution for different hydrogenation perfection rates towards the formation of nanocage. The curve for 100% perfection rate is replotted from Fig. 3.9C for comparison.

Figure 3.17. Another set of randomly generated defective hydrogenation patterns and their resulting graphene nanocages. Hydrogenation perfection rate: **(A)** 89.2%. **(B)** 78.3%. **(C)** 69.6%.

Figure 3.18. **(A)** Hydrogenation and folding induced non-uniform charge distribution in the graphene nanocage. **(B)** Mapping of positive and negative charges in the graphene nanocage. **(C-E)** The opening process of the graphene nanocage under the electrostatic force induced by an external electric field. **(F-H)** Upon removing the external electric field, the partially open graphene nanocage closes up spontaneously.

Figure 3.19. **(A)** Simulation model of an empty graphene nanocage immersed in a hydrogen reservoir. **(B)** A cross-section view of the hydrogen reservoir when the graphene nanocage is closed in a dynamics simulation (for visual clarity, the nanocage is not shown). **(C)** The slight opening of graphene nanocage gives rise to gaps and pores along the edges and corners. For visual clarity, the ambient hydrogen atoms are not shown. **(D)** Sequential snapshots of the

cross-section view of the hydrogen reservoir showing the adsorption of hydrogen into the inner volume of the nanocage. For visual clarity, the nanocage is not shown. **(E)** The evolution of the number of hydrogen atoms adsorbed into the nanocage and the corresponding weighted percentage of hydrogen storage. **(F)** The evolution of the effective volume density of hydrogen adsorbed inside the graphene nanocage. The dashed shows the level of ambient volume density of hydrogen atoms.

Figure 3.20. Release of hydrogen stored inside a graphene nanocage at an elevated temperature (300K). Starting configuration is the same structure as in Fig. 3.14A. Increasing pressure of stored hydrogen at elevated temperature causes the partial opening of the four edges of the graphene nanocage that are not covalently sealed, which allows the hydrogen atoms to spray out. After 193 ps, majority of stored hydrogen atoms are released. The simulation is in NVT ensemble and by Nose-Hoover thermostat. Hydrogen molecules are colored in red.

Figure 4.1. STM measurements of graphene drumheads. **(A)** Optical image of the gated graphene device. The device consists of a single graphene layer placed over an array of pits (1.1 μm in diameter, 100 nm in depth) etched in SiO_2 (300 nm)/Si substrate. **(B)** Magnified optical image of the device in (A). The single layer graphene region is marked by a red line. **(C)** Scanning electron microscope (SEM) image of the device. STM topographic images, 20 nm by 20 nm, on the supported graphene **(D)** and suspended graphene membrane **(E)**. The insets show the graphene atomic lattice images (5 nm by 5 nm). The inset grey scales cover the range of ± 0.2 nm. **(F)** Topographic height histograms from the images in (D) and (E).

Figure 4.2. STM images of the deformed graphene membrane induced by the competing forces from the probe tip pulling up on the membrane and the back-gate electric field pulling down on the membrane. The STM images are shown for various gate potentials from 0 to 50 V. At 50 V the membrane is being pulled into the pit in the substrate.

Figure 4.3. **(A)** STM topographic profiles obtained while scanning from graphene supported onto the SiO_2 substrate to the suspended region over a pit in the substrate as a function of tunneling bias at a fixed gate potential of 0 V and tunneling current of 50 pA. **(B)** SEM image of the STM probe tip showing a probe diameter of 110 nm.

Figure 4.4. STS dI/dV gate maps of graphene measured at 0 T magnetic field for **(A)** graphene-on- SiO_2 (50 nm from the pit's edge). STS dI/dV gate maps of graphene measured at 8 T magnetic field for **(B)** graphene-on- SiO_2 (50 nm from the pit's edge), **(C)** graphene-on- SiO_2 (10 nm from the pit's edge), and **(D)** suspended graphene (10 nm from the pit's edge into the membrane). The color scale is the dI/dV magnitude, which varies from 0.05 nS (dark) to 1.7 nS (bright) to 1.2 nS (bright).

Figure 4.5. STS of a suspended graphene membrane. **(A)** dI/dV gate map spectra on the suspended graphene membrane at $B = 0$ T. Each map is built of dI/dV vs. V_B spectra taken at multiple fixed V_{GATE} . The color scale is the dI/dV magnitude, which varies from 0.05 nS (dark) to 1.7 nS (bright) for (A) and to 1.2 nS (bright) for (B-D). The white rectangle shows the region where individual spectra are obtained and plotted in (E). The blue arrows indicate spectral bands with positive slope that become more resolved at higher fields in (B) and (C). **(B and C)** dI/dV gate map spectra on the suspended graphene membrane at **(B)** $B = 5$ T and **(C)** $B = 8$ T. The white rectangle in (C) shows the region where individual spectra are obtained and plotted in (F). **(D)** dI/dV gate map spectra at $B = 8$ T, showing the variability in the measurements when moving off and back on the membrane. **(E)** dI/dV vs. V_B spectra from the $B = 0$ T gate map in (A) for gate voltages varying from -1 V to 1 V. **(F)** dI/dV vs. V_B spectra from the $B = 8$ T gate

map in (C) for gate voltages varying from 5 V to 6 V. The spectra are shifted vertically for clarity in (E) and (F). (G) The quantum dot addition energies corresponding to the difference in dI/dV peak positions in the spectra from the gate maps in (C) red symbols, and (D) blue symbols. Energies are converted from bias voltages using the lever arm, $E = \alpha V_B$, where $\alpha = 0.45 \pm 0.03$. The error bars in (G) are dominated by the statistical error in α , which was determined from one standard deviation uncertainties in the measured slopes of the charging lines in the gate maps.

Figure 4.6. Atomistic model of iridium STM tip in MD simulations.

Figure 4.7. The effect of the applied downward force on the calculated membrane shapes for the case of the tip above the center of the membrane. The profiles, from top to bottom, correspond to applied forces of 0, 0.012, 0.037, and 0.061 pN per atom, respectively.

Figure 4.8. STM images and simulations of the deformed graphene membrane induced by competing forces of the STM probe tip and the back gate electric field. (A-D) STM topographic images of the graphene membrane for different gate voltages: 0 V (A), 20 V (B), 40 V (C) and 60 V (D). The membrane is deformed by upward forces from the STM tip and a downward force due to the electric field from the applied V_{GATE} . (E) Atomistic model showing deformations in the graphene membrane interacting with the STM tip. The radii of the tip and membrane in this model are 2.5 nm and 25 nm, respectively. (F) Calculated membrane shapes at the critical tip height for horizontal tip positions of 2.5 nm (black curve), 5.2 nm (blue curve) and 25 nm (red curve) from the membrane edge. A back gate force of 0.012 pN was applied to each atom in the membrane. The grey dashed curve is an envelope showing the membrane height as seen in an STM measurement.

Figure 4.9. Strain components (A) u_{xx} (B) u_{yy} , and (C) u_{xy} as calculated from the per-atom stresses in LAMMPS for the tip over the center of the membrane with zero applied force.

Figure 4.10. Simulations of a graphene membrane shape and corresponding strain and pseudomagnetic field. (A) Simulation of the graphene membrane shape with the STM tip positioned over the center of the membrane when no back gate force is applied. The inset shows a zoomed-in region where the strain is maximal. The radii of the tip and membrane in this model are 2.5 nm and 25 nm, respectively. (B) The pseudomagnetic field, calculated from the strain in (A) (Fig. 4.9), shows spatially alternating fields with three-fold symmetry which can spatially confine carriers.

Figure 4.11. (A) Carbon atom representation of different orders of CG graphene beads. Purple triangles serve as the visual guide showing the inherent correlation between different orders of CG beads. (B) Coarse-grained scheme lattices composed of different orders of CG graphene beads, which preserve the hexagon pattern. Beads are colored in accordance with (A). (C) Left: CG computational model. The STM tip is coarse grained as a single spherical bead and graphene is composed of CG beads of a given CG order as depicted in (A). Right: Comparison of the calculated deflection of the graphene membrane of 50 nm in diameter between the CG method and the fully atomistic molecular dynamics simulations in Ref. (80).

Figure 4.12. Simulation results of STM tip-induced deformation in graphene drumheads and the resulting pseudomagnetic field. Here there is no electrostatic force from a back-gate electrode and the STM probe tip is centered. (A) Out of plane deflection contour. (B-D): Strain components u_{xx} , u_{yy} and u_{xy} , respectively. (E) Top view of the associated pseudomagnetic

field. **(F)** Zoomed-in perspective view of the pseudomagnetic field in the center region of the graphene drumhead.

Figure 4.13. **(A-C)** Intensity of STM tip-induced pseudomagnetic field (blue diamonds) and the corresponding QD size (red dots) as a function of the diameter of the graphene drumhead, for various STM probe tip diameters. The dashed line in (A), (B) and (C) estimates a threshold size of the graphene drumhead that delineates two regimes of the dependence of pseudomagnetic field on graphene drumhead diameter. **(D)** The dependence of the intensity of STM tip-induced pseudomagnetic field (blue diamonds) and the corresponding QD size (red dots) on the diameter of the STM probe tip, for a graphene drumhead of diameter of 1100 nm. The dashed arrows in (D) outline the saturation trend of such a dependence, as the size of the STM probe tip increases. Here there is no electrostatic force from a back-gate electrode and the STM probe tip is positioned above the center of the graphene drumhead.

Figure 4.14. Finite element simulations reveal the highly localized strain distribution in a circular region in the vicinity of the STM probe tip. **(A)** Schematics of the finite element simulation model. The red circle denotes the fixed boundary and the smaller circle near the center defines the loading zone, where the effect of tip/graphene interaction is represented by a uniformly distributed pressure. **(B)** Strain component contours in a cylindrical coordinate system for graphene drumheads of three different diameters. For visual clarity, the strain distribution inside the loading zone (white circle) is not shown. All zoomed-in contours have the same size, which reveal the rather similar strain field in the vicinity of the STM tip, which is the origin of the insensitivity of the pseudomagnetic field to the graphene drumhead size, when the graphene is much larger than the STM probe tip.

Figure 4.15. CG simulation results of the STM tip-induced deformation of the graphene drumhead and associated pseudomagnetic field when a back-gate force is applied and the STM tip is at off-centered locations. Here the diameter of the graphene drumhead is 1.1 μm . **(A)** and **(D)** show the deflection of the graphene drumhead across its diameter. **(B)**, **(C)**, **(E)** and **(F)** show the corresponding pseudomagnetic fields. Case #0: center-positioned STM probe tip with zero back-gate force, replotted from Fig. 4.12 for comparison. Case #1 and case #2: center-positioned STM probe tip with downward back-gate forces of 9.65×10^{-4} eV/Å and 1.61×10^{-3} eV/Å per CG bead, respectively. Case #3 and case #4: tip off-center-positioned by 440 nm and 490 nm with zero back-gate force, respectively. Insets show zoomed-in images of the pseudomagnetic field in the vicinity of the STM probe tip.

Figure. 4.16. Producing uniform pseudomagnetic fields in a planar shaped graphene strip under uniaxial stretch. **(A)** Schematic showing a graphene nanoribbon of varying width under a uniaxial stretch producing a pseudomagnetic field, B_{ps} . The red circle denotes cyclotron orbits in the field giving rise to pseudo-Landau levels in (H). **(B to D)** Contour plots of the resulting strain components in the graphene, ϵ_{xx} , ϵ_{yy} and ϵ_{xy} , respectively, under a 5 % uniaxial stretch. **(E)** Resulting pseudomagnetic fields in the graphene nanoribbon shown in (A) under a uniaxial stretch of 5 %, 10 % and 15 %, respectively. **(F)** Intensity of the pseudomagnetic field as the function of location along the centerline of the graphene ribbon for various applied uniaxial stretches. **(G)** Intensity of the pseudomagnetic field is shown to be linearly proportional to the applied uniaxial stretch and inversely proportional to the length of the graphene ribbon L . **(H)** Local density of states of unstrained graphene and graphene with a constant strain gradient determined by density functional theory calculations. $N=0$ and $N=\pm 1, \pm 2, \pm 3$ Landau levels, corresponding to cyclotron motion in a magnetic field are seen to emerge in the strained graphene, demonstrating a uniform pseudomagnetic field. The wiggles in the results for the

unstrained case result from finite size effects in the calculations. See Section 4.2.4 for further discussion.

Figure 4.17. Producing uniform pseudomagnetic fields in a planar graphene-based heterostructures under uniaxial stretch. **(A)** Schematic showing a 2D hetero-structure consisting of graphene and graphane (or h-BN) bonded to a center piece of graphene under a uniaxial stretch. **(B)** Left: Intensity of the resulting pseudomagnetic field in the graphene domain of a graphene/graphane and a graphene/h-BN hetero-structure, respectively, under a 15 % uniaxial stretch. Here the top/bottom width ratio of the graphene domain $f_r = 0.5$; Right: Contour plot of the resulting pseudomagnetic field in the graphene/graphane hetero-structure. **(C)** Left: Intensity of the resulting pseudomagnetic field in the graphene domain of a graphene/graphane and a graphene/h-BN hetero-structure, respectively, under a 15 % uniaxial stretch. Here the top/bottom width ratio of the graphene domain $f_r = 0$; Right: Contour plot of the resulting pseudomagnetic field in the graphene/graphane hetero-structure.

Figure 4.18. Pseudomagnetic fields in patterned graphene heterostructures superlattices. **(A)** Schematic of a suitably patterned long graphene nanoribbon (left) and the contour plot of the resulting pseudomagnetic field under a 15 % uniaxial stretch (right). **(B)** Schematic of a suitably patterned graphene nanomesh (left) and the contour plot of the resulting pseudomagnetic field under a 15 % uniaxial stretch (right). **(C)** Schematic of a suitably patterned graphene-based 2D superlattice structure (left) and the contour plot of the resulting pseudomagnetic field under a 15 % uniaxial stretch (right). The scale for B_{ps} is from -200 T to 200 T.

Figure 4.19. **(A)** Distribution of ϵ_{yy} in a graphene nanoribbon (as in Fig. 4.16A) subject to a uniaxial applied stretch of 15 %. The bottom panel clearly shows the linear distribution (i.e., constant gradient) of ϵ_{yy} in the nanoribbon. **(B)** A molecular model within a local region in the nanoribbon (indicated by the boxed area in A). The box in B denotes the molecular model containing 32 carbon. The lengths of characteristic carbon-carbon bonds are labeled and the corresponding bond-stretching strains are shaded using the same color scale as in A. **(C)** The DFT model is made of two molecular models in B that are patched head-to-head along their short edges with higher ϵ_{yy} . The box denotes the supercell containing 64 carbon atoms and periodic boundary conditions are applied to the edges of the supercell. **(D)** The DFT model for the unstrained case of the molecular model in C.

Figure 4.20. Linear scaling between the pseudo peak energies E_N from DFT results as shown in Fig. 1H and \sqrt{N} , where N is the peak index.

Figure 4.21. **(A)** The geometry of 25 nm long graphene nanoribbons of three top/bottom width ratio $f_r = 0.35, 0.5,$ and $0.7,$ respectively, with two their long edges of each nanoribbon prescribed by Eq. (4.2.16). **(B)** The corresponding intensities of the resulting pseudomagnetic field from finite element simulations under a 5 % uniaxial stretch.

Figure 4.22. **(A)** Atomistic simulation models for the graphene nanoribbon. **(B-D)** Atomistic simulation results on pseudomagnetic fields in the graphene nanoribbon under a uniaxial stretch of 5 %, 10 % and 15 %, respectively.

Figure 4.23. **(A)** Atomistic simulation models for a graphene/graphane 2D hetero-structure with straight material domain boundary. **(B)** Atomistic simulation results on pseudomagnetic fields in the graphene domain in (A) under a uniaxial stretch of 15 %. **(C)** Atomistic simulation

models for the graphene/h-BN 2D hetero-structure with straight material domain boundary. **(D)** Atomistic simulation results on pseudomagnetic fields in the graphene domain in **(C)** under a uniaxial stretch of 15 %.

Figure 5.1 A bottom-up scalable CG simulation scheme of graphene. **(A-C)** Mapping from atomic graphene (cyan) to 1st order CG beads (red), to 2nd order CG beads (green), and to 3rd order CG beads (grey). Note that the hexagonal lattice symmetry is maintained in all orders of CG. **(D-F)** Schematics of CG parameterization strategies to determine bond force constant via equi-biaxial stretching **(D)**, bond angle constant via equi-biaxial bending **(E)**, and van der Waals constants via out-of-plane separation **(F)**, respectively.

Figure 5.2 **(A)** CG model for the patterned GNM. **(B-G)** Snapshots of the deformed GNM under various applied tensile strains. Red arrow indicates the direction of applied tensile load. **(H)** Resultant force in the GNM as a function of applied elongation. The light green shaded region highlights the extremely-compliant region of the GNM while the light blue shaded region highlights the highly-compliant region with an effective stiffness of about 15.8 N/m. Here $L_G = 351$ nm, $W_G = 199$ nm, $L_C = 50$ nm and $W_R = 2$ nm.

Figure 5.3 Effect of pattern geometry of GNM on the deformation behavior and stretchability of GNM. **(A-C)**: Resultant force in GNM as a function of applied elongation for varying W_R (2 nm, 4 nm and 8 nm) with a fixed $L_C = 50$ nm; **(E-G)**: Varying L_C (50 nm, 75 nm and 100 nm) with a fixed $W_R = 2$ nm; **(I-K)**: W_R (2 nm, 4 nm and 8 nm) with a fixed ratio $L_C/W_R = 25$. **(D)**, **(H)**, and **(L)**: Comparing the corresponding effective stiffness of the GNM in highly compliant stage (shaded in light blue) with that of pristine graphene. Total number of carbon atoms in the corresponding graphene network: (a) 353,552; (b) 671,536; (c) 981, 040; (f) 479,408; (g) 815,408; (j) 1,041,584; (k) 4,158,272 (simulation done by CG of 2nd order given the GNM in micron size).

Figure 5.4 **(A)** A possible design of a biaxially stretchable functional structure with stiff device islands (hosting device components) interconnected via GNMs. Applied tension can be largely accommodated by the extremely compliant GNMs elongating along their armchair directions, with minimal elongation along other directions. **(B)** Tensile behavior of the GNM in Fig. 5.2 under elongation along its zigzag direction, which shows the similar two deformation stages. Dashed arrow shows armchair direction, which has 30° rotation from zigzag direction.

Figure 5.5. An anomalous but desirable scaling law of mechanical properties requires defeating the conventional conflict between strength and toughness.

Figure 5.6. **(A)** Hierarchical structure of wood fibers and the characteristic of cellulose fibrils. Note the rich inter-chain hydrogen bonds among neighboring cellulose molecular chains. **(B)** Atomic structure of a cellulose chain repeat unit. Note the six hydroxyl groups (red circles) in each repeat unit.

Figure 5.7. An anomalous scaling law of strength and toughness of cellulose nanopaper. **(A)** Schematic of cellulose nanopaper, made of a random network of NFC fibers. Inset shows the HRTEM image of a ~11 nm NFC fiber. **(B)** Stress-strain curves of cellulose paper made of cellulose fibers of various mean diameters. As the cellulose fiber diameter decreases from μm scale to nm scale, both tensile strength and ductility of the cellulose paper increases significantly, leading to an anomalous scaling law shown in **(C)**: The smaller, the stronger AND the tougher. **(D)** further reveals that the ultimate tensile strength scales inversely with the square root of cellulose fiber diameter. **(E)** Optical (inset) and SEM images of a CNT film

made of network of CNTs. **(F)** Lack of inter-CNT hydrogen bonds, the CNT film has a much lower tensile strength and toughness than the cellulose nanopaper, although the constituent CNT bundles and NFC fibers have comparable diameter (11 nm).

Figure 5.8. SEM images of **(A)** the surface of the as-made cellulose nanopaper (with a mean diameter of NFC fibers of 28 nm) and **(B)** the surface of the as-made CNT paper, both showing random distribution of constituent fibers. **(C and D)** SEM images of the cross-section of failure of the cellulose nanopaper and CNT paper, respectively, after the tensile tests. In both C and D, it is evident that the initially random network of constituent fibers aligns along the tensile loading direction indicated by the arrows.

Figure 5.9. Envisioned molecular-level toughening mechanism of cellulose nanopaper: Failure involves a cascade of hydrogen bond forming, breaking and re-forming events, which dissipate a significant amount of energy, thus lead to much enhanced fracture toughness of cellulose nanopaper.

Figure 5.10. Atomistic simulations to demonstrate the hydrogen bond breaking and re-forming events among cellulose molecular chains. **(A)** Simulation model of a cellulose bundle contains seven cellulose molecular chains. Top view only shows the middle three chains for visual clarity. **(B)** Variation of total potential energy as a function of the sliding displacement of the center cellulose chain out of the bundle. Insets clearly show the hydrogen bond breaking and re-forming events (dotted circles), each of which dissipates energy. **(C)** illustrates relative cellulose chain sliding, during which a series of hydrogen bond breaking and re-forming events happen when neighboring hydroxyl groups come close to each other. The boxed region shows the evolution of newly formed hydrogen bonding region during pulling-out process. Only middle three chains are shown for visual clarity.

Figure 5.11. **(A)** Simulation models of the two surface areas in direct contact for parallel sliding between two NFC fibers (top panel) and that between two SWCNT bundles (bottom panel). **(C)** Variation of total potential energy as a function of relative displacement of parallel sliding between two NFC fibers (green) and that between two SWCNT bundles (blue). The contribution from hydrogen bonds between NFC fibers (red) is included for comparison. **(E)** The evolution of resistant force during parallel sliding of two neighboring NFC fibers (red) and two neighboring SWCNT bundles (blue). **(B), (D)** and **(F)**: The results for the case of perpendicular sliding, in correspondence to A., C. and E., respectively.

Figure 5.12. Cross-section view of the interface between two neighboring NFCs in Fig. 5.11. The contact surface is along (110) plane of the $I\beta$ cellulose nanocrystal structure.

Figure 5.13. **(A)** Schematic of a GO-NFC hybrid microfiber consisting of aligned GO nanosheets and NFC chains along the microfiber direction. The synergistic interaction between NFC and GO leads to greatly improved mechanical strength, elastic modulus and toughness. **(B)** Structural representation of how metal ion (Ca^{2+}) infiltration further increases the bonding between building blocks in the hybrid microfiber.

Figure 5.14. **(A)** AFM image of a GO nanosheet; inset is an optical image of the GO nanosheet solution. **(B)** AFM image of NFC; inset is an optical image of the NFC solution. **(C)** Polarized optical microscopy image of the GO-NFC liquid crystal solution showing a typical nematic LC phase; inset is an optical image of the GO-NFC solution used for wet spinning. **(D)** Polarized optical microscopy image of the GO-NFC solution after drying which shows clear alignment.

Figure 5.15. **(A)** Wet spinning process where 4 hybrid microfibers are spun at once. **(B)** Optical image of fibers from the 1 mL spinning solution wrapped around a 15 cm diameter steel stick. **(C)** SEM image of two hybrid microfibers twisted together. **(D)** POM image of a hybrid microfiber after extrusion from a syringe. **(E)** POM image of a hybrid microfiber that has dried in air for 10 s. **(F)** POM image of a hybrid microfiber under tension after drying completely in air.

Figure 5.16. Typical stress-strain curves of tensile testing GO microfibers, NFC microfibers, and GO-NFC hybrid microfibers before **(A)** and after **(B)** metal ion infiltration.

Figure 5.17. Schematics depicting the cross section. **(A)**: GO microfiber. **(B)**: GO-NFC hybrid microfiber. **(C)**: GO-NFC hybrid microfiber after infiltration. The GO microfiber shows a corrugated rough surface and loose GO nanosheet packing. When NFC is added, the GO-NFC hybrid microfiber possesses a smoother surface and a denser building block packing. After infiltration in the 10 wt% CaCl_2 solution, the fiber surface is even smoother and possesses an even denser building block packing compared to the GO-NFC hybrid microfiber. SEM images of the surface morphology. **(D)**: Porous GO microfiber. **(E)** GO-NFC hybrid microfiber. **(F)**: GO-NFC hybrid microfiber after metal ion infiltration from the CaCl_2 solution. After NFC is added, the surface becomes dense and smooth but after infiltration, the fiber becomes exceptionally dense and smooth. SEM images displaying the cross section of GO-NFC hybrid microfiber. **(G-I)**: Before CaCl_2 infiltration. **(J-L)**: After CaCl_2 infiltration.

Figure 5.18. **(A-B)** Schematics showing the role of NFC by providing additional bonding options between GO sheets. **(C-D)** Molecular dynamics models for GO sheets with and without NFC. Insets show typical equilibrium structural configurations from different perspectives before the top sheet slides. **(E)** Comparison of the sliding force as a function of sliding displacement between the two cases (i.e. with and without NFC).

Figure 5.19. **(A-B)** Schematics show the role NFC plays in providing additional bonding options between the GO sheets (-O- only). **(C-D)** Molecular dynamics models for GO sheets (-O- only) with and without NFC. Insets show typical equilibrium structural configurations from different perspectives before the top sheet slides. **(E)** Comparison of the sliding force as a function of sliding displacement between the two cases (i.e. with and without NFC).

Figure 5.20. **(A-B)** Schematics demonstrate the role that GO plays by providing additional bonding sites (dashed boxes) between the NFC chains. **(C-D)** Molecular dynamics models for NFC chains with and without GO nanosheets. Insets show typical equilibrium structural configurations from different perspectives before the right NFC chains slide out. **(E)** Comparison of the sliding force as a function of sliding displacement between the above two cases.

Chapter 1: Introduction

1.1. Background and motivation

When numerous carbon atoms are densely packed into a honeycomb lattice in a plane with an inter-atomic distance approximately 0.142 nm, they form a two-dimensional (2D) crystal that has inspired an outburst of research endeavors regarding this material in various fields for over a decade. This groundbreaking material is called graphene, as epitomized by the 2010 Nobel Prize in Physics, opening up a new era in materials science, physics and engineering. Graphene is considered as the building block of all members in the carbon family, such as fullerenes, carbon nanotubes and graphite (Fig. 1.1).

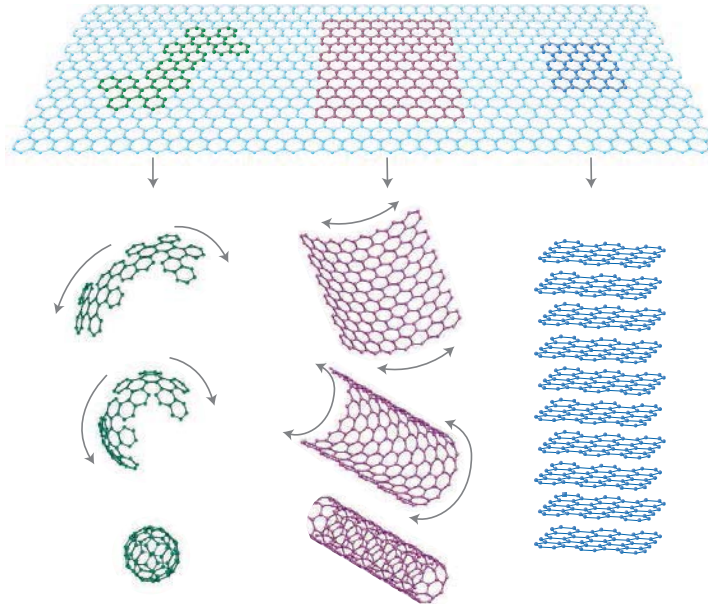


Figure 1.1. Carbon family members are derived from graphene (1).

In 2004, the scientist at the University of Manchester first reported that they have obtained planar graphene on silicon substrate by using scotch tape to peel off thin layers from bulk graphite (2), which was thought to be a 3D integral of multiple monolayer graphene. The rationale behind this idea with scotch tape is surprisingly straightforward. Since graphite is just many graphene sheets stacked together by weak van der Waals force, the mechanical exfoliation can easily break the bonds between graphene layers and leave graphite flakes with different thickness on the tape. Soon the existence of graphene in a free state was confirmed by other research groups (3) as well as the fabrication of free-standing graphene (4).

For over a decade, the method to fabricate graphene has evolved painstakingly. Mechanical exfoliation (2) is the most straightforward method to fabricate graphene, yet it suffers from the rather small graphene size and low efficiency. During the search of desirable fabrication method, the first objective is to achieve massive production of graphene, which has been fulfilled by methods such as chemical vapor deposition (CVD) on metal substrate (5-8), graphene oxide reduction (9) and epitaxial growth on silicon carbide substrate (10). However, those methods suffer from limited grain size of single-crystalline graphene. The second objective is then to obtain large-sized single-crystalline graphene while maintaining the massive productivity. Only until very recently, single-crystalline graphene with grain size up to centimeters has been fabricated (11, 12), which is a giant leap towards the commercial realization of various functional devices based on single-crystalline graphene.

1.1.1. Superior material properties of graphene

It is the combination of a variety of superior material properties in one that makes graphene amazingly significant in advancing the frontier of materials science, physics and engineering, which is literally unprecedented. These superior material properties are mostly due to the unique nature of graphene's 2D planar structure. Nobel Prize in Physics was awarded for the rise of graphene, only after 6 years of its experimental discovery.

Mechanical properties

Being the strongest material ever discovered, graphene has the young's modulus of ~ 1 TPa and the tensile strength of 130 GPa, which is 200 times larger than that of steel (13). Its fracture strain is up to 25% (13). Atomistic simulations show that the fracture strain is lower for the uniaxial tension along armchair direction than along zigzag direction (14).

Negative coefficient of thermal expansion

Unlike most materials that expand in volume when the temperature rises, graphene shrinks when heated up, leading to the formation of wrinkles. The experimental measured coefficient of thermal expansion (CTE) is $\sim -7 \times 10^{-6} \text{ K}^{-1}$ at room temperature (15).

Quantum Hall effect

In graphene, the electrons are confined in a two-dimensional space, which offers ideal platform to experimentally probe the quantum Hall effect, which is a typical quantum-mechanically enhanced transport phenomena when electrons are confined in two-dimensional materials. In particular, an unusual half-integer quantum Hall effect for both electron and hole carries in graphene has been observed (3), leading to potential applications in carbon based electronic and magneto-electronic devices.

Band structure

Intrinsic graphene is a zero-gap semiconductor (2). Nevertheless, graphene nanoribbon with a finite width shows a completely different band structure (16, 17). Experimentally a 200 meV energy gap can be achieved by narrowing graphene nanoribbon to a width of 15 nm (18). For bilayer graphene, the energy gap up to 250 meV can be tuned by two gate voltages (19).

Dirac fermions

In the band structure of intrinsic graphene, there is a linear dispersion relation for the electron and hole carriers close to the Fermi level. This leads to zero effective mass for electrons and holes (1). As their behavior can be described by the Dirac equation, they are also called Dirac fermions (20). They mimic relativistic particles with zero mass and have an effective “speed of light”.

Electron mobility and electronic conductivity

Graphene has the highest electron mobility ever measured. At room temperature, its electron mobility is in excess of $15,000 \text{ cm}^2\text{V}^{-1}\text{s}^{-1}$, 100 times higher than that of silicon

(21). Graphene also has the lowest known resistivity ($10^{-6}\Omega \cdot \text{cm}$) at room temperature, less than that of silver (22).

1.1.2. Morphologic properties of graphene

Ripples/wrinkles are expected to strongly influence electronic properties by inducing pseudomagnetic fields and changing local potentials (23-28). Therefore, manipulating the morphology of graphene has a profound significance in engineering its electronic properties.

Both experiments and atomistic simulations have shown that the free-standing graphene has intrinsic ripples (4, 29). The success to control the ripple orientation, wavelength and amplitude in suspended graphene has opened up new possibilities for strain engineering of graphene on its electrical and optical properties (15), and sp^2 -to- sp^3 band gap creation at selective locations by means of functionalization (30).

Graphene is only one-atom thick and has strong adhesion (31), making it convenient to use substrate surfaces or nanoscale scaffolds to regulate the morphology of graphene. High-resolution scanning tunneling microscopy (STM) have indicated that the morphology of SiO_2 substrate supported graphene can closely matches that of the SiO_2 over the entire range of length scales with nearly 99% fidelity (32). It has been demonstrated that graphene and few-layer graphene can partially conform to the surface morphology of various substrates (e.g., GaAs, InGaAs and SiO_2) (33-37). In particular, graphene and few-layer graphene can conform to substrate-supported nanoparticles (NPs). Depending on the thickness of graphene layers and the dispersion density of nanoparticles, the percolation of wrinkles in graphene can be tuned (38).

1.1.3. Unconventional graphene nanostructures and their potential applications

Carbon nanoscroll

Carbon nanoscroll (CNS) is formed by rolling a graphene sheet into a scroll like structure (Fig. 1.2) (39). Since its discovery in 2003 (40), CNS has been employed in wide applications such as hydrogen storage, gigahertz oscillators, nanopumps, nanoactuators, supercapacitors, tunable water channel and drug delivery (41-47).

There are several ways to fabricate CNSs. The experimental discovery of CNSs was adopting a chemical approach, in which graphite was first intercalated using alkali metals and then the resulting exfoliated graphite could transform into scrolls upon sonication (40). Another experiment showed that when immersed in isopropyl alcohol (IPA) solution, a SiO₂-supported graphene monolayer could spontaneously roll up to form a CNS (48). Molecular dynamics simulations have shown that, carbon nanotubes, nanowires, can activate the folding of freestanding graphene to form CNSs (48, 49). Experimentally, the nanowire templated scrolling of graphene was reported (50). Until very recently, it was reported that nanoparticles induced CNSs formation could help realize superlubricity (51).

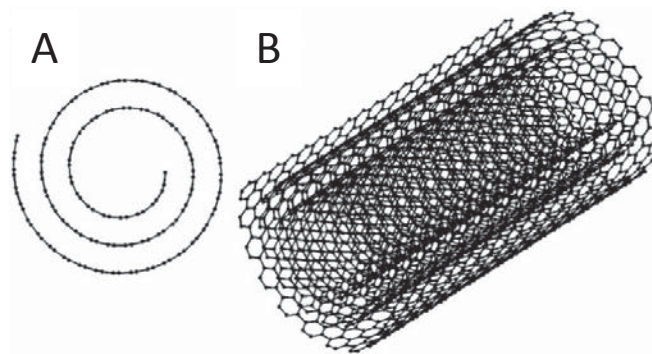


Figure 1.2. Structure of carbon nanoscroll (39). (A) End view. (B) Perspective view.

Graphane

Although bulk graphite is a rather chemical inert material, the surface of each single layer graphene is quite reactive. Graphane is the name for a class of hydrogenated graphene structures, in which every carbon atom of the graphene layer is covalently bonded to a hydrogen atom, as shown in Fig. 1.3. Such functionalization causes the hybridization of the carbon atoms in graphene changing from sp^2 to sp^3 . As a result, the graphene layer is no longer a perfectly planar structure (52). Hydrogenation changes the graphene's mechanical and electrical properties, while such process is reported to be reversible (30).

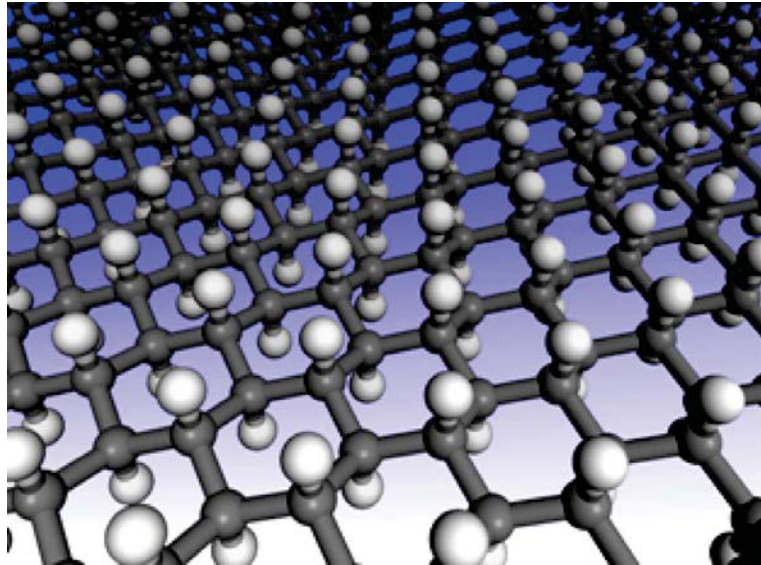


Figure 1.3. Structure of graphane (52). The carbon atoms are shown in gray and the hydrogen atoms in white.

Graphene quantum dot

Graphene can be used as the base material for electronic circuitry that is envisaged to consist of nanometer-sized elements (1, 53). As an alternative of graphene nanoribbon,

zero-dimensional graphene quantum dot has exhibited extraordinary properties (54, 55). The graphene quantum dot devices can be carved entirely from graphene. At large sizes (>100 nm), they behave as conventional single-electron transistors, exhibiting periodic Coulomb blockade peaks. For quantum dots smaller than 100 nanometers, the peaks become strongly nonperiodic, indicating a major contribution of quantum confinement. For even smaller devices (<30nm), the experimental behavior is completely dominated by quantum confinement. Short constrictions of only a few nanometers in width remain conductive and reveal a confinement gap of up to 0.5 eV, demonstrating the possibility of molecular-scale electronics based on graphene.

Since the graphene quantum dot is rather small in size (Fig. 1.4), the fabrication of graphene quantum dot has been subjected to intensive investigation (56-58).

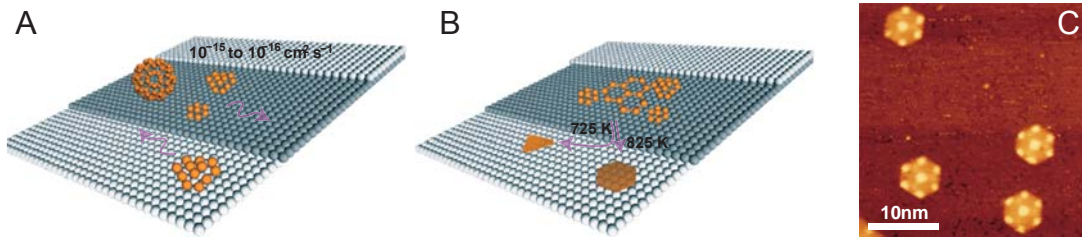


Figure 1.4. A growth mechanism and experimental image for graphene quantum dot (GQD) (58). **(A)** Schematic showing that the majority of C₆₀ molecules adsorb on the terrace, and these decompose to produce carbon clusters with restricted mobility. **(B)** Schematic showing that temperature-dependent growth of GQDs with different equilibrium shape from the aggregation of the surface diffused carbon clusters. **(C)** STM image for hexagonal equilibrium shaped GQDs produced from C₆₀ derived carbon clusters.

Graphene nanomesh

Processing graphene sheets into nanoribbons with widths of less than 10 nm can open up a bandgap that is large enough for room-temperature transistor operation, but nanoribbon devices often have low driving currents or transconductances (60, 61).

Moreover, practical devices and circuits will require the production of dense arrays of ordered nanoribbons, which remains a significant challenge (62, 63). Therefore graphene nanomesh (GNM) has emerged as a new type of carbon nanostructure which has been subjected to intensive study, largely due to its novel electronic properties (59, 64, 65). Geometrically, graphene nanomesh is a large-scale patterned network that connects numerous graphene nanoribbons. It is the semiconducting properties of graphene nanoribbons that render GNM the potential application in electronic devices.

Figure 1.5 illustrates an approach to fabricating GNMs (59). A 10-nm-thick silicon oxide (SiO_x) film is first evaporated onto graphene as the protecting layer and also as the grafting substrate for the subsequent block copolymer nanopatterning. The poly(styrene-block-methyl methacrylate) (P(S-b-MMA)) block copolymer thin film with cylindrical domains normal to the surface is then fabricated as used as the etching template, and a CHF_3 -based reactive-ion etch (RIE) process followed by oxygen plasma etch is used to punch holes into the graphene layer. The resulting graphene nanomeshes can have neck widths as low as 5nm. Graphene nanomesh field-effect transistors made from such materials can support currents nearly 100 times greater than individual graphene nanoribbon devices and the on-off ratio can be tuned by varying the neck width.

A method to fabricate GNM on a large scale has been developed (64). The method is based on patterning graphene using self-assembled monolayers of monodisperse colloidal microspheres (Fig. 1.6). The resulting GNMs exhibit promising electronic properties featuring high conductivities and ON-OFF ratios. The apparent advantages

of the present method are the possibilities of fabricating GNMs with different periodicities, ranging from ~ 100 nm to several μm , and also varying the periodicity of the GNM and the neck width independently, which should result in graphene nanostructures with different electronic properties.

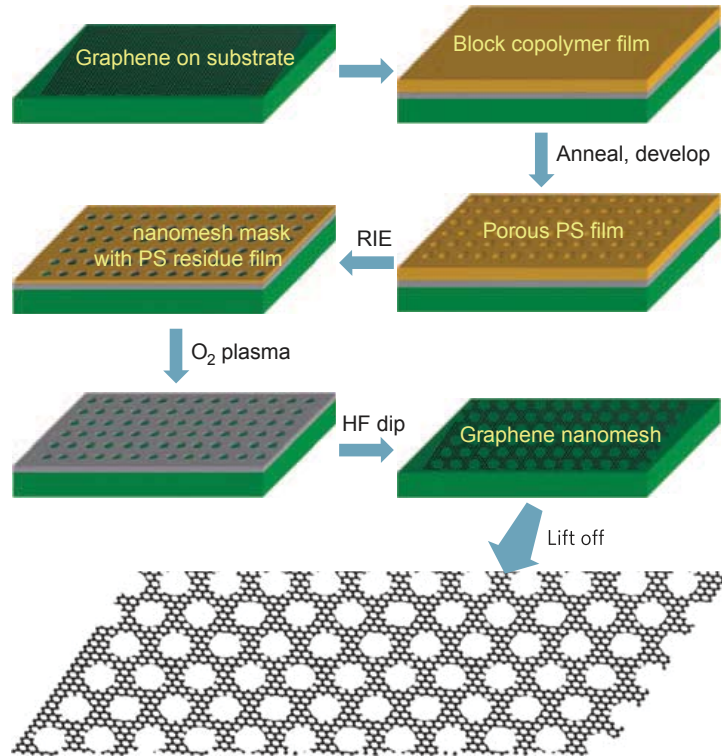


Figure 1.5. Schematic of fabrication of a graphene nanomesh (59).

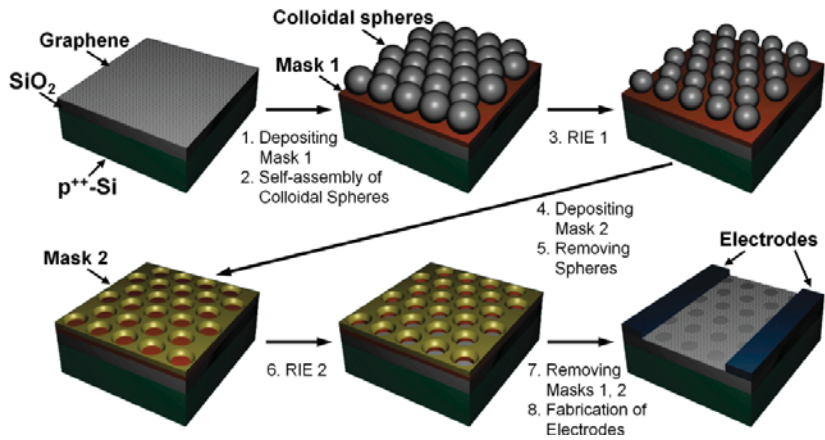


Figure 1.6. Scheme of the fabrication of large-scale graphene nanomesh (64).

Graphene-based hydrogel

Hydrogels are soft materials incorporating interconnected polymer chains with a significant amount of water retained in the network structure. This is most often due to the presence and self-assembly of small gelling molecules which may covalently or physically cross-link the macromolecules. Hydrogels have many potential uses in biomedical and tissue engineering as well as sensor technology. Hybrid materials involving both organic polymers and inorganic particles such as clays have been studied with the aim to improve the mechanical properties of the hydrogel.

Recent studies have also focused on incorporating graphene into hydrogels to create multifunctional materials (66-69). Gelation using graphene is attractive due to the high surface area to volume ratio of the particles as well as the ability to engineer three dimensional materials with vastly improved mechanical properties. For example, it has been demonstrated that graphene oxide and DNA can be self-assembled into a hydrogel with high mechanical strength, stability and adsorption capacity (70). A tough and highly stretchable graphene oxide/polyacrylamide (GO/PAM) nanocomposite hydrogels (Fig. 1.7) has been fabricated and the fracture elongation is over 3000% (71). This is a demonstration of the fabrication of such hydrogels with high tensile strength, high toughness and superior ductility by adding a small amount of GO as the cross-linker. These enhancements resulted from the combination of high specific surface area of GO and the strong interfacial interaction between GO and the polymer matrix (71).

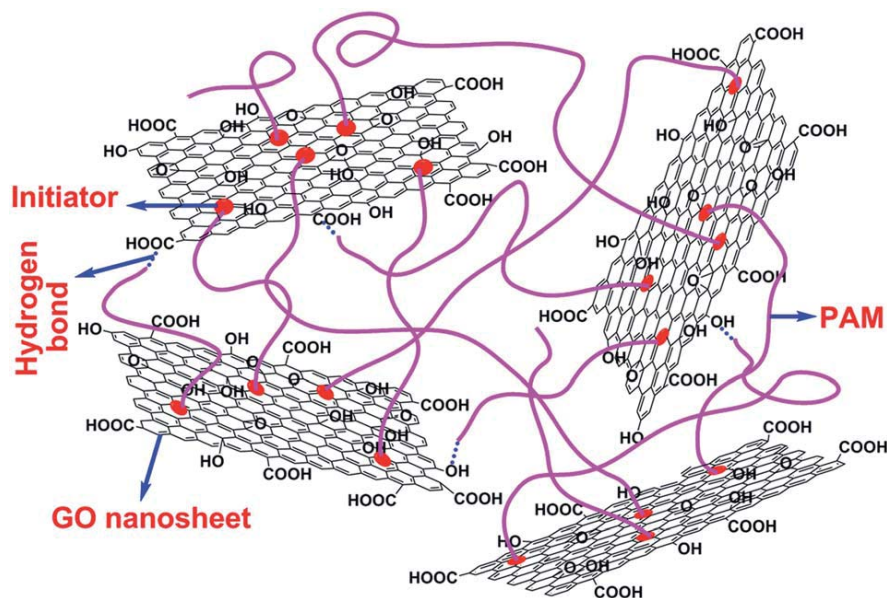


Figure 1.7. GO as the cross-linker in a PAM/GO nanocomposite hydrogel (71).

1.2. Scope and goals of this dissertation research

This dissertation research has several topics, which combined contribute to two major visions about graphene:

- Manipulating the morphology of graphene and mechanical strain in graphene has a great significance in engineering its electronic properties and designing unconventional carbon nanostructures.
- Manipulating the surface chemistry of graphene (i.e., functionalization, oxidization, etc.), geometry of graphene and the interaction between graphene and other nanomaterials can give rise to an array of unconventional nanostructures and materials with desirable mechanical properties (i.e., stretchability) and functionalities.

Chapter 2 studies the formation of wrinkles in graphene regulated by nanoparticles, which enables the design of potential graphene-based electronics. Inspired by recent progresses on functionalization and patterning of graphene, Chapter 3 demonstrates hydrogenation assisted manipulation of graphene's morphology, a feasible and robust approach to enabling the formation of unconventional carbon nanostructures, through systematic molecular dynamics simulations. Chapter 4 presents a comprehensive investigation to the design of pseudomagnetic field in graphene via strain engineering. Chapter 5 provides a pioneering study on the engineering of the strength, toughness, compliance, stretchability of graphene-based unconventional nanomaterials. In Chapter 6, the major findings and contributions of the dissertation are summarized and discussed, followed by an outlook of future work.

Chapter 2: Programmable wrinkling morphology of graphene

Wrinkle formation is an important feature that can enable novel design of electronic devices. Graphene with curvature has a finite energy gap while flat graphene has zero energy gap. For example, a wide-bandgap metal-semiconductor-metal nanostructure can be made entirely from graphene due to patterned curved geometry (Fig. 2.1A) (72). Figure 2.1B shows that the geometry of wrinkles directly affects graphene's energy gap (73). When graphene is placed on a pre-stretched substrate, a crumpling/rippling pattern can be generated upon releasing the pre-strain in the substrate. For example, Fig. 2.2A shows that a graphene sheet initially placed on a biaxially pre-stretched substrate crumples after the strain in the substrate is released (74). The wettability and resistance of the crumpled graphene surface can be tuned. Figure 2.2B shows the formation of periodically rippled graphene nanoribbons in a similar fashion. The resistance of such rippled graphene device can be modulated (75).

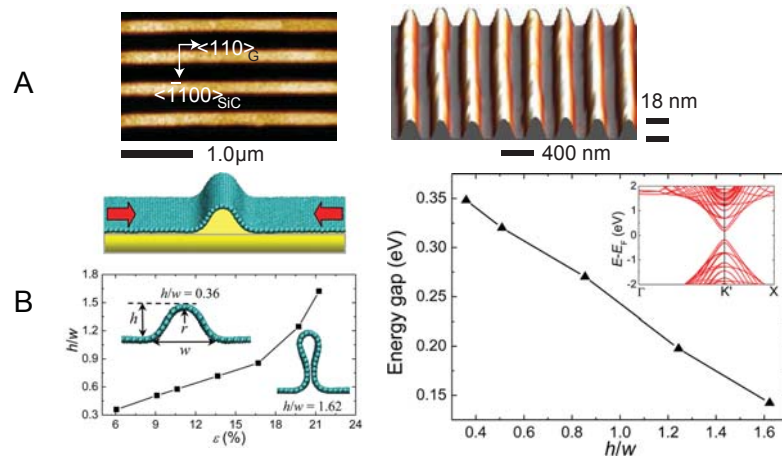


Figure 2.1. Wrinkles in graphene on rigid substrate (72, 73). (A) Left: AFM top view of sidewall ribbons showing their long-range order. Right: Perspective AFM view of 18-nm-deep graphitized trenches. (B) Left: A wrinkle is created by applying a uniaxial in-plane compression on substrate-supported graphene sheet. The compressive strain is related to the size ratio of wrinkle height to width. Right: Energy gap for different size ratios.

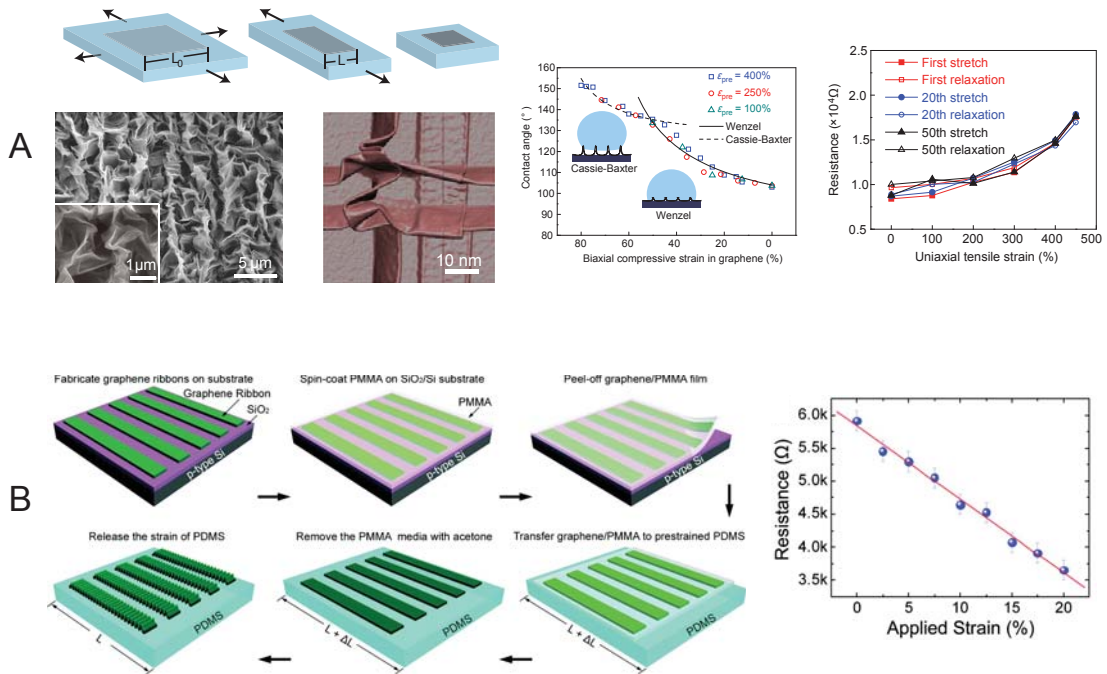


Figure 2.2. Wrinkles in graphene on stretchable substrate (74, 75). **(A)** Crumpled graphene after the release of pre-biaxial-strain in substrate. The wettability and resistance of such crumpled surface can be tuned by further applying tensile strain. **(B)** Rippled graphene nanoribbons after the release of pre-uniaxial-strain in substrate. The resistance of such rippled graphene device can be modulated by applied strain.

The significance of the wrinkles in graphene has motivated the research work in this chapter. In Section 2.1, we first study the morphology of a graphene bilayer with intercalating silicon nanoparticles. In Section 2.2, we investigate the wrinkling morphology of a graphene monolayer on a substrate decorated with silicon dioxide nanoparticles.

2.1. Morphology of a graphene bilayer intercalated by nanoparticles

The dispersion of the silicon (Si) nanoparticles (NPs) in between graphene layers is governed by the energetic interplay between the graphene layers and the Si NPs (76). The typical size of the Si NPs dispersed in between graphene layers is a few nanometers in diameter, much larger than the equilibrium graphene-graphene interlayer distance

(~0.34 nm). As a result, the graphene layers are intercalated by the Si NPs and assume corrugated morphology to wrap around the Si NPs (77). Such corrugated morphology of the graphene layers results from the following energetic interplay. On the one hand, the graphene-graphene interlayer interaction is mainly van de Waals type. Therefore, the graphene layers tend to assume their equilibrium distance to reduce the interaction energy. On the other hand, the corrugation of graphene layers due to Si NP intercalation causes the bending and stretching of the graphene, and thus leads to an increase of the graphene strain energy. The tighter the graphene layers wrap around the Si NPs, the higher the resulting graphene strain energy, and the lower the graphene-graphene interaction energy. The equilibrium morphology of the graphene-NP structure is dictated by minimizing the total free energy of the structure, which includes two dominant contributions, i.e., the graphene strain energy and the graphene-graphene interaction energy. Given the large in-plane dimension of the graphene (on the order of microns or higher), the weak interaction between the graphene and Si NPs (also van de Waals type) is of secondary significance in the total free energy. So is the strain energy of the Si NPs, which is negligible due to the weak graphene-Si interaction and out-of-plane flexibility of the graphene.

We first conduct molecular dynamics (MD) simulations to determine the equilibrium morphology of the graphene layers intercalated by a single Si NP, which correspond to the limiting case when the Si NPs are widely dispersed in between graphene layers thus the interaction among Si NPs is negligible. In consideration of the computational cost, we model a graphene bilayer intercalated by a Si NP, corresponding to the two closest neighbor graphene layers that wrap around the Si NP in a real material. Such a

simplified model can capture the dominant energetic interplay, given that the graphene-graphene interlayer interaction decays quickly as their distance increases, and thus the contribution from the next neighbor graphene layers to the interaction energy is of secondary significance. In the MD simulations, each graphene layer has a size of 50 nm by 70 nm. Single crystal Si NPs of various diameters (i.e., 2~6 nm) are used to study the effect of NP size on the intercalated graphene morphology. The carbon-carbon (C-C) covalent bonds in the graphene are described by the adaptive intermolecular reactive bond order (AIREBO) potential (78). The non-bonded graphene-graphene interlayer interaction and the graphene-Si interaction are described by two Lennard-Jones pair potentials , $V_{C-C}(r) = 4\epsilon_{C-C}(\sigma_{C-C}^{12}/r^{12} - \sigma_{C-C}^{12}/r^6)$ and $V_{C-Si}(r) = 4\epsilon_{C-Si}(\sigma_{C-Si}^{12}/r^{12} - \sigma_{C-Si}^{12}/r^6)$, respectively, where $\epsilon_{C-C} = 0.00284\text{eV}$, $\sigma_{C-C} = 0.34\text{ nm}$, $\epsilon_{C-Si} = 0.00213\text{eV}$, and $\sigma_{C-Si} = 0.15\text{ nm}$. To reduce the computation cost, the Si NP is assumed to be rigid (i.e., whose bonding energy remains as a constant). In each MD simulation case, the graphene bilayer is prescribed with an initial morphology that, near the Si NP, it bulges out into a conical dome in each layer to house the Si NP inside and far away from the Si NP, it remains flat with an interlayer distance of 0.6 nm. The Si NP is first fixed and the graphene bilayer is equilibrated for 30 ps to minimize the dependence of the final results on the initial prescribed morphology, then the Si NP is set free to evolve with the graphene bilayer until an equilibrium is reached. The MD simulations are carried out using LAMMPS (79) with Canonical Ensemble at temperature 300 K and with time step 1 fs.

Figure 2.3 shows the simulated morphology of graphene intercalated by a single Si NP of various diameters, $d_{NP} = 2\text{ nm}, 3\text{ nm}, 4\text{ nm}, 5\text{ nm}$ and 6 nm , respectively. For

visual clarity, the top panel in Fig. 2.3 shows the top graphene layer and the bottom one shows the Si nanoparticle and the bottom graphene layer. If the Si NP is small (e.g., $d_{NP} = 2 \text{ nm}$), each graphene layer bulges out into a dome to wrap around the Si NP. As the size of the Si NP increases, the graphene layers start to form ridged morphology to wrap around the Si NP. The locations of such ridges are approximately complementary in the top and bottom graphene layers.

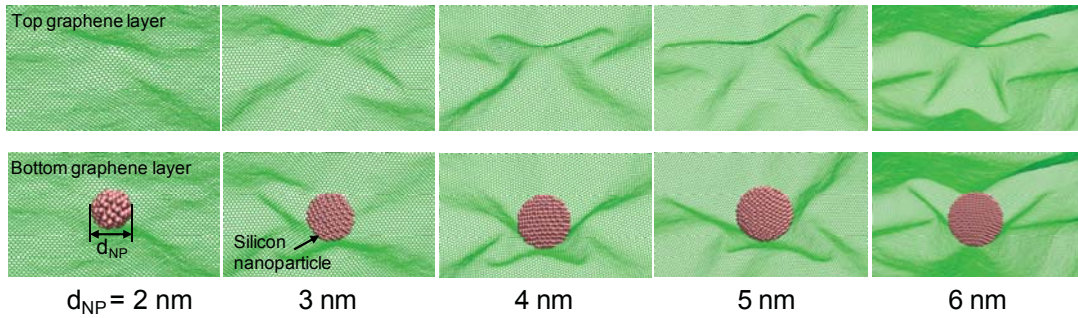


Figure 2.3. The morphology of graphene intercalated by a single Si NP of various diameters, d_{NP} . For visual clarity, the top panel shows the top graphene layer and the bottom one shows the Si NP and the bottom graphene layer (only the portion near the Si NP is shown). Note the ridged morphology formation as d_{NP} increases.

The formation of ridged morphology in the graphene bilayer can be understood as follows. As the size of the Si NP increases, forming a smooth conical dome in each graphene layer to wrap around the Si NP requires deflecting and stretching the graphene bilayer in a larger area. The resulting increase in the graphene strain energy and the graphene-graphene interaction energy becomes larger than that due to forming ridged morphology. In ridged morphology of the graphene, even though the curvature of the graphene corrugation along the ridges is higher than that of a smooth conical dome, it only requires corrugating a smaller area of the graphene layers and the graphene portions between neighboring ridges are much less corrugated and have an interlayer

distance closer to its equilibrium value. As a result, ridged morphology of the graphene corresponds to a lower total free energy state, thus is more favorable.

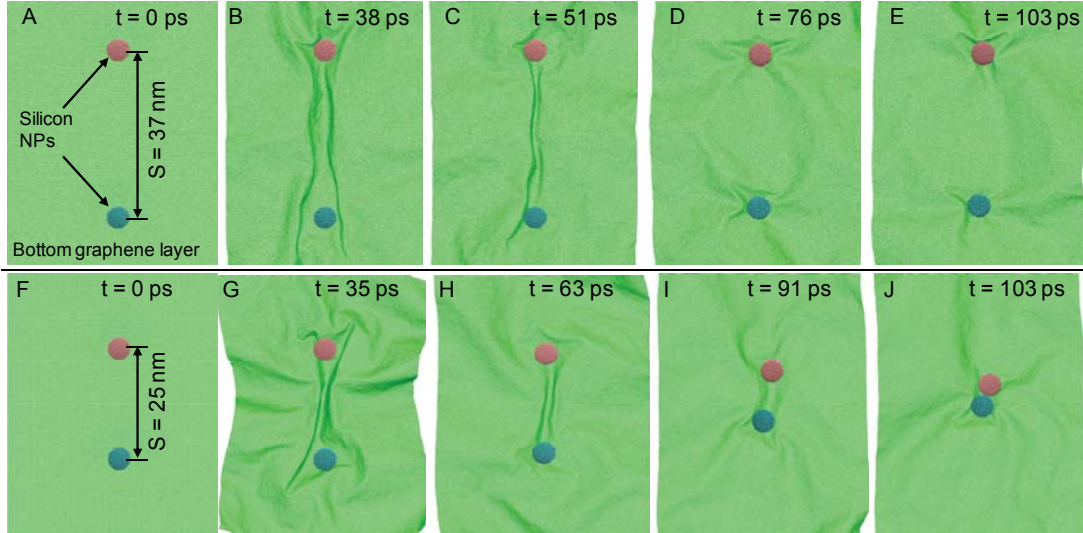


Figure 2.4. (A-E) The morphologic evolution of the Si NP-graphene system over simulation time. For visual clarity, only the bottom graphene layer and the Si NPs are shown. When the distance between the two Si NPs is sufficiently large (here $d_{NP} = 5nm$, and $S = 37nm$), the two Si NPs remain dispersed and are wrapped individually by the graphene bilayer. The intercalated graphene morphology near each Si NP is similar to that shown in Fig. 2.3. (F-J) When the distance between the two Si NPs is below a critical value (here $d_{NP} = 5nm$, and $S = 25nm$), the two Si NPs evolve to come closer and eventually bundle together.

We next consider how the structural morphology of the Si NP-graphene system evolves as the dispersion distance between the Si NPs varies. To capture the dominant underlying physics of such a morphologic evolution within reasonable computation cost, we model a graphene bilayer intercalated by two neighboring Si NPs. For a given Si NP size, MD simulations are conducted over a range of Si NP dispersion distance. Two modes of morphologic evolution emerge from the simulations, as illustrated in Fig. 2.4. If the dispersion distance between Si NPs, denoted by S , is sufficiently large (e.g., $37nm$), the graphene bilayer in between two neighboring Si NPs is first intercalated to form a long tunneling wrinkle (Fig. 2.4B). The tunnel formation,

however, results in increased strain energy in the graphene, therefore is energetically unfavorable. As a result, the long tunneling wrinkle in the graphene bilayer evolves to disappear, preventing the two Si NPs to migrate toward each other (Fig. 2.4C and D). At equilibrium, the Si NPs remain dispersed and are individually wrapped by the graphene (Fig. 2.4E). The intercalated morphology of the graphene near each Si NP is similar to that depicted in Fig. 2.3. If the dispersion distance between the Si NPs is small (e.g., 25nm), the intercalated graphene bilayer between the two neighboring Si NPs can form a short and stable tunneling wrinkle, which facilitates the migration of the two Si NPs toward each other. As the two Si NPs evolve to come closer, the length of the tunnel becomes shorter (e.g., Fig. 2.4H and I), resulting in a decrease of the strain energy of the graphene, which is thus energetically favorable. Eventually, the two Si NPs evolve to form a bundle, which is wrapped together by the graphene bilayer (Fig. 2.4J).

Also emerging from extensive MD simulations is a critical dispersion distance of Si NPs, S_{cr} , above which the Si NPs remain dispersed while the tunneling wrinkle disappears and below which the Si NPs evolve to bundle together through a stable tunneling wrinkle. Figure 2.5 plots S_{cr} as a function of the diameter of the Si NP, d_{NP} . There is an approximately linear dependence of S_{cr} on d_{NP} , i.e., $S_{cr} \approx 10d_{NP} - 16.8$. Results from the present study captures the dominant underlying energetics of NP intercalating in between graphene layers. It reveals a unique type of the wrinkling instability in free-standing graphene bilayer intercalated by free-moving nanoparticles. A further investigation on the wrinkling instability of graphene regulated by motion-free nanoparticles is discussed in Section 2.2. On a separate note, results in Fig. 2.5 can

serve as guidance for the material and structural design of Si NP-graphene nanocomposites as anode materials for lithium-ion batteries (77). For example, for a given design criteria of charging capacity, the maximum volume expansion of the Si NPs upon lithiation can be estimated. The corresponding enlarged size of the Si NPs, instead of the size of pristine Si NPs, should be used to determine a critical dispersion distance to prevent the aggregation of the Si NPs.

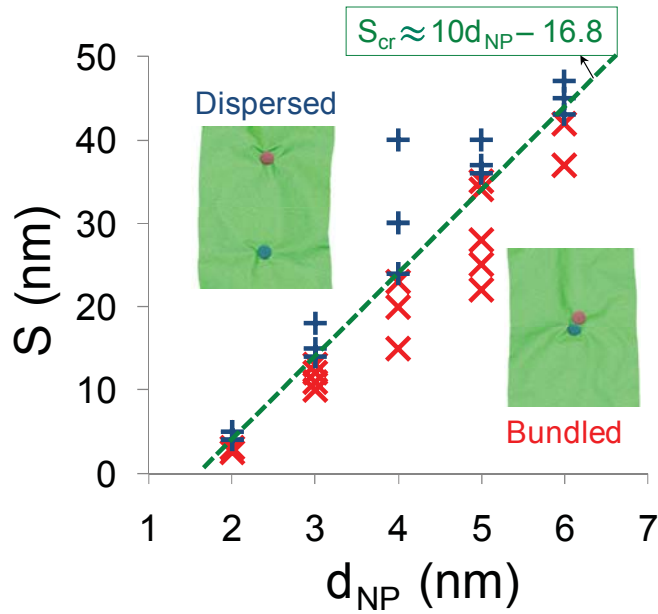


Figure 2.5. A phase diagram of the morphologic evolution of the Si NP-graphene system in the space of NP distance and diameter. “+” denote the MD simulation cases in which Si NPs remain dispersed and “x” denote those in which Si NPs evolve to bundle together. A critical dispersion distance of the Si NPs, S_{cr} , can be determined, which has an approximately linear dependence on d_{NP} .

2.2. Wrinkle formation in graphene on substrate-supported nanoparticles

2.2.1. Introduction

Graphene is a flexible, atomically thin membrane with remarkable electronic, mechanical and chemical properties (1, 13, 80). Two-dimensional nature of graphene renders its extra-large surface-to-volume ratio, giving rise to morphological varieties

such as intrinsic ripples, extrinsic wrinkles and folds (29, 76, 81-86), and other folded carbon nanostructures (43, 48, 49, 83, 87-91). In particular, the wrinkling formation in graphene has received considerable attention, largely due to its potential in manipulating the electronic properties of graphene (38, 72, 73, 92). For example, when graphene is bent to a certain curvature, a band gap is generated and that locally curved portion acts semiconducting while the flat graphene is highly conductive (72, 73, 92). Since the morphology of atomically thin graphene is strongly tied to its electronics properties (53), random wrinkling formation leads to unpredictable graphene properties, which are undesirable for nanoelectronic devices for which precise control is the key. Therefore controlling the graphene morphology over large areas is crucial in enabling future graphene-based applications.

The extrinsic morphology of graphene on a substrate can be regulated (37, 81, 93-97). When a layer of graphene is placed on patterned substrate surfaces, the graphene conforms to the substrate surface pattern (37, 72, 96, 97). In addition, the topological feature of the substrate surface can be regulated by introducing external scaffolds (81, 93). For example, the morphology of graphene intercalated by Si nanowires evenly patterned in parallel on a SiO₂ substrate is governed by the nanowire diameter and inter-nanowire spacing (93). While the graphene on patterned one-dimensional nanowires is rather regular by forming parallel grooves, the extrinsic graphene morphology regulated by zero-dimensional nanoparticles (NPs) has more complicated features (38, 81). For example, when a small Si NP intercalates in between a graphene bilayer, each layer wraps around the Si NP, forming a conical dome in graphene. As the size of the Si NP increases, both graphene layers wrinkles and form ridge-like morphology. When

two neighboring Si NPs intercalate in between two graphene layers, depending on the NP size and spacing, wrinkling pattern in graphene can evolve dynamically (81). In a recent experiment (38), the wrinkling of graphene deposited on a SiO₂ substrate decorated with SiO₂ NPs is investigated. It is found that the NP dispersion density has a direct influence on the wrinkling pattern in graphene (Fig. 2.6B). For example, when the dispersion density is high enough, the percolation of wrinkles in graphene is observed; when the dispersion density is low, the graphene layer detaches from the substrate only in a small region around the NPs. It suggests a feasible approach to programming the electronic signature of graphene through guided formation of wrinkles.

2.2.2. Experimental observation of graphene morphology on substrate-supported nanoparticles

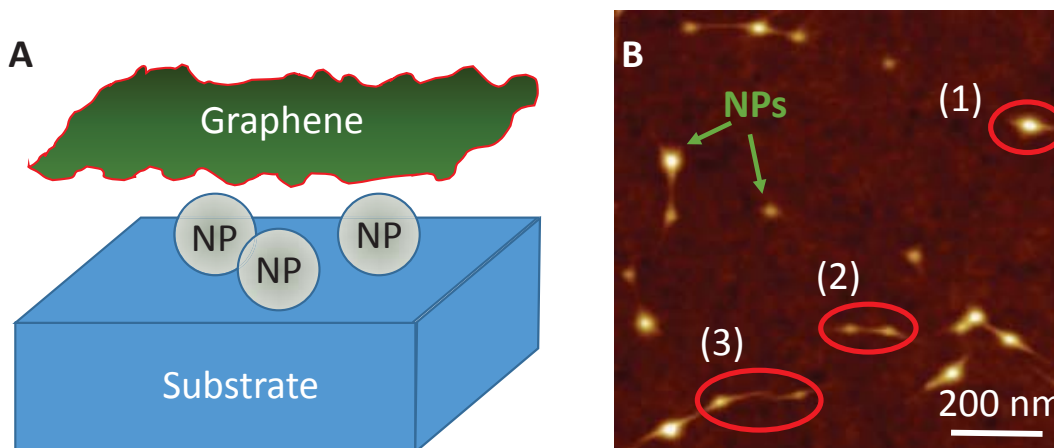


Figure 2.6. (A) Schematics of graphene covering a substrate with dispersed NPs (not to scale). (B) Atomic force microscopy image of the wrinkled morphology of a monolayer graphene covering a SiO₂ substrate with dispersed SiO₂ NPs. The atomic force microscopy image is reprinted from Ref. (38), under the terms of the Creative Commons Attribution 3.0 License. Three representative types of wrinkling morphology (highlighted by red circles) can be observed: (1) wrinkling of graphene on isolated NP; (2) wrinkling of graphene bridging two neighboring NPs; (3) wrinkling of graphene on quasi-isolated NPs.

Figure 2.6A presents a schematic of graphene covering a substrate with dispersed NPs. This can be experimentally achieved by means of spin coating the NPs onto a substrate (38). A graphene monolayer is then mechanically exfoliated from graphite onto the substrate decorated with NPs. Figure 2.6B shows a typical atomic force microscopy image of a monolayer graphene covering a SiO₂ NP-dispersed substrate surface. Depending the NP dispersion distance, three representative types of wrinkling morphology of graphene can be identified. On an isolated NP (sufficiently large distance from other NPs, e.g., labeled area (1) in Fig. 2.6B), the graphene bulges locally to wrap around the NP to form a dome-shaped extrusion. On a NP of relatively large size, two wrinkles originate from the bulged graphene dome near the NP protrusion location in opposite directions and gradually terminate after a certain distance, beyond which graphene completely adheres to the substrate surface. For convenience, hereinafter, such a wrinkle that originates from a graphene protrusion and terminates over a distance is termed as a tipped wrinkle. When two NPs are relatively close to each other (e.g., labeled area (2) in Fig. 2.6B), the graphene wrinkles to bridge the two protrusions induced by NP intercalation. Such a wrinkling morphology is hereinafter termed as a tunneling wrinkle. A more delicate third scenario exists when two NPs are separated by a distance that is neither far enough to form two isolated sets of tipped wrinkles near the NPs and nor close enough to form a tunneling wrinkle in between the two NPs. Instead, two wrinkles run in parallel between the two NPs and terminate near the middle with a short overlap near their tips. The above experimental observation suggests that a critical distance between two neighboring NPs may exist, below which a tunneling wrinkle forms. Since a regular tunneling wrinkle has the most desirable

geometrical features for engineering the electronic properties of graphene (72, 73, 92), the dependence of such a critical distance to form tunneling wrinkles on the NP size is intriguing. Motivated by the above observations, we perform systematic MD simulations to shed quantitative insights on these intriguing but less understood phenomena.

2.2.3. A semi-continuum formulation of graphene/substrate cohesive law

The origin of the wrinkling is due to the strong adhesion of graphene to its underlying substrate. Such interaction is mainly van der Waals (vdW) type. In order to simulate the graphene/substrate adhesion energy in the experiments with a rationally reduced MD model to ease computational expenses, below we perform theoretical analysis on the relationship between the continuum-scale adhesion energy and the atomic-pair interaction energy. The energy between two atoms of distance r due to vdW force is usually represented by a Lennard-Jones 6-12 potential,

$$V(r) = 4\epsilon \left(\frac{\sigma^{12}}{r^{12}} - \frac{\sigma^6}{r^6} \right), \quad (2.1)$$

where $\sqrt[6]{2}\sigma$ is the equilibrium distance between atoms and ϵ is the bond energy at the equilibrium distance. In order to establish a semi-continuum cohesive law between a graphene monolayer and a substrate with a separation distance of h (Fig. 2.7), we homogenize carbon atoms in the graphene and represent them by an area density ρ_g (99). We discretize the substrate into multiple atomic layers along its thickness direction but treat each layer as continuum in its plane so that we can homogenize the substrate atoms in each layer. Taking the substrate surface layer as an example (shaded

part in Fig. 2.7), we represent the atoms in this layer by an area density ρ_s . The distance between a point $(0, 0)$ in the graphene and a point (x, y) in the substrate surface layer is $r = \sqrt{x^2 + y^2 + h^2}$. The energy due to the vdW force is given by $V(r)$. For an infinitesimal graphene area dA_g , the energy stored due to the vdW force is

$$\rho_g dA_g \int V(r) \rho_s dA_s = \rho_g \rho_s dA_g \int V(r) dx dy, \quad (2.2)$$

The cohesive energy Φ induced by the substrate surface layer is the energy per unit area of graphene, and is therefore given by

$$\Phi = \rho_g \rho_s \int V(r) dx dy = 4\epsilon \rho_g \rho_s \pi \left(\frac{\sigma^{12}}{5h^{10}} - \frac{\sigma^6}{2h^4} \right). \quad (2.3)$$

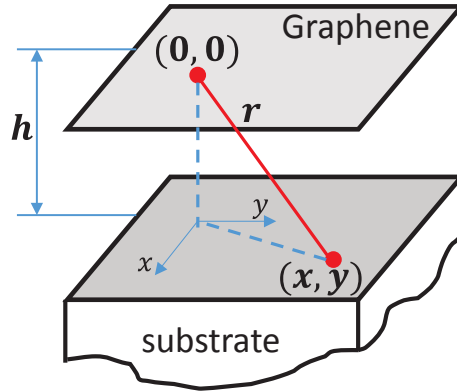


Figure 2.7. A schematic of a flat graphene monolayer on a substrate with a separation distance of h .

Finally, the total graphene-substrate adhesion energy can be computed by summing up individual cohesive energy induced by all the atomic layers in the substrate. This way, the continuum-scale graphene-substrate adhesion energy is correlated with their atomic-pair vdW interaction energy. Furthermore, considering the decaying nature of vdW interaction, a reasonable estimate of adhesion energy can be achieved by adding up the contribution from the first few top atomic layers in the substrate, while the

energy contribution from substrate layers underneath is rather negligible. In this sense, the above semi-continuum approach can be readily employed in practice. This approach is used in Section 2.2.4 to benchmark the parameters in MD simulations to guarantee reasonable agreement with experimental measurement of graphene-substrate adhesion.

2.2.4. Wrinkling morphology of graphene on substrate-supported nanoparticles

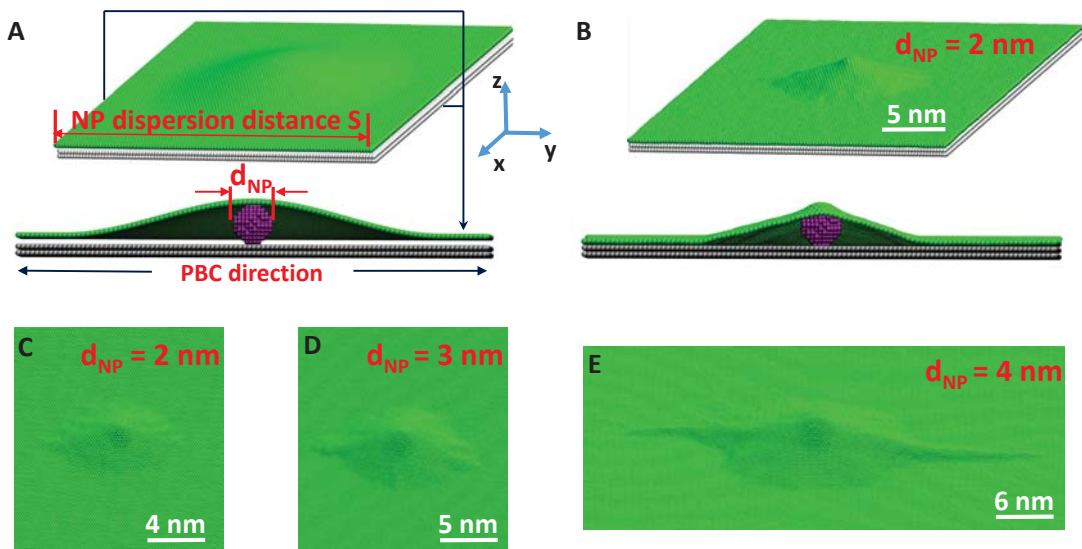


Figure 2.8. (A) MD simulation model. Inset shows the cross-section view of the initial configuration. Periodical boundary condition (PBC) is applied in y direction, so that the length of the simulation box along the PBC direction represents the NP dispersion distance S . (B) The typical equilibrium morphology of graphene on a small and isolated NP on the substrate. (C-E) Variation of wrinkling morphology of graphene on an isolated NP with increasing size.

Figure 2.8A depicts the MD simulations model. To reduce computational cost of systematic parametric study using MD, the substrate is represented by two fixed layers of graphene. This strategy is justified considering the decaying nature of the vdW force between graphene and a stiff substrate, and further shown below to be reasonable to represent the key underlying interaction between the graphene and the substrate. The monolayer graphene is initially prescribed with a smooth bulged-out geometry to cover

the NP that intercalates in between the graphene and the underlying stiff substrate. Periodical boundary condition (PBC) is applied in the y direction. Given the nature of periodical boundary condition, the model in Fig. 2.8A simulates an array of NPs of diameter d_{NP} with a uniform dispersion distance S , intercalating in between the graphene and the substrate.

The simulations are carried out using Large-scale Atomic/Molecular Massively Parallel Simulator (LAMMPS) (79). All the simulations is carried out in NVT ensemble at 300K. The carbon-carbon interaction in the graphene layer is described by AIREBO potential (78). The NP is modeled as a rigid body and takes the face centered cubic crystal structure. The vdW interaction between each NP atom and each carbon atom in the monolayer graphene or the substrate is modeled by a Lennard Jones potential $V_{CN}(r) = 4\epsilon_{CN}\left(\frac{\sigma_{CN}^{12}}{r^{12}} - \frac{\sigma_{CN}^6}{r^6}\right)$, where $\epsilon_{CN} = 0.0127 \text{ eV}$, $\sigma_{CN} = 0.29 \text{ nm}$. The interaction between each carbon atom in the monolayer graphene and each carbon atom in the substrate is also modeled by a Lennard Jones potential $V_{CC}(r) = 4\epsilon_{CC}\left(\frac{\sigma_{CC}^{12}}{r^{12}} - \frac{\sigma_{CC}^6}{r^6}\right)$, where $\epsilon_{CC} = 0.00852 \text{ eV}$, $\sigma_{CC} = 0.29 \text{ nm}$. Using Eq. (2.3), the above parameters yield an adhesion energy of the monolayer graphene to the substrate as

$$\Phi_{total} = \Phi_{s1} + \Phi_{s2} = 4\epsilon_{CC}\rho_c^2\pi\left(\frac{\sigma_{CC}^{12}}{5h_{s1}^{10}} - \frac{\sigma_{CC}^6}{2h_{s1}^4}\right) + 4\epsilon_{CC}\rho_c^2\pi\left(\frac{\sigma_{CC}^{12}}{5h_{s2}^{10}} - \frac{\sigma_{CC}^6}{2h_{s2}^4}\right), \quad (2.4)$$

where the subscripts $s1$ and $s2$ denote the 1st and 2nd substrate carbon atomic layer in the MD model, respectively, so that $h_{s1} = 0.34 \text{ nm}$, $h_{s2} = 0.68 \text{ nm}$ and $\rho_c = \frac{4}{3\sqrt{3}l_0^2}$, in which l_0 is the equilibrium bond length of graphene and takes the value of 0.142 nm .

The corresponding adhesion energy $|\Phi_{total}| \cong 0.5 \text{ J/m}^2$ is in good agreement with the recent experimental measurement of monolayer graphene adhesion energy on a SiO_2 substrate ($\sim 0.45 \text{ J/m}^2$) (31), which justifies the modeling strategy and the choice of parameters in our MD simulations. To clarify the substrate thickness effect on the adhesion energy, we further calculate the adhesion energy for the situations, in which there are two (used in the present study), three, four fixed graphene layers in the substrate, with the interlayer spacing of 0.34 nm. The corresponding adhesion energies calculated from the semi-continuum model are 0.5054 J/m^2 , 0.5123 J/m^2 , and 0.5145 J/m^2 for a substrate with two, three and four fixed graphene layers, respectively. In other words, the adhesion energy calculated from our continuum model by using a substrate of two graphene layers agrees well with those by using a thicker substrate within less than 2%, which further justifies the modeling strategy adopted here.

Figure 2.8B shows a typical equilibrium morphology of graphene when it covers a relatively small NP and the NP dispersion distance S is large (e.g., $d_{NP} = 2 \text{ nm}$, $S = 25 \text{ nm}$) so that this NP is isolated. Due to the intercalation by the NP and the strong adhesion of the monolayer graphene to the substrate, a small region of graphene around the NP delaminates from the substrate and locally forms a dome-like morphology. Figure 2.8C-E show the variation of graphene morphology as the NP size increases. When $d_{NP} = 3 \text{ nm}$ (Fig. 2.8D, $S = 36 \text{ nm}$), the onset of tipped wrinkles occurs. When $d_{NP} = 4 \text{ nm}$ (Fig. 2.8E, $S = 60 \text{ nm}$), two long tipped wrinkles extend from the NP-intercalated graphene dome in opposite directions, resembling the experimental observation in Fig. 2.6B (circled area 1). The formation of tipped wrinkles can be understood as follows. As the size of the NP increases, forming a smooth conical dome

in the graphene monolayer to wrap around the NP requires deflecting and stretching the graphene in a larger area. The resulting increase in the graphene strain energy and the graphene-substrate interaction energy becomes higher than that due to forming tipped wrinkles. In the wrinkling graphene morphology, even though the curvature of the graphene corrugation along the wrinkles is higher than that of a smooth conical dome, it only requires corrugating a smaller area of the graphene and the graphene portions away from the wrinkles are much less corrugated and have an interlayer distance closer to its equilibrium value. As a result, the formation of tipped wrinkles corresponds to a lower total free energy state, thus is more favorable.

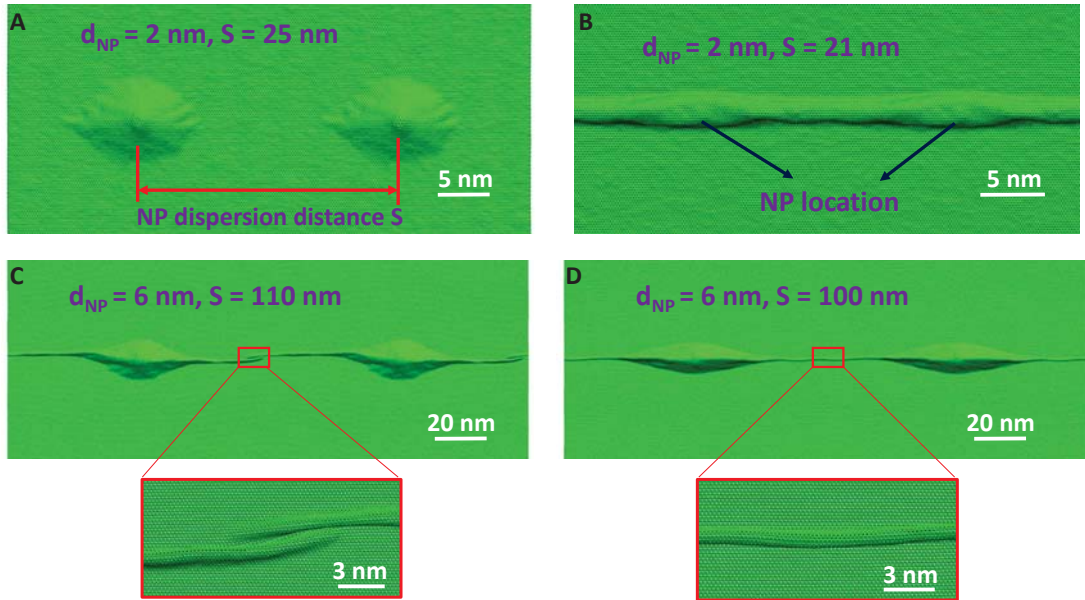


Figure 2.9. Wrinkling morphology of graphene on NPs with relatively small dispersion distance. For visual guidance, two periodical images are combined along the PBC direction. For $d_{NP} = 2$ nm: (A) The two NP-intercalated graphene domes remain isolated when dispersion distance $S = 25$ nm. (B) A tunneling wrinkle forms between two NPs, when $S = 21$ nm. For $d_{NP} = 6$ nm: (C) Two long tipped wrinkles run in parallel between neighboring NPs and terminate in the middle with a short overlap but their tips remain distinct from each other (inset) when $S = 110$ nm. (D) When $S = 100$ nm, a tunneling wrinkle forms between two neighboring NPs.

We next consider the morphological evolution of the graphene intercalated by NPs on substrate as the NP dispersion distance varies. Similar materials parameters and

numerical strategy as those described above are used in the MD simulations. For a given NP size, MD simulations are conducted over a range of NP dispersion distance. Two modes of morphologic evolution emerge from the simulations, as illustrated in Fig. 2.9. If the NP dispersion distance S is sufficiently large (e.g., $S = 25$ nm for $d_{NP} = 2$ nm), the graphene is intercalated to form two isolated conical domes (Fig. 2.9A, similar to the results shown in Fig. 2.8B-E). If the NP dispersion distance S is small enough (e.g., $S = 21$ nm for $d_{NP} = 2$ nm), the graphene in between two neighboring NPs is intercalated to form a tunneling wrinkle (Fig. 2.9B). For NPs with larger sizes, similar transition of graphene wrinkling morphology could be observed with more delicate features. As shown in Fig. 2.9C, when the dispersion distance S is 110nm for $d_{NP} = 6$ nm, the resulting equilibrium morphology of graphene resembles the typical experimental observation in Fig. 2.6B (circled area 3). From each protrusions, there are two long tipped wrinkles reaching out and orienting toward its nearby protrusions. Although the tip ends have a slight overlap, no signs of further merging into a tunneling wrinkle is observed. This can be interpreted as a critical intermediate transitional state between formations of tunneling wrinkles and tipped wrinkles. Further increase in the NP dispersion distance S results in completely isolated tipped wrinkles, and the morphology of graphene around each protrusion resembles those shown in experiments (e.g., Fig. 2.6B, circled area 1). However, further decrease in the NP dispersion distance S leads to the formation of tunneling wrinkles. As shown in Fig. 2.9D, when $S = 100$ nm and $d_{NP} = 6$ nm, a long tunneling wrinkle bridges the two graphene protrusions induced by NP intercalation, resembling the experimental observation in Fig. 2.6B (circled area 2).

2.2.5. A critical nanoparticle dispersion distance for tunneling wrinkle instability of graphene on substrate-supported nanoparticles

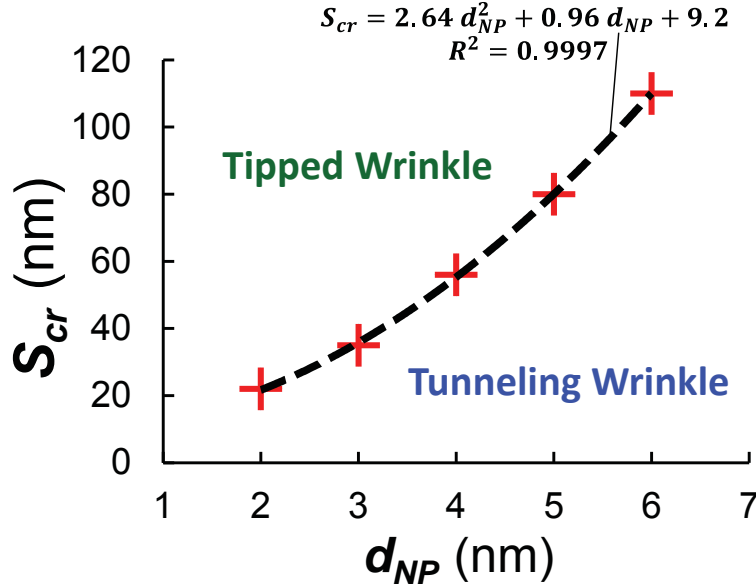


Figure 2.10. A diagram of the wrinkling instability of graphene morphology on substrate-supported NPs in the space of NP dispersion distance and diameter.

Also emerging from extensive MD simulation study is a critical dispersion distance of NPs, S_{cr} , for a given NP size, below which tunneling wrinkles form to bridge neighboring NPs and above which isolated tipped wrinkles form, extending from the NP-intercalated graphene dome. Figure 2.10 plots S_{cr} as a function of d_{NP} . Such a curve delineates a boundary that separates the space of NP dispersion distance and NP diameter into two regions of wrinkling morphology of graphene as labeled in Fig. 2.10. The S_{cr} - d_{NP} curve can be fitted into a second-order polynomial as shown in Fig. 2.10, with an R-squared value of fitting 0.9997. Results in Fig. 2.10 can well account for the experimental observation in Ref. (38), in which the mean diameter of NPs is 7.4 ± 2.2 nm. By using the fitted polynomial function, the critical NP dispersion distance is

estimated to be around 200 nm, which agrees well with the experimental results (e.g., Fig. 2.10B). In this sense, the diagram depicted in Fig. 2.10 can therefore be used to guide the programmable design of wrinkling formation in graphene on substrate-supported NPs.

2.2.6. Stretchable substrate: Insights on programming wrinkles in graphene

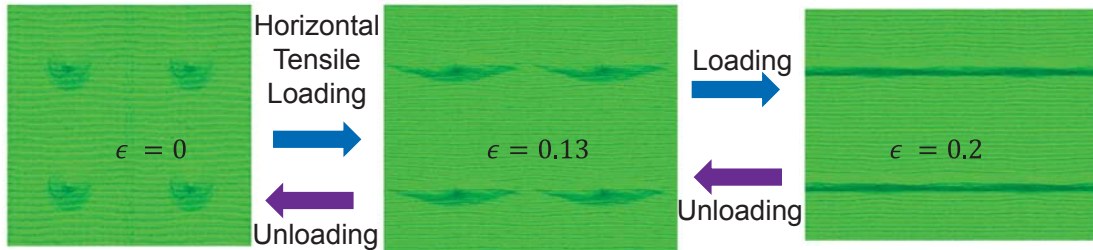


Figure 2.11. A mechanism revealed by MD simulations to produce tunable and reversible wrinkles for graphene on stretchable substrate. PBC is applied along loading direction.

Finally we point out a mechanism that help gain further control on the formation of wrinkles. Our MD simulations (Fig. 2.11) show that when graphene is deposited on a stretchable substrate decorated with NPs, the application of mechanical strain on the entire structure can help produce tunneling wrinkles that are initially not formed as the distance between NPs is larger than the critical dispersion distance. The strain-induced wrinkles can have morphologies ranging from tipped wrinkles and tunneling wrinkles depending on the strain magnitude. The direction of the wrinkles is aligned with the applied strain direction. Considering the diagram as shown in Fig. 2.10, we can envision abundant strategies to actively control the wrinkles in graphene. For example, NPs can be patterned on stretchable substrate (74, 75) with a dispersion distance slightly larger than the critical dispersion distance. Then certain mechanical strain can serves as ON-OFF switch for the long tunneling wrinkles along certain directions.

2.3. Chapter summary

We first investigate the morphology of a graphene bilayer intercalated by nanoparticles. We find a critical dispersion distance of the NPs, above which the Si NPs remain dispersed while the tunneling wrinkle disappears and below which the Si NPs evolve to bundle together through a stable tunneling wrinkle. A roughly linear dependence of the critical distance of the Si NPs on its size is revealed. We then investigate the wrinkling morphologic evolution of graphene on substrate-supported NPs. We also find critical dispersion distance of the NPs below which tunneling wrinkles form. A second-order polynomial dependence of such a critical NP dispersion distance on NP size is revealed, which agrees well with experimental observation. Such a second-order polynomial dependence is of practical importance in the sense that it can be applied to substrates with different adhesion interaction with monolayer graphene. All three coefficients in the second-order polynomial function can be readily parameterized from simple experimental tests. The resulting fitting function can then be used to guide the selection of NP size and dispersion density to achieve desirable wrinkling morphology of graphene. Results from the present study offer further insights into the formation of wrinkles in graphene deposited on a substrate surface with engineered protrusions (100-103) and can thus potentially enable novel design of graphene-based electronics. For example, by introducing NPs or substrate substructures in an ordered pattern on the substrate surface, even richer features of the wrinkling instability of the covering graphene could be realized. These opportunities can be further explored in the regime of stretchable substrate (74, 75). We call for further theoretical and experimental studies.

Chapter 3: Functionalization enabled unconventional carbon nanostructures

3.1. Hydrogenation enabled scrolling of graphene

Graphene's two-dimensional structure exposes its entire volume to its surrounding, rendering highly amenable surface chemistry. Tremendous efforts have been placed on the chemical functionalization of pristine graphene by adsorbing foreign atoms, molecules and functional groups on its surface (30, 104-109), motivated by the great potential of controllably tailoring the electronic structure of graphene. In particular, hydrogenation of graphene involves attaching atomic hydrogen to the carbon atoms in graphene. As a result, the hybridization of carbon atoms in graphene is changed from sp^2 into sp^3 and the two-dimensional atomic structure of pristine graphene is distorted into three-dimensional locally at each adsorbed hydrogen atom (30). Significant progresses have been made on controlled hydrogenation of graphene, with the aim to fine-tune graphene properties. For example, single-sided hydrogenation of pristine graphene has been demonstrated (30, 110-113). Hybrid superlattices made of patterned hydrogenation of a pristine graphene can be fabricated in a controlled fashion on both macroscopic and microscopic scales (114). These progresses on programmable hydrogenation of graphene open up new pathways to controlling the morphology of graphene and therefore enable the exploration of graphene-based novel nanomaterials. Here, we demonstrate spontaneous scrolling of graphene enabled by single-sided hydrogenation, using molecular dynamics simulations. We show that, by controlling the size and shape of the hydrogenated region, a graphene nanoribbon can

spontaneously scroll up into a carbon nanoscroll (CNS). Results from the present study shed light on a simple and robust solution to address the challenge of fabricating high quality CNSs, and therefore facilitate the realization of unconventional device concepts enabled by the open topology of CNSs.

A CNS is formed by rolling up a monolayer graphene into a spiral multilayer nanostructure, whose core size is highly tunable by relative sliding between adjacent layers (89, 90). In other words, a CNS is topologically open, fundamentally distinct from a tubular CNT, which is topologically closed. The open and highly tunable structure of CNSs, combining with the exceptional mechanical and electronic properties inherited from the basal graphene (13, 53), has inspired an array of novel nano-device applications, such as hydrogen storage medium (41, 115), water and ion channels (47), ultrafast nano-oscillators (42, 43) and translational nano-actuators (45). Enthusiasm aside, the realization of these promising applications hinges upon feasible and reliable fabrication of high quality CNSs, which remains as a significant challenge. A completely rolled-up CNS is energetically more favorable than its basal graphene in a planar form, given that the reduction of the van der Waals (vdW) interaction energy among carbon layers in the CNS overbalances the increase of strain energy due to the bending of graphene (90). Formation of a CNS, however, requires a sufficiently large driving force to overcome the energy barrier for initial curling and rolling of the basal graphene before its continuous scrolling into a CNS. Existing chemical approaches to overcoming such an initial energy barrier to form CNSs include applying high-energy sonication to exfoliated graphite sheets (40) or immersing a SiO₂-supported graphene monolayer in isopropyl alcohol solution (48). In general, these chemical approaches to

fabricating CNSs suffer from possible contamination of chemical residue, and also the difficulty in controlling the rolling initiation and rolling direction. Concepts of physical approaches to fabricating CNSs involve using a CNT of suitable diameter (49) or a water nanodroplet (83) to overcome the initial energy barrier of graphene scrolling. These physical approaches, however, requires precise positioning of the CNT or water nanodroplet at the edge of the basal graphene, which is rather challenging.

Hydrogenation of a carbon atom in a pristine graphene produces an sp^3 carbon-hydrogen (C-H) bond, which gives rise to a local structural change around that carbon atom. Specifically, the chemically adsorbed hydrogen atom attracts its bonded carbon atom while repels other neighboring carbon atoms. As a result, the three initially planar carbon-carbon (C-C) bonds associated with the hydrogenated carbon atom are distorted and locally bend away from the hydrogen atom. If hydrogen atoms are chemically adsorbed by the carbon atoms in pristine graphene on both its sides in an alternative manner, the resulting hydrogenated graphene (termed as graphane (30, 52, 116) overall remains a rather planar morphology as the local out-of-plane distortion of the C-C bonds cancel each other. However, if the graphene is single-sided hydrogenated, the local distortion at each hydrogenated carbon atom is accumulated (84). As a demonstration of such an accumulated effect, Fig. 3.1 shows that a graphene nanoribbon with one row of hydrogenation on the same side along an armchair line fold up to about 160° , while two rows of hydrogenation along neighboring armchair lines on the same side result in further folding of the graphene nanoribbon to about 135° . Similarly, one row of hydrogenation along a zigzag line on the same side result in folding of the graphene nanoribbon to about 130° , while two rows of hydrogenation

along neighboring zigzag lines on the same side result in further folding of the graphene nanoribbon to about 100° .

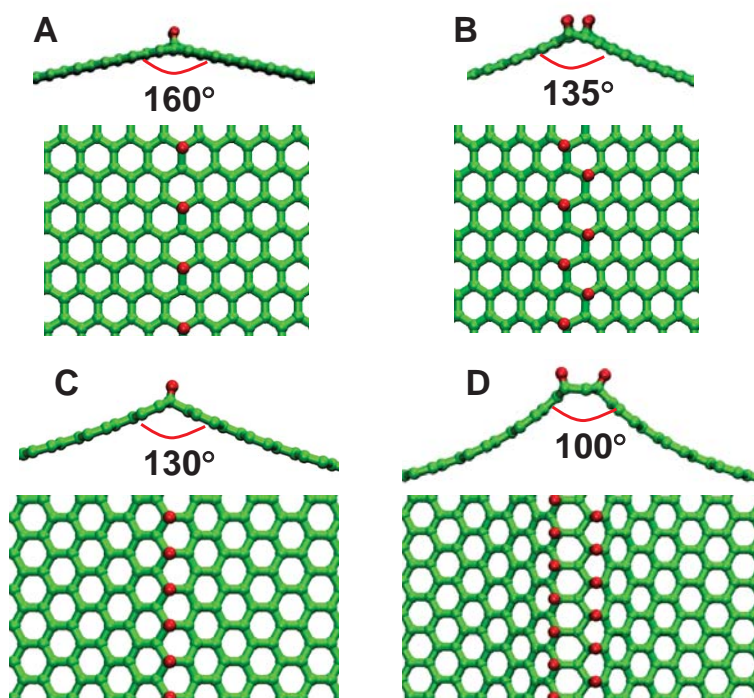


Figure 3.1. (A) Side view (top) and top view (bottom) of the equilibrium shape of a graphene nanoribbon (green) with one row of hydrogenation (red) on the same side along an armchair line. The graphene folds along the hydrogenation line to about 160° . (B) Two rows of hydrogenation along neighboring armchair lines on the same side result in further folding of the graphene nanoribbon to about 135° . (C) One row of hydrogenation along a zigzag line on the same side result in folding of the graphene nanoribbon to about 130° . (D) Two rows of hydrogenation along neighboring zigzag lines on the same side result in further folding of the graphene nanoribbon to about 100° .

Results in Fig. 3.1 suggest that if sufficient carbon atoms in the graphene are hydrogenated on one side, the graphene morphology can be altered in a manner curving toward another side. Furthermore, if the curving of the graphene can be achieved in a controlled fashion, it can serve as a feasible approach to overcoming the initial energy barrier of graphene scrolling into a CNS. To explore such a promising approach to addressing the challenge to fabricate high quality CNSs, we perform systematic

molecular dynamics simulations to investigate the hydrogenation enabled scrolling of graphene, with particular focus on deciphering the key parameters that govern the successful scrolling of graphene into CNSs.

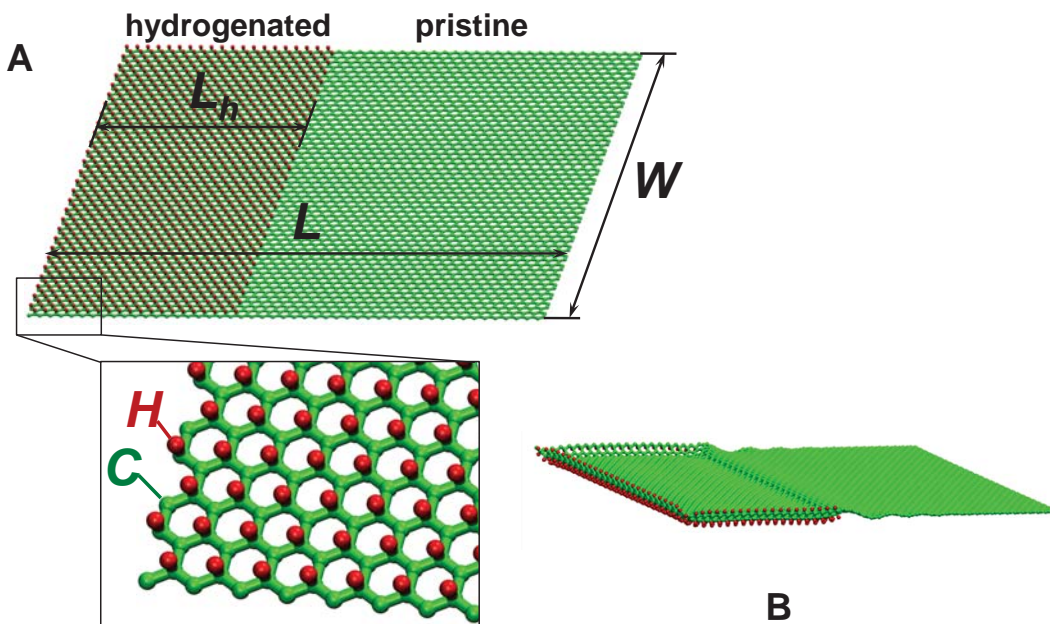


Figure 3.2. (A) Simulation model of a graphene of a length L and a width W that is single-sided hydrogenated at one end in a length of L_h . Inset shows the detailed lattice structure of the hydrogenated region. (B) Energy minimized structure of the model.

Figure 3.2A depicts the simulation model of a graphene of a length L and a width W that is single-sided hydrogenated at one end in a length of L_h . In each carbon hexagon in the hydrogenated region, one hydrogen atom is chemically bonded to each of the three carbon atoms in alternating lattice positions (see inset of Fig. 3.2A). Therefore, half of the carbon atoms in the hydrogenated region are bonded with hydrogen atoms on the same side. In the simulations, the C-C and C-H bonds in the graphene as well as the non-bonded C-C and C-H interactions are described by the Adaptive intermolecular Reactive Empirical Bond Order (AIREBO) potential (78). Molecular dynamics simulations of the graphene scrolling are carried out using Large-scale

Atomic/Molecular Massively Parallel Simulator (LAMMPS) (79) with Canonical Ensemble at a temperature of 300K. Before running dynamic simulations, the energy of the system is first minimized by using conjugate gradient (CG) algorithm until either the total energy change between successive iterations divided by the energy magnitude is less than or equal to 10^{-6} or the total force is less than 10^{-5} eV/Å°. The energy minimized structure is shown in Fig. 3.2B.

We first consider a square shaped graphene, i.e., $L=W$, and investigate the effect of the length of the hydrogenated region L_h on the scrolling of such a graphene. Emerging from the simulation results are three types of scrolling behavior of partially single-sided hydrogenated graphene, as shown in Fig. 3.3. Here, $L=W=12$ nm. If the length of the hydrogenated region L_h is just a small fraction of the graphene width, (e.g., $L_h/W=0.3$), the graphene can only scroll up partially.

Figures 3.3A-D plot the sequential snapshots of the graphene at 1ps, 5ps, 28ps, and 47ps in the simulation, respectively. At the beginning, all three free edges of the rectangular hydrogenated region curl up toward the opposite side of hydrogenation (Fig. 3.3A). The curling of the long free edge then becomes dominant and leads to the scrolling of the hydrogenated portion of the graphene (Figs. 3.3B-D), driven by both the hydrogenation-induced local lattice distortion and the reduction of the vdW interaction energy among the atoms in the hydrogenated region, as clearly indicated by the decrease in potential energy of the system in Fig. 3.3E (from state (A) to state (D)). Note that at the end of the partial scrolling process of the hydrogenated portion (Fig. 3.3B), the translational kinetic energy of the partial scroll leads to the tendency of

further scrolling of the graphene over the pristine region. However, this further scrolling is at the price of further increase of the graphene strain energy, which roughly scales with the square of the graphene curvature.

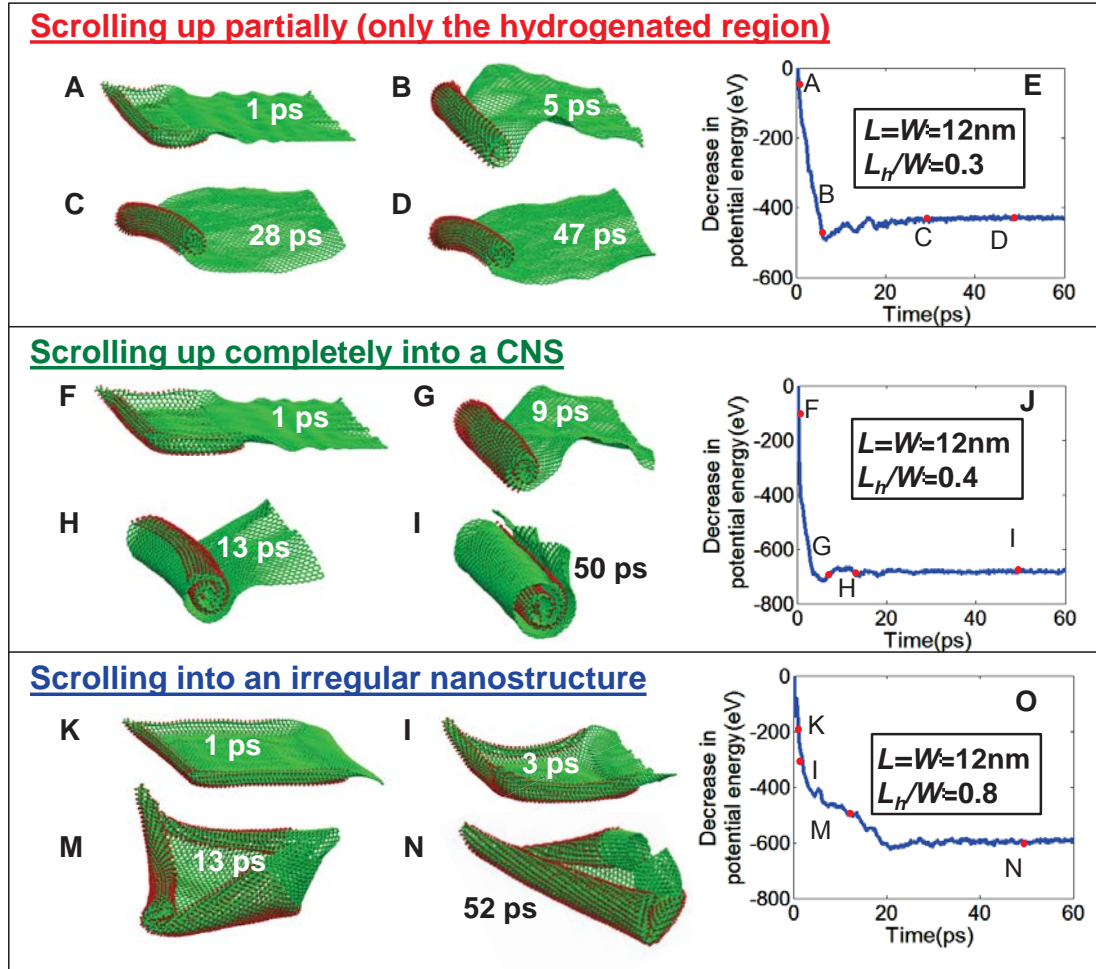


Figure 3.3. Three types of scrolling behavior of partially single-sided hydrogenated graphene. Here $L=W=12$ nm. When $L_h/W=0.3$, the graphene can only scroll up partially, as shown in sequential snapshots of the graphene morphology at (A) 1ps, (B) 5ps, (C) 28ps and (D) 47ps, respectively. When $L_h/W=0.4$, the graphene can completely scroll up into a CNS, as shown in sequential snapshots of the graphene morphology at (F) 1ps, (G) 9ps, (H) 13ps and (I) 50ps, respectively. When $L_h/W=0.8$, the graphene scrolls into an irregular nanostructure, as shown in sequential snapshots of the graphene morphology at (K) 1ps, (L) 3ps, (M) 13ps and (N) 52ps, respectively. (E), (J) and (O) plots the evolution of the system potential energy as simulation time for the above three cases, respectively.

For a small value of L_h (e.g., 3.4 nm in Figs. 3.3A-D), the radius of the partially scrolled graphene in the hydrogenated region (e.g., Fig. 3.3B) is small, indicating a large curvature of graphene if further scrolling occurs, which leads to an increase of the strain energy of the graphene that overweighs the reduction of the vdW interaction energy among the carbon layers. Without sufficient driving force, the partial scroll oscillates back and forth for a few times (as indicated by the fluctuation of potential energy profile in Fig. 3.3E) before the excess translational kinetic energy is dissipated. At the steady state, scrolling only occurs in the hydrogenated region of the graphene and the pristine region remain planar (e.g., Fig. 3.3D).

If single-sided hydrogenation is introduced in a proper size in the graphene (e.g., $L_h/W=0.4$), the initial scrolling of the hydrogenated region results in a partial CNS of relatively larger radius, leading to a modest increase of the graphene strain energy in further scrolling process that can be sufficiently driven the further reduction of vdW interaction energy among carbon layers. As a result, continuous scrolling proceeds throughout the whole graphene, leading to the formation of a CNS that remains stable at 300K, as illustrated in Figs. 3.3F-J. However, if the hydrogenated region is too large (e.g., $L_h/W=0.8$), the three free edges of such a region are of comparable length, and therefore the curling up and subsequent scrolling of these three edges indeed constrain each other (e.g., Figs. 3.3K-M), preventing the dominant scrolling of one edge and thus the formation of a complete CNS. Eventually the graphene rolls up into an irregular nanostructure (Fig. 3.3N).

We next carry out systematic molecular dynamics simulations to explore the scrolling behaviors of a square-shaped graphene of a wide range of size (from 6 nm to 21 nm) with various sizes of hydrogenated area (i.e., L_h/W ranges from 0.2 to 0.8). Figure 3.4 shows the morphology of these graphene at equilibrium. Emerging from the parametric study are the same three types of scrolling behavior of partially single-sided hydrogenated graphene as depicted in Fig. 3.3. Furthermore, it turns out that for a given size of square-shaped graphene, its scrolling behavior depends strongly on the relative size of the hydrogenated region (i.e., L_h/W) rather than its absolute size (i.e., L_h).

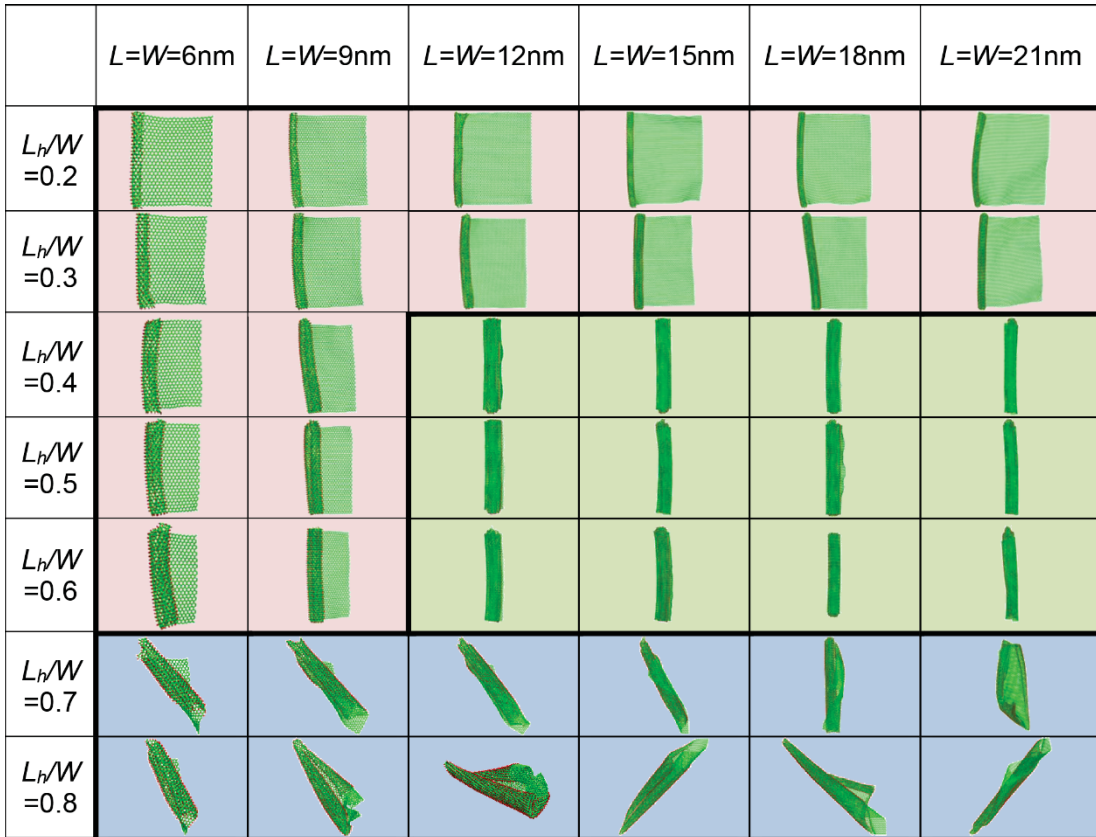


Figure 3.4. The equilibrium morphology of a square-shaped graphene of a wide range of size (from 6 nm to 21 nm) with various sizes of hydrogenated area (i.e., L_h/W ranges from 0.2 to 0.8).

Figure 3.5 plots a diagram of the three types of scrolling behavior of partially single-sided hydrogenated graphene in the parametric space spanned by L_h/W and W . If the graphene size is sufficiently large (e.g., $W \geq 12$ nm), there exists a range of the relative size of the hydrogenated region (i.e., $0.4 \leq L_h/W \leq 0.6$), in which the partially hydrogenated graphene can successfully scroll up into a complete and stable CNS (similar as in Fig. 3.3I). Such a range of value of L_h/W is approximately independent of the graphene size. If the hydrogenated region is too small (i.e., $L_h/W < 0.4$), only the hydrogenated region can scroll up while the pristine region of the graphene remains planar (similar as in Fig. 3.3D). If the hydrogenated region is too large (i.e., $L_h/W > 0.6$), the competing curling up and scrolling of the three free edges eventually result in an irregular nanostructure (similar as in Fig. 3.3N).

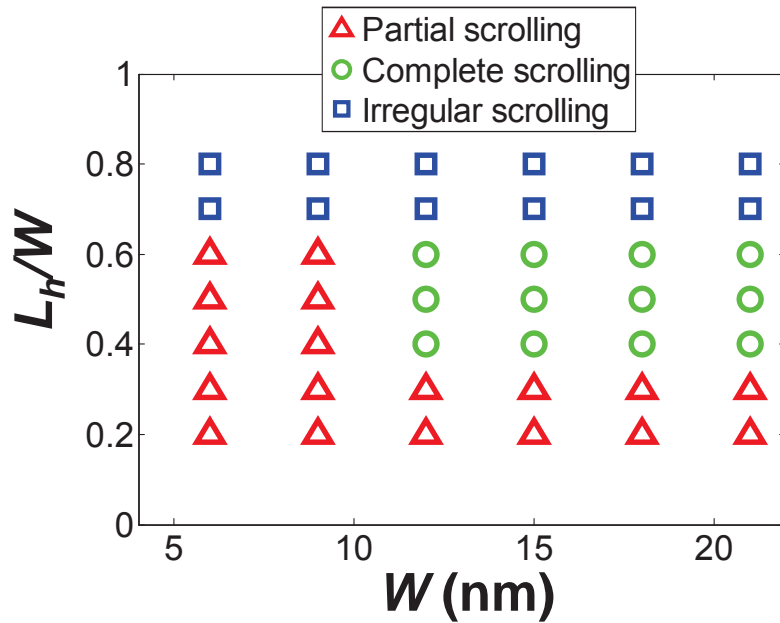


Figure 3.5. A diagram of the three types of scrolling behavior of partially single-sided hydrogenated graphene in the parametric space spanned by L_h/W and W .

By contrast, if the graphene size is small (e.g., $W < 12$ nm), the partially single-sided hydrogenated graphene can either only partially scroll up the hydrogenated region if $L_h/W < 0.6$ or scroll into an irregular nanostructure if $L_h/W > 0.6$. In other words, the graphene of a small size cannot completely scroll up into a stable CNS. This can be understood as follows. As the graphene size decreases, besides the aforementioned energetic competition between the increasing strain energy and the decreasing vdW interaction energy of the graphene, the intrinsic edge ripples in the graphene becomes more significant in the energetic interplay to determine the graphene scrolling behavior. The nature of the bonding structure of the free edges in graphene dictates an intrinsic compressive edge stress along the edges, resulting in the ripples along the free edges of the graphene (117). In other words, rolling up a graphene involves smoothing down (at least partially) the intrinsic edge ripples, posing additional energy barrier to the scrolling process. While the driving force of further scrolling of graphene roughly scales with the graphene width, the additional energy barrier due to the intrinsic ripples along the two edges along the scrolling direction is approximately independent of the graphene size. Therefore, there exists a critical graphene size, below which there is no sufficient driving force to overcome the energy barriers due to edge ripples. As a result, the graphene cannot completely scroll up into a stable CNS.

To understand the finding that the scrolling behaviors of partially single-sided hydrogenated graphene depends on L_h/W rather than L_h/L , Figs. 3.6A-D and E-H compare the scrolling behaviors of two graphene nanoribbons with same values of $L = 21$ nm and $L_h = 8.4$ nm (thus $L_h/L = 0.4$) but different value of W (12 nm and 21 nm, thus $L_h/W = 0.7$ and 0.4, respectively).

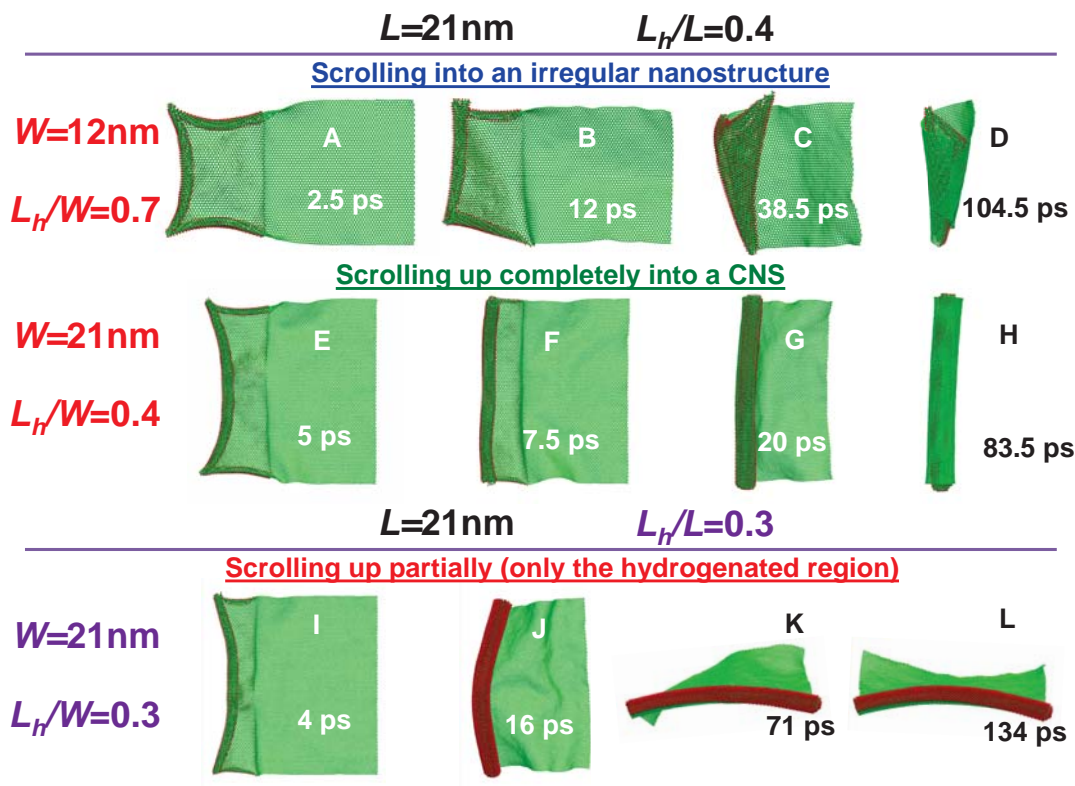


Figure 3.6. (A-D) Morphologic evolution of a partially single-sided hydrogenated graphene nanoribbon ($L=21\text{nm}$, $L_h=8.4\text{nm}$ and $W=12\text{nm}$), which ends up as an irregular nanostructure. (E-H) Morphologic evolution of a graphene nanoribbon ($L=21\text{nm}$, $L_h=8.4\text{nm}$ and $W=21\text{nm}$), which fully rolls up into a stable CNS. (I-L) Morphologic evolution of a graphene nanoribbon ($L=21\text{nm}$, $L_h=6.3\text{nm}$ and $W=21\text{nm}$), which can only partially roll up the hydrogenated portion (highlighted in red). Perspective views from the side in (K) and (L) reveal that the partial CNS tends to bend toward its outer edge that separates the hydrogenated and pristine portions of the graphene.

In both cases, all three free edges of the hydrogenated portion tend to curl up at the initial stage. For the case of a large ratio $L_h/W=0.7$ (Figs. 3.6A-D), the sizes of such three free edges are comparable, so are the driving forces for further scrolling of the three edges. Consequently, the competing further scrolling of these three edges results in an irregular nanostructure. For the case of a small ratio $L_h/W=0.4$ (Figs. 3.6E-H), however, the free edge of the hydrogenated portion at the left end of the graphene nanoribbon is much longer than the other free hydrogenated edges. As a result, the further scrolling of this long free edge gains more momentum that is sufficient to unfold

the initial curling along the other two short hydrogenated edges and further continue to roll up the rest of the graphene nanoribbon into a complete CNS. The above comparison clearly demonstrates that the scrolling behavior of partially single-sided hydrogenated graphene is governed by L_h/W rather than L_h/L .

Figure 3.5 show that there exists a minimum length of the hydrogenated portion of the graphene nanoribbon, below which the partial scrolling of the hydrogenated portion cannot proceed further to roll up the pristine portion. To shed light on the theoretical understanding of this finding, we consider a simple analytic model to estimate the minimum radius of the partial scroll that can proceed further. As discussed above, the further scrolling is governed by the competition between the increase of elastic energy of the pristine portion of graphene and the decrease of the interfacial energy of the system. An infinitesimal increment of the radius of the scrolled part dR leads to a bending-induced increment of elastic energy $dE = (\pi DW/hR)dR$, where D is the bending rigidity of pristine graphene and h is equilibrium interlayer distance of graphene, and an increment of interfacial energy $d\Gamma = 2\pi\gamma WdR$, where γ is the surface energy of graphene. The equilibrium of total energy determines a critical radius $R_{cr} = D/2\gamma h$, above which further scrolling becomes energetically favorable. Taking $D = 0.225nN \cdot nm$, $\gamma = 0.4 N/m$, and $h = 0.34 nm$, one get $R_{cr} \approx 0.83 nm$. Such an estimate agrees well with the prediction from Fig. 3.5. For example, for the case of $L = W = 12nm$ and $L_h = 4.8nm$, molecular dynamics simulation shows that the radius of the partial scroll of the hydrogenated portion is about 0.8 nm and it can further proceed to roll up the whole graphene nanoribbon into a complete CNS. By contrast, for the case of $L = W = 12nm$ and $L_h = 3.6nm$, simulation shows that the radius of the partial scroll

is about 0.5 nm and the pristine portion of the graphene nanoribbon remains unscrolled at steady state. Note that as the width of the graphene nanoribbon increases, the above simple analytic consideration tends to underestimate the minimum length of the hydrogenated portion to allow further scrolling. For example, as shown in Figs. 3.6I-L ($L = W = 21\text{nm}$ and $L_h = 6.3\text{nm}$), even though the radius of the partial scroll is greater than the predicted critical value of 0.8 nm, it still cannot further roll up the rest of the graphene nanoribbon. Figures 3.6K-L reveal that a small value of L_h/W ($=0.3$) dictates a slim partial scroll that tends to bend toward its outer edge that separates the hydrogenated and pristine portions of the graphene as an effort to further release the hydrogenation-induced lattice distortion. The curved profile of the partial scroll imposes further energy barrier and thus prevents further scrolling. On the other hand, a larger value of L_h/W ($=0.4$) leads to a thicker partial scroll that is stiff enough to remain roughly straight and thus can continue rolling up the rest of the graphene nanoribbon, as predicted by simulation results in Fig. 3.4 and Fig. 3.5. The above discussion further explains that the scrolling behavior of partially single-sided hydrogenated graphene depends strongly on L_h/W , rather than L_h .

We then further investigate the effect of the length of the partially single-sided hydrogenated graphene on its scrolling behavior. To this end, we increase the length of the graphene for those simulation cases in Fig. 3.5, so that $L > W$. We find that the simulation results are rather similar to those described in Fig. 3.5. For example, if a square shaped graphene with a proper size of the hydrogenated region (i.e., $0.4 \leq L_h/W \leq 0.6$) can completely scroll up into a stable CNS, so does a rectangular graphene with the same values of W and L_h/W but a larger value of $L > W$. As a demonstration, Fig.

3.7 plots the scrolling process of a partially single-sided hydrogenated graphene ($W=12$ nm, $L=30$ nm, and $L_h/W= 0.4$) along with the evolution of the total potential energy of the system. After the hydrogenated region scrolls up, the rolling process continues until the complete formation of a CNS that remains stable at 300K. The negligible effect of the length of graphene on its scrolling behavior can be readily explained as follows. Once the scrolling can proceed into the pristine region of the graphene, further scrolling involves wrapping of the graphene around a partial CNS of increasing radius. In other words, the energy barrier for further scrolling is ever decreasing. By contrast, the driving force for further scrolling remains roughly unchanged. Consequently, a rectangular graphene with a proper size of the hydrogenated region can always completely scroll up into a stable CNS. In this sense, the diagram in Fig. 3.5 can be also applicable to predict the scrolling behaviors of rectangular graphene.

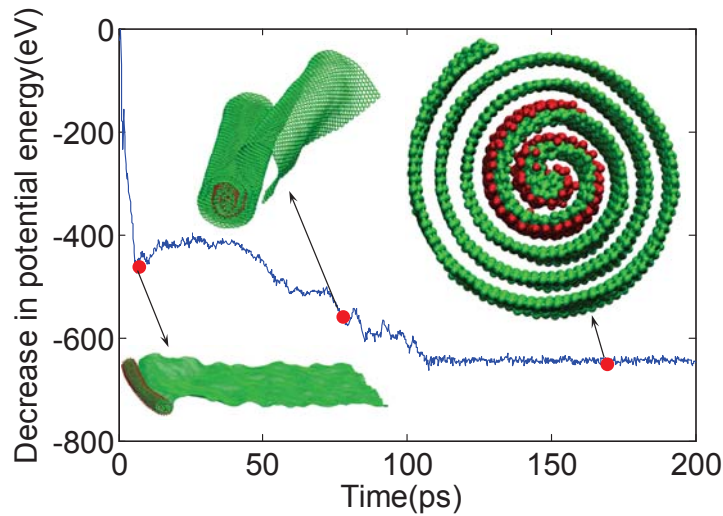


Figure 3.7. The evolution of the system potential energy of a 12 nm by 30 nm partially single-sided hydrogenated graphene as a function of simulation time. The hydrogenation enabled scrolling causes continuous decrease in the potential energy, leading to a complete CNS that remains stable at 300K.

In conclusion, we demonstrate the spontaneous scrolling of graphene that is partially hydrogenated at one side, using molecular dynamics simulations. The curling up and scrolling of the hydrogenated region of the graphene is due to the accumulated effect of the local lattice distortion in the graphene at each adsorbed hydrogen atom. We show that, if a proper size of the graphene is single-sided hydrogenated, the scrolling of the hydrogenated region can proceed continuously into the pristine region of the graphene and further throughout the whole graphene. As a result, the graphene scrolls into a complete CNS, which remains stable at room temperature. Systematic parametric study leads to a diagram in the space of the relative size of the hydrogenated region and the graphene width that delineates three types of scrolling behavior of partially single-sided hydrogenated graphene. Such a diagram can serve as quantitative guidelines that shed important light on a feasible and promising solution to address the challenge of fabricating high quality CNSs. Since hydrogenation is a reversible process, the chemically adsorbed hydrogen can be evaporated at an elevated temperature. The resulting CNS from the scrolling of a partially hydrogenated graphene could be potentially further treated to be hydrogen free while maintaining its scrolled form, as a CNS has a lower energy than its basal pristine graphene. With the ever maturing nanopatterning technique to hydrogenate graphene at high spatial resolution and precision (114, 118), the hydrogenation-enabled formation of CNSs holds great potential to enable further applications of CNS-based novel devices.

3.2. Hydrogenation assisted graphene origami and its application

The malleable nature of atomically thin graphene makes it a potential candidate material for nanoscale origami, a promising bottom-up nanomanufacturing approach to fabricating nanobuilding blocks of desirable shapes. The success of graphene origami hinges upon precise and facile control of graphene morphology, which still remains as a significant challenge. Inspired by recent progresses on functionalization and patterning of graphene, we demonstrate hydrogenation-assisted graphene origami (HAGO), a feasible and robust approach to enabling the formation of unconventional carbon nanostructures, through systematic molecular dynamics simulations. A unique and desirable feature of HAGO-enabled nanostructures is the programmable tunability of their morphology via an external electric field. In particular, we demonstrate reversible opening and closing of a HAGO-enabled graphene nanocage, a mechanism that is crucial to achieve molecular mass uptake, storage, and release. HAGO holds promise to enable an array of carbon nanostructures of desirable functionalities by design. As an example, we demonstrate HAGO-enabled high-density hydrogen storage with a weighted percentage exceeding the ultimate goal of US Department of Energy.

3.2.1. Motivation

Graphene has emerged as an extraordinary material with its capability to accommodate an array of remarkable electronic, mechanical and chemical properties (1, 13, 80). Extra-large surface-to-volume ratio renders graphene a highly flexible morphology, giving rise to intriguing observations such as ripples, wrinkles and folds (29, 76, 81-83) as well as the potential to transform into other novel carbon nanostructures (43, 48,

49, 83, 87-91). In particular, self-folding of graphene (83), or graphene origami (119-121), has been subjected to intensive study due to the need to fabricate unconventional nanostructures *via* approaches beyond conventional material preparation techniques. Progresses in patterning graphene with atomic-scale precision have further paved the way toward achieving graphene origami in a programmable fashion (120-125). For example, water nanodroplet can activate the self-folding of graphene flake cut in a particular cross shape (83). The unique feature of such an unconventional bottom-up nanomanufacture technique is that a material building block can self-assemble into a final folded structure, which is typically energetically more favorable and thus more stable than the original building block (126).

In general, non-bonded adhesion, such as van der Waals (vdW) forces, plays a crucial role in overcoming the energy barrier (*e.g.*, bending energy) in order to fold graphene as well as stabilizing the folded nanostructure against the perturbation from thermal fluctuation. A direct example is that a carbon nanoscroll can hold its spiral morphology rather stably *via* vdW forces distributed among interlayers over a large surface area (43, 48, 49, 83, 87-91). On the other hand, manipulating or neutralizing the interlayer vdW interaction can significantly affect the morphology of the carbon nanoscroll due to its open and tunable topology (47).

By suitably programming the original graphene building blocks, the resulting folded nanostructures of graphene can be customized to take various unique morphology and topology that are otherwise impossible in conventional carbon nanostructures, such as carbon nanotube and fullerene. Such novel nanostructures can overcome some intrinsic

difficulties that the conventional carbon nanostructures would inevitably suffer for certain applications. For example, the hollow nature of carbon nanotube (127) and fullerene (128) has motivated the proposal of using such materials as hydrogen storage medium, yet the fact that large size carbon nanotubes and fullerene become structurally unstable poses a practical limitation on storage capacity. By contrast, suitably folded graphene nanostructures can serve as nanocapsules or nanocontainers to host molecular-scale cargo of desirable quantity (129, 130), which has profound implications in molecular vessel and drug delivery applications (131). For example, as to be shown here, a graphene nanocage can stably store hydrogen molecules with a weighted percentage of 9.7%, exceeding US Department of Energy (DOE)'s ultimate goal of 7.5% (132).

The two dimensional nature of graphene makes the chemical functionalization of graphene a promising approach to modulating the graphene properties (30, 104-109). For example, hydrogenation of graphene (30, 52, 114) involves bonding atomic hydrogen to the carbon atoms in graphene. Such a reaction changes the hybridization of graphene from sp^2 into sp^3 . As a result, the two-dimensional atomic structure of pristine graphene is distorted (87, 88, 118). Significant progresses have been achieved on controllable hydrogenation of graphene. For example, single-sided hydrogenation of pristine graphene has been theoretically and experimentally explored (30, 87, 88, 110, 112, 113, 118, 133-135). Hybrid superlattices made of patterned hydrogenation can be fabricated in a controlled fashion on both macroscopic and microscopic scales (114). Recent studies show that hydrogen chemisorption in graphene can be enhanced by local curvature in a graphene sheet (133, 136, 137). It has also been shown that a

graphene sheet can closely conform to the sharp features on a substrate surface (*e.g.*, extrusions and edges) (38, 98, 138, 139), leading to large local curvature in the graphene. These findings suggest the feasibility of precise hydrogenation (*e.g.*, in atomic rows) of graphene in a programmable fashion. These advances on programmable bonding of atomic hydrogen to carbon atoms in pristine graphene open up new avenues for manipulating the morphology of graphene and therefore exploring graphene-based novel nanomaterials.

Here, we use molecular dynamics (MD) simulations to demonstrate the hydrogenation assisted graphene origami (HAGO), in which initially planar, suitably patterned graphene can self-assemble into three dimensional nanoscale objects of desirable geometric shapes. We further demonstrate that the HAGO process can be modulated by an external electric field, enabling programmable opening and closing of the resulting three dimensional nano-objects, a desirable feature to achieve molecular mass manipulation, storage and delivery. To benchmark this unique feature, we demonstrate using HAGO-enabled nanocage for controllable uptake and release of fullerenes and nanoparticles as well as ultra-high density of hydrogen storage.

3.2.2. Morphologically tunable graphene nanocage and its application

Hydrogenation of a carbon atom in pristine graphene generates an sp^3 carbon-hydrogen (C-H) bond, which induces a local structural change around that carbon atom. The chemically adsorbed hydrogen atom attracts its bonded carbon atom while repels other neighboring carbon atoms. Therefore, the three initially planar carbon-carbon (C-C) bonds associated with the hydrogenated carbon atom would locally bend away from

the hydrogen atom. If the graphene is hydrogenated on both sides, the resulting hydrogenated graphene (termed as graphane (30, 52)) would overall remain a rather planar morphology because the local distortions of the C-C bonds neutralize each other. Nevertheless, if the graphene is single-sided hydrogenated, the local distortion at each hydrogenated carbon atom is accumulated (84). For example, if hydrogenation lines are introduced in one side of a graphene, the accumulated distortion can effectively fold the graphene along the hydrogenation lines to a certain angle. Figure 3.8 shows that such a folding angle at equilibrium increases when the number of rows of hydrogenation increases. In particular, it is found that the folding angle can be tailored to be close to 90° (e.g., Figs. 3.8B, E), which offers the possibility to potentially form a stable folded substructure that consists of two faces that are folded nearly perpendicularly along the hydrogenation lines. The HAGO process often involves a cascade of or simultaneous events of such folding steps, as to be shown below.

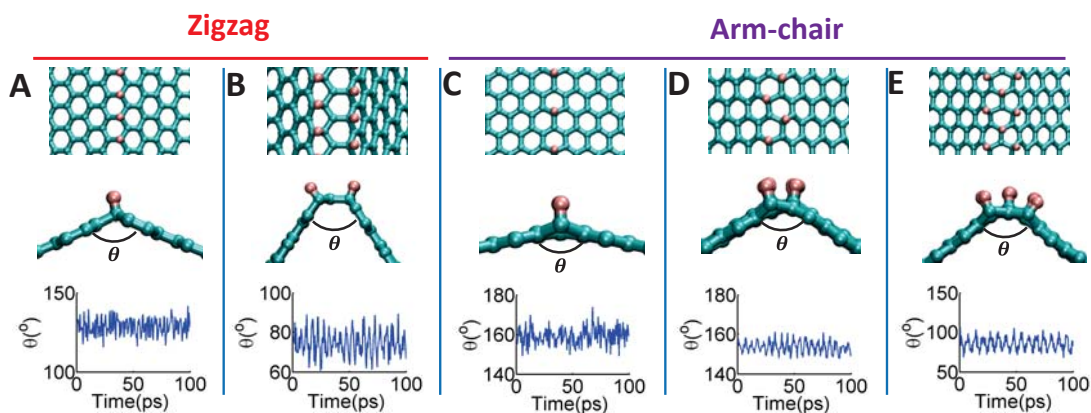


Figure 3.8. Top view and side view of graphene structures folded to an angle due to single-sided hydrogenation along various lines at equilibrium. (A) one-line and (B) two-line hydrogenation are introduced along zigzag direction of graphene lattice, respectively. (C)-(E): one-line, two-line, and three-line hydrogenation are introduced along arm-chair direction of graphene lattice, respectively. The bottom row plots the variation of the folding angle at 300K over time, which is shown to be minimum, indicating robust stability of the folded substructure.

Using MD simulations, we have successfully demonstrated an unconventional nanostructure enabled by HAGO, hexahedral nanocage (Fig. 3.9). In the simulations, the C-C and C-H bonds in the graphene as well as the non-bonded C-C and C-H interactions are described by AIREBO potential (78). The simulations are carried out using Large-scale Atomic/Molecular Massively Parallel Simulator (LAMMPS) (79).

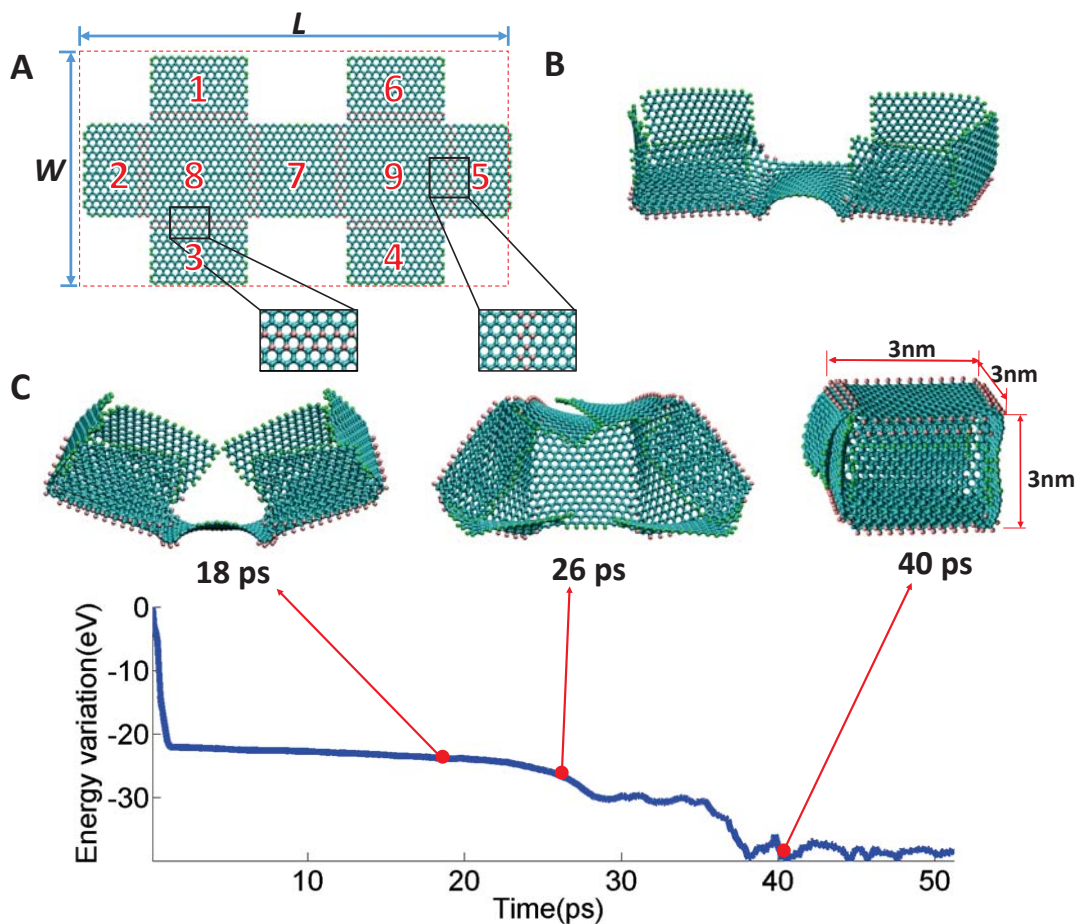


Figure 3.9. (A) Double-cross shaped graphene flake to achieve HAGO-enabled hexahedral graphene nanocage. Insets show the hydrogenation lines, which demarcate the graphene flake into nine regions (labeled by numbers). (B) Energy-minimized structure by conjugate gradient (CG) and steepest descent algorithm. (C) Further energy minimization towards the formation of a graphene nanocage.

Figure 3.9A depicts our simulation model to achieve HAGO-enabled hexahedral graphene nanocage. The double-cross shaped graphene flake is cut out of a rectangular

graphene with a length $L = 13.2\text{nm}$ and a width $W = 7.1\text{nm}$. Rows of single-sided hydrogenation are introduced along the expected edges, which demarcate the graphene flake into nine regions. Hereinafter, each such a region is referred to as a graphene wall. Each of the six outer graphene walls (labeled 1-6) has three free edges and the center graphene wall (labeled 7) has only two free edges, while the remaining two graphene walls (labeled 8 and 9) have no free edges. Carbon atoms along the free edges of the graphene flake are saturated by hydrogen atoms to avoid unwanted bond formation during the self-assembling process. Figure 3.9B shows the structural configuration after the initial energy minimization. Figure 3.9C shows the further structural evolution. At 18 ps, all six outer graphene walls are in the process of bending upward, which later fold along the hydrogenated edges up to about 90° . At 26 ps, the two graphene walls (labeled 8 and 9) are in the process of bending upward, which causes the two sets of folded graphene walls (1-2-3 and 4-5-6) to come close to each other, resembling the closing of a venus flytrap. At 40 ps, the two sets of folded graphene walls overlap with each other. Due to geometrical constraints and inter-wall vdW interaction, an outer graphene wall on the left slides above or beneath another outer graphene wall on the right. The vdW interaction further drives the tightening of the folded structure and serves as the inter-wall adhesives to stabilize the final structure. As a result, a quasi-cubic hexahedral graphene nanocage is formed.

In practice, hydrogenation process of graphene may not be as perfect as the ideal case (*e.g.*, Fig. 3.9A). In other words, defective hydrogenation (*e.g.*, missing hydrogen atoms) could occur in a random fashion. To this end, we have carried out further simulations of patterned graphene with random imperfection in hydrogenation. These

further studies reveal that HAGO is a rather robust self-assembly process with a strong tolerance to possible imperfect hydrogenation. For example, we show that the graphene nanocage can still be successfully formed even if only less than 70% of single-side hydrogenation from the ideal case is achieved (as detailed in Section 3.2.5).

In the HAGO-enabled graphene nanocage, the inter-wall vdW interaction energy plays a key role in maintaining the nanocage structural stability. Therefore, manipulation of such an interaction energy potentially offers the morphological tunability of the graphene nanocage (*e.g.*, controllable opening and closing). We next show that an external electric field can effectively reduce the inter-wall adhesion. Therefore, by tuning the external electric field, facile control of the morphology of graphene nanocage can be achieved. An external electric field can cause the polarization of carbon atoms in graphene. As a result, the inter-graphene-layer interaction can be changed. For example, it is shown that an electric field can effectively cause the radial expansion of a carbon nanoscroll due to the polarization induced decrease of inter-graphene-layer adhesion (47). Recently first-principle calculations have revealed the dependence of the effective dielectric constant in graphene structures on external electric field (140, 141). For a graphene bilayer, both in-plane and out-of-plane polarizations are shown to increase as the electric field increases (140). When a graphene bilayer is subjected to an out-of-plane electric field, the inter-layer adhesion is reported to decrease with increasing electric field intensity and the two graphene layers can be easily separated when the electric field intensity reaches above $1.8\text{V}/\text{\AA}$ (140). Here we show that the effective inter-layer adhesion of a graphene bilayer (*e.g.*, the overlapping walls in the HAGO-enabled graphene nanocage) also decreases when

the bilayer is subjected to an electric field parallel to the graphene plane. The effective inter-layer adhesion γ_{eff} consists of the contribution of the inter-layer vdW interaction and that of the inter-layer dipole interaction, *i.e.*, $\gamma_{eff} = \gamma_{vdW} + \gamma_{dipole}$; the dipole-induced surface energy can be deduced as $\gamma_{dipole} = \frac{d\Phi_{dipole}}{dS}$, where Φ_{dipole} is the total dipole-dipole interaction energy and S is the total surface area of the graphene (see Section 3.2.4).

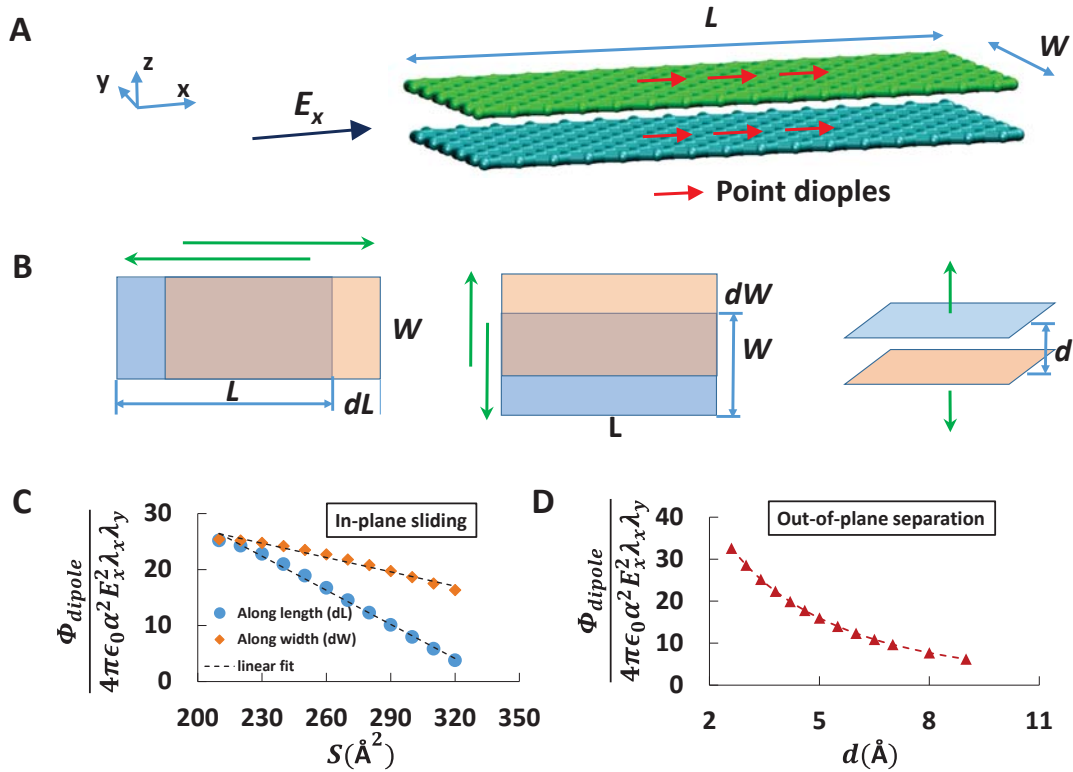


Figure 3.10. (A) Under an external electric field parallel to the plane of a graphene bilayer, point dipoles of the same direction as the electric field form in the graphene bilayer. (B) Schematics of in-plane sliding (left and middle panels) and out-of-plane separation (right panel) of the graphene bilayer. (C) As the two graphene layers slide off each other in the plane, the normalized dipole-dipole interaction energy decreases as the total surface area of the bilayer (e.g., $2(L+dL)W$ or $2L(W+dW)$) increases. (D) Similarly, as the two graphene layers separate out-of-plane, such an energy also decreases as the separation distance increases.

Figure 3.10A shows a schematic of dipole orientations when a graphene bilayer is subjected to an in-plane electric field. Figure 3.10C plots the normalized Φ_{dipole} as a

function of S as the graphene bilayer slide off each other (*i.e.*, $dS = 2LdW$ or $dS = 2WdL$, Fig. 3.10B). Figure 3.10C shows that Φ_{dipole} monotonically decreases as the inter layer sliding proceeds in two representative directions, indicating that under an in-plane electric field, in-plane sliding of a graphene bilayer is energetically favorable. Fig. 3.10D further shows that normalized Φ_{dipole} also decreases as the inter-layer separation distance increases, indicating that inter-layer out-of-plane separation is also energetically favorable. In addition, the hydrogenation and its induced folding of graphene can also lead to a non-uniform charge distribution (thus global polarization) in the HAGO-enabled graphene nanocage (Fig. 3.18 in Section 3.2.6). We have further shown that such a global polarization can also facilitate the opening of the nanocage when subjected to an external electric field (See Section 3.2.6). The above analysis suggests that an external electric field can reduce the effective inter-wall adhesion in a HAGO-enabled graphene nanocage, a unique feature that can potentially enable facile control of the morphology of graphene nanocage *via* tuning the external electric field.

Inspired by the above feature, we next demonstrate controlled opening and closing of HAGO-enabled graphene nanocage (Fig. 3.11), an otherwise hard to achieve but highly desirable mechanism for molecular mass manipulation. To capture the effect of external electric field on the effective inter-wall adhesion, the C-C pair potential is represented by a modified Lennard Jones potential $V_{CC}(r) = 4\lambda_{CC}\varepsilon_{CC}\left(\frac{\sigma_{CC}^{12}}{r^{12}} - \frac{\sigma_{CC}^6}{r^6}\right)$, where $\varepsilon_{CC}=0.00284$ eV, $\sigma_{CC}=0.34$ nm, and λ_{CC} (≤ 1) is a tuning factor that is to represent the effect of electric field (*e.g.*, $\lambda_{CC} = 1$ when there is no external electric field). As shown in Fig. 3.11, natural vdW interactions facilitate the formation of a

closed nanocage, which can be then opened up by applying an external electric field. Upon removing the electric field, the opened graphene nanostructure closes spontaneously, driven by vdW interactions. The controlled opening and closing of the graphene nanocage are reversible and repeatable by turning on and off the external electric field. Such a change of nanocage morphology can be readily understood as follows. In the HAGO-enabled formation of graphene nanocage, the closing of the nanocage leads to the decrease of inter-wall vdW interaction energy, which counterbalances the increase of folding induced bending energy. On the other hand, subjected to a sufficiently strong electric field, the effective inter-wall adhesion decreases, to some extent that is not able to hold up the nanocage. As a result, the nanocage opens up to relax the excessive bending energy.

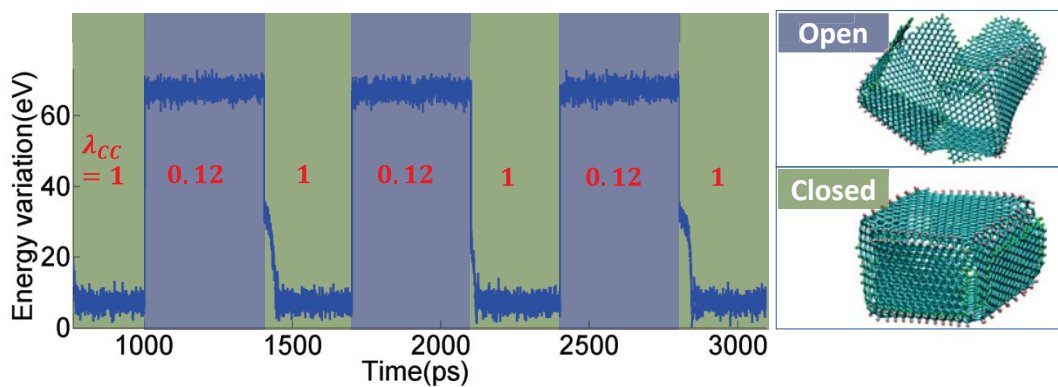


Figure 3.11. Controlled opening and closing of graphene nanocage via tuning effective inter-wall adhesion. $\lambda_{CC}=1$: without applied electric field, nanocage is closed; $\lambda_{CC}=0.12$: under an applied electric field, inter-wall adhesion decreases, leading to the opening of the nanocage under thermal fluctuation. The simulation is done in the NVT ensemble at 300K.

The controlled opening and closing of such graphene nanocages have practical significance, *e.g.*, to be used as a nanovessel or nanocontainer to achieve molecular mass delivery (129-131). As a demonstration of such a functionality, we study the uptake and release of C_{60} molecules using a HAGO-enabled graphene nanocage. A

closed nanocage is first immersed into a reservoir of C_{60} molecules, as shown in Fig. 3.12A. The MD simulation using AIREBO potential is carried out with NVT ensemble at a temperature of 300K. Reflective wall boundary condition is imposed in all three dimensions of the simulation box to simulate a constant feed of C_{60} molecules.

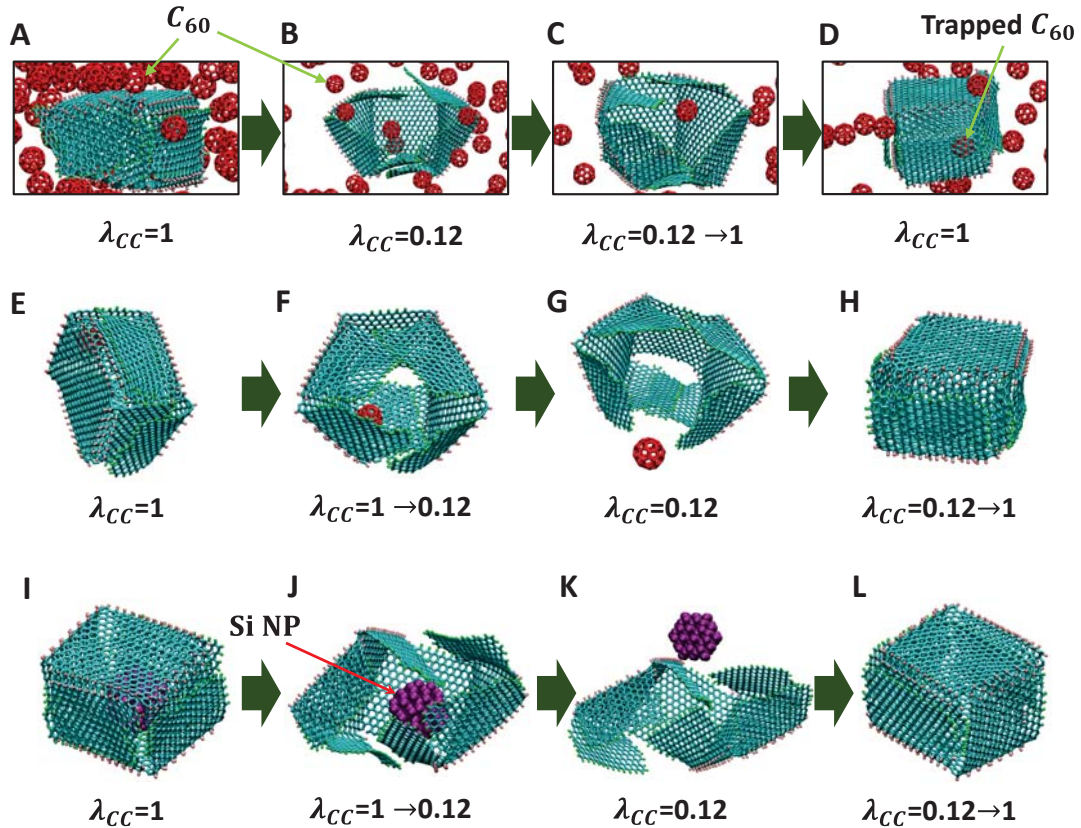


Figure 3.12. (A-D): Controlled opening and closing of a graphene nanocage immersed in a C_{60} reservoir can enable the uptake of C_{60} molecules by the nanocage. (E-H): After the cargo-loaded nanocage is transported to the destination, the stored C_{60} molecule can be released by the electric field induced opening of the nanocage. (I-L) Release of a silicon nanoparticle from a graphene nanocage under the same mechanism.

Initially, C_{60} molecules evolve to adhere to the outer surface of the graphene nanocage due to vdW adhesion. When an electric field is applied (*e.g.*, λ_{CC} decreases from 1 to 0.12), the nanocage opens up. Driven by thermal noise, some C_{60} molecules could migrate into the inner space of the nanocage. Upon turning off the electric field, the

nanocage closes spontaneously, and these C_{60} molecules are uptaken and stored inside the nanocage (Figs. 3.12A-D). After the nanocage with the cargo load (*e.g.*, C_{60}) is transported to a designated destination, then release of the cargo load can be achieved by applying an electric field to open up the nanocage, followed by the migration of the C_{60} molecules out of the nanocage driven by thermal fluctuation (Figs. 3.12E-H). We have also demonstrated the uptake and release of other molecular mass (*e.g.*, silicon nanoparticles, Figs. 3.12I-L) using the HAGO-enabled graphene nanocage under the same mechanisms. Note that, despite of the possible uncertainty of the thermally driven process, programmable uptake, storage, and release of molecular mass could be implemented by controlling a large amount of HAGO-enabled graphene nanocages *via* a global electric field.

An external electric field can also facilitate the formation of graphene nanocages of large sizes that are otherwise challenging to achieve. Figure 3.13 shows the electric field assisted formation of a graphene nanocage with a size of 9 nm by 9 nm by 12 nm. Figure 3.13A and B show two snapshots during the energy minimization process. When the graphene flake becomes larger, it becomes easier to fluctuate out-of-plane. As a result, neighboring graphene walls evolve to partially attach to each other driven by vdW adhesion, preventing the desirable formation of a nanocage. Such an unwanted feature can be overcome by the help of external electric field. As shown in Fig. 3.13 D-F, upon applying an electric field followed by turning it off, the initially collapsed graphene structure first partially open up and finally fold up into a rather regular hexahedron nanocage.

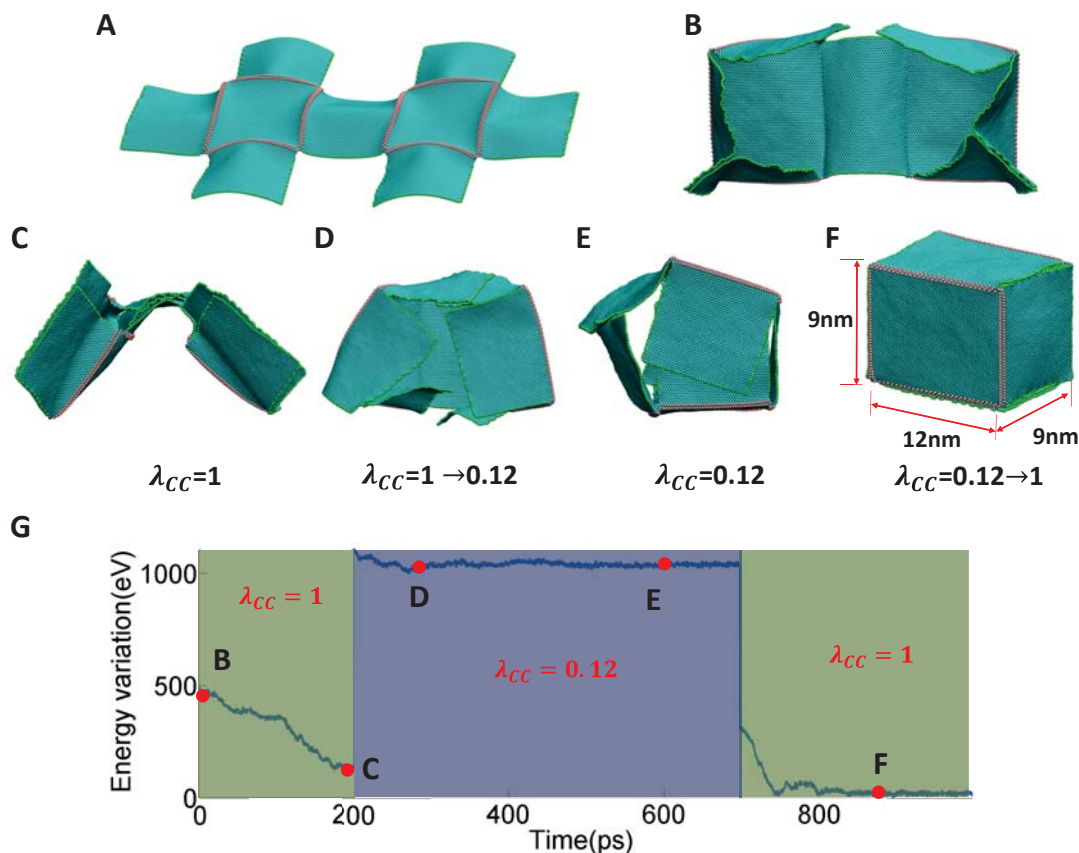


Figure 3.13. (A) Patterned graphene is suitably hydrogenated to form a graphene nanocage of large size. (B) Morphology after initial energy minimization. (C-F) Electric field assisted formation of large size graphene nanocage. (G) Evolution of potential energy from (B) to (F), indicating that the electric field can help prevent the graphene nanostructure trapped in unwanted metastable state (C) and facilitate the formation of the final nanocage (F), a thermodynamically stable state.

The effect of the electric field in such a process can be understood as follows. In the presence of an electric field, the effective inter-wall adhesion decreases, which cannot balance the excessive bending energy in the initially collapsed and distorted graphene structure. As a result, the entire graphene structure first partially opens up to release excessive bending energy, then gradually evolve toward lower energy configuration (Fig. 3.13D, E). After such a priming process and followed by restoring the natural inter-wall vdW adhesion by turning off the electric field, the graphene structure finally evolves into a regular nanocage as desired, which corresponds to the lowest energy

level as shown in Fig. 3.13 G. In other words, the electric field can help prevent the graphene structure getting stuck in unwanted metastable states and thus facilitate the formation of the thermodynamically stable graphene nanostructure. Results in Fig. 3.13 further demonstrate the feasibility and robustness of the programmable HAGO process.

The tunable and robust morphology HAGO-enabled graphene nanocage as well as its hollow nature with a volumetric capacity of nearly 1000 nm^3 (*e.g.*, Fig. 3.13F) render attractive attributes for potential applications such as nanoscale pressure tank (*127, 128*). To benchmark such potentials, here we demonstrate high density hydrogen storage enabled by graphene. Giant fullerenes have been proposed to serve as a medium of high density hydrogen storage (*128*), but their closed nature poses intrinsic challenge to uptake and release of hydrogen as such a process involve breaking covalent C-C bonds thus are irreversible. By contrast, a HAGO-enabled graphene nanocage can be repeatedly opened and closed *via* facile control of an external electric field, making reversible uptake and release of hydrogen feasible. Although the graphene nanocage is not fully sealed by covalent bonds as in a giant fullerene, the inter-wall adhesion over large areas indeed allows it to sustain sufficiently high pressure (thus store a large amount of hydrogen molecules inside). In addition, when an empty nanocage is immersed in a hydrogen reservoir, a slight opening of the nanocage effectively gives rise to the formation of gaps or pores along the edge and corner of the nanocage, a feature that allows the adsorption of hydrogen atoms into the inner volume of the nanocage (See Section 3.2.7) (*142, 143*).

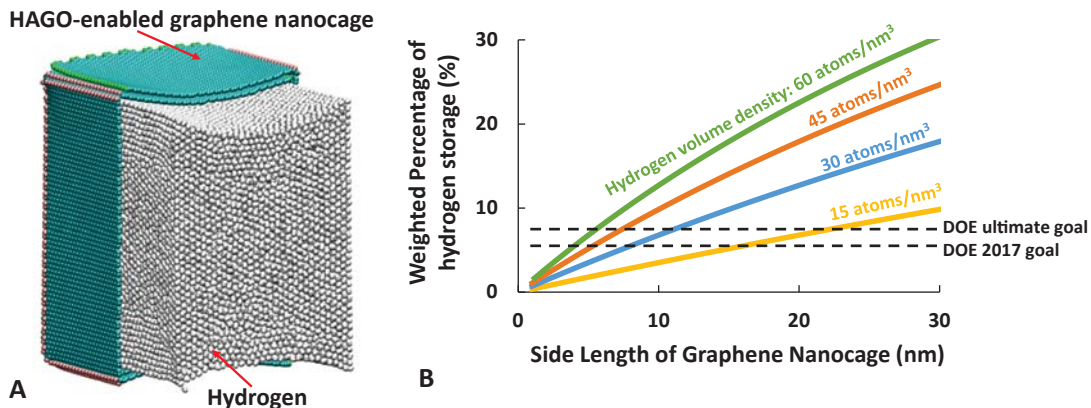


Figure 3.14. (A) High density hydrogen storage in HAGO-enabled graphene nanocage, with a weighted percentage of 9.7%, beyond the US DOE ultimate goal of 7.5% for hydrogen storage. For visual clarity, only half of the nanocage is shown. (B) Weighted percentage of hydrogen storage in HAGO-enabled graphene nanocage as a function of the side length of a cubic graphene nanocage, for four different hydrogen volume densities inside the nanocage. Dashed lines denote US DOE ultimate goal and year 2017 goal on hydrogen storage density.

As shown in Fig. 3.14A, the graphene nanocage in Fig. 3.13 can host 47,880 hydrogen atoms in its inner volume at a temperature of 70K. During the MD simulation, no escaping of the hydrogen is observed at such a temperature. The graphene nanocage contains 37,130 carbon atoms and 1468 initially chemically adsorbed hydrogen atoms. Therefore, the weighted percentage of the hydrogen storage is about 9.7%, which exceeds the US DOE target of 5.5% for the year 2017 and the ultimate goal of 7.5% (132), indicating the promising potential of HAGO-enabled graphene nanocage as a high density hydrogen storage medium.

The hydrogen storage density using graphene nanocage depends on the nanocage size, which can be estimated by a simple model. Consider a cubic graphene nanocage formed *via* HAGO process with side length of L , let ρ_c be the *area* density of graphene, ρ_h be the volume density of the stored hydrogen, m_h and m_c be the atomic mass of hydrogen

and carbon atoms, respectively. The weighted percentage of hydrogen storage in such a graphene nanocage can be estimated by $\frac{m_h \rho_h L^3}{m_h \rho_h L^3 + 9m_c \rho_c L^2}$.

Fig. 3.14B plots the weighted percentage of hydrogen storage as a function of graphene nanocage size L , for four different hydrogen volume density. As shown in Fig. 3.14B, the hydrogen storage capacity increases as the graphene nanocage size increases, in an approximately linear fashion. For example, to reach the DOE's ultimate goal for hydrogen storage density, graphene nanocages of size greater than 12 nm and 6 nm are needed, for the hydrogen volume density of 30 atom/nm³ and 60 atom/nm³, respectively. We have also shown that such hydrogen volume density levels can be feasibly achieved by tuning the ambient hydrogen reservoir pressure (see Section 3.2.7). In this sense, the above estimation offers a rule-of-thumb guideline for the design of graphene nanocage to achieve certain hydrogen storage density. The hydrogen atoms stored inside the graphene nanocage can also be effectively released by elevating the temperature (details available in Section 3.2.8).

In summary, through systematic MD simulations, we demonstrate a feasible and robust hydrogenation-assisted graphene origami (HAGO) process. We further reveal that an HAGO-enabled graphene nanocage can be reversibly opened and closed in a programmable fashion *via* the facile control of an external electric field, a desirable feature that can enable controllable molecular mass uptake, storage, and release, as well as high density hydrogen storage. These promising applications of HAGO process and HAGO-enabled novel nanostructures call for further experimental investigations to explore their full potential.

3.2.3. *Simulation methods*

C-C and C-H bonds in the graphene as well as the non-bonded C-C and C-H interactions are described by AIREBO potential (78). The simulations are carried out using Large-scale Atomic/Molecular Massively Parallel Simulator (LAMMPS) (79). The time step for all simulations is set to be 0.5 femtoseconds (fs).

Molecular dynamics simulations in Fig. 3.8, Fig. 3.11, Fig. 3.12 and Figs. 3.13C-F are done in NVT ensemble at 300K and by Nose-Hoover thermostat.

Molecular dynamics simulations in Fig. 3.14A are done in NVT ensemble at 70K and by Nose-Hoover thermostat.

Figure 3.9 is to demonstrate that HAGO is intrinsically energetically favorable; therefore energy minimization simulations are done in NVE ensemble (not NVT) in Fig. 3.9. Energy minimization simulations in Fig. 3.9 (also in Fig. 3.13A and B) are first done by conjugate gradient (CG) algorithm followed by steepest descent algorithm until either the total energy change between successive iterations divided by the energy magnitude is less than or equal to 10^{-10} or the total force is less than 10^{-5} eV \AA^{-1} . However, both conjugate gradient and steepest descent algorithm are highly possible to find a local energy minimum point. To gain further approach to global energy minimum configuration, we adopted an alternate way of relaxing a system by running dynamics with a small or limited time step. The simulation is then running in NVE ensemble with the restriction that the maximum distance an atom can move in one time step is 0.1 \AA . The time step is set to be 0.5 femtoseconds (fs).

3.2.4. Dipole-dipole interaction

The dipole-dipole interactions (47) can be described as $V(\vec{r}_{ij}) = \frac{1}{4\pi\epsilon_0|\vec{r}_{ij}|^3} \left[|\vec{p}_i||\vec{p}_j| - \frac{3(\vec{r}_{ij}\cdot\vec{p}_i)(\vec{r}_{ij}\cdot\vec{p}_j)}{|\vec{r}_{ij}|^2} \right]$, where \vec{r}_{ij} is the distance between dipole i and dipole j, $\vec{p}_i = 4\pi\epsilon_0\alpha_i\vec{E}$ the induced dipole moment, \vec{E} the applied electric field, ϵ_0 the vacuum permittivity, and α_i the polarizability of atom i. Assume $\vec{E} = (E_x, 0, 0)$ and the carbon planes are in parallel with the electric field. Only the dipole-dipole interaction between two layers is considered because they are expected to act against the vdW adhesion the most. Let $\vec{r}_{ij} = (x_j - x_i, y_j - y_i, z_j - z_i)$ and assuming constant polarizability for each carbon atom $\alpha_i = \alpha_j = \alpha$, we have

$$V(\vec{r}_{ij}) = \frac{4\pi\epsilon_0\alpha^2 E_x^2}{((x_i - x_j)^2 + (y_i - y_j)^2 + d^2)^{\frac{3}{2}}} - \frac{12\pi\epsilon_0\alpha^2 E_x^2 (x_j - x_i)^2}{((x_i - x_j)^2 + (y_i - y_j)^2 + d^2)^{\frac{5}{2}}}$$

spacing. The total dipole-dipole interaction energy is $\Phi_{\text{dipole}} = \sum_{i \neq j} V(\vec{r}_{ij})$, from which the dipole-induced surface energy can be deduced as $\gamma_{\text{dipole}} = \frac{d\Phi_{\text{dipole}}}{dS} =$

$\frac{d\Phi_{\text{dipole}}}{2(WdL + LdW)}$. The total dipole-dipole interaction energy can be calculated as

$$\Phi_{\text{dipole}} = \lambda_x \lambda_y \int_{x_1^{\min}}^{x_1^{\max}} \int_{x_2^{\min}}^{x_2^{\max}} \int_{y_1^{\min}}^{y_1^{\max}} \int_{y_2^{\min}}^{y_2^{\max}} \frac{4\pi\epsilon_0\alpha^2 E_x^2}{((x_1 - x_2)^2 + (y_1 - y_2)^2 + d^2)^{\frac{3}{2}}} - \frac{12\pi\epsilon_0\alpha^2 E_x^2 (x_2 - x_1)^2}{((x_1 - x_2)^2 + (y_1 - y_2)^2 + d^2)^{\frac{5}{2}}} dx_1 dx_2 dy_1 dy_2$$

where λ_x and λ_y are the dipole density along x and y direction.

3.2.5. Effect of imperfection in hydrogenation pattern on HAGO

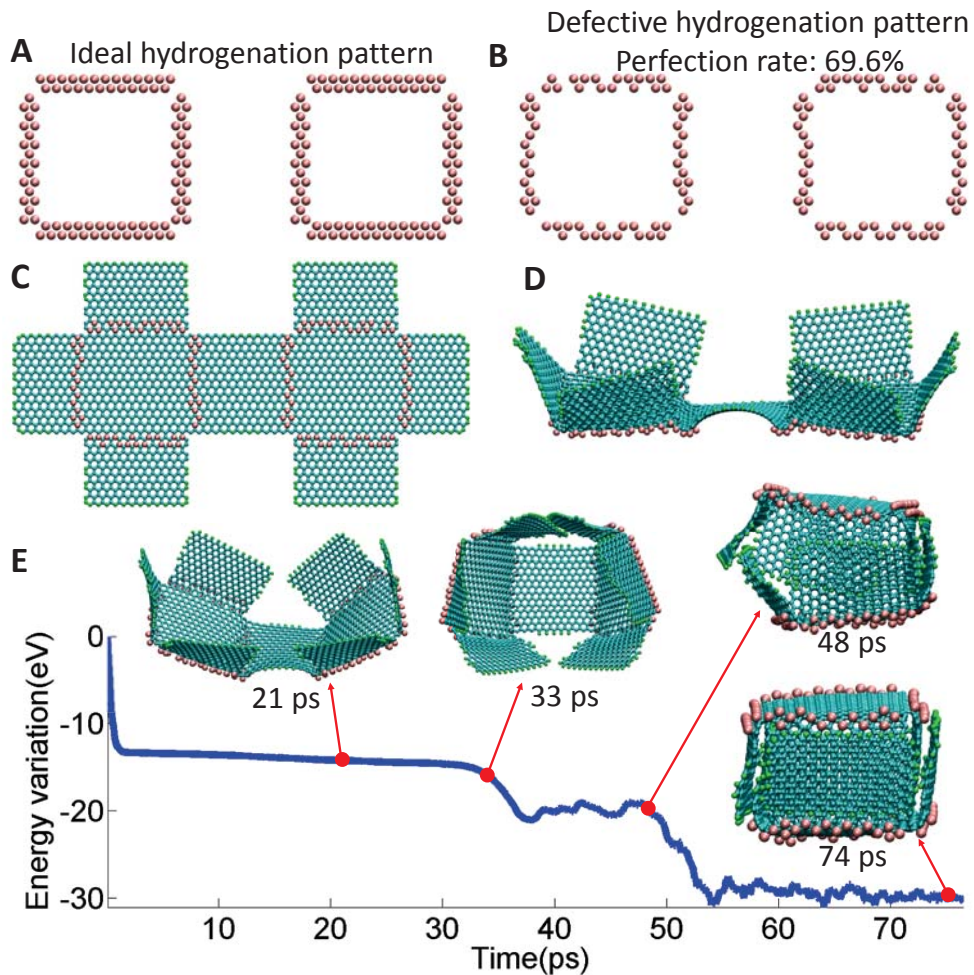


Figure 3.15. (A) Complete single-sided hydrogenation pattern, with 184 hydrogen atoms, as in Fig. 3.9. For visual clarity, only hydrogen atoms are shown. (B) A randomly generated defective hydrogenation pattern, which contains 128 hydrogen atoms (i.e., the perfection rate is 69.6%). (C) Double-cross shaped graphene flake with the defective hydrogenation pattern of (B). (D) Energy-minimized structure in (C) by conjugate gradient and steepest descent algorithm. (E) Further energy minimization towards the formation of a graphene nanocage.

We further investigate the formation of graphene nanocage with the influence of the defective hydrogenation. To this end, we employ the same simulation methodology as in Fig. 3.9 in order to make direct comparison. As a reference, Fig. 3.15A shows the complete hydrogenation pattern as in Fig. 3.9 with 184 hydrogen atoms (the carbon atoms are not shown for visual clarity). Defective hydrogenation patterns are generated

by randomly removing hydrogen atoms from the complete hydrogenation pattern. Three defective levels are considered, with 20, 40 and 56 hydrogen atoms removed from the complete hydrogenation pattern, corresponding to the perfection rate of 89.2% (Fig. 3.16A), 78.3% (Fig.3.16B) and 69.6% (Fig. 3.15B), respectively.

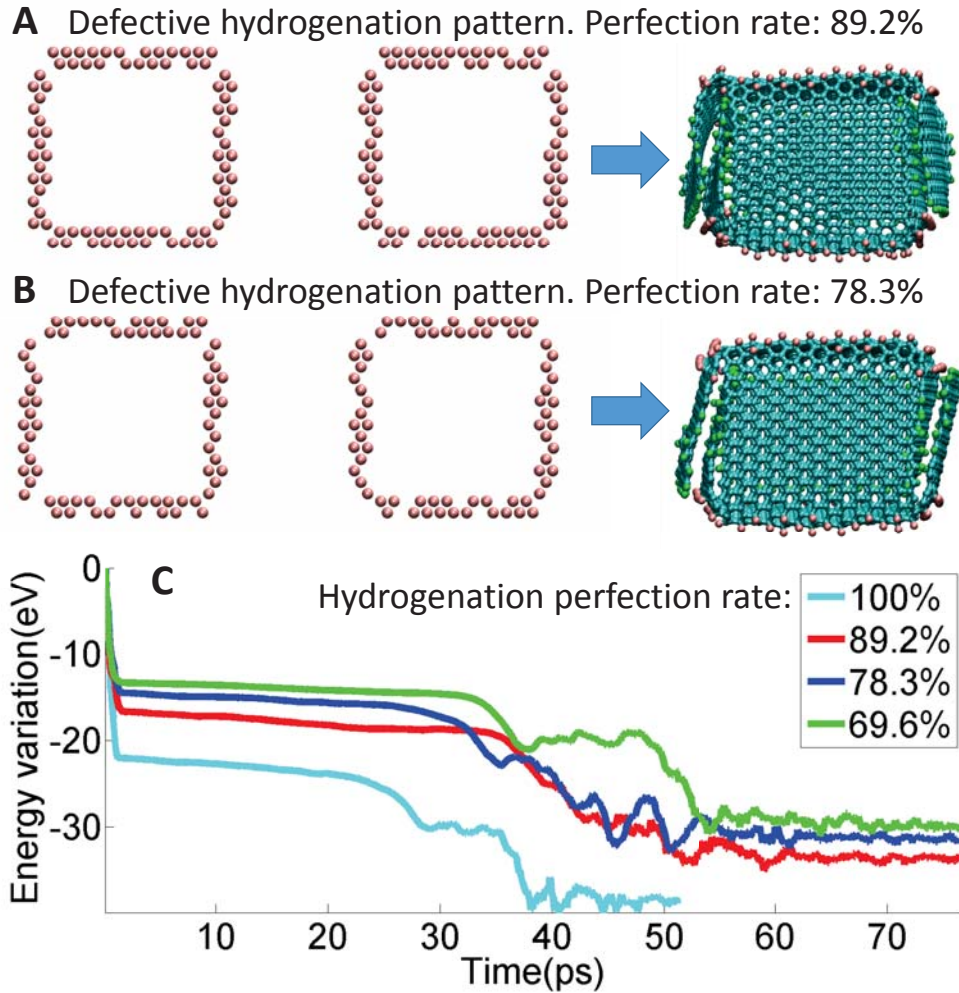
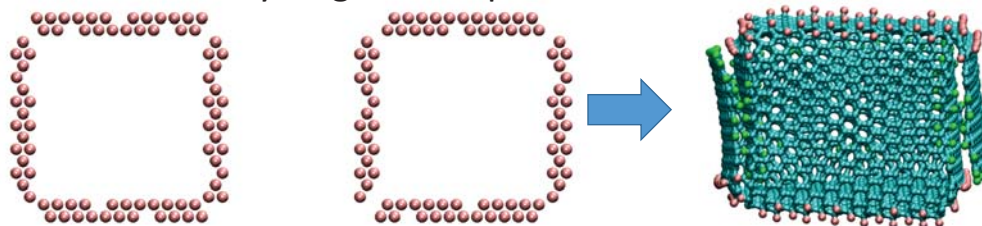


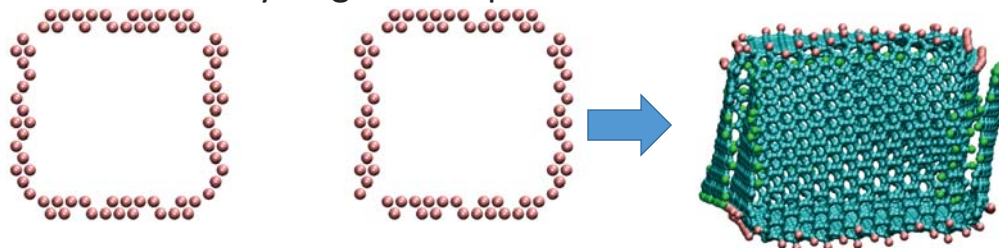
Figure 3.16. (A) Randomly generated defective hydrogenation pattern with 164 hydrogen atoms (perfection rate 89.2%) and its resulting graphene nanocage. (B) Randomly generated defective hydrogenation pattern with 144 hydrogen atoms (perfection rate 78.3%) and its resulting graphene nanocage. (C) Comparison of the energy evolution for different hydrogenation perfection rates towards the formation of nanocage. The curve for 100% perfection rate is replotted from Fig. 3.9C for comparison.

It turns out that in all three cases of defective hydrogenation, the HAGO-driven formation of graphene nanocage can still be achieved. Figure 3.15E plots the sequential snapshots of the nanocage formation and the corresponding energy evolution for the case of perfection rate of 69.6%, which reveal a process quite similar with the case of complete hydrogenation as shown in Fig. 3.9. Figure 3.16A and B further show the final shape of the nanocages formed under the hydrogenation perfection rate of 89.2% and 78.3%, respectively. No appreciable difference in the final shapes is found in all simulation cases once the graphene nanocage is finally formed. To further illustrate the effect of the imperfection in hydrogenation on the kinetics of nanocage formation, Fig.3.16C compares the energy evolution of the simulated structure under hydrogenation perfection rates of 100% (complete hydrogenation, as in Fig. 3.9C), 89.2%, 78.3% and 69.9%, respectively. Figure 3.16A and B show the defective hydrogenation pattern with the perfection rate of 89.2% and 78.3%, respectively, and also the final shape of the resulting nanocage structure. Similar significant drops of energy as the patterned graphene folds up and the nanocage forms occur in all four cases. The time needed to form a graphene nanocage as well as the equilibrium energy level increases slightly as the hydrogenation perfection rate decreases. Nonetheless, all curves in Fig. 3.16C suggest that the HAGO-driven process of patterned graphene with defective hydrogenation is energetically favorable.

A Defective hydrogenation pattern. Perfection rate: 89.2%



B Defective hydrogenation pattern. Perfection rate: 78.3%



C Defective hydrogenation pattern. Perfection rate: 69.6%

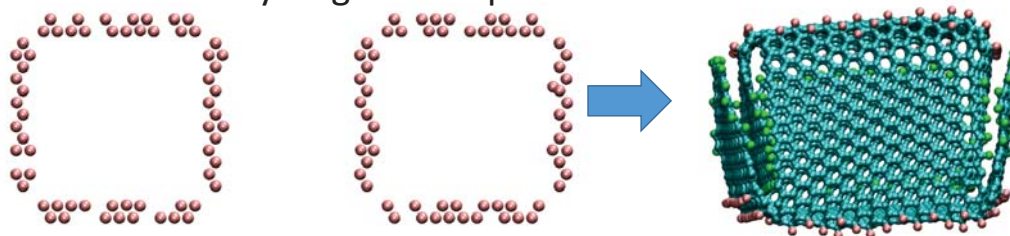


Figure 3.17. Another set of randomly generated defective hydrogenation patterns and their resulting graphene nanocages. Hydrogenation perfection rate: (A) 89.2%. (B) 78.3%. (C) 69.6%.

To further demonstrate the robustness of HAGO-driven process is insensitive to the randomness of the defective hydrogenation, Fig. 3.17 shows another set of three randomly generated defective hydrogenation patterns with perfection rate of 89.2%, 78.3%, and 69.9%, respectively, all of which leads to successful formation of a graphene nanocage in a similar fashion as shown in Fig. 3.15 and Fig. 3.16. The above studies clearly demonstrate that HAGO is a rather robust self-assembly process with a strong tolerance to possible imperfect hydrogenation in practices.

3.2.6. Effect of hydrogenation and folding induced global polarization on the morphology of graphene nanocage under an external electric field

Beside the local point dipoles induced by an external electric field, intrinsic global polarization could also occur in a HAGO-enabled nanostructure. Such an intrinsic polarization results from the non-uniform distribution of charges in the resulting nanostructures due to hydrogenation and folding.

Figure 3.18A shows the charge distribution in the resulting graphene nanocage. The initial charge for every atom in the graphene nanocage structure is set to zero. The equilibrium charge distribution is calculated by the ReaxFF potential implemented in LAMMPS package. Due to the difference of electronegativity between hydrogen and carbon atoms, the hydrogen atoms that reside on the edges of the nanocage have the highest positive charge; The carbon atoms that are bonded to those hydrogen atoms have the highest negative charge while other carbon atoms have charges with extremely low magnitude. Subject to an external electric field, the positively charged hydrogen atoms and the negatively charged carbon atoms that are bonded to these hydrogen atoms would experience local electrostatic forces in opposite directions. As a result, the folded edges in the nanocage would subject to localized electrostatic moments.

Figure 3.18B further clarifies the distribution of the positive and negative charges in the nanocage, which adopts an alternating pattern. For example, most part of the top surface is negatively charged, while the edges are positively charged. Similarly, the middle portion of the side surface is negatively charged, while the edges and some portion near the edges are positively charged. Such alternating polarization patterns

give rise to the formation of large molecular dipoles within the nanocage. An external electric field can interact with such dipoles and thus change the morphology of the graphene nanocage.

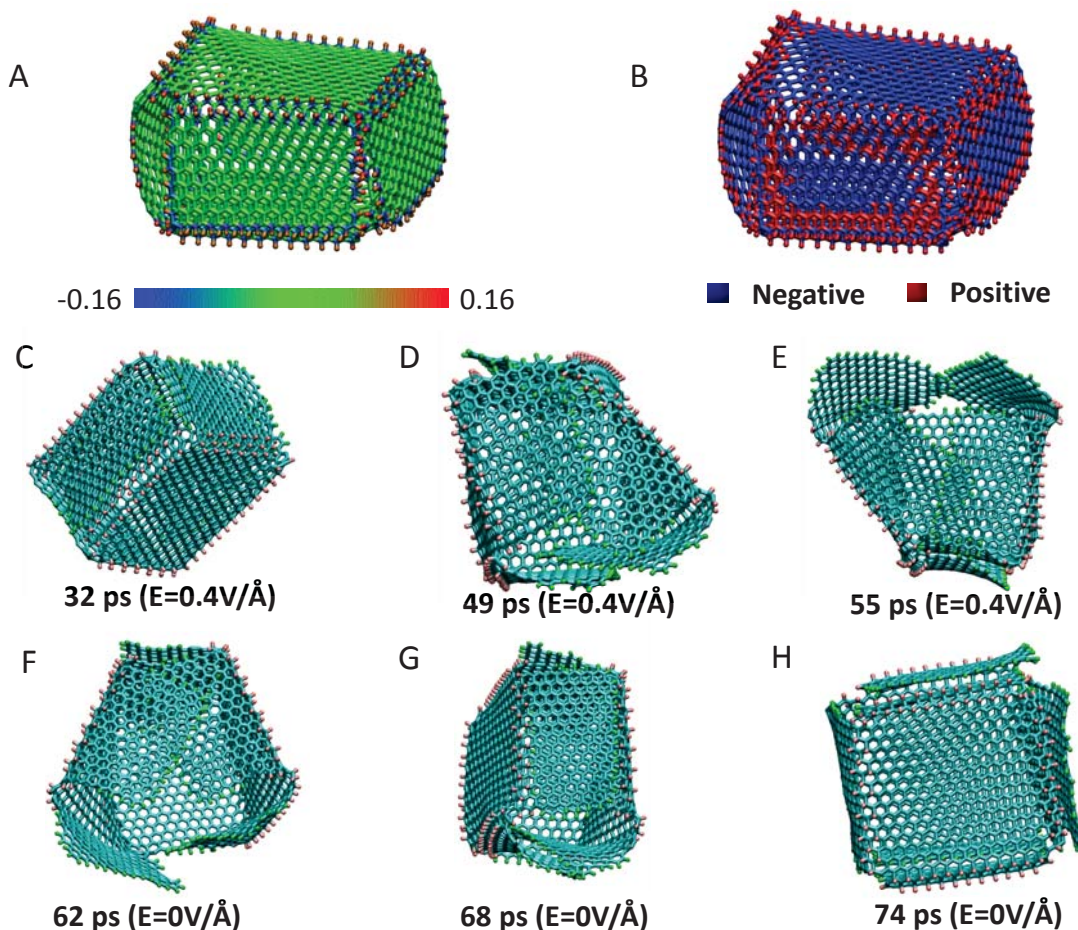


Figure 3.18. (A) Hydrogenation and folding induced non-uniform charge distribution in the graphene nanocage. (B) Mapping of positive and negative charges in the graphene nanocage. (C-E) The opening process of the graphene nanocage under the electrostatic force induced by an external electric field. (F-H) Upon removing the external electric field, the partially open graphene nanocage closes up spontaneously.

To demonstrate such an effect of external electric field on the morphology change of the graphene nanocage, we explicitly prescribe a constant electric field in the MD simulation, which is carried out in NVT ensemble at a temperature of 300K. The electric field is assigned along a fixed direction and the effect of electric field intensity

is studied. Subject to a weak electric field (*e.g.*, with an intensity of $0.1\text{V}/\text{\AA}$), no appreciable morphology change of the nanocage is observed as the resulting electrostatic force or moment is not strong enough to overcome the stabilizing interactions such as inter-wall vdW forces. However, subject to an electric field of intensity of $0.4\text{V}/\text{\AA}$, the graphene nanocage becomes unstable and fails to maintain its hexahedral shape. Figure 3.18C to E show the sequential snapshots of the resultant opening process of the graphene nanocage under such an electric field. When the electric field is turned off after the nanocage opens up, the partially unfolded structure can gradually recover its hexahedral configuration, as shown in Figs. 3.18F to H. The above analysis reveals that the hydrogenation and folding induced intrinsic polarization of the graphene nanocage indeed facilitates the programmable opening of the nanocage via an external electric field.

3.2.7. Hydrogen storage process in a graphene nanocage immersed in a hydrogen reservoir

We investigate the hydrogen storage process using a graphene nanocage. Figure 3.19A shows the simulation model, an initially empty cubic graphene nanocage (about 3 nm by 3 nm by 3 nm) formed by HAGO process is placed in a hydrogen reservoir with a cubic cavity of proper size to fit the nanocage. A cubic simulation box (8.6 nm by 8.6 nm by 8.6 nm) is used with periodical boundary condition prescribed in all three principal directions. Effectively, such a simulation models the scenario of a large number of empty graphene nanocages immersed in a vast hydrogen reservoir in a

periodical fashion. The simulation is done in 70K in NVT ensemble and by Nose-Hoover thermostat.

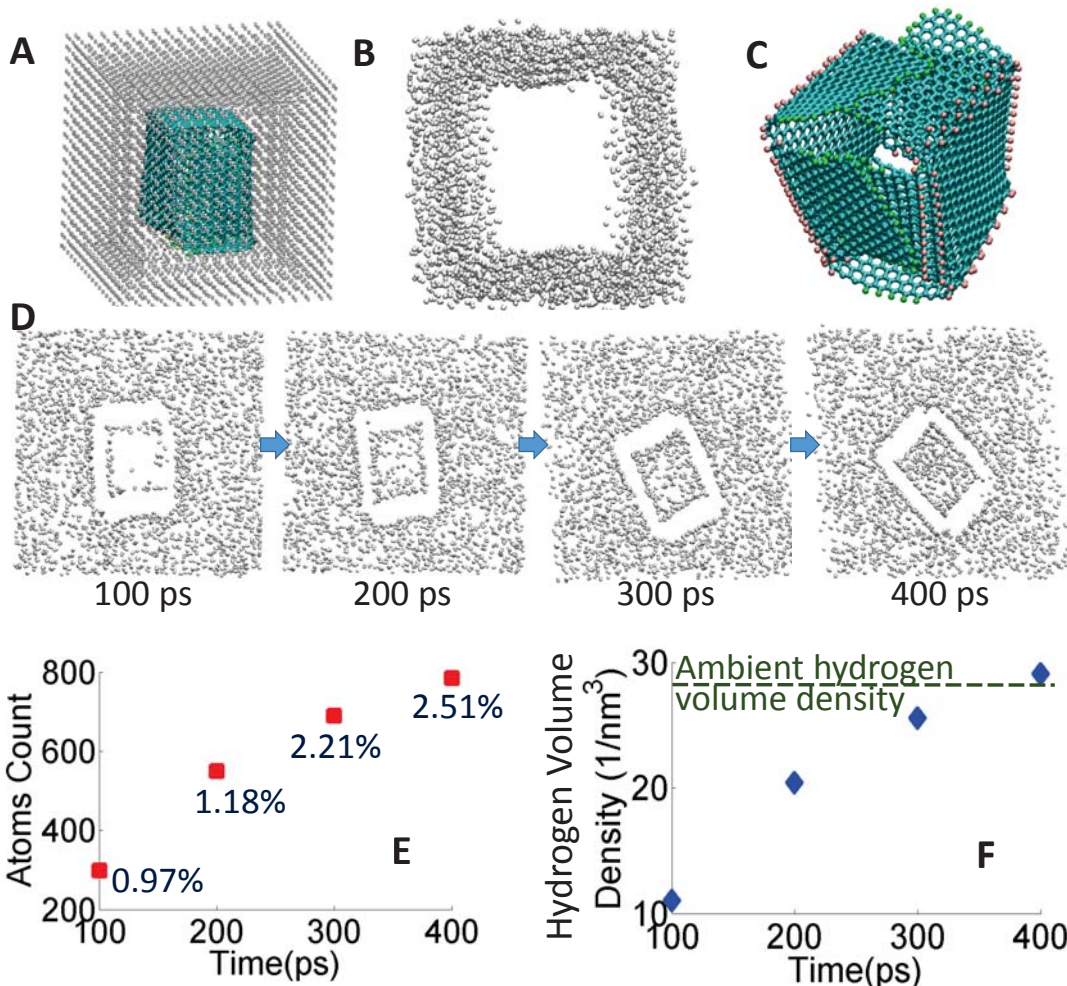


Figure 3.19. (A) Simulation model of an empty graphene nanocage immersed in a hydrogen reservoir. (B) A cross-section view of the hydrogen reservoir when the graphene nanocage is closed in a dynamics simulation (for visual clarity, the nanocage is not shown). (C) The slight opening of graphene nanocage gives rise to gaps and pores along the edges and corners. For visual clarity, the ambient hydrogen atoms are not shown. (D) Sequential snapshots of the cross-section view of the hydrogen reservoir showing the adsorption of hydrogen into the inner volume of the nanocage. For visual clarity, the nanocage is not shown. (E) The evolution of the number of hydrogen atoms adsorbed into the nanocage and the corresponding weighted percentage of hydrogen storage. (F) The evolution of the effective volume density of hydrogen adsorbed inside the graphene nanocage. The dashed shows the level of ambient volume density of hydrogen atoms.

Figure 3.19B shows a typical cross-section view of the hydrogen reservoir when the nanocage remains closed in a dynamics simulation (for visual clarity the nanocage is not shown). When an electric field is applied (*i. e.*, $\lambda_{CC} = 0.05$ in Fig. 3.19C), the slight opening of the nanocage against the outer pressure from the hydrogen reservoir creates gaps and pores along the edges and corners of the nanocage, through which the hydrogen can diffuse into the inner volume of the nanocage. Figure 3.19D shows several snapshots of the cross-section views of the hydrogen reservoir, revealing the gradual adsorption process of hydrogen into the inner volume of the nanocage. The adsorption process lasts for 400 ps, during which the electric field is first on for 50 ps and then off for 50 ps, and such a pattern is repeated during the 400 ps. Figure 3.19E further plots the number of hydrogen atoms adsorbed into the nanocage and the corresponding weighted percentage of hydrogen storage at four stages shown in Fig. 3.19D. It is shown that, a weighted percentage of hydrogen storage of 2.51% can be achieved using a graphene nanocage with a dimension about 3 nm by 3 nm by 3 nm. This weighted percentage is smaller than that shown in Fig. 3.19A due to the relatively smaller nanocage dimension used here. Fig. 3.19F plots the evolution of the effective volume density of hydrogen adsorbed inside the graphene nanocage, which shows an increasing trend of the hydrogen volume density inside the nanocage. At the equilibrium, the hydrogen atoms adsorbed inside the nanocage reaches a volume density comparable to the ambient hydrogen volume density (defined as the total number of hydrogen atoms in the simulation box divided by the volume of the simulation box). This result suggests that it is possible to tune the hydrogen storage density in graphene nanocage by varying the pressure of the hydrogen reservoir (*e.g.*,

a higher storage density achieved by increasing the reservoir pressure), a desirable feature for hydrogen storage.

3.2.8. Temperature-modulated release of hydrogen atoms from graphene nanocage

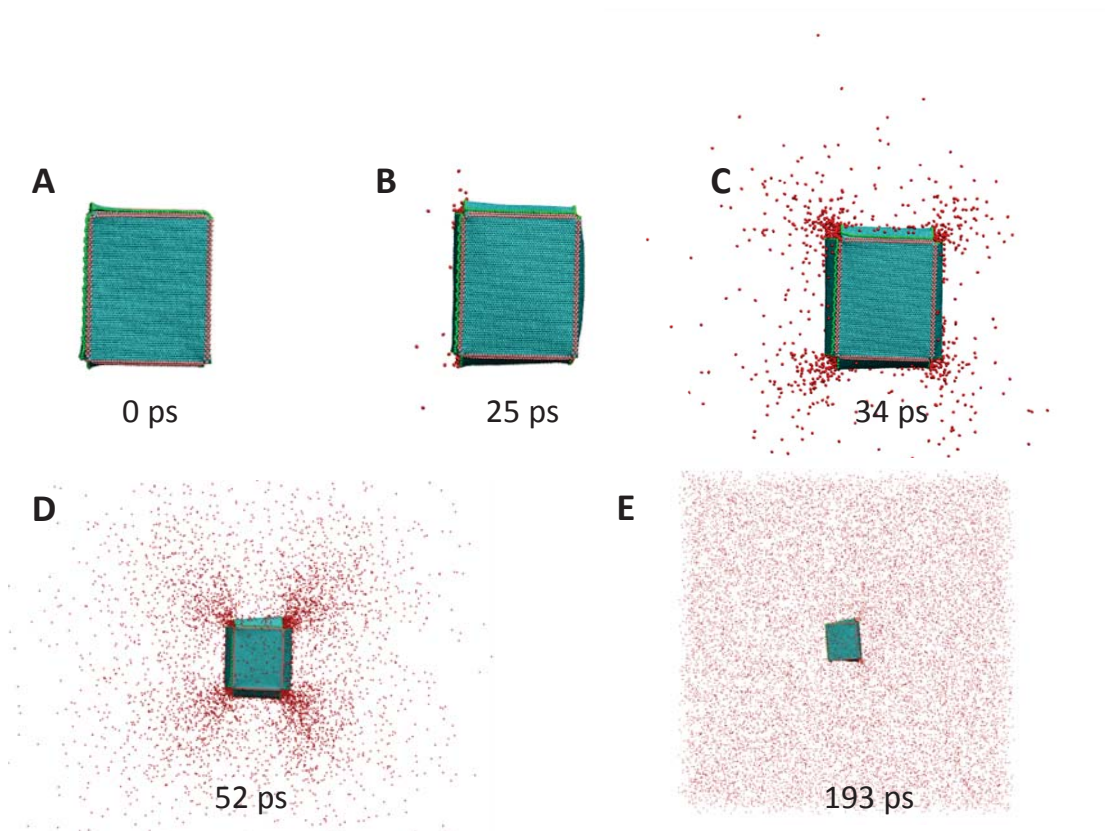


Figure 3.20. Release of hydrogen stored inside a graphene nanocage at an elevated temperature (300K). Starting configuration is the same structure as in Fig. 3.14A. Increasing pressure of stored hydrogen at elevated temperature causes the partial opening of the four edges of the graphene nanocage that are not covalently sealed, which allows the hydrogen atoms to spray out. After 193 ps, majority of stored hydrogen atoms are released. The simulation is in NVT ensemble and by Nose-Hoover thermostat. Hydrogen molecules are colored in red.

To demonstrate a feasible and safe approach to releasing the hydrogen atoms stored in the graphene nanocage (*e.g.*, Fig. 3.14A), we further investigate the effect of temperature on hydrogen release. When the temperature is elevated, the kinetic energy of the hydrogen atoms increases. As a result, the pressure exerted by the hydrogen to the graphene nanocage increases. Since the graphene nanocage is not covalently

bonded but rather sealed via vdW interaction, the increase in the kinetic energy of the hydrogen atoms could eventually outweigh the vdW adhesion energy that holds the graphene nanocage if the temperature is sufficiently high. As a result, the graphene nanocage could partially open up so that hydrogen atoms can escape from the nanocage. To demonstrate the above effect, we use the hydrogen-filled graphene nanocage structure in Fig. 3.14A as the starting configuration and perform molecular dynamics simulations in NVT ensemble to increase the temperature to 300 K by Nose-Hoover thermostat. As shown in Fig. 3.20, at a higher temperature, the four edges of the graphene nanocage that are not covalently sealed start to open up under the increased internal pressure from the hydrogen atoms. As a result, pressurized hydrogen atoms spray out from the open edges. At 193 ps, majority of the hydrogen atoms initially stored inside the graphene nanocage are successfully released and fill up the entire simulation box. These results suggest that elevating temperature can be an effective and feasible mechanism to release the hydrogen atoms stored inside the graphene nanocage.

3.3. Chapter summary

Hydrogenation of graphene leads to local bond distortion of each hydrogenated carbon atoms. Therefore, programmable hydrogenation of graphene can open up new pathways to controlling the morphology of graphene and therefore enable the exploration of graphene-based unconventional nanomaterials. The malleable nature of atomically thin graphene makes it a potential candidate material for nanoscale origami, a promising bottom-up nanomanufacturing approach to fabricating nano-building

blocks of desirable shapes. The success of graphene origami hinges upon precise and facile control of graphene morphology, which still remains as a significant challenge. Inspired by recent progresses on functionalization and patterning of graphene, we demonstrate hydrogenation assisted graphene origami (HAGO), a feasible and robust approach to enabling the formation of unconventional carbon nanostructures, through systematic molecular dynamics simulations.

As a pioneer study, we first show that single-sided hydrogenation can cause the scrolling of graphene. If a proper size of the graphene is hydrogenated in one side, the graphene can completely scroll up in to a carbon nanoscroll (CNS) that remains stable at room temperature. We perform extensive simulations to delineate a diagram in which three types of scrolling behavior of partially single-sided hydrogenated graphene are identified in the parameter space spanned by the hydrogenation size and the graphene size. Such a diagram can serve as quantitative guidelines that shed important light on a feasible solution to address the challenge of fabricating high quality CNSs, whose open topology holds promise to enable novel nanodevices. A unique and desirable feature of HAGO-enabled nanostructures is the programmable tunability of their morphology via an external electric field. In particular, we demonstrate reversible opening and closing of a HAGO-enabled graphene nanocage, a mechanism that is crucial to achieve molecular mass uptake, storage and release. HAGO holds promise to enable an array of carbon nanostructures of desirable functionalities by design. As an example, we demonstrate HAGO-enabled high-density hydrogen storage with a weighted percentage exceeding the ultimate goal of US Department of Energy.

Chapter 4: Strain engineering of graphene: Pseudomagnetic field

4.1. Electromechanics of graphene drumhead – generating pseudomagnetic field

The electro-mechanical properties of a suspended graphene layer were determined by scanning tunneling microscopy (STM) and spectroscopy (STS) measurements. A graphene membrane was continuously deformed by controlling the competing interactions with a STM probe tip and the electric field from a back gate electrode. The probe tip induced deformation created a localized strain field in the graphene lattice. STS measurements on the deformed suspended graphene display an electronic spectrum completely different from graphene supported by a substrate. The spectrum indicates the formation of a spatially confined quantum dot, in agreement with recent predictions of confinement by strain induced pseudomagnetic fields.

While these experimental findings are intriguing, their further implementation in nanoelectronic devices hinges upon the knowledge of key underpinning parameters, which still remain elusive. We first carry out molecular dynamics simulations of the graphene membrane mechanics and morphology on a scaled-down model as a pioneer study. We then carry out systematic coarse grained, (CG), simulations to offer a mechanistic interpretation of STM tip-induced straining of the graphene drumhead. Our findings reveal the effect of (i) the position of the STM probe tip relative to the graphene drumhead center, (ii) the sizes of both the STM probe tip and graphene drumhead, as well as (iii) the applied back-gate voltage, on the induced strain field and

corresponding pseudomagnetic field. These results can offer quantitative guidance for future design and implementation of reversible and on-demand formation of graphene QDs in nanoelectronics.

4.1.1. Quantum dot in suspended graphene without physical barriers

When graphene sheets are suspended, some unwanted electrical potential disturbances may not appear when compared with the graphene sheets that are supported by substrates. For example, while initial measurements of graphene devices on SiO₂ insulating substrates achieved carrier mobilities of $\approx 5000 \text{ cm}^2 \text{ V}^{-1} \text{ s}^{-1}$ (144), removing the substrate by suspending graphene resulted in mobilities in excess of $200,000 \text{ cm}^2 \text{ V}^{-1} \text{ s}^{-1}$ at low temperatures (145). These differences shows that substrate-induced potential disorder due to impurities and strain can play a role in the electronic properties of graphene. Recently, strain engineering of electronic properties of graphene has attracted significant attention, which can be described through the generation of local pseudo scalar and magnetic fields by strain (23, 146-153). For example, strain generated pseudomagnetic fields equivalent to a real magnetic field as high as 300 T have been reported (148). However, a number of questions remain regarding the structure and electronic properties of suspended graphene layers.

Here we present scanning tunneling microscopy (STM) and scanning tunneling spectroscopy (STS) measurements of suspended graphene drumheads in a back-gated graphene device structure. Stable STM measurements on the suspended graphene are achieved by carefully approaching the membrane with very slow scanning speeds. It is observed that both the van der Waals forces from the STM probe tip and electrostatic

force induced by back gate voltage can induce substantial mechanical deformation in the suspended graphene membranes. We can continuously tune the visible membrane shape measured as a tip height from concave to convex by adjusting the electrostatic force. We have determined that the induced strain in the graphene membrane mainly originates from the tip-membrane interaction, dramatically altering the electronic spectrum of graphene compared to the measurements of graphene directly supported by a substrate (154, 155). In particular, multiple quartet bands of peaks are observed in the differential conductance spectra characteristic of charge confinement in a quantum dot.

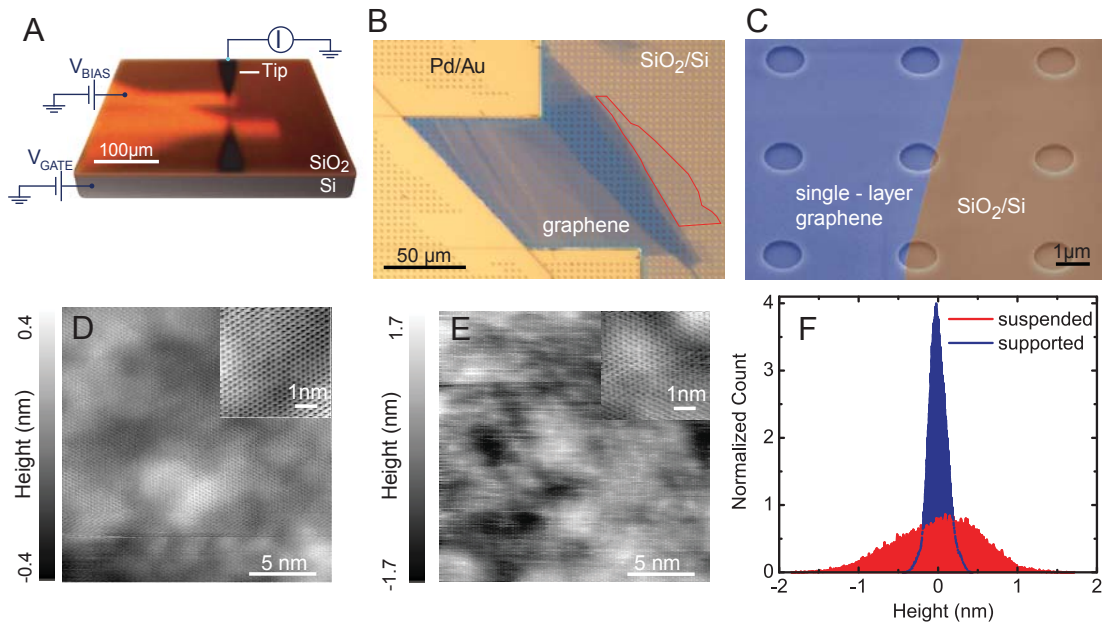


Figure 4.1. STM measurements of graphene drumheads. (A) Optical image of the gated graphene device. The device consists of a single graphene layer placed over an array of pits (1.1 μm in diameter, 100 nm in depth) etched in SiO_2 (300 nm)/Si substrate. (B) Magnified optical image of the device in (A). The single layer graphene region is marked by a red line. (C) Scanning electron microscope (SEM) image of the device. STM topographic images, 20 nm by 20 nm, on the supported graphene (D) and suspended graphene membrane (E). The insets show the graphene atomic lattice images (5 nm by 5 nm). The inset grey scales cover the range of ± 0.2 nm. (F) Topographic height histograms from the images in (D) and (E).

Figures 4.1, A to C, show the geometry of our graphene device used in this study. An array of pits was fabricated in SiO₂/Si substrates, 1.1 μm in diameter and 100 nm in depth, by shallow plasma etching of SiO₂ (Fig. 4.1C). Graphene flakes were exfoliated onto the pre-patterned SiO₂/Si substrate via mechanical exfoliation of natural graphite and contacted using a Pd/Au electrode deposited via a stencil mask (Fig.4.1B). After fabrication, the STM probe tip was aligned onto the device in ultrahigh vacuum by using an external optical microscope prior to cooling the STM module in a custom STM system operating at 4 K (156).

STM topographic images of single-layer supported and suspended graphene over an area of 20 nm by 20 nm are shown in Fig. 4.1, D and E, respectively. On small length scales, the graphene honeycomb lattice was clearly resolved on both supported and suspended graphene, with comparable corrugation amplitudes (Figs. 4.1, D and E, insets). On the 20 nm length scale, the peak-to-peak height corrugation on the suspended graphene was about four times larger than that of the supported graphene on the SiO₂ substrate over this scan area range (Fig. 4.1F).

In the experiment, stable STM measurements on the suspended graphene were achieved by carefully approaching the graphene membrane with very slow scanning speeds. Both the van der Waals (vdW) force from the STM probe tip and an electrostatic force from the applied back-gate voltage induced substantial mechanical deformations in the suspended graphene membrane, as shown in Fig. 4.2. The deformation could be tuned to be either outward from the surface or inward into the pit

under the suspended graphene depending on the strength of the back gate potential, V_{GATE} .

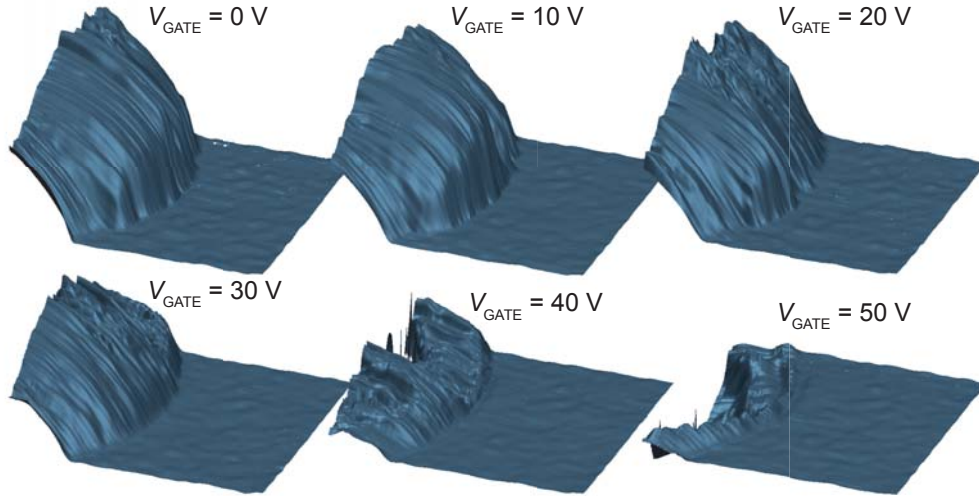


Figure 4.2. STM images of the deformed graphene membrane induced by the competing forces from the probe tip pulling up on the membrane and the back-gate electric field pulling down on the membrane. The STM images are shown for various gate potentials from 0 to 50 V. At 50 V the membrane is being pulled into the pit in the substrate.

The graphene deformation in Fig. 4.2 is caused by the STM probe tip pulling up on the membrane and the electric field from the back gate electrode pulling it down. As seen in Fig. 4.2, the deformation starts to curve downward into the pit when the force from the back gate electrode overtakes the force from the tip at a back gate potential of ≈ 50 V. In contrast, we did not observe a substantial effect on the deformation from the tip electric field.

Figure 4.3A shows the membrane profile for a series of tip potentials at a fixed back gate potential. While some trend of larger deformation with increasing tip potential is seen in Fig. 4.3A, the effect is much smaller than that from the back gate potential, and almost within the noise or variations obtained when scanning over the membrane. These results can be understood based on consideration of the size of the probe tip

relative to membrane and how the membrane is shaped by the tip forces. The typical global diameter of our STM probe tips is on the order of 110 nm (Fig. 4.3B). The lack of an effect from the tip potential variation in the STM profiles in Fig. 4.3A indicates that the vdW forces from the probe tip dominate the force from the tip potential. However, the electric force from the probe tip may be somewhat masked from how the STM servo is adjusting the probe tip to keep a constant tunneling gap. As both the vdW force and probe tip electric field pull on the graphene membrane, the STM feedback loop pulls the tip back to the point of maintaining a tunneling gap set by the tunneling current setpoint, *i.e.*, just before it would release the graphene membrane. Therefore the additional and localized force from the tip potential may not significantly alter the graphene profile shape, which is dominated by the vdW force. It is important to note that the profiles observed in Fig. 4.2 are then a result of dragging the top of the cusp point of the pulled-up membrane as the tip is rastered, *i.e.*, the profiles in Fig. 4.2 are not the static shape of the graphene membrane.

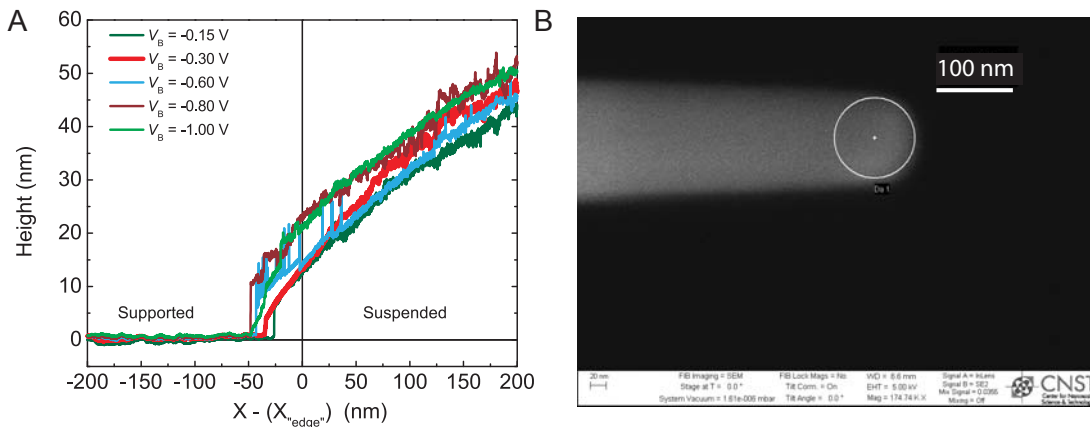


Figure 4.3. (A) STM topographic profiles obtained while scanning from graphene supported onto the SiO_2 substrate to the suspended region over a pit in the substrate as a function of tunneling bias at a fixed gate potential of 0 V and tunneling current of 50 pA. (B) SEM image of the STM probe tip showing a probe diameter of 110 nm.

To study the electronic properties of the suspended graphene membranes we applied high-resolution gate mapping STS measurements in which individual dI/dV spectra are measured at a fixed spatial location as a function of both tunneling bias, V_B , and back gate voltages, V_{GATE} (Fig. 4.4, Fig. 4.5) (154, 157). The dI/dV spectra, proportional to the local density of states, were used to examine how the suspension of the graphene affects its electronic spectrum.

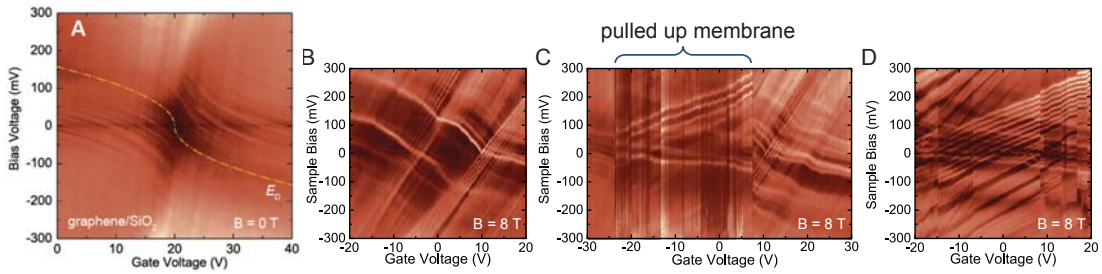


Figure 4.4. STS dI/dV gate maps of graphene measured at 0 T magnetic field for (A) graphene-on-SiO₂ (50 nm from the pit's edge). STS dI/dV gate maps of graphene measured at 8 T magnetic field for (B) graphene-on-SiO₂ (50 nm from the pit's edge), (C) graphene-on-SiO₂ (10 nm from the pit's edge), and (D) suspended graphene (10 nm from the pit's edge into the membrane). The color scale is the dI/dV magnitude, which varies from 0.05 nS (dark) to 1.7 nS (bright) to 1.2 nS (bright).

Gate mapping tunneling spectroscopy measurements of suspended graphene are very different from measurements of graphene supported on SiO₂ substrates (Fig. 4.4). The spectroscopic measurements of supported graphene at B = 0 T are characterized by a minimum in the differential conductance at the Dirac point (155). The position of the Dirac point in zero magnetic field varies in energy as a function of gate voltage as shown by the dashed line in Fig. 4.4A. The tunneling spectroscopy measurements on suspended graphene in zero applied magnetic field can be directly compared to supported graphene, by comparing Fig. 4.5A with Fig. 4.4A.

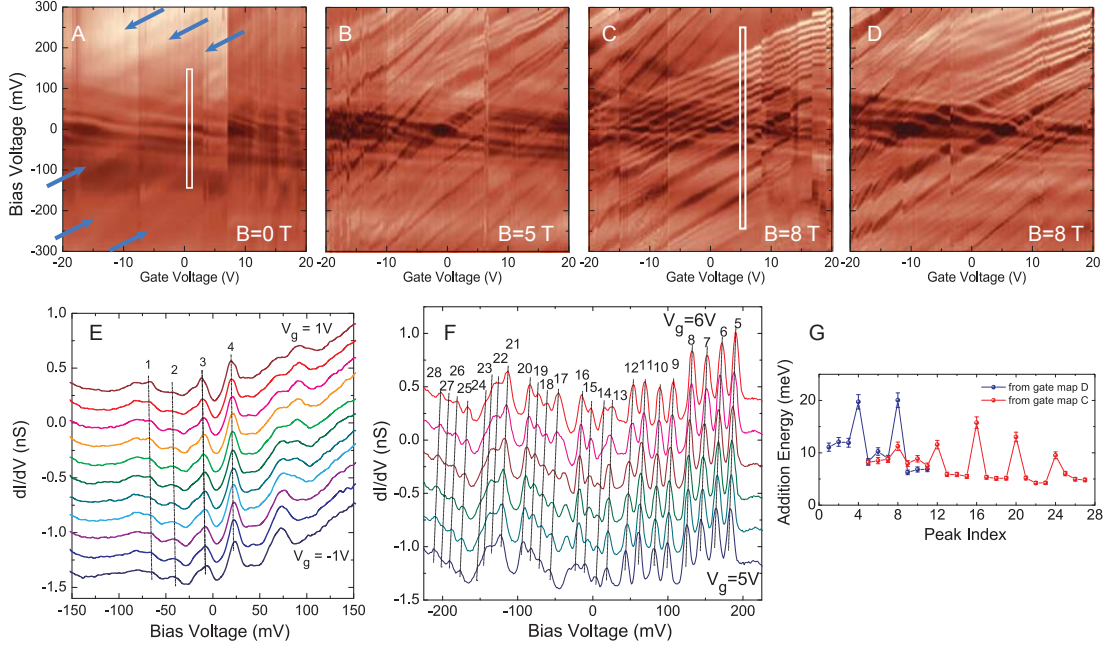


Figure 4.5. STS of a suspended graphene membrane. **(A)** dI/dV gate map spectra on the suspended graphene membrane at $B = 0$ T. Each map is built of dI/dV vs. V_B spectra taken at multiple fixed V_{GATE} . The color scale is the dI/dV magnitude, which varies from 0.05 nS (dark) to 1.7 nS (bright) for (A) and to 1.2 nS (bright) for (B-D). The white rectangle shows the region where individual spectra are obtained and plotted in (E). The blue arrows indicate spectral bands with positive slope that become more resolved at higher fields in (B) and (C). **(B and C)** dI/dV gate map spectra on the suspended graphene membrane at **(B)** $B = 5$ T and **(C)** $B = 8$ T. The white rectangle in (C) shows the region where individual spectra are obtained and plotted in (F). **(D)** dI/dV gate map spectra at $B = 8$ T, showing the variability in the measurements when moving off and back on the membrane. **(E)** dI/dV vs. V_B spectra from the $B = 0$ T gate map in (A) for gate voltages varying from -1 V to 1 V. **(F)** dI/dV vs. V_B spectra from the $B = 8$ T gate map in (C) for gate voltages varying from 5 V to 6 V. The spectra are shifted vertically for clarity in (E) and (F). **(G)** The quantum dot addition energies corresponding to the difference in dI/dV peak positions in the spectra from the gate maps in (C) red symbols, and (D) blue symbols. Energies are converted from bias voltages using the lever arm, $E = \alpha V_B$, where $\alpha = 0.45 \pm 0.03$. The error bars in (G) are dominated by the statistical error in α , which was determined from one standard deviation uncertainties in the measured slopes of the charging lines in the gate maps.

A distinct minimum corresponding to the Dirac point can no longer be identified on the suspended graphene. In an applied magnetic field, as the tip approaches the membrane edge, the membrane can be delaminated while the graphene is still supported by the substrate within about 50 nm of the membrane edge. This can be seen in the membrane profiles in Fig. 4.3A, and also in gate maps in this vicinity in Fig. 4.4C. Once the tip is

on the suspended membrane, the tunneling spectra in the gate map change from those of the graphene on the supported areas, as seen in Fig. 4.4D. This indicates that the induced strain in the suspended graphene drumhead originating from the tip-membrane interactions dramatically alters the electronic spectrum of graphene charge carriers, compared to the electronic spectrum of graphene directly supported by a substrate, as seen by comparing Fig. 4.4B with Fig. 4.4D.

In zero applied magnetic field the dI/dV gate map (Fig. 4.5A) showed a new series of states seen as lines with a small negative slope with increasing gate voltage (almost horizontal across the gate map). In addition, a series of broad bands with positive slopes were observed, as indicated with the blue arrows in Fig. 4.5A. These latter features with positive slopes became more resolved in an applied magnetic field, seen at $B = 5$ T (Fig. 4.5 B) and $B = 8$ T (Figs. 4.5C and D, Fig. 4.4D), resembling the spectral signatures of quantum dots (QD) (154, 158). To further explore the analogy with QD physics, we examine the energy scales in the spectral maps of the suspended graphene. As an example, dI/dV spectra, that are parts of the gate maps in Fig. 4.5A and Fig. 4.5C, are shown in Fig. 4.5E and Fig. 4.5F, respectively. The peaks in Fig. 4.5E corresponding to the horizontal lines in the zero field gate map (Fig. 4.5A) showed a separation of approximately 30 mV for the first few states. In contrast, the peaks in Fig. 4.5F that form the positive slope bands were seen in groups of four with a spacing of ≈ 20 mV. This grouping is similar to the four-fold charging peaks in QDs observed in graphene (154) or carbon nanotubes (158), and reflects the four-fold degeneracy of the dot levels caused by electron spin and valley quantum numbers. These dI/dV peaks are caused by an opening up of a transport channel at the Fermi energy associated with a

single-electron addition to the QD. The peaks appeared as tilted lines in the map because the QD energy levels are controlled by a linear combination of the gate voltage and tip bias.

In the following, we use this analogy to determine the energy scale and the size of the QD from the measured slopes and spacing of the charging lines. The vertical voltage bias axis is converted to the quantum dot energy spacing using the lever arm, $E = \alpha V_B$, where $\alpha = C_B / C_T \approx 0.4$, C_B is the graphene layer to graphene QD capacitance, and C_T the total capacitance of the quantum dot. In Fig. 4.5G we plot the energy difference between the levels from the gate maps in Fig. 4.5C (red symbols) and Fig. 4.5D (blue symbols). The energy spacing of the individual levels indeed follows the classic energy spectrum of a quantum dot (159), $e^2 / C_T + \Delta E_{N+1}$, where e^2 / C_T is the charging energy of the four-fold degenerate levels of a graphene quantum dot (base line in Fig. 4.5G), and the additional energy, $\Delta E_{N+1} = E_{N+1} - E_N$, separating each band (spikes in Fig. 4.5G), corresponds to the energy needed to reach the next quantum dot level. Here, e is the electron charge. The charging energies, varying from (11.7 ± 0.5) to (5.3 ± 0.7) meV in Fig. 4.5G, correspond to quantum dots with diameters in a range from (34 ± 2) to (53 ± 5) nm (We determined the 1 SD error estimates in the QD sizes by combining the 1 SD in the addition energy variation for the first and last set of energies in Fig. 4.5G, together with the 1 SD uncertainties in the measured slopes of the charging lines in the gate maps.). This dot size is consistent with a simple estimate based on the number of electrons added to the dot for a given range of gate voltage. In the gate map (Fig. 4.5C) we see approximately 5 quartet bands over the gate voltage range of 40 V,

corresponding to the addition of 20 electrons to the quantum dot. Using the gate capacitance of 5.85 nF cm^{-2} (100 nm vacuum plus 200 nm oxide) yields a rough estimate of the dot diameter of 42 nm.

4.1.2. Understand the formation of quantum dot: A molecular dynamics study

The profile of the membrane as measured by the tip height cannot explain the formation of a QD. To understand the local and the global membrane deformation and the corresponding strain induced in the immediate vicinity of the STM tip, we performed molecular dynamics simulations on a scaled-down model as a pilot study.

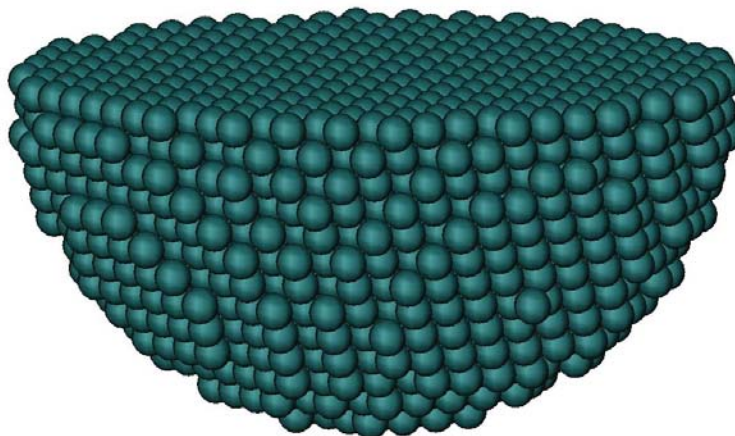


Figure 4.6. Atomistic model of iridium STM tip in MD simulations.

The molecular dynamics (MD) simulations were conducted using the LAMMPS (79). The crystal structure of iridium is Face-Centered Cubic (FCC) with lattice constant of 0.384 nm. The STM tip was initially modeled as a hemisphere, as shown in Fig. 4.6. The top surface of this tip is oriented in the $[100]$ direction, although the effect of crystal orientation is negligible at the MD length scale considered.

The nonbonded interaction between iridium and carbon atoms was modeled using a Lennard-Jones (LJ) 6-12 potential. The parameters were developed through the customary Lorentz-Berthelot mixing rules, using Ir-Ir and C-C parameters from the Universal Force Field (160). The AIREBO potential (78) was used to model the interaction of the carbon atoms within the graphene membrane (including the C-C nonbonded parameters). The atomic interactions within the iridium tip itself were not included since geometrical changes in the tip are expected to have a negligible effect at the length scale under consideration. The tip/membrane model was scaled down from the experimental system to reduce computational expense. Thus, a tip radius of 2.5 nm and a graphene membrane radius of 25.0 nm were used.

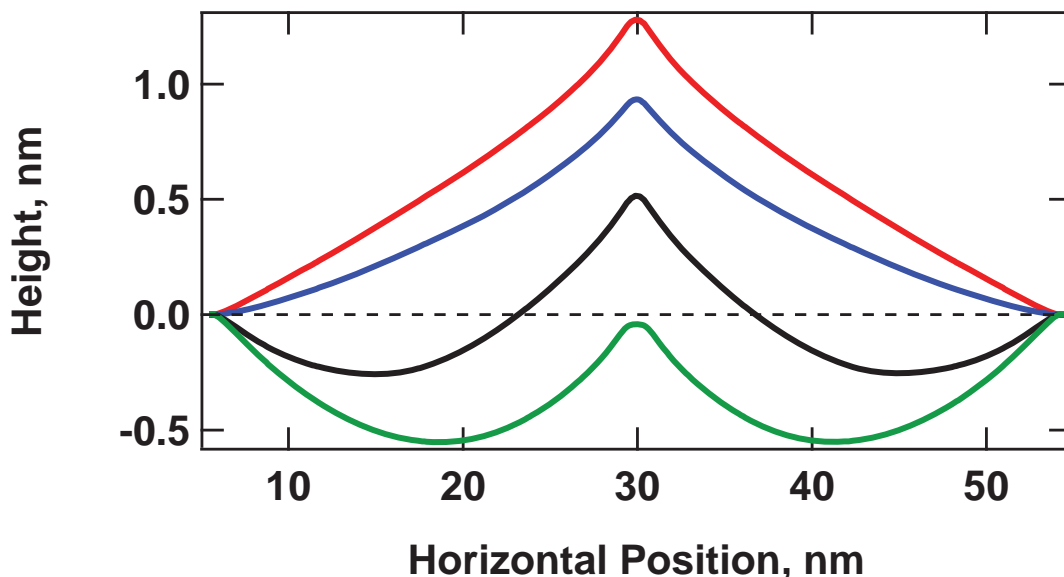


Figure 4.7. The effect of the applied downward force on the calculated membrane shapes for the case of the tip above the center of the membrane. The profiles, from top to bottom, correspond to applied forces of 0, 0.012, 0.037, and 0.061 pN per atom, respectively.

Simulations were conducted for three horizontal tip locations with respect to the membrane: 2.5 nm from the edge, 5.2 nm from the edge and the center of the membrane. In each case, the simulation began with the tip pressed down into the

membrane. The tip was gradually retracted from the membrane in increments of 0.006 nm while the membrane was allowed to relax at a temperature of 5 K. The membrane initially maintained contact with the tip, but eventually a critical point was reached at which the membrane could no longer maintain contact with the tip. The geometry for this critical height was then optimized to absolute zero. Finally, to obtain higher resolution in the membrane height, zero Kelvin calculations were conducted in which the tip was raised further from this optimized geometry in increments of 0.001 nm until tip-membrane contact could not be sustained. This provided the equilibrium membrane geometries for the critical heights at the three horizontal tip locations. This exercise was repeated for different levels of “gate force,” which was simulated by applying a downward force of equal magnitude to each atom of the membrane. The force applied to each atom ranged from 0 to 0.06 pN per atom. Shown in Fig. 4.7 is the effect of the applied force level on the critical membrane shape for the case of the tip above the center of the membrane. The red profile corresponds to zero force. The blue, black, and green profiles correspond to downward forces of 0.012, 0.037, and 0.061 pN per atom, respectively.

Figure 4.8E illustrates the atomistic model used, showing the tip at the critical height above the pulled-up membrane. In Fig. 4.8F the membrane shapes at the critical tip height are plotted together for three tip locations on a membrane, for a back gate force of 0.012 pN per atom. The computational simulations show that the deformation in the graphene membrane induced by the probe tip is formed locally. The simulations further demonstrate that the measured membrane profiles are not caused by a static membrane deformation, but one that continuously changes with the tip position. As the STM tip

is rastered across a membrane, the cusp of the deformation follows the tip (Fig. 4.8F), and the dome-like shapes recorded in STM images (Figs. 4.8, A to D) are the envelopes tracing the cusp peak as illustrated by the dashed line in Fig. 4.8F.

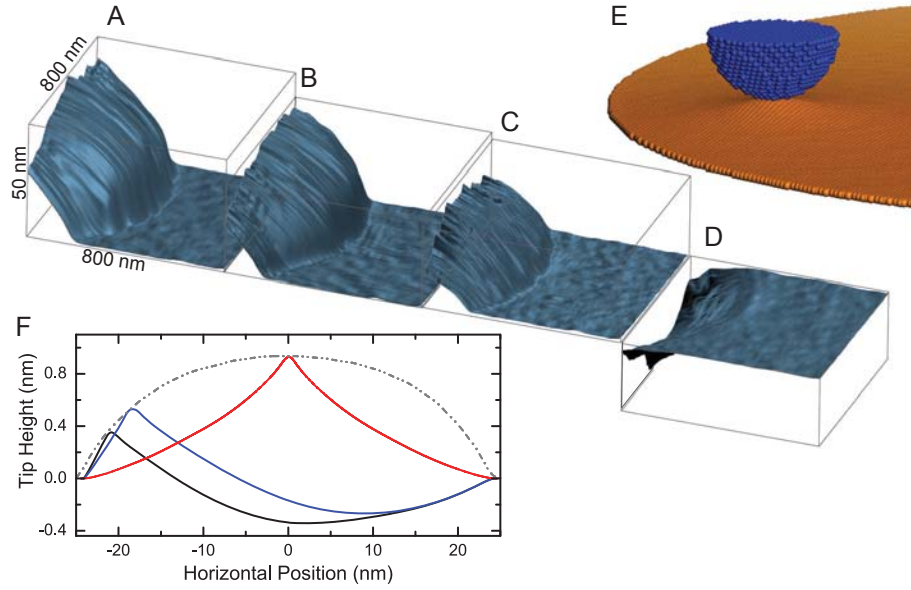


Figure 4.8. STM images and simulations of the deformed graphene membrane induced by competing forces of the STM probe tip and the back gate electric field. **(A-D)** STM topographic images of the graphene membrane for different gate voltages: 0 V (A), 20 V (B), 40 V (C) and 60 V (D). The membrane is deformed by upward forces from the STM tip and a downward force due to the electric field from the applied V_{GATE} . **(E)** Atomistic model showing deformations in the graphene membrane interacting with the STM tip. The radii of the tip and membrane in this model are 2.5 nm and 25 nm, respectively. **(F)** Calculated membrane shapes at the critical tip height for horizontal tip positions of 2.5 nm (black curve), 5.2 nm (blue curve) and 25 nm (red curve) from the membrane edge. A back gate force of 0.012 pN was applied to each atom in the membrane. The grey dashed curve is an envelope showing the membrane height as seen in an STM measurement.

The per-atom stress values obtained from LAMMPS were used to calculate the per-atom strain for a given equilibrium membrane geometry by utilizing the constitutive equations for a linear isotropic material. LAMMPS uses a stress*volume formulation, which means that the computed quantity is in units of pressure*volume. Thus, calculated values must be scaled by the effective per-atom volume. Figure 4.9 shows the strain components u_{xx} , u_{yy} , and u_{xy} used to calculate the pseudomagnetic field.

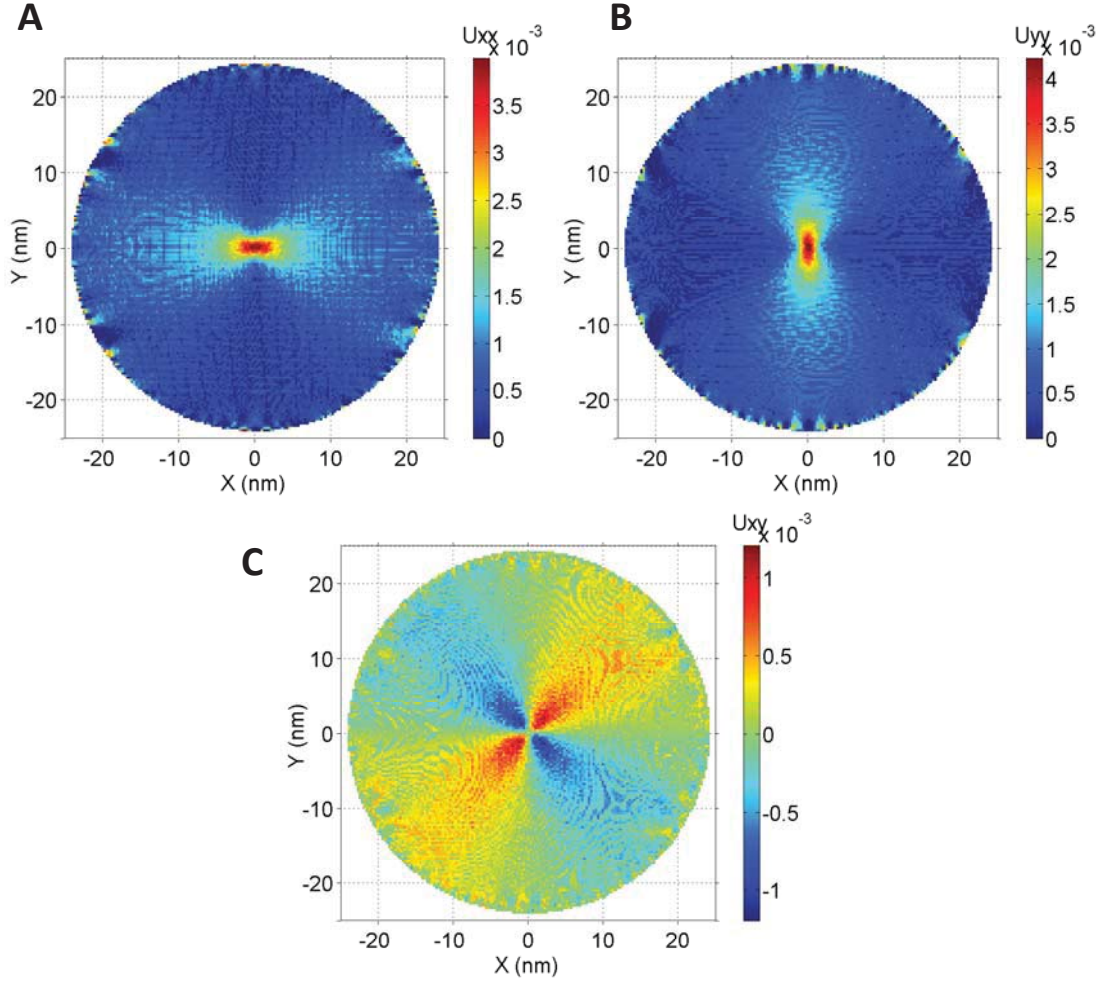


Figure 4.9. Strain components (A) u_{xx} (B) u_{yy} , and (C) u_{xy} as calculated from the per-atom stresses in LAMMPS for the tip over the center of the membrane with zero applied force.

To calculate the pseudomagnetic field, the pseudogauge field $\mathbf{A}_{ps}(\mathbf{r})$ is calculated as (147, 149),

$$\mathbf{A}_{ps} = \frac{t\beta}{ev_F} (u_{xx} - u_{yy}, -2u_{xy}), \quad (4.1.1)$$

where we take the dimensionless coupling constant $\beta=2.5$, the hopping energy $t=2.8$ eV, and the Fermi velocity $v_F = 1 \times 10^6$ m s⁻¹. The pseudomagnetic field is given by

$\mathbf{B}_{ps} = \nabla \times \mathbf{A}_{ps}$ and is shown in Fig. 4.10.

The mechanical simulations also show that the deformation in the graphene lattice induced a strain in the membrane (Fig. 4.10A), which was localized on the small scale of the probe tip diameter (5 nm) used in the simulation. Because the local deformation of the membrane under the tip does not change substantially as the probe tip moved across the membrane (Fig. 4.8F), the local strain field is fairly constant as the probe tip is moved across the membrane as well. The simulations also showed that the tip induced cusp in the deformed membrane remains as the overall membrane is pulled down by the back gate (Fig. 4.7).

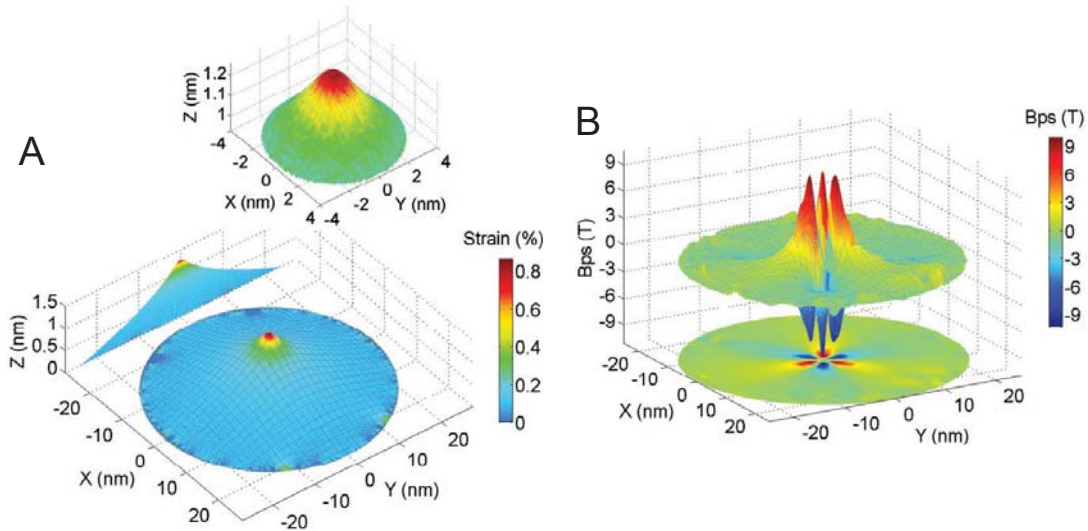


Figure 4.10. Simulations of a graphene membrane shape and corresponding strain and pseudomagnetic field. **(A)** Simulation of the graphene membrane shape with the STM tip positioned over the center of the membrane when no back gate force is applied. The inset shows a zoomed-in region where the strain is maximal. The radii of the tip and membrane in this model are 2.5 nm and 25 nm, respectively. **(B)** The pseudomagnetic field, calculated from the strain in (A) (Fig. 4.9), shows spatially alternating fields with three-fold symmetry which can spatially confine carriers.

Peak areal strains up to $\approx 1\%$ are predicted (Fig. 4.10A) in the graphene lattice directly under the tip. This amount of strain would produce pseudofields that could directly affect the graphene charge carriers (23, 146-153). The symmetry of the pseudofields is

determined by the corresponding symmetry of the strain field. For example, a uniform pseudomagnetic field requires a special strain field (147) distorted with 3-fold symmetry. In our case, a rotationally symmetric strain field generates a 3-fold pseudomagnetic field with alternating signs (149, 150). Figure 4.10B shows the calculated pseudomagnetic field for the strain field in Fig. 4.10A for the suspended membrane resulting in alternating spatial fields of ± 10 T. The region where the pseudofield is maximal is ≈ 10 nm in diameter for the 50 nm membrane diameter used in the simulation. Carriers in graphene can penetrate large potential barriers due to the effect of Klein tunneling (161), and physical barriers are typically engineered (162) to confine carriers. The pseudomagnetic field spatially confines the graphene carriers curving the classical trajectories and forming clockwise and counter-clockwise orbits around the alternating peaks of the pseudomagnetic fields (149, 150). However, some electronic states corresponding to classic snake orbits that propagates along the lines where pseudomagnetic field changes sign will be not confined. We suggest that the application of external magnetic field suppresses such leaky orbits by canceling one component of the pseudomagnetic field that opposes the applied magnetic field, which improves the overall confinement as observed in Fig. 4.5, B-D.

We associate the Coulomb charging characteristics observed on the pulled up graphene membrane (Fig. 4.5G) with the strain generated spatial confinement in a graphene quantum dot due to alternating pseudomagnetic fields (Fig. 4.10B). The dot size estimated from the Coulomb charging energies in the gate maps (Fig. 4.5G) is about 34 to 53 nm in diameter, while in a scaled-down model the size of the estimated pseudofield is about 10 nm in diameter and 10 T in magnitude. We are not able to

estimate the pseudofield intensity that is present in our drumhead device, largely due to the limitation of the computational expense of the model size allowed by molecular dynamics simulation.

4.1.3. Design quantum dot device: A coarse-grained study

As discussed in Section 4.1.1 and 4.1.2, the STS experimental study reveals that the pseudomagnetic fields induced in a freestanding graphene membrane give rise to a repeating series of a four-multiplet peak structure in the local density of states, which was interpreted as confinement of graphene charge carriers in a quantum dot (QD) (80). The STS experimental data also suggest that although the tip-induced QD is quite leaky, an external applied magnetic field can further improve the overall spatial confinement of graphene charge carriers. In addition, the simulations show that such a QD formed right under the STM probe tip follows the tip trajectory as it rasters across the graphene drumhead, while the resulting pseudomagnetic field and QD size remain nearly unchanged. Given the large elastic deformability of graphene and the retractability of the STM probe tip, the above results suggest a facile approach toward reversible and on-demand formation of graphene QDs, a desirable feature for graphene-based nanoelectronics (54, 163-166).

Promising potential aside, further implementation of such a feature hinges upon quantitative understanding of several issues that still remain unexplored. For example, how do the intensity of the resulting pseudomagnetic field and the QD size depend on the characteristic size of the graphene drumhead as well as on the size of the STM probe tip? What are the effects of back-gate voltage and probe tip position on the resulting

pseudomagnetic field and QD? Answers to these questions are crucial to achieve spatially confined QDs in graphene with tunable intensity and size.

To address the aforementioned unanswered questions, here we present a systematic study using a coarse-grained (CG) modeling scheme to offer a mechanistic interpretation of STM tip-induced straining of a graphene drumhead. Our investigations reveal how the position of the STM probe tip relative to the graphene drumhead center, the sizes of both the STM probe tip and graphene drumhead, as well as the applied back-gate voltage, affect the induced strain field and corresponding pseudomagnetic field. The predictions of our simulations are validated by agreement with our recent experimental measurements (80), and thus the results from our parametric modeling study can serve as guidelines for future design and implementation of reversible and on-demand formation of graphene QDs in nanoelectronics.

Given the relatively large sizes of both the suspended graphene drumhead ($\approx 1.1 \mu\text{m}$ diameter) and the STM probe tip ($\approx 110 \text{ nm}$ radius) used in the experiments, fully atomistic simulations of the STM tip-induced deformations in the graphene drumhead are prohibited due to the limit of computation capacity. To model the related tip induced deformations in graphene, we adopt a scalable bottom-up CG simulation scheme (Chapter 5.1) (167), which is recapped below. Figure 4.11A shows the carbon atom representations of CG beads of the first three orders. Note that a CG scheme of N^{th} order allows for a reduction of computation model size by 4^{N+1} times. For example, one 3rd order CG bead represents 256 carbon atoms, which significantly reduces the

computational expense. One unique feature of this CG scheme is its self-similarity in lattice structure. That is, the hexagonal lattice structure of graphene, the origin of many exceptional graphene properties, is maintained in the CG lattice structure of any order (Fig. 4.11B). The mass of the CG bead and the bond length between two CG beads of any order can be deduced recursively. Due to the nature of the vdW interaction, only a small portion of the STM probe tip interacts with the graphene drumhead. Without loss of generality, in the simulation model we coarse-grain the STM probe tip as a spherical bead, which approximates the real shape of the probe tip (Fig. 4.3B), and since the global shape of the real STM probe tip in experiments plays a minor role in determining the deformation in the graphene drumhead. As the vdW interaction decays significantly beyond 1 nm, the interaction from the tip will mainly result from the portion of the tip that is in very close proximity to the membrane. Therefore the shape of the tip beyond a few nm away from the membrane is not very significant. To better simulate the STM experiment, the diameter of the CG spherical bead is taken to be equal to the curvature of the real STM probe tip. The left panel in Fig. 4.11C describes a typical CG computational model in the present study. The tip is positioned slightly above the membrane at the desired horizontal position, relative to the center of the graphene drumhead and is held at a fixed position while the membrane relaxes with its edge atoms fixed. The choice of a proper order of CG scheme is tip-size and graphene-size dependent. A proper order of CG scheme is selected so that, on one hand, the CG graphene bead lattice is small enough to capture the fine features of the localized deformations in the graphene drumhead, and on the other hand, large enough to reasonably reduce the computational cost.

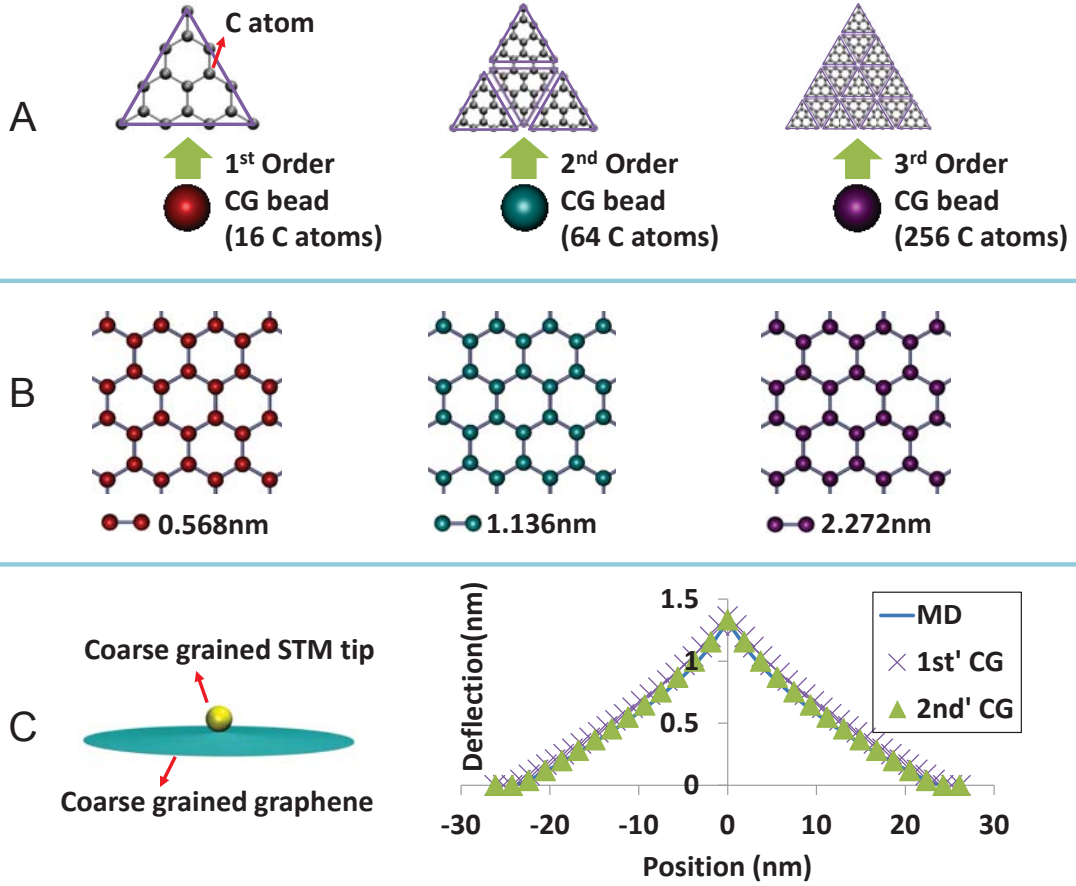


Figure 4.11. (A) Carbon atom representation of different orders of CG graphene beads. Purple triangles serve as the visual guide showing the inherent correlation between different orders of CG beads. (B) Coarse-grained scheme lattices composed of different orders of CG graphene beads, which preserve the hexagon pattern. Beads are colored in accordance with (A). (C) Left: CG computational model. The STM tip is coarse grained as a single spherical bead and graphene is composed of CG beads of a given CG order as depicted in (A). Right: Comparison of the calculated deflection of the graphene membrane of 50 nm in diameter between the CG method and the fully atomistic molecular dynamics simulations in Ref. (80).

The energy expression for the above CG scheme includes bonded energy terms and non-bonded energy terms. The bonded terms consist of two-body bond energy and three-body angle energy as

$$U_{bonding}(r_{ij}, \theta_{ijk}) = \sum \frac{1}{2} K_b (r_{ij} - r_0)^2 + \sum \frac{1}{2} K_\theta (\cos \theta_{ijk} - \cos \theta_0)^2, \quad (4.1.3.1)$$

where K_b and K_θ are the bond force constant and angle force constant, respectively, r_{ij} is the distance between the i^{th} and j^{th} CG beads while r_0 is its corresponding equilibrium distance; θ_{ijk} is the angle formed between the i - j bond and j - k bond and θ_0 is the corresponding equilibrium angle. The STM tip-induced deformations in the graphene drumhead are largely due to stretching and bending, while twisting of the graphene lattice is expected to be of secondary significance. Therefore, energy terms for the torsion are not considered in the CG scheme to reduce the computation expense.

The bond force constant is determined by equating the potential energies of an atomistic graphene structure and its CG counterpart under equal biaxial stretching (no change in the three-body angle energy), while the angle force constant is determined by equating the potential energies of an atomistic graphene structure and its CG counterpart under equal biaxial bending (in a scenario where changes in the two-body bond energy are highly suppressed). It turns out that the bond force constant is the same for all CG levels and can be determined from the Morse potential for C-C bonds (168) to be $47.46 \text{ eV} \cdot \text{\AA}^{-2}$. The angle force constants are analytically derived to be 93.23 eV , 372.91 eV and 1491.66 eV for the 1st, 2nd and 3rd order CG schemes, respectively.

The non-bonded term includes the vdW interaction between the CG graphene beads and the CG STM tip bead, which is fitted using a shifted Lennard-Jones (LJ) potential as

$$E = 4\epsilon \left[\left(\frac{\sigma}{r-\Delta} \right)^{12} - \left(\frac{\sigma}{r-\Delta} \right)^6 \right], \quad (4.1.3.2)$$

with a variable Δ to accommodate a CG STM tip with a non-zero diameter. The parameters in this shifted LJ potential can be determined by equating its value to the total vdW interaction energy between an atomistic iridium spherical tip and a triangular atomistic graphene flake represented by CG graphene beads of a given order (e.g., as in Fig. 4.11A). The interatomic pair interaction between iridium and carbon atoms is modeled using the conventional LJ 6-12 potential, the parameters of which are determined through the customary Lorentz-Berthelot mixing rules, using the iridium-iridium and carbon-carbon parameters from the universal force field (160). All CG simulations were implemented within the Large-scale Atomic/Molecular Massively Parallel Simulator (LAMMPS) (79).

The right panel of Fig. 4.11C compares CG simulation results with fully atomistic molecular dynamics simulation results of the STM tip-induced deformations in a graphene drumhead with a diameter of 50 nm. Here the STM probe tip is positioned above the center of the graphene drumhead and there is no electrostatic force from the back gate electrode. In the CG simulations, the STM probe tip is gradually retracted from the graphene drumhead until a critical point is reached, at which further retraction of the tip would result in the loss of tip-graphene contact. In each step of the CG simulations, the energy of the system is minimized by using the conjugate gradient algorithm until either the total energy change between successive iterations divided by the energy magnitude is less than or equal to 10^{-6} , or the total force is less than 10^{-5} eV/Å. As seen in Fig. 4.11C both the 1st and 2nd order CG simulation schemes agree quite well with fully atomistic simulations of a 50 nm graphene drumhead. This justifies the validity of our CG simulation scheme.

I. STM tip-induced localized deformations of graphene drumheads and the associated pseudomagnetic field

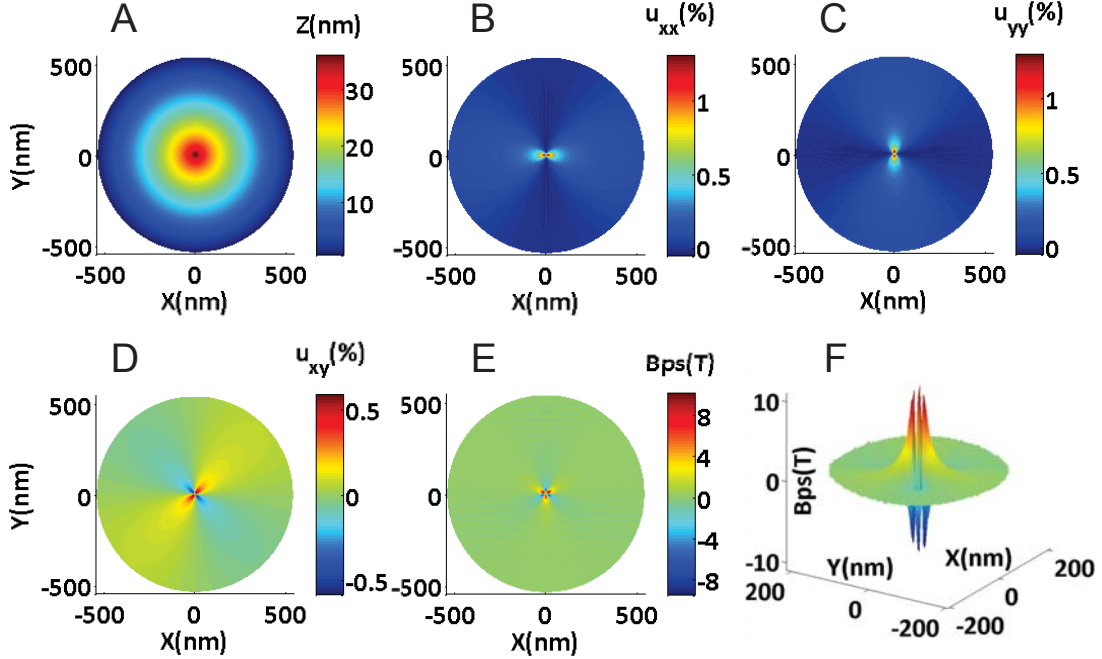


Figure 4.12. Simulation results of STM tip-induced deformation in graphene drumheads and the resulting pseudomagnetic field. Here there is no electrostatic force from a back-gate electrode and the STM probe tip is centered. (A) Out of plane deflection contour. (B-D): Strain components u_{xx} , u_{yy} and u_{xy} , respectively. (E) Top view of the associated pseudomagnetic field. (F) Zoomed-in perspective view of the pseudomagnetic field in the center region of the graphene drumhead.

Following the CG modeling strategy described above, we next apply the 3rd order CG scheme to study the STM tip-induced localized deformation in the graphene drumhead used in the experiment as well as the resulting pseudomagnetic field. We first consider the case without an electrostatic force from the back gate. The diameters of the STM probe tip and the graphene drumhead are taken to be 110 nm and 1100 nm, respectively.

Figure 4.12A shows the contour plot of the out-of-plane deflection of the graphene drumhead, when the STM probe tip is center-positioned at the critical height. The

induced deformations have an axisymmetric tent-like shape about the center as the out-of-plane deflection gradually increases away from the edge and peaks in the immediate vicinity of the STM probe tip.

Figures 4.12B-D show the contour plots of the components of the Lagrange strain tensor in the deformed graphene drumhead, with a peak value of normal strain up to 1.4 % and peak shear strain up to 0.55 %. It has been shown that the lattice distortions due to strain in graphene introduce effective gauge fields in the Dirac Hamiltonian, which shift the \mathbf{K} and \mathbf{K}' points in the Brillouin zone in opposite directions, much like the effect of an applied perpendicular magnetic field (147). The resulting gauge field, \mathbf{A} , leads to a pseudomagnetic field, \mathbf{B}_{ps} , which acts on the electrons and hole charge carriers in graphene. The strain-induced pseudogauge field \mathbf{A}_{ps} is calculated from the strain components, u_{ij} , as (147, 149, 169, 170)

$$\mathbf{A}_{ps} = \frac{t\beta}{ev_F} (u_{xx} - u_{yy}, -2u_{xy}), \quad (4.1.3.3)$$

where $\beta = 2.5$ is the dimensionless coupling constant, $t = 2.8$ eV is the hopping energy and $v_F = 1 \times 10^6$ m s⁻¹ is the Fermi velocity. The pseudomagnetic field can be computed as $\mathbf{B}_{ps} = \nabla \times \mathbf{A}_{ps}$. The resultant pseudomagnetic field can be denoted by a vector, whose magnitude can be expressed as

$$B_{ps} = \frac{t\beta}{ev_F} \left(\frac{\partial(-2u_{xy})}{\partial x} - \frac{\partial(u_{xx}-u_{yy})}{\partial y} \right). \quad (4.1.3.4)$$

Equation (4.1.3.4) shows that the intensity of the pseudomagnetic field scales with the magnitude of the strain gradient rather than with the strain. As a result, even though the

STM tip-induced strain magnitude in the graphene drumhead is modest, the highly localized nature of the deformations dictates large strain gradients, which, in turn, leads to significant pseudomagnetic fields in the graphene drumhead. Furthermore, in a cylindrical coordinate system (r, θ) , for axially symmetrical situations, Eq. (4.1.3.4) can be transformed into

$$B_{ps} = \frac{t\beta}{ev_F} \sin 3\theta \left(-\frac{\partial(u_{rr}-u_{\theta\theta})}{\partial r} + \frac{2(u_{rr}-u_{\theta\theta})}{r} \right). \quad (4.1.3.5)$$

This suggests that a strain field in graphene having rotational symmetry can lead to a pseudomagnetic field with a threefold symmetry (as a result of the pre-factor $\sin 3\theta$), as opposed to a strain field with threefold symmetry leading to a uniform pseudomagnetic field (147).

Figures 4.12E and F present the pseudomagnetic field associated with the tip-induced localized strain field in the graphene drumhead, which assumes a clover-leaf threefold symmetry with alternating intensity peaks of about ± 10 T. Our recent experiments further reveal that such pseudomagnetic fields in the graphene drumhead could directly affect the graphene electronic properties in a sense analogous to the charge carrier confining effect in a lithographically defined QD (80). As shown in Fig. 4.12E, the pseudomagnetic fields are mostly located at the drumhead's center within a region of ≈ 40 nm in diameter, which agrees well with the effective QD size (≈ 42 nm in diameter) estimated from the charging energies in the STS gate maps measured in the experiment (Fig. 4.5F) (80). Such a good agreement on the estimated QD size from two distinct approaches serves as further evidence of the effectiveness and precision of the CG simulation scheme.

II. Dependence of the pseudomagnetic field on graphene membrane size and STM tip size

We carry out a parametric study to investigate the effects of the STM tip size and the graphene drumhead diameter on the intensity of the strain-induced pseudomagnetic field and the associated QD size. It is shown that in all simulation cases, corresponding to the center-positioned STM probe tip, the interaction between the STM probe tip and the graphene drumhead leads to tent-like deformations of the graphene drumhead similar to that shown in Fig. 4.12A. In general, for a given STM tip size, a larger graphene drumhead corresponds to an overall larger amplitude of the out-of-plane deformations. However, as shown in Eqs. (4.1.3.4) and (4.1.3.5), the resulting pseudomagnetic field depends much more strongly on the strain gradient than on the displacement and strain of the graphene drumhead. Therefore, it is the highly localized strain field in the graphene at the immediate vicinity of the STM tip that dictates the nature of the pseudomagnetic field and the associated QD formation.

Figure 4.13 summarizes the findings of the above parametric study. It shows the dependence of the magnitude of the induced pseudomagnetic field and the characteristic size of the formed QD on the diameters of the STM probe tip and the graphene drumhead. For a given STM tip size, there exists a threshold graphene diameter (about 400 nm, indicated by a dashed line in Figs. 4.13A-C) that delineates two regimes for the above mentioned dependences. For graphene drumheads with diameters smaller than the threshold value, the intensity of strain-induced pseudomagnetic field decreases, while the corresponding QD size increases, as the

graphene diameter increases. For such graphene drumheads, the smaller the STM tip size, the smaller the resulting QD, but the stronger the pseudomagnetic field. For example, for STM tip sizes of 45 nm, 75 nm and 110 nm and for a fixed graphene membrane diameter of 250 nm, the corresponding pseudomagnetic fields and QD sizes are 23 T, 16 T, 13 T, and 13 nm, 18 nm, 29 nm, respectively.

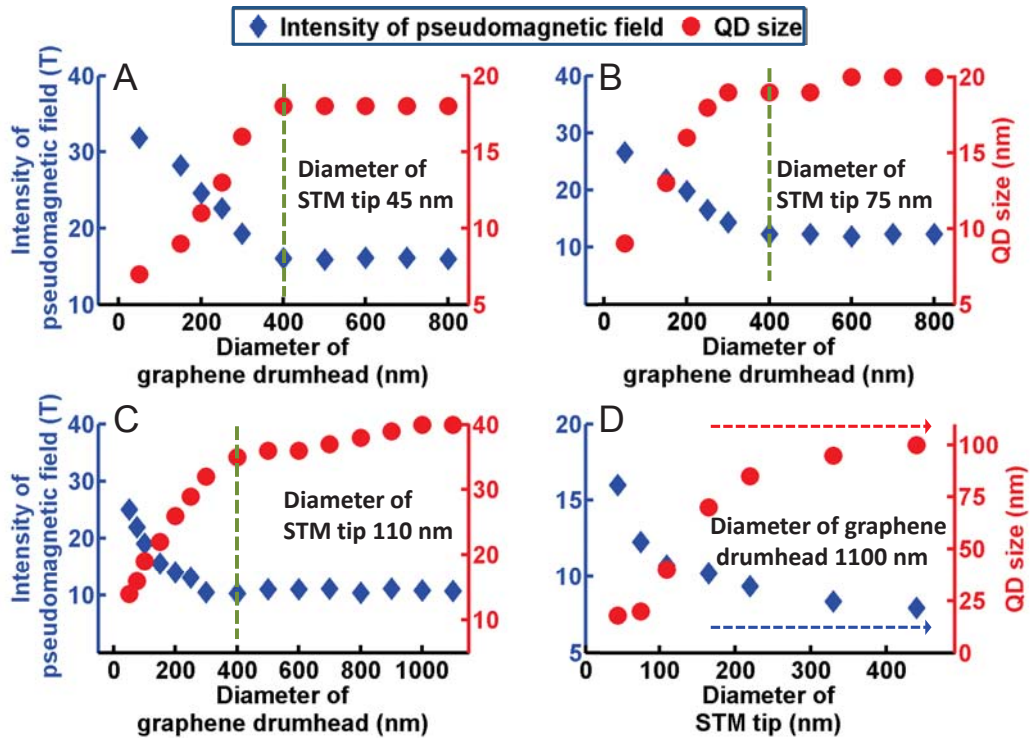


Figure 4.13. (A-C) Intensity of STM tip-induced pseudomagnetic field (blue diamonds) and the corresponding QD size (red dots) as a function of the diameter of the graphene drumhead, for various STM probe tip diameters. The dashed line in (A), (B) and (C) estimates a threshold size of the graphene drumhead that delineates two regimes of the dependence of pseudomagnetic field on graphene drumhead diameter. (D) The dependence of the intensity of STM tip-induced pseudomagnetic field (blue diamonds) and the corresponding QD size (red dots) on the diameter of the STM probe tip, for a graphene drumhead of diameter of 1100 nm. The dashed arrows in (D) outline the saturation trend of such a dependence, as the size of the STM probe tip increases. Here there is no electrostatic force from a back-gate electrode and the STM probe tip is positioned above the center of the graphene drumhead.

Figure 4.13D further reveals that for the graphene drumhead of diameter comparable to those in the experiments (1100 nm), the intensity of pseudomagnetic field decreases

while the QD size increases as the STM probe tip diameter increases. However we observe a saturation trend for both the intensity of pseudomagnetic field and QD size as the STM tip size continues increasing. The above dependence on the STM tip size can be understood as follows. The interaction force exerted by the STM probe tip on the graphene drumhead is to some extent analogous to the effect of a pole sticking out of a circular tent at its center (as is evident from the tent-like morphology of the graphene drumhead). A smaller STM tip acts like a sharper pole, which leads to a smaller size of the region with highly localized deformation in the tent (corresponding to the QD size in strained graphene), but a higher strain concentration in such a region (i.e., higher strain gradient) corresponds to a greater intensity of the pseudomagnetic field in the strained graphene. Here the overall out-of-plane deflection of the tent (or the graphene drumhead) is less significant. As the STM tip size keeps increasing beyond a certain value, the STM tip starts to interact with the graphene in a way similar to a nearly flat surface. As a result, further increases in STM tip size would not significantly change the interaction region between STM tip and membrane, which gives rise to the saturation trend as shown in Fig. 4.13D.

On the other hand, for graphene drumheads with diameters larger than the threshold value, both the pseudomagnetic fields and the associated QD sizes become nearly independent of the graphene drumhead diameter, as is evident from the plateaus in the curves shown in Figs. 4.13A-C. The plateau values of both the intensity of pseudomagnetic field and the associated QD size are higher for a larger STM probe tip diameter, although the increases are rather insignificant. This can be understood as follows: even though the amplitude of out-of-plane deflection of the graphene

drumhead increases as the graphene size increases, the portion of graphene with high strain concentration occurs only in a rather localized region in the vicinity of the STM probe tip with a size and strain field profile that are nearly insensitive to the graphene size.

To further demonstrate such an understanding, we employ the finite element method (FEM) to reveal the tip-induced strain distribution in the graphene drumhead. Equation (4.1.3.5) suggests that the pseudomagnetic field depends on the spatial distribution of strain components u_{rr} and $u_{\theta\theta}$. In the finite element method, the graphene drumhead is modeled with general purpose, large-strain quadrilateral shell elements (S4R), which allow for finite membrane strain (171). The graphene drumhead has a thickness of 1.317 Å, a Young's modulus of 1 TPa and a Poisson's ratio of 0.19 (172). The outer edge of the circular graphene drumhead is fixed. As the interaction force exerted by the STM tip on the graphene is quite complicated, we represent its effect by applying a uniformly distributed upward pressure at a central circular region (referred to as the 'loading zone') on the drumhead (Fig. 4.14A). As suggested by the CG simulations, when the graphene size is much larger than the STM tip size, the size of the loading zone is assumed to be constant. In the finite element simulations, the diameter of the loading zone is set to be 10 nm, estimated from the critical contact area in the CG simulations with a STM tip of 110 nm in diameter. The amplitude of the applied pressure is estimated from the maximum of a vdW force between the CG tip bead and CG graphene beads. The finite element simulations are carried out using ABAQUS software.

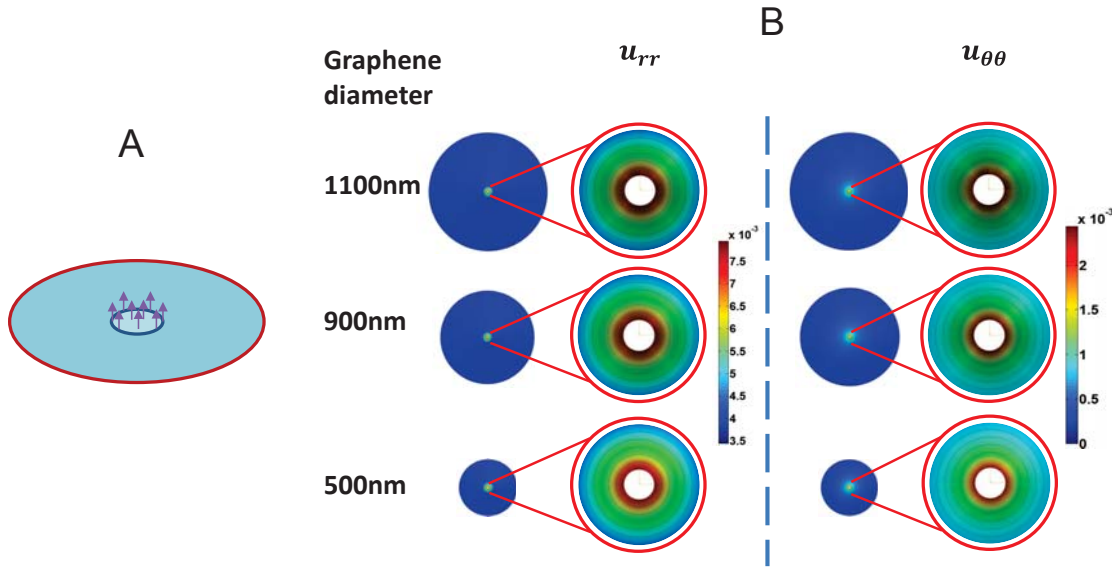


Figure 4.14. Finite element simulations reveal the highly localized strain distribution in a circular region in the vicinity of the STM probe tip. **(A)** Schematics of the finite element simulation model. The red circle denotes the fixed boundary and the smaller circle near the center defines the loading zone, where the effect of tip/graphene interaction is represented by a uniformly distributed pressure. **(B)** Strain component contours in a cylindrical coordinate system for graphene drumheads of three different diameters. For visual clarity, the strain distribution inside the loading zone (white circle) is not shown. All zoomed-in contours have the same size, which reveal the rather similar strain field in the vicinity of the STM tip, which is the origin of the insensitivity of the pseudomagnetic field to the graphene drumhead size, when the graphene is much larger than the STM probe tip.

Figure 4.14B plots the FEM simulation results of the contour of the two strain components u_{rr} and $u_{\theta\theta}$ in circular graphene drumheads of three different diameters (500 nm, 900 nm and 1100 nm) which are greater than the threshold diameter of about 400 nm. By zooming in on a circular region of diameter of 20 nm at the center of the graphene (highlighted by red circles in Fig. 4.14B), it is shown that both the magnitude and spatial distribution of the two polar strain components u_{rr} and $u_{\theta\theta}$ in such a circular region are nearly the same for the three graphene drumheads of different diameters, which explains the nearly constant pseudomagnetic field intensity as well as the QD size as the graphene drumhead is larger than a threshold diameter. On one hand, the FEM findings reveal that as the size of the graphene drumhead becomes large

enough compared with the STM tip, the strain field in the graphene, within the same area beneath the tip, becomes less and less dependent on the drumhead size, therefore dictating the saturation trend of the QD size as a function of drumhead size. On the other hand, the agreement between CG and FEM results further suggests that continuum mechanics modeling indeed can provide reasonable prediction to the STM-tip-induced localized deformation in the graphene membrane, and thus offer reasonable insight on the resulting pseudomagnetic field in graphene. This feature becomes particularly attractive in practice for a graphene device with a size too large to be modeled even by the scalable CG, for which FEM can be an effective modeling approach to study its device behavior.

III. Effect of back-gate force and STM tip location on the strain-induced pseudomagnetic field

Our experiments show that a back-gate voltage applied to the graphene device shown in Fig. 4.1A can tune the deformation of the graphene drumhead. For example, the back-gate voltage exerts a distributed force on the graphene drumhead that counteracts the vdW attractive force from the STM tip (Fig. 4.2). As a result, the overall amplitude of the out-of-plane deflection of the graphene drumhead decreases as the back-gate voltage increases. The graphene drumhead can even dip down into the pit on the SiO₂ substrate if a sufficiently high back-gate voltage is applied. What remains unclear is if the back-gate voltage can also change the strain-induced pseudomagnetic field. To address this issue, we carry out CG simulations to model the deformation of the graphene drumhead subject to both the STM tip interaction and a back-gate voltage.

The effect of the back-gate voltage is represented by a uniform force applied downward on each CG graphene bead.

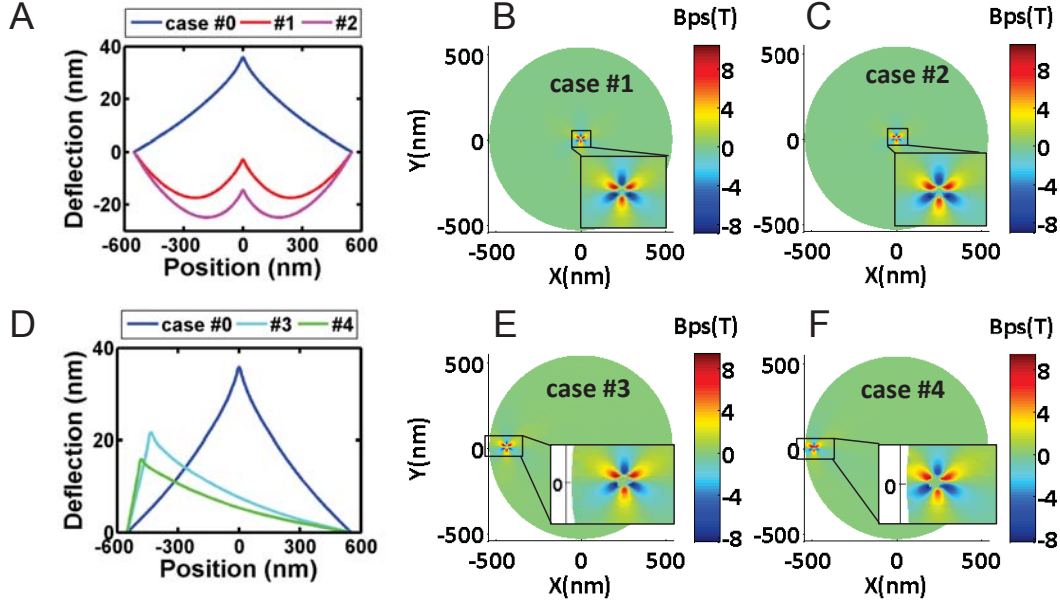


Figure 4.15. CG simulation results of the STM tip-induced deformation of the graphene drumhead and associated pseudomagnetic field when a back-gate force is applied and the STM tip is at off-centered locations. Here the diameter of the graphene drumhead is $1.1 \mu\text{m}$. (A) and (D) show the deflection of the graphene drumhead across its diameter. (B), (C), (E) and (F) show the corresponding pseudomagnetic fields. Case #0: center-positioned STM probe tip with zero back-gate force, replotted from Fig. 4.12 for comparison. Case #1 and case #2: center-positioned STM probe tip with downward back-gate forces of $9.65 \times 10^{-4} \text{ eV/\AA}$ and $1.61 \times 10^{-3} \text{ eV/\AA}$ per CG bead, respectively. Case #3 and case #4: tip off-center-positioned by 440 nm and 490 nm with zero back-gate force, respectively. Insets show zoomed-in images of the pseudomagnetic field in the vicinity of the STM probe tip.

Figure 4.15A compares the deflections of the graphene drumhead across its diameter in three cases: zero back-gate force as in Fig. 4.12A, with a back-gate force of $9.65 \times 10^{-4} \text{ eV/\AA}$, and $1.61 \times 10^{-3} \text{ eV/\AA}$ per CG bead, respectively. It is evident that the back-gate voltage effectively “pulls down” the graphene drumhead. The higher the back-gate voltage (i.e., larger back-gate force), the more the graphene drumhead dips downward. However, the shape of the cusp formed beneath the STM tip in all three cases appears rather similar, indicating a highly localized strain effect. Figures 4.15B-C show the

corresponding pseudomagnetic fields for the two cases with a back-gate force. It turns out that both the intensity and the spatial distribution (e.g., threefold clover-leaf symmetry) of the pseudomagnetic field, and therefore the corresponding QD size, remain nearly the same as in the case of no back-gate voltage (Fig. 4.12E). This result suggests that a back-gate voltage only affects the overall deformed shape of the graphene drumhead but has nearly no effect on the STM tip-induced localized strain field and thus the pseudomagnetic field. Similar observations also hold for the cases where the STM tip is positioned in an off-centered location. Figure 4.15D shows that as the STM tip navigates away from the centered location on the graphene drumhead, the overall deflection of the graphene decreases and the global rotational symmetry of the deformed shape of the graphene disappears, but the highly localized deformation near the cusp beneath the STM tip remains nearly the same. Figures 4.15E-F further reveal that the resulting pseudomagnetic field when the STM tip is off-center-positioned (even quite close to the fixed edge, e.g., 490 nm off-centered as shown in Fig. 4.15F) is almost the same as when the tip is center-positioned. The above results reveal that the STM tip-induced pseudomagnetic field and the corresponding QD are nearly independent of the STM tip location and the back-gate voltage.

4.1.4. Concluding remarks

Scanning tunneling microscopy/spectroscopy (STM/STS) experimental studies of suspended graphene drumheads and related molecular dynamics simulations revealed that an STM probe tip can interact with a suspended graphene drumhead and generate a highly localized radially symmetric strain field in graphene right under the STM

probe tip (80). This strain field, in turn, leads to a pseudomagnetic field of three-fold symmetry in graphene. We conducted molecular dynamics (MD) simulations and systematic coarse grained (CG) simulations to study the STM tip-induced deformation in a suspended graphene drumhead with a diameter up to 1.1 μm , which enables investigations of the strain-induced pseudomagnetic field and the associated spatially confined QD generated in the graphene drumheads. The CG simulation results are validated by excellent agreement with both the results from the fully atomistic MD simulation of a scaled-down model and the STM/STS experimental measurements. A parametric study via comprehensive CG simulations reveals the dependence of the strain-induced pseudomagnetic field and the associated QD size on the diameters of the graphene drumhead and the STM probe tip. There exists a threshold size of graphene drumhead, below which the intensity of the pseudomagnetic field increases but the associated QD size decreases as the graphene drumhead size decreases, and above which both the pseudomagnetic field and the associated QD become nearly independent of the graphene drumhead size. There exists a threshold size of the STM probe tip, below which the intensity of the pseudomagnetic field increases but the associated QD size decreases as the STM probe tip size decreases, and above which both the pseudomagnetic field and the associated QD become nearly independent of the STM probe tip size. These results suggest two possible regimes of STM tip-induced spatially confining QDs in a graphene drumhead, in one of which a tunable QD size and intensity can be explored, and in another of which a robust spatially confining QD that can maneuver in association with the motion of the STM tip becomes possible.

Results from the present study offer quantitative guidance for further explorations of strain engineering of suspended graphene drumheads.

4.2. Programmable extreme pseudomagnetic fields in graphene – finding the right shape

4.2.1 Motivation

Being able to influence the motion of charge carriers, strain-induced pseudomagnetic fields in graphene have been explored as a potential approach to engineering the electronic states of graphene. There has been experimental evidence of enormous pseudomagnetic fields (up to 300 T) in locally strained graphene nanobubbles (*148*) and graphene drumheads (*80*), which inspires enthusiasm in exploring the abundant potential of strain engineering of graphene, as well as charge carrier behavior under extreme magnetic fields that otherwise do not exist in normal laboratory environments (*147, 149, 173-177*). Enthusiasm aside, there exist significant challenges that hinder further explorations of these fertile opportunities to full potential. For example, existing experiments demonstrate pseudomagnetic fields in highly localized regions of graphene with a non-planar morphology (*80, 148*), which poses tremendous challenge for experimental control and characterization of the resulting fields. Further challenge originates from the dependence of the symmetry of the strain-induced pseudomagnetic field on the strain gradient in graphene. As a result, an axisymmetric strain field in graphene leads to a pseudomagnetic field of rotational threefold symmetry (*80, 147, 149, 174, 175*). By contrast, a uniform pseudomagnetic field in a planar graphene with tunable intensity is highly desirable for systematic investigations. In principle, such a

uniform pseudomagnetic field can be achieved by introducing a strain field of threefold symmetry in graphene (147, 176), which requires equal-triaxial loading of atomically thin graphene, a technical challenge already prohibitive in bulk materials. So far, a viable solution to generate a pseudomagnetic field in graphene with controllable distribution and amplitude over a large planar area under a feasible loading scheme still remains highly desirable but elusive.

The ever-maturing programmable patterning (17, 59, 64, 120, 122-125, 167, 178-180) and functionalization (30, 87, 109, 110, 114, 118, 181, 182) of graphene has enabled a class of graphene-based unconventional nanostructures with exceptional functionalities, such as nanoribbon (183), nanomesh (59) and hybrid superlattices (114). Significant progress has also been made on fabricating high quality in-plane heteroepitaxial nanostructures that consist of different monolayer two-dimensional (2D) crystals, such as graphene, hydrogenated graphene (graphane) and hexagonal boron nitride (h-BN) (184-187). Furthermore, controllable and nondestructive generation of uniaxial strains (up to more than 10 %) in graphene has been successfully demonstrated recently (188). Motivated by these advances, here we reveal a feasible and effective mechanism to achieve programmable pseudomagnetic fields in a planar graphene by a simple uniaxial stretch. We demonstrate two new possible approaches: 1) by tailoring the planar edge geometry of a graphene strip, and 2) by patterning in-plane graphene-based hetero-structures. These feasible-to-implement approaches yield rich features necessary for systematic studies of pseudomagnetic fields in strain engineered graphene geometries, as demonstrated below.

4.2.2 Programmable extreme pseudomagnetic fields

When the graphene lattice is strained, the main effect is to modify the hopping energy between the two graphene sublattices. The modified energies add a term to the momentum operators in the low energy Dirac Hamiltonian, in the same way a vector potential is added for electromagnetic fields. This gives a very useful way to relate the mechanical deformation in graphene with a gauge field that acts on the graphene electronic structure (80, 147, 149, 173-177). The pseudomagnetic field, B_{ps} , is given by the 2D curl of the mechanically derived gauge field. For elastic deformations, the pseudomagnetic field in graphene is related to the strain field in the plane of the graphene as (80, 147, 149, 173-177)

$$B_{\text{ps}} = \frac{t\beta}{ev_F} \left[-2 \frac{\partial \epsilon_{xy}}{\partial x} - \frac{\partial}{\partial y} (\epsilon_{xx} - \epsilon_{yy}) \right], \quad (4.2.1)$$

where $\beta = 2.5$ is a dimensionless coupling constant, $t = 2.8$ eV is the hopping energy, $v_F = 1 \times 10^6$ m s⁻¹ is the Fermi velocity, and ϵ_{xx} , ϵ_{yy} , and ϵ_{xy} are the components of the strain tensor of the graphene. The x -axis is along the zigzag direction of graphene lattice. The field in Eq. (4.2.1) is for one graphene valley, with opposite sign for the other valley.

We consider the pseudomagnetic field under the special case of uniaxial stretch [see Section 4.2.3] given by,

$$B_{\text{ps}} = \frac{3t\beta}{ev_F} (1 + \nu) \frac{\partial \epsilon_{yy}}{\partial y}. \quad (4.2.2)$$

The above formulation reveals that a programmable pseudomagnetic field is achieved if the strain gradient $\frac{\partial \epsilon_{yy}}{\partial y}$ in graphene can be engineered under a simple uniaxial stretch.

For example, a constant strain gradient $\frac{\partial \epsilon_{yy}}{\partial y}$ in graphene (i.e., a linear distribution of tensile strain in the armchair direction) can result in a uniform pseudomagnetic field over a large area of graphene; a highly desirable feature to enable direct experimental characterization of the resulting field.

To demonstrate the feasibility to engineer the strain field in graphene under a simple uniaxial stretch, we first consider a graphene nanoribbon of length L that is patterned into a shape with a varying width $W(y)$ and subject to an applied uniaxial tensile strain ϵ_{app} along its length in the y direction (Fig. 4.16A). The geometry of the two long edges of the graphene nanoribbon is defined by a shape function $f(y) = W(y)/W_0$, where $W_0 = W(0)$ denotes the basal width of the graphene nanoribbon. When $L \gg W(y)$, it is reasonable to assume that ϵ_{yy} is constant along any cross-section cut in x direction and only varies along y direction. This assumption is justified in the majority part of the graphene nanoribbon except in the vicinity of its four corners, as verified by both finite element modeling and atomistic simulations (see Section 4.2.9). Considering the force balance along any cross-section cut in x direction, it is shown that (see Section 4.2.5)

$$\frac{\partial \epsilon_{yy}}{\partial y} = -\frac{F}{E_g W_0 h} \frac{1}{f^2} \frac{df}{dy}, \quad (4.2.3)$$

where F is the applied force at the ends of graphene nanoribbon necessary to generate the uniaxial tensile strain ϵ_{app} , E_{g} and h are the Young's Modulus and thickness of graphene, respectively.

Thus from Eq. (4.2.2), the resulting pseudomagnetic field in such a patterned graphene nanoribbon is given by,

$$B_{\text{ps}} = - \frac{3t\beta F}{ev_{\text{F}}E_{\text{g}}W_0h} (1 + \nu) \frac{1}{f^2} \frac{df}{dy}. \quad (4.2.4)$$

Equation (4.2.4) reveals that a tunable pseudomagnetic field is achieved under a uniaxial stretch by engineering the shape of the graphene nanoribbon. For example, to achieve a uniform pseudomagnetic field, the corresponding shape function is shown to be

$$f(y) = \frac{f_{\text{r}} L}{f_{\text{r}}(L - y) + y}, \quad (4.2.5)$$

where $f_{\text{r}} = f(L)$ denotes the ratio between the widths of the top and bottom ends of the graphene nanoribbon. The intensity of the resulting uniform pseudomagnetic field (see Section 4.2.5) is given by,

$$B_{\text{ps}} = \frac{6t\beta}{ev_{\text{F}}} \frac{\epsilon_{\text{app}}}{L} \frac{(1-f_{\text{r}})}{(1+f_{\text{r}})} (1 + \nu). \quad (4.2.6)$$

To verify the above elasticity-based theoretical prediction, we performed numerical simulations using both finite element method and atomistic simulations (Sections 4.2.7 and 4.2.9 for simulation details) to calculate the strains and pseudomagnetic field using

Eq. (4.2.1), which lead to results well in agreement with the above theory, Eqs. (4.2.2-4.2.6), as elaborated below.

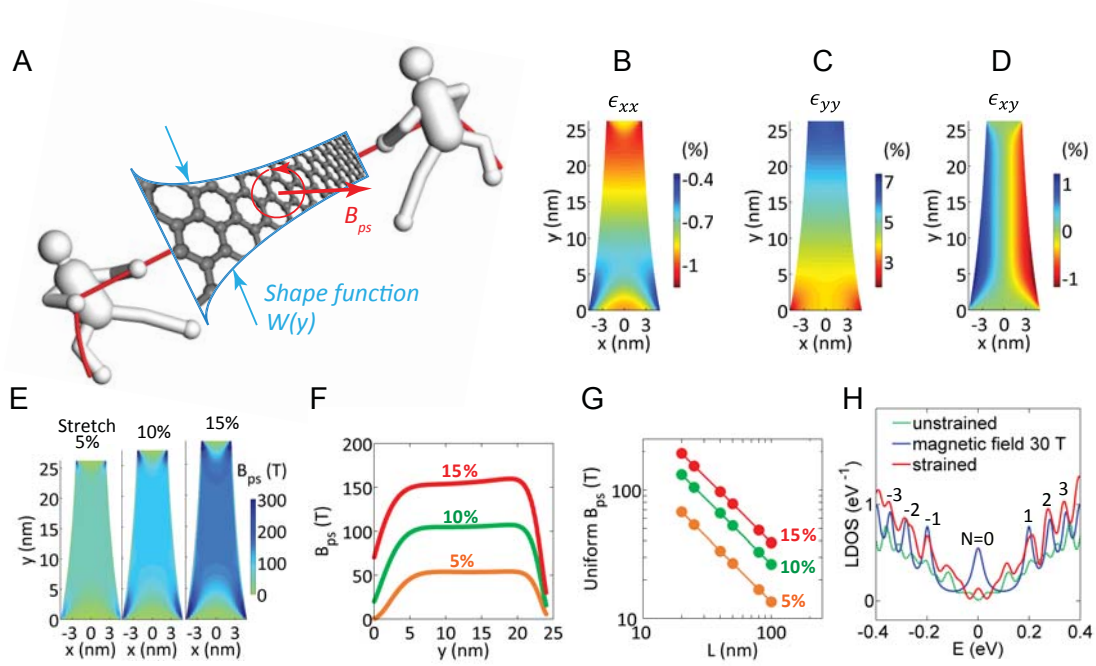


Figure. 4.16. Producing uniform pseudomagnetic fields in a planar shaped graphene strip under uniaxial stretch. **(A)** Schematic showing a graphene nanoribbon of varying width under a uniaxial stretch producing a pseudomagnetic field, B_{ps} . The red circle denotes cyclotron orbits in the field giving rise to pseudo-Landau levels in **(H)**. **(B to D)** Contour plots of the resulting strain components in the graphene, ϵ_{xx} , ϵ_{yy} and ϵ_{xy} , respectively, under a 5 % uniaxial stretch. **(E)** Resulting pseudomagnetic fields in the graphene nanoribbon shown in **(A)** under a uniaxial stretch of 5 %, 10 % and 15 %, respectively. **(F)** Intensity of the pseudomagnetic field as the function of location along the centerline of the graphene ribbon for various applied uniaxial stretches. **(G)** Intensity of the pseudomagnetic field is shown to be linearly proportional to the applied uniaxial stretch and inversely proportional to the length of the graphene ribbon L . **(H)** Local density of states of unstrained graphene and graphene with a constant strain gradient determined by density functional theory calculations. $N=0$ and $N=\pm 1, \pm 2, \pm 3$ Landau levels, corresponding to cyclotron motion in a magnetic field are seen to emerge in the strained graphene, demonstrating a uniform pseudomagnetic field. The wiggles in the results for the unstrained case result from finite size effects in the calculations. See Section 4.2.4 for further discussion.

Figure 4.16A shows the schematic of a graphene nanoribbon of $L = 25$ nm, $W_0 = 10$ nm, $f_r = 0.5$, with two long edges prescribed by the shape function in Eq. (4.2.5).

The ribbon is subject to an applied unidirectional stretch of 5 % in its length direction.

Figure 4.16, B to D, plots the components of the resulting strain in the graphene, ϵ_{xx} ,

ϵ_{yy} and ϵ_{xy} , respectively, from finite element simulations. In the majority portion of the graphene except its four corners, ϵ_{xx} and ϵ_{yy} show a linear distribution along y direction (also see Fig. 4.19A), while ϵ_{xy} shows a linear distribution along x direction. From Eq. (4.2.2), such a strain distribution will result in a rather uniform pseudomagnetic field in the graphene nanoribbon.

Figure 4.16E plots the resulting pseudomagnetic fields in the graphene nanoribbon under an applied uniaxial stretch of 5 %, 10 % and 15 %, respectively, all of which clearly show a uniform distribution in nearly the entire graphene ribbon except at its four corners. The intensity of the pseudomagnetic field as the function of location along the centerline of the graphene ribbon is shown in Fig. 4.16F, for various applied uniaxial stretches. For each case, the plateau in a large portion of the curve shows a rather uniform and strong pseudomagnetic field along the centerline of the graphene nanoribbon (e.g., ≈ 150 T under a 15 % stretch). Further parametric studies (Fig. 4.16G) reveal that the intensity of resulting pseudomagnetic field is linearly proportional to the applied uniaxial stretch ϵ_{app} and inversely proportional to the length of the graphene ribbon L , in excellent agreement with the dependence from the theoretic prediction in Eq. (4.2.6) (See Section 4.2.7 for details). Our atomistic simulation results (Fig. 4.22 in Section 4.2.9) further verify both the uniform distribution of the resulting pseudomagnetic field in the graphene nanoribbon and the agreement on the field intensity with the results from finite element simulations. As additional verification, our density functional theory calculation produces pseudo-Landau levels, corresponding to cyclotron motion in a magnetic field (Fig. 4.16H), attesting to the

presence of a strain-induced pseudomagnetic field for a graphene under a strain field of constant $\frac{\partial \epsilon_{yy}}{\partial y}$ (See Section 4.2.4 for details).

Equation (4.2.6) also suggests another geometric dimension to tailor the intensity of pseudomagnetic field: tuning the top/bottom width ratio f_r of the graphene nanoribbon. For nanoribbons with the same length, a smaller f_r leads to more strain localization (i.e., a higher strain gradient) in the graphene nanoribbon, and thus a higher intensity of the pseudomagnetic field. Figure 4.21 shows the geometry of 25 nm long graphene nanoribbons with three top/bottom width ratios, $f_r = 0.35, 0.5,$ and $0.7,$ with the two long edges of each nanoribbon prescribed by Eq. (4.2.5). The corresponding intensities of the resulting pseudomagnetic field from finite element simulations, as shown in Fig. 4.21B, are in excellent agreement with the prediction from Eq. (4.2.6).

The programmable pseudomagnetic field in planar graphene demonstrated above essentially originates from determining a shape function which yields a tunable effective stiffness in various locations of the graphene, which in turn leads to non-uniform distribution of strain under a uniaxial stretch. From a different point of view, the graphene nanoribbon in Fig. 4.16A can be regarded as a lateral 2D heterostructure, consisting of a pristine graphene nanoribbon and two patches on its side made of 2D material (vacuum) with zero stiffness (e.g., Fig. 4.17A). As a result, the effective stiffness of the graphene nanoribbon at different cross-section decreases from the wider end to the narrower end. The above mechanistic understanding indeed opens up more versatile approaches to achieving a programmable pseudomagnetic field in planar graphene heterostructures, which we further explore as follows.

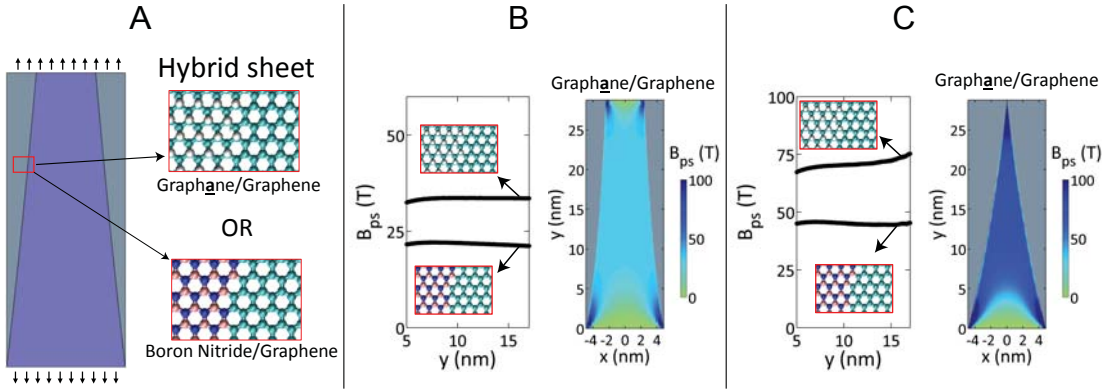


Figure 4.17. Producing uniform pseudomagnetic fields in a planar graphene-based heterostructures under uniaxial stretch. (A) Schematic showing a 2D hetero-structure consisting of graphane and graphene (or h-BN) bonded to a center piece of graphene under a uniaxial stretch. (B) Left: Intensity of the resulting pseudomagnetic field in the graphene domain of a graphene/graphane and a graphene/h-BN hetero-structure, respectively, under a 15 % uniaxial stretch. Here the top/bottom width ratio of the graphene domain $f_r = 0.5$; Right: Contour plot of the resulting pseudomagnetic field in the graphene/graphane hetero-structure. (C) Left: Intensity of the resulting pseudomagnetic field in the graphene domain of a graphene/graphane and a graphene/h-BN hetero-structure, respectively, under a 15 % uniaxial stretch. Here the top/bottom width ratio of the graphene domain $f_r = 0$; Right: Contour plot of the resulting pseudomagnetic field in the graphene/graphane hetero-structure.

Recent experiments demonstrate facile fabrication of high quality in-plane hetero-epitaxial nanostructures such as graphene/graphane and graphene/h-BN hetero-structures in a single 2D atomic layer (184-187). The more corrugated lattice structures of graphane and h-BN lead to an in-plane stiffness smaller than that of pristine graphene. It is expected that such in-plane hetero-structures with proper geometry (shape function) can be tuned to have a suitable variation of effective stiffness, and thus allow for a desirable strain distribution to enable programmable pseudomagnetic fields in the graphene portion under a uniaxial stretch.

Consider a rectangular 2D hetero-structure with a graphene nanoribbon and two patches of another 2D crystal of effective stiffness E_h (e.g., graphane or h-BN, Fig. 4.17A). Following a similar theoretical formulation as for the graphene nanoribbon shown above, it is shown that a programmable pseudomagnetic field in the graphene

domain can be achieved by tailoring its geometry in the 2D hetero-structure. For example, a suitable shape function $f(y)$ of the two long edges of the graphene domain can be solved so that a uniaxial stretch in y direction can generate a uniform pseudomagnetic field in the graphene domain (see Section 4.2.6 for details).

To verify the above theoretical prediction, we carried out both finite element modeling and atomistic simulations of two types of 2D hetero-structures, graphene/graphane and graphene/h-BN, respectively, under uniaxial stretch, as shown in Fig. 4.17A. The intensity of the resulting pseudomagnetic field in the graphene domain of a graphene/graphane and a graphene/h-BN hetero-structure, are shown in Fig. 4.17B, respectively. Here the top/bottom width ratio of the graphene domain $f_r = 0.5$, and the applied stretch is 15 %. A rather uniform distribution of the pseudomagnetic field is clearly evident, with an intensity of ≈ 33 T (graphene/graphane) and ≈ 22 T (graphene/h-BN), respectively, in good agreement with theoretical predictions. There exists a unique advantage of using a 2D hetero-structure over a pure graphene nanoribbon. It is shown that a stronger pseudomagnetic field can be generated in a graphene nanoribbon (or domain in 2D hetero-structure) with a smaller top/bottom width ratio f_r , with all other parameters kept the same (Eq. (4.2.26) in Section 4.2.6). To maximize such a tunability on field intensity, a graphene nanoribbon with $f_r = 0$ (the narrower end shrinks to a point) is desirable, but applying uniaxial stretch to such a nanostructure becomes prohibitive given its sharp tip. By contrast, a tipped graphene domain in a 2D hetero-structure is feasible to fabricate and a uniaxial stretch can be readily applied to the rectangular 2D hetero-structure. Figure 4.17C demonstrates the resulting pseudomagnetic field in two types of such a hetero-structure, with an elevated average

intensity of ≈ 70 T (graphene/graphane) and ≈ 45 T (graphene/h-BN), respectively, in comparison with those in Fig. 4.17B ($f_r = 0.5$, all other parameter being the same). Further atomistic simulations (Fig. 4.23) show good agreement with the above finite element modeling results in terms of both distribution and intensity of the resulting pseudomagnetic field.

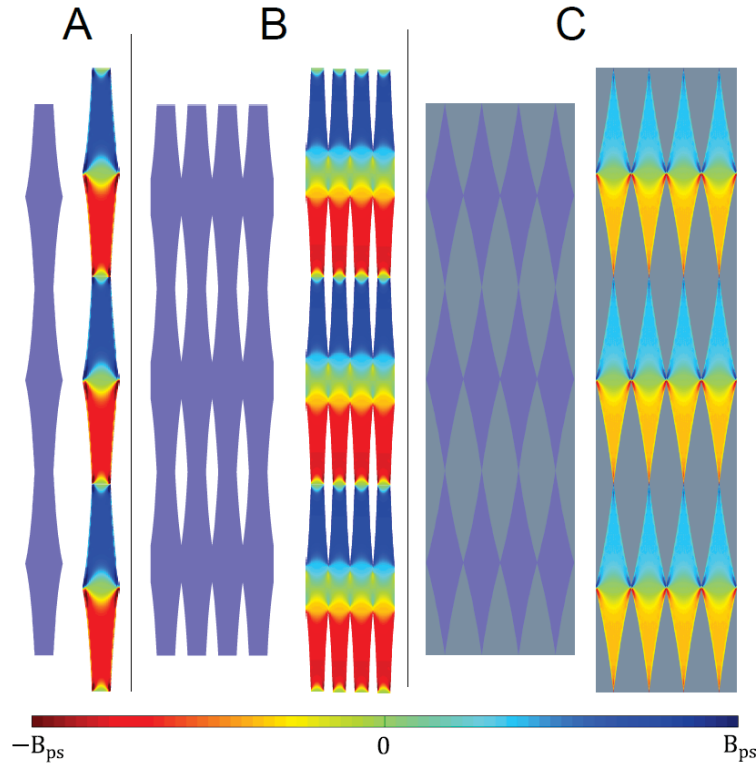


Figure 4.18. Pseudomagnetic fields in patterned graphene heterostructures superlattices. **(A)** Schematic of a suitably patterned long graphene nanoribbon (left) and the contour plot of the resulting pseudomagnetic field under a 15 % uniaxial stretch (right). **(B)** Schematic of a suitably patterned graphene nanomesh (left) and the contour plot of the resulting pseudomagnetic field under a 15 % uniaxial stretch (right). **(C)** Schematic of a suitably patterned graphene-based 2D superlattice structure (left) and the contour plot of the resulting pseudomagnetic field under a 15 % uniaxial stretch (right). The scale for B_{ps} is from -200 T to 200 T.

In conclusion, we offer a long-sought solution to achieving a programmable pseudomagnetic field in planar graphene over a large area via a feasible and effective strain-engineering mechanism. Our method utilizes a shape function applied to a planar

graphene sheet to achieve a constant strain gradient when applying a simple uniaxial stretch to a graphene ribbon (Fig. 4.16A). We demonstrate such a mechanism in both graphene nanoribbons and graphene-based 2D hetero-structures with resulting pseudomagnetic fields possessing a uniform distribution and a tunable intensity over a wide range of 0 T to 200 T. Such a programmable pseudomagnetic field under a uniaxial stretch results from the tunable effective stiffness of graphene by tailoring its geometry, so that the challenge of generating controllable strain gradient in graphene can be resolved by patterning the shape of a graphene nanoribbon or the graphene domain in a 2D hetero-structure, a viable approach with the ever advancing 2D nanofabrication technologies. These feasible-to-implement approaches can yield rich rewards from systematic studies of pseudomagnetic fields in graphene, which are extreme fields compared to normal laboratory field strengths, and can be arbitrarily patterned in 2D. For example, a repeating programmable pseudomagnetic field can be generated in a wide range of structures over large areas by repeating the suitable geometrical patterns, e.g., a long graphene ribbon (Fig. 4.18A), a graphene nanomesh (Fig. 4.18B), and a graphene-based 2D superlattice structure (Fig. 4.18C). The geometrical nature of the concept demonstrated in the present study is applicable to other 2D materials, and thus sheds light on fertile opportunities of strain engineering of a wide range of 2D materials for future investigations.

4.2.3. Pseudomagnetic field under uniaxial stretch

The constitutive law of a 2D elastic material correlates the stress σ_{ij} and the strain ϵ_{ij} in the form of

$$\sigma_{xx} = \frac{E}{1-\nu^2}(\epsilon_{xx} + \nu\epsilon_{yy}), \sigma_{yy} = \frac{E}{1-\nu^2}(\epsilon_{yy} + \nu\epsilon_{xx}),$$

and

$$\sigma_{xy} = 2G\epsilon_{xy}, \quad (4.2.7)$$

where E is the Young's modulus, ν is Poisson's ratio and $G = \frac{E}{2(1+\nu)}$ is the shear modulus of the material. Stress equilibrium requires

$$\frac{\partial\sigma_{xx}}{\partial x} + \frac{\partial\sigma_{yx}}{\partial y} = 0, \frac{\partial\sigma_{xy}}{\partial x} + \frac{\partial\sigma_{yy}}{\partial y} = 0. \quad (4.2.8)$$

Combining Eqs. (4.2.7-4.2.8) leads to

$$\begin{aligned} \frac{E}{1-\nu^2} \left(\frac{\partial\epsilon_{xx}}{\partial x} + \frac{\nu\partial\epsilon_{yy}}{\partial x} \right) + 2G \frac{\partial\epsilon_{xy}}{\partial y} &= 0, \\ \frac{E}{1-\nu^2} \left(\frac{\partial\epsilon_{yy}}{\partial y} + \frac{\nu\partial\epsilon_{xx}}{\partial y} \right) + 2G \frac{\partial\epsilon_{xy}}{\partial x} &= 0. \end{aligned} \quad (4.2.9)$$

When the graphene is subject to a uniaxial stretch along the armchair direction in its plane, $\epsilon_{xx} = -\nu\epsilon_{yy}$, and Eq. (4.2.9) becomes

$$\frac{\partial\epsilon_{xy}}{\partial y} = 0, \frac{\partial\epsilon_{xy}}{\partial x} = -(1 + \nu) \frac{\partial\epsilon_{yy}}{\partial y}. \quad (4.2.10)$$

Substituting Eq. (4.2.10) into Eq. (4.2.1) of the main text leads to Eq. (4.2.2).

4.2.4. Pseudo-Landau levels when $\frac{\partial\epsilon_{yy}}{\partial y} = \text{constant}$

We calculate the local density of states (LDOS) using density functional theory (DFT) applied to a scaled down graphene nanoribbon. Pseudo-Landau levels appear in the

LDOS due to the strain generated pseudomagnetic field. To compare the pseudofields to the results from finite element calculations, we point out that the DFT calculations will underestimate the pseudomagnetic field. As to be explained in details below, the molecular model for DFT calculations is subject to a finite constant strain gradient $\frac{\partial \epsilon_{yy}}{\partial y}$, but $\frac{\partial \epsilon_{xy}}{\partial x} = 0$ and $\frac{\partial \epsilon_{xx}}{\partial y} = 0$. By contrast, in a graphene nanoribbon under uniaxial stretch, $\frac{\partial \epsilon_{xy}}{\partial x}$ and $\frac{\partial \epsilon_{xx}}{\partial y}$ are related to $\frac{\partial \epsilon_{yy}}{\partial y}$ (e.g., Eq. (4.2.10)) and thus generally non-zero. Following the analysis in section 4.2.3 and comparing with Eq. (4.2.2), the resulting DFT generated pseudomagnetic field will then be given by,

$$B_{\text{ps}}^{\text{DFT}} = \frac{\beta}{\alpha} \frac{\partial \epsilon_{yy}}{\partial y} = \frac{B_{\text{ps}}}{3(1+\nu)}. \quad (4.2.11)$$

Figure 4.19A shows the distribution of ϵ_{yy} in a graphene nanoribbon (as in Fig. 4.16A) subject to a uniaxial applied stretch of 15 %, obtained from finite element simulations. The bottom panel in Fig. 4.19A clearly shows a constant gradient of ϵ_{yy} in the nanoribbon.

We first consider a molecular model representing a local region (indicated by the boxed area in Fig. 4.19A) in the nanoribbon. Figure 4.19B shows the atomistic details of the molecular model labeled with characteristic bond lengths and bond-stretching strains. The positions of the carbon atoms in this molecular model are prescribed so that the corresponding strain gradient of ϵ_{yy} is 0.0036 nm^{-1} , in accordance with strain gradient obtained from finite element simulations. Two such molecular models are patched head-to-head along their short edges with higher ϵ_{yy} to define the molecular model for

DFT calculations (Fig. 4.19C). Periodic boundary conditions are applied along both horizontal and vertical directions of the DFT molecular model while a vacuum region of 10 nm is set along out-of-plane direction. As a result, such a model indeed represents an infinitely large graphene subject to alternating strain gradients along its armchair direction, which can effectively eliminate the artificial edge effects in the LDOS (147). As a control calculation, we also construct the unstrained molecular model by relaxing all carbon-carbon bond length in Fig. 4.19C to that in pristine graphene (1.42 Å, Fig. 4.19D).

We perform first-principle DFT calculations in a supercell configuration by utilizing the SIESTA code (189). The generalized gradient approximation (GGA) in the framework of Perdew-Burke-Ernzerhof (PBE) is adopted for the exchange-correlation potential. Numerical atomic orbitals with double zeta plus polarization (DZP) are used for basis set, with a plane-wave energy cutoff of 4080 eV (300 Ry). Self-consistent Field (SCF) tolerance is set to 10^{-6} . A $160 \times 5 \times 1$ Monkhorst-Pack k -point mesh is used for Brillouin zone integration in the strained model (Fig. 4.19C), while a $140 \times 5 \times 1$ Monkhorst-Pack k -point mesh is used in the unstrained model (Fig. 4.19D), in order to ensure comparable k points separation. For LDOS calculations, the mesh along x and y directions is increased to 50 times of its initial size while the number of k points in out-of-plane direction is kept as one. For example, an $8000 \times 250 \times 1$ mesh is used for the LDOS calculation of the strained model. The peak broadening width for LDOS calculation is 0.02 eV. The electronic smearing temperature during the calculation is 300 K.

shows the linear scaling relation between the DFT pseudo peak energies and the square root of the orbital index, N .

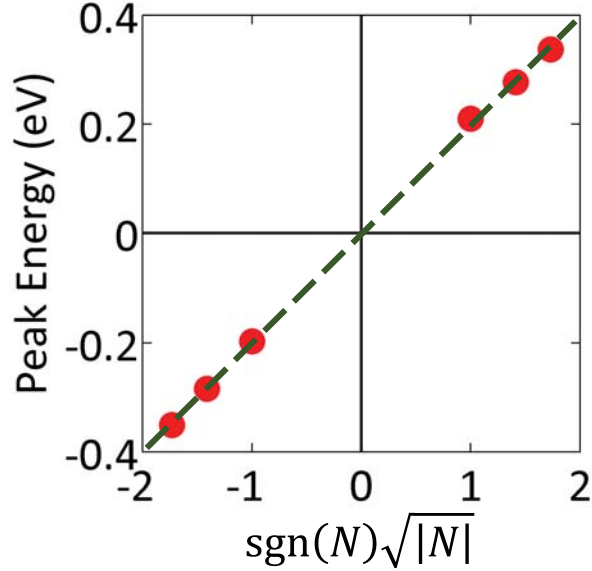


Figure 4.20. Linear scaling between the pseudo peak energies E_N from DFT results as shown in Fig. 1H and $\sqrt{|N|}$, where N is the peak index.

The intensity of the pseudomagnetic field can be estimated by the energy spacing between pseudo Landau level peak positions from DFT calculations (3, 148)

$$B_{\text{ps}}^{\text{DFT}} = \frac{\left(\frac{E_N - E_{\text{Dirac}}}{\text{sgn}(N)}\right)^2}{2e\hbar v_F^2 |N|} \quad (4.2.12)$$

From Fig. 4.20, the energy spacing between pseudo peak $N=0$ (E_{Dirac}) and $N=1$ (E_1) is ~ 0.21 eV, which gives $B_{\text{ps}}^{\text{DFT}} \cong 33.63$ T. Using Eq. (4.2.11) gives $B_{\text{ps}} \cong 118$ T, which roughly agrees with the FEM result (≈ 150 T), as shown in Fig. 4.16F. The difference in the estimated intensities of the pseudomagnetic field might result from the unrealistic enforcement of $\frac{\partial \epsilon_{xy}}{\partial x} = 0$ and $\frac{\partial \epsilon_{xx}}{\partial y} = 0$ in the DFT model. Nonetheless, the above DFT

calculations offers solid evidence attesting to the presence of a strain-induced pseudomagnetic field, as suggested by Eq. (4.2).

4.2.5. Solving optimal shape function for a uniform pseudomagnetic field in a graphene nanoribbon under a uniaxial stretch

Force balance along any cross-section cut of the graphene nanoribbon in Fig. 4.16A in y direction gives

$$F = E_g f(y) W_0 h \epsilon_{yy}, \quad (4.2.13)$$

where F is the applied force at the ends of graphene nanoribbon necessary to generate the uniaxial tensile strain ϵ_{app} . E_g and h are the Young's Modulus and thickness of graphene, respectively. Re-arrange Eq. (4.2.13) and take derivative with respect to y , we get

$$\frac{\partial \epsilon_{yy}}{\partial y} = -\frac{F}{E_g W_0 h} \frac{1}{f^2} \frac{df}{dy}. \quad (4.2.14)$$

For a uniform strain gradient $\frac{\partial \epsilon_{yy}}{\partial y}$, Eq. (4.2.3) gives the governing equation of the optimal shape function,

$$\frac{1}{f^2} \frac{df}{dy} = C, \quad (4.2.15)$$

where C is a constant. Using the boundary conditions of $f(0) = 1$ and $f(L) = f_r (\neq 0)$, the solution of the shape function is given by

$$f(y) = \frac{f_r L}{f_r (L - y) + y}, \quad (4.2.16)$$

and

$$C = \frac{f_r^{-1}}{f_r L}. \quad (4.2.17)$$

The unknown quantity F in Eq. (4.2.13) can be related to the global deformation by the loading-deformation condition

$$\int_0^L \epsilon_{yy} dy = \Delta L \quad (4.2.18)$$

where

$$\epsilon_{yy} = \frac{F}{E_g W_0 h} \frac{1}{f(y)} \quad (4.2.19)$$

and ΔL is the change in length of the graphene nanoribbon under uniaxial stretch so that $\epsilon_{app} = \Delta L/L$.

Equations (4.2.18) and (4.2.19) lead to

$$F = \frac{2 \Delta L E_g f_r W_0 h}{(1 + f_r)L} \quad (4.2.20)$$

Substituting Eqs. (4.2.16) and (4.2.20) into Eq. (4.2.4) gives

$$B_{ps} = \frac{6t\beta}{ev_F} \frac{\epsilon_{app}}{L} \frac{(1-f_r)}{(1+f_r)} (1 + \nu), \quad (4.2.21)$$

4.2.6. Solving the optimal shape function for a uniform pseudomagnetic field in a graphene-based 2D hetero-structure under a uniaxial stretch

Force balance along any cross-section of the 2D hetero-structure gives

$$E_g W_0 h f(y) \epsilon_{yy} + E_h W_0 h (1 - f(y)) \epsilon_{yy} = F, \quad (4.2.22)$$

so that

$$\frac{\partial \epsilon_{yy}}{\partial y} = -\frac{F}{E_g W_0 h} \frac{\left(1 - \frac{E_h}{E_g}\right) \frac{df}{dy}}{\left(\left(1 - \frac{E_h}{E_g}\right) f + \frac{E_h}{E_g}\right)^2}. \quad (4.2.23)$$

Solving $\frac{\partial \epsilon_{yy}}{\partial y} = \text{constant}$ gives

$$f(y) = \frac{\frac{E_h}{E_g} - \left(\left(1 - f_r \left(1 - \frac{E_h}{E_g}\right) + \frac{E_h}{E_g}\right)^{-1} \frac{y}{L} - 1\right)^{-1}}{1 - \frac{E_h}{E_g}} \quad (4.2.24)$$

Following a similar strategy as in Section 4.2.5, one gets

$$\frac{\partial \epsilon_{yy}}{\partial y} = \frac{2 \epsilon_{\text{app}} (1 - f_r) \left(1 - \frac{E_h}{E_g}\right)}{L \left(1 + f_r \left(1 - \frac{E_h}{E_g}\right) + \frac{E_h}{E_g}\right)} \quad (4.2.25)$$

and

$$B_{\text{ps}} = \frac{6t\beta}{e v_F} \frac{\epsilon_{\text{app}} (1 - f_r) \left(1 - \frac{E_h}{E_g}\right)}{L \left(1 + f_r \left(1 - \frac{E_h}{E_g}\right) + \frac{E_h}{E_g}\right)} (1 + \nu). \quad (4.2.26)$$

Equation (4.2.26) suggests that the larger the difference in stiffness of the constituent materials in the 2D hetero-structure (i.e., smaller $\frac{E_h}{E_g}$), the more intensive the resulting pseudomagnetic field.

Note that Equation (4.2.26) reduces to Eq. (4.2.6) when $\frac{E_h}{E_g} = 0$ (i.e., a graphene nanoribbon).

4.2.7. Finite element modeling and comparison with elasticity-based theoretical prediction

Graphene, as well as graphane and h-BN, are modeled as linear elastic materials with Young's Moduli of 1 TPa, 0.73 TPa, 0.82 TPa and Poisson's ratios of 0.17, 0.08, 0.22, respectively (190-193). Large-strain quadrilateral shell elements (S4R), which allow for finite membrane strain, are used for modeling all materials.

All material intrinsic thickness is set to 0.34 nm. In finite element models, the bottom edge of the graphene nanoribbon (or the 2D hetero-structure) is fixed in y direction. A displacement u in y direction is applied at the top edge, so that $\epsilon_{appl} = u/L$. Both top edge and bottom edge are allowed to deform along x direction. The two long edges are free.

The modeling is carried out using finite element method. The strain distribution obtained from finite element modeling is then plugged into Eq. (4.21) to calculate the intensity of the resulting pseudomagnetic field (Fig. 4.16, E to G), which is then compared with the field intensity theoretically predicted using Eq. (4.2.6).

The comparison between the results from finite element simulations (Fig. 4.16, E to F) and those from elasticity-based theoretic prediction (Eq. (4.2.6)) shows that the theory modestly underestimates the intensity of resulting pseudomagnetic field (defined by the plateau value). This can be attributed to the assumption of linear distribution of ϵ_{yy} (or ϵ_{xx}) over the entire length and linear distribution of ϵ_{xy} over the entire width of the graphene nanoribbon in the theory. As shown in Fig. 4.16 (B-D), such an assumption

holds for the graphene nanoribbon except its four corners, leading to an effective length of the ribbon shorter than the entire length and thus a higher intensity of pseudomagnetic field.

4.2.8. Effect of top/bottom width ratio on pseudomagnetic field in a graphene nanoribbon

Figure 4.21A shows three 25-nm long graphene nanoribbons with different top-bottom ratios $f_r = 0.35, 0.5,$ and 0.7 . The basal width is 10 nm. Their two long edges are prescribed by the optimized shape function given in Eq. (4.2.16).

Figure 4.21B shows the finite element modeling results on the effect of top-bottom width ratio f_r on the intensity of the resulting pseudomagnetic field. The smaller the top-bottom width ratio, the higher the strain gradient in the graphene, and thus the stronger the resulting pseudomagnetic field, which agrees well with our theoretical prediction (Eq. (4.2.21)).

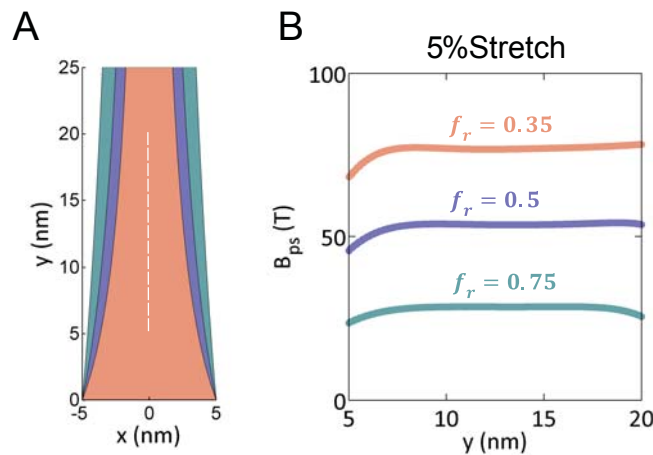


Figure 4.21. (A) The geometry of 25 nm long graphene nanoribbons of three top/bottom width ratio $f_r = 0.35, 0.5,$ and 0.7 , respectively, with two their long edges of each nanoribbon prescribed by Eq. (4.2.16). (B) The corresponding intensities of the resulting pseudomagnetic field from finite element simulations under a 5% uniaxial stretch.

4.2.9. Atomistic simulations

The atomistic simulations are carried out using Large-scale Atomic/Molecular Massively Parallel Simulator (LAMMPS) (79). Figures 4.22A and 4.23A show the atomistic simulation models for the graphene nanoribbon and graphene-based 2D hetero-structure, respectively. Each model contains two graphene nanoribbons, the same as shown in Fig. 4.16B (or two 2D hetero-structures as same as shown in Fig. 4.17A), which are covalently bonded along their wider ends in a mirroring fashion. Periodic boundary condition is applied along the vertical (loading) direction, therefore the atomistic model indeed represents a long graphene nanoribbon (e.g., Fig. 4.18A) or a large graphene-based 2D hetero-superlattice structure (e.g., Fig. 4.18C) with a repeating unit defined by Figs. S4A and S5A, respectively.

For simulations of graphene nanoribbons and graphene/graphane hetero-structures, the carbon-carbon (C-C) and carbon-hydrogen (C-H) bonds in the graphene as well as the non-bonded C-C and C-H interactions are described by the Adaptive intermolecular Reactive Empirical Bond Order (AIREBO) potential (78). For simulations of graphene/h-BN hetero-structures, the atomic interactions are described by the Tersoff potential (194, 195). The molecular mechanics simulations are carried out at zero K temperature. The loading is applied by gradually elongate the simulation box along vertical direction. At each loading step, the energy of the system is first minimized by using conjugate gradient algorithm until either the total energy change between successive iterations divided by the energy magnitude is less than or equal to 10^{-8} or the total force is less than 10^{-5} eV/nm. The strain components, determined by Lagrange

strain tensor in the deformed state, are used to calculate the resulting pseudomagnetic field.

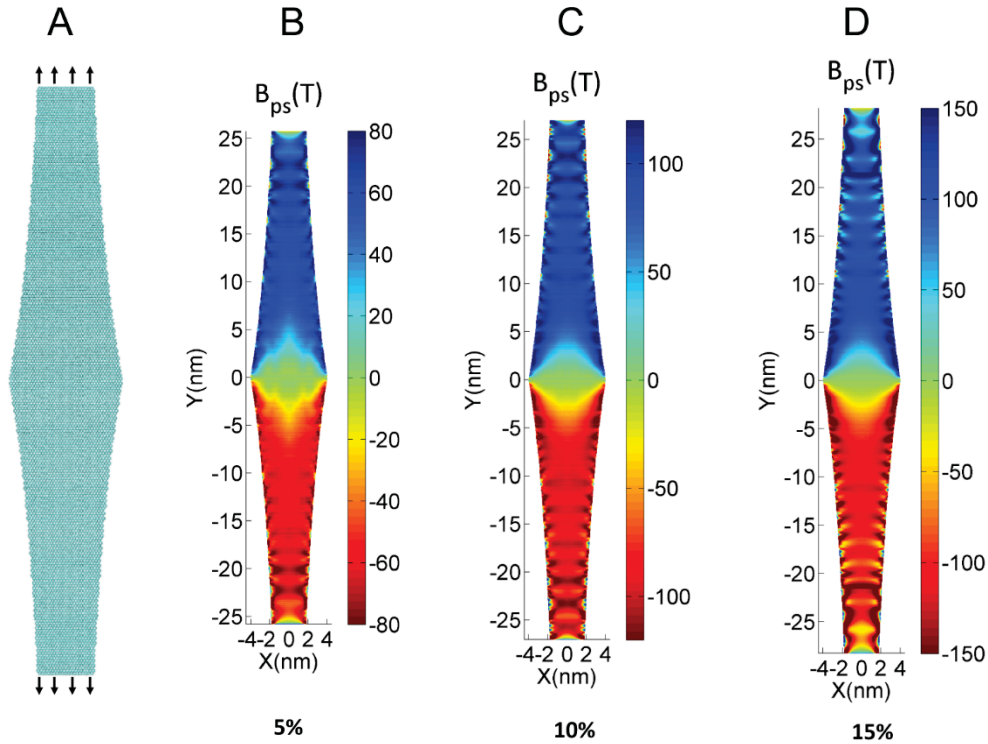


Figure 4.22. (A) Atomistic simulation models for the graphene nanoribbon. (B-D) Atomistic simulation results on pseudomagnetic fields in the graphene nanoribbon under a uniaxial stretch of 5 %, 10 % and 15 %, respectively.

Figure 4.22 (B-D) plots the resulting pseudomagnetic field in the graphene nanoribbon under a uniaxial stretch of 5 %, 10 % and 15 %, respectively. The corresponding averaged intensity of the pseudomagnetic field near the central region of the top or bottom part is approximately 55 T, 100 T, and 125 T, respectively, in excellent agreement with the prediction from finite element modeling (Fig. 4.16E). The ripple-like feature in the contour of pseudomagnetic field along the long edges coincides with the non-smooth and discrete nature of the long edges of the graphene nanoribbon to fit the shape function.

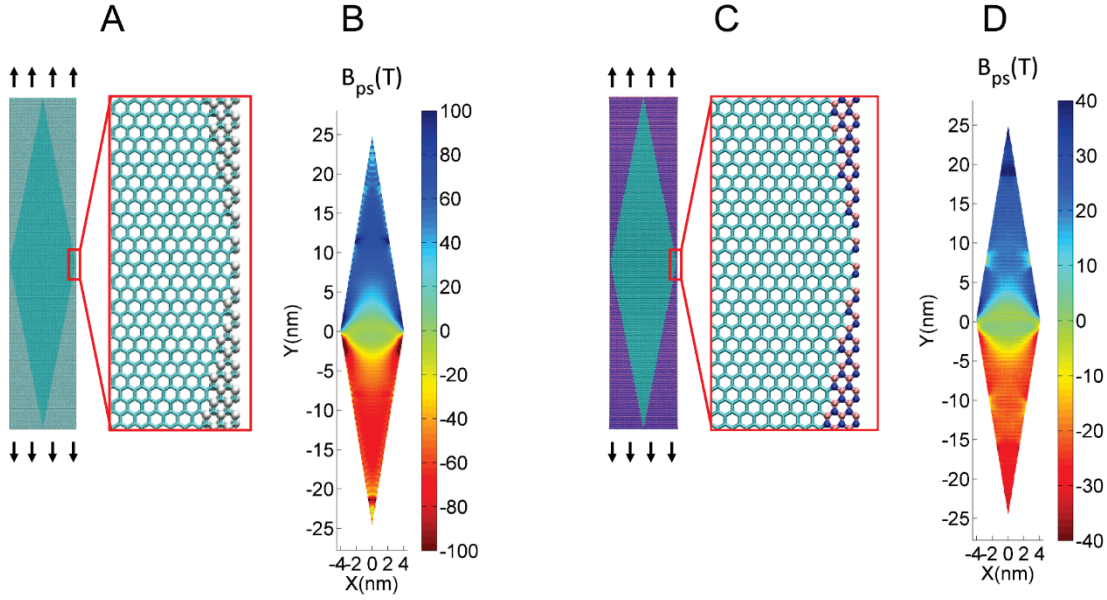


Figure 4.23. (A) Atomistic simulation models for a graphene/graphane 2D hetero-structure with straight material domain boundary. (B) Atomistic simulation results on pseudomagnetic fields in the graphene domain in (A) under a uniaxial stretch of 15 %. (C) Atomistic simulation models for the graphene/h-BN 2D hetero-structure with straight material domain boundary. (D) Atomistic simulation results on pseudomagnetic fields in the graphene domain in (C) under a uniaxial stretch of 15 %.

Figure 4.23 shows the quasi-uniform pseudomagnetic field in graphene/graphane and graphene/h-BN 2D hetero-structures with *straight* domain boundary, under a uniaxial stretch of 15 %.

4.3. Chapter summary

Recent experiments reveal that a scanning tunneling microscopy (STM) probe tip can generate a highly localized strain field in a graphene drumhead, which in turn leads to a pseudomagnetic field in the graphene that can effectively confine charge carriers in a way similar to a spatially confined quantum dot (QD). We carry out systematic molecular dynamics and coarse-grained simulations to reveal the effect of the STM tip size and graphene drumhead size as well as the influence from the back-gate voltage

and the tip location on the induced strain field and corresponding pseudomagnetic field. These results can offer guidance for design of reversible and on-demand formation of graphene QDs in nanoelectronics.

Many of the properties of graphene are tied to its lattice structure, allowing for tuning of charge carrier dynamics through mechanical strain. The graphene electro-mechanical coupling yields very large pseudomagnetic fields for small strain fields, up to hundreds of Tesla, which offer new scientific opportunities unattainable with ordinary laboratory magnets. Significant challenges exist in investigation of pseudomagnetic fields, limited by the non-planar graphene geometries in existing demonstrations and the lack of a viable approach to controlling the distribution and intensity of the pseudomagnetic field. We have demonstrated two new approaches to generating large pseudomagnetic fields with uniform distributions in a planar graphene sheet over a large area. We achieve this by patterning the planar graphene geometry and graphene-based hetero-structures with a shape function to engineer a desired strain gradient. Our method is geometrical, opening up new fertile opportunities of strain engineering of electronic properties of 2D materials in general.

Chapter 5: Strain engineering of compliance, stretchability, strength, toughness in graphene-based nanostructures

5.1. Extremely compliant and highly stretchable patterned graphene

Graphene has attracted lots of attention because of its exceptional electronic, mechanical and chemical properties (1, 13, 80). For example, being ultra-thin and electronically stable down to sub-nanometer, graphene is explored as a potential solution to address the physical limit of silicon-based electronics. More intriguingly, the optical transparency and mechanical durability of graphene further motivate its potential application in emerging flexible and stretchable electronics technology, such as electronic skins, smart textile, paper-like displays, etc (196-205). Existing explorations of these opportunities have mainly focused on the electronic performance of graphene devices. A crucial challenge to successful application of graphene in flexible and stretchable electronics, however, remains largely unexplored. Applications such as electronic skins and epidermal electronics require interfacing with biological tissues and elastomeric substrates, which are extremely compliant (e.g., with a stiffness ranging from ~ 1 KPa (tissues) to 100s KPa (elastomers)). By contrast, pristine graphene has an ultra-high stiffness (~ 1 TPa) (13). Such a huge mechanical mismatch (7-9 orders of magnitude) between graphene and its interfacing materials poses a significant challenge in the functionality and reliability of these flexible and stretchable devices, which are often required to sustain large, repeatable deformation in operation. To address such a challenge, in this section we demonstrate a feasible and promising solution by patterning pristine graphene into large area graphene nanomesh (GNM).

Through a bottom-up scalable coarse-grained (CG) simulation scheme, we show that suitably patterned GNM can be made extremely compliant (with a negligible stiffness) up to elongation about 20% and then remain highly compliant (e.g., with an effective stiffness more than 20 times lower than that of pristine graphene) up to elongation about 50%. The extremely compliant and highly stretchable GNM (vs. pristine graphene with a tensile failure strain of about 20%) thus holds promise to meet the stringent operating requirements of flexible and stretchable electronics, while the associated desirable tunability of the electronic properties of GNM could further inspire devices with multi-functionalities.

Pristine graphene has zero band-gap, an intrinsic challenge for logic applications (20, 206). Graphene nanoribbons with a width of less than 10 nm offer a possible solution by rendering a band-gap suitable for room-temperature transistor operation (16, 18, 60, 207-209). However, graphene nanoribbon device cannot meet the needs of practical devices and circuits that require the fabrication of dense arrays of ordered nanoribbons (60-63). GNM, a network of percolating graphene nanoribbons with an ordered pattern, is proposed and fabricated as an effort to overcome such difficulties of graphene nanoribbons by opening up band-gap in a large sheet of patterned graphene as a semiconducting thin film (59, 64, 65, 178-180). It has been demonstrated that GNM can be applied as gas sensors with a high sensitivity (210). Enthusiasm for GNM-based devices aside, existing research on GNM mainly focuses on its electronic properties, while little study, if not none, has been reported on its mechanical properties, which are crucial for integrating GNM into flexible and stretchable electronic devices or interfacing with other materials (211-213). Lack of such mechanics studies can be

partially attributed to the fact that the GNM fabricated and used in devices has a length scale ranging from 100s nanometer up to microns (64, 180, 210), making fully atomistic study of the mechanical behaviors of GNM computationally prohibitive (214, 215). To overcome such a difficulty, we present a scalable bottom-up CG simulation scheme of graphene, which enables the systematic mechanics study of the GNM of practical length scale.

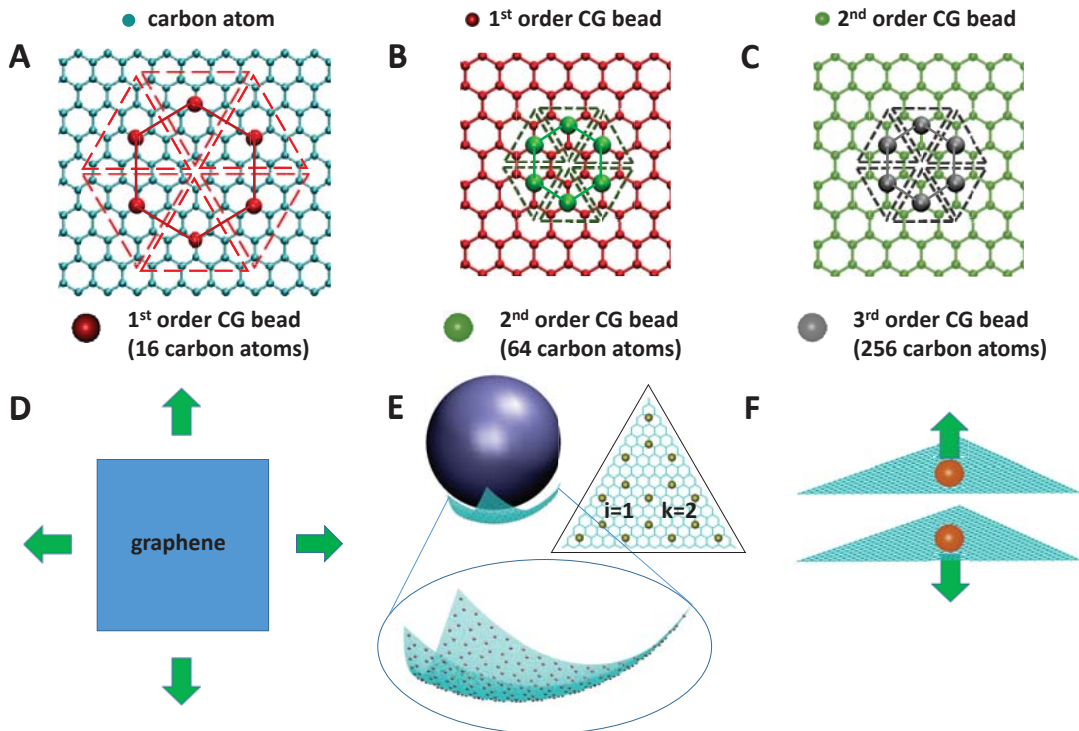


Figure 5.1 A bottom-up scalable CG simulation scheme of graphene. (A-C) Mapping from atomic graphene (cyan) to 1st order CG beads (red), to 2nd order CG beads (green), and to 3rd order CG beads (grey). Note that the hexagonal lattice symmetry is maintained in all orders of CG. (D-F) Schematics of CG parameterization strategies to determine bond force constant via equi-biaxial stretching (D), bond angle constant via equi-biaxial bending (E), and van der Waals constants via out-of-plane separation (F), respectively.

The uniqueness of our CG simulation scheme of graphene is twofold. First, it is a bottom-up approach, starting from the atomic structure of graphene, and scalable to any orders of CG levels. Therefore, such a CG scheme can be tailored to be suitable to simulate graphene systems of a wide range of length scales. Second, the hexagonal

lattice symmetry, the origin of many exceptional properties of graphene, is maintained in all orders of CG levels. Such a feature maximizes the intrinsic similarity between the atomic structure and CG structure of graphene, the key to high precision and fidelity of CG simulations. Figures 5.1A-C show the representations of the first three orders of CG levels, respectively. The building block of 1st order CG, termed as 1st order CG bead, represents 16 carbon atoms within an equilateral triangle in the atomic graphene structure (Fig. 5.1A). As a result, the 1st order CG beads can fill up the two dimensional space by being packed into the same hexagonal lattice as in atomic graphene, but with a larger bead-bead bond length (0.568 nm vs. 0.142 nm of carbon-carbon atomic bond length). One 2nd order CG bead represents four 1st order CG beads within an equilateral triangle (Fig. 5.1B), so that the 2nd order CG beads can fill up the two dimensional space in a hexagonal lattice with an even larger bead-bead bond length (1.136 nm). Such a CG procedure can then be scaled up recursively (i.e., Fig. 5.1C) to any higher order, while the hexagonal lattice symmetry is maintained in the CG structure of any order. As a result, the CG scheme of N^{th} order allows for a reduction of computation size by 4^{N+1} folds. For example, one 3rd order CG bead represents 256 carbon atoms (Fig. 5.1C), which can significantly reduce the computational expense. The mass of the CG bead and the bead-bead bond length of any CG order can be deduced recursively. The bonded energy terms of the CG scheme consist of a two-body bond energy and three-body angle energy as $U_{bonding}(r_{ij}, \theta_{ijk}) = \sum \frac{1}{2} K_b (r_{ij} - r_0)^2 + \sum \frac{1}{2} K_\theta (\cos \theta_{ijk} - \cos \theta_0)^2$, where r_{ij} is the distance between the i^{th} and j^{th} bonded CG beads with r_0 being its corresponding equilibrium distance; θ_{ijk} is the angle between the i - j bond and j - k bond with $\theta_0=120^\circ$ being its corresponding equilibrium angle; K_b

and K_θ are bond force constant and angle force constant, respectively. The non-bonded term includes the van der Waals (vdW) interaction between CG beads. This bottom-up scalable CG scheme allows straightforward yet rigorous determination of the bonded energy parameters without any fitting, as to be detailed as follows. Table 5.1 lists the values of CG parameterization used in this study. All CG simulations are implemented using modeling code LAMMPS (79).

Table 5.1. CG parameters used in simulations

	1 st order CG	2 nd order CG	3 rd order CG
r_0	0.568 nm	1.136 nm	2.272 nm
K_b	47.46 eV·Å ⁻² (same for all CG orders)		
K_θ	93.23 eV	372.91 eV	1491.66 eV
σ	0.34 nm (same for all CG orders)		
ϵ	0.00666 eV	0.00483 eV	0.00337 eV

The bond force constant is determined recursively by equating the potential energies of a square atomic graphene and its CG counterparts of any order under equi-biaxial stretching (no change in the three-body angle energy) (Fig. 5.1D). Denote K_{bi} , ρ_i , r_{0i} as the bond force constant, bond density (per unit area) and equilibrium bond length for the i^{th} order CG, respectively; A_0 and A as the area of graphene before and after the equi-biaxial stretching, respectively. The strain in each bond (both atomic bond and CG bond) is therefore determined as $e = \sqrt{A/A_0} - 1$. The total bond force energy after deformation for the i^{th} order CG is determined as $E_{bi} = A_0 \rho_i \times \frac{1}{2} K_{bi} (e r_{0i})^2 =$

$\frac{1}{\sqrt{3}}K_{bi}A_0\left(\sqrt{\frac{A}{A_0}}-1\right)^2$ (note that for a hexagonal lattice of the i^{th} order CG, $\rho_i r_{0i}^2 = 2/\sqrt{3}$). By equating the total bond force energy for different CG orders, e.g., $E_{b(i+1)} = E_{bi}$, we have $K_{b(i+1)} = K_{bi}$. In other words, the bond force constants of CG levels of all orders are the same, another intrinsic advantage of our scalable CG scheme.

The angle force constant is determined by equating the potential energies of an atomic graphene and its CG counterpart under equi-biaxial bending (i.e., by conforming to a rigid spherical surface so that the change in the bond force energy is highly suppressed, Fig. 5.1E). Consider a unit cell of graphene in the shape of an equilateral triangle that is coarse-grained into the i^{th} order and contains 4^k CG beads (k is independent of CG order i). Therefore, such a unit cell denotes an atomic graphene with 4^{k+i+1} carbon atoms (e.g., inset of Fig. 5.1E shows the case of $i=1, k=2$). Given the self-similarity in lattice structures of atomic and CG graphene, the change of the bond angle between two neighboring carbon-carbon bonds in atomic graphene is the same as that between two neighboring CG bonds in CG graphene, when conforming to the same spherical surface. Denote $K_{\theta A}$ and $K_{\theta i}$ as the angle force constant of atomic graphene and CG graphene of i^{th} order, respectively, and the bond angle after deformation as θ . The total angle force energy in the atomic graphene is $E_{aA} = 4^{k+i+1} \times 3 \times \frac{1}{2} k_{\theta A} (\cos\theta - \cos\theta_0)^2$, while that in the CG graphene is $E_{ai} = 4^k \times 3 \times \frac{1}{2} k_{\theta i} (\cos\theta - \cos\theta_0)^2$. By $E_{aA} = E_{ai}$, we get $k_{\theta i} = 4^{i+1} k_{\theta A}$, correlating the angle force constant in CG of i^{th} order with the atomic angle force constant of graphene (216-218).

The vdW interaction between the CG beads is fitted in a Lennard-Jones pair potential as $E_{vdW} = 4\epsilon \left[\left(\frac{\sigma}{r} \right)^{12} - \left(\frac{\sigma}{r} \right)^6 \right]$, while the CG beads for a given order are treated as triangle particles (79). For all orders of CG, σ is set to be 0.34 nm. ϵ is fitted to represent the energy needed to separate two pieces of triangular atomic graphene that a given order CG bead represents (Fig. 5.1F), from equilibrium distance (0.34nm) to infinity.

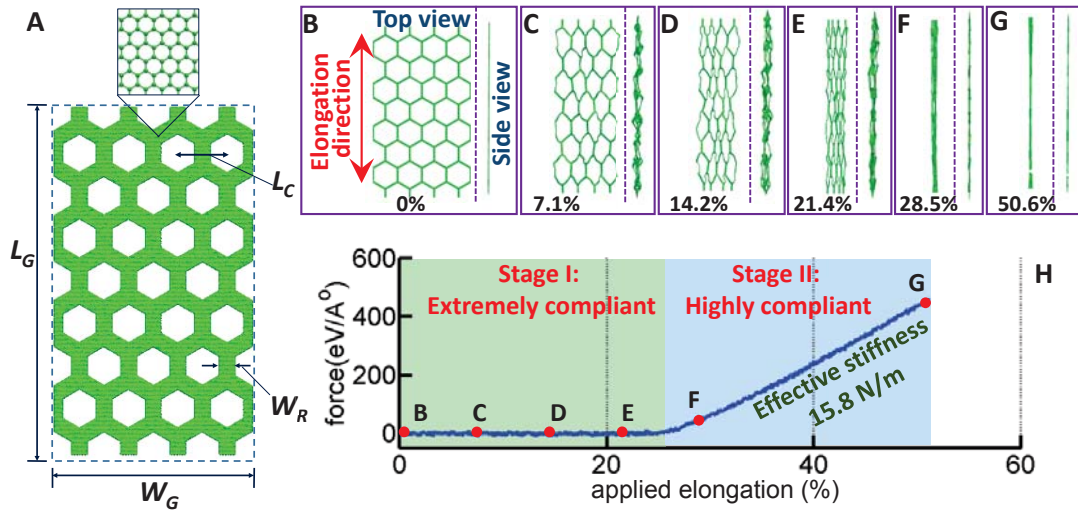


Figure 5.2 (A) CG model for the patterned GNM. (B-G) Snapshots of the deformed GNM under various applied tensile strains. Red arrow indicates the direction of applied tensile load. (H) Resultant force in the GNM as a function of applied elongation. The light green shaded region highlights the extremely-compliant region of the GNM while the light blue shaded region highlights the highly-compliant region with an effective stiffness of about 15.8 N/m. Here $L_G = 351$ nm, $W_G = 199$ nm, $L_C = 50$ nm and $W_R = 2$ nm.

Figure 5.2A depicts the CG simulation model for GNM in experiments with hexagonal-shaped holes patterned in a hexagonal lattice in a planar monolayer graphene (59, 64, 65, 178, 179, 211, 212). The geometry of the GNM is defined by two parameters: the spacing between two neighboring hexagonal holes (termed as GNM lattice constant and denoted by L_C) and the graphene nanoribbon width (W_R). The global size of the CG model measures $W_G \times L_G$. The choice of a proper order of CG scheme is global-size

dependent in the sense that, on one hand, the CG graphene bead is small enough to capture the fine features of the deformation under loading, and on the other hand, large enough to reasonably reduce the computational cost. Hereinafter, 1st Order CG is used in all simulations of GNM unless noted otherwise.

Figures 5.2B-G show the deformed shape of a GNM under various applied elongation along the armchair direction of the graphene nanoribbon network (indicated by the red arrow in Fig. 5.2B). Here $L_G = 351$ nm, $W_G = 199$ nm, $L_C = 50$ nm and $W_R = 2$ nm, which corresponds to a patterned graphene with 353,552 carbon atoms. We implement displacement loading and the CG structure is equilibrated for every displacement increment. The CG simulation is done at 300 K by canonical ensemble and by Nose-Hoover thermostat. Figure 5.2H plots the resultant force in the GNM as a function of the applied elongation, which clearly depicts two stages of the GNM deformation. In the first stage, the GNM can readily elongate up to about 25% without appreciable resultant force. In other words, the GNM is extremely compliant with nearly zero stiffness. As shown in Figs. 5.2B-E, the elongation of the GNM in this stage is accommodated by deflecting and twisting the initially planar and tortuous graphene nanoribbon network out of its plane, while individual graphene nanoribbons barely stretch. It has been shown that suitable patterning can significantly increase the stretchability of various materials under the similar deformation mechanism (219, 220). In the second stage, the applied elongation further straightens and stretches the graphene nanoribbon network (Fig. 5.2F) until the final fracture of the GNM at about 50% elongation (Fig. 5.2G). The fracture of the GNM results from breaking of the CG bonds that are stretched beyond 22% tensile strain, which is taken as the average for

the failure strains of pristine graphene in armchair (17%) and zigzag (27%) directions (14, 193). The effective stiffness of the GNM in the second stage, defined as the average slope of the corresponding curve in Fig. 5.2H normalized by initial cross-section width (W_G), is shown to be 15.8 N/m, more than 22 times lower than that of the pristine graphene (340 N/m) (13). In other words, the GNM is still highly compliant in the second deformation stage. Furthermore, the two-stage deformation behavior of GNM leads to a stretchability beyond 50%, much higher than tensile failure strain of pristine graphene (14, 193).

The two-stage deformation behavior and the ultra-high compliance and stretchability of the GNM as revealed in Fig. 5.2 are shown to hold for GNMs with a wide range of pattern geometry. Figure 5.3 reports quantitative study on the effect of pattern geometry on GNM deformation behavior. For a given GNM lattice constant L_C , as the graphene nanoribbon width W_R decreases (Figs. 5.3A-C), the stretchability of GNM increases, the range of elongation for GNM being extremely compliant increases, and the effective stiffness of GNM in the second deformation stage decreases (Fig. 5.3D), though all these changes are modest. For a given W_R , as L_C increases (Figs. 5.3E-G), both the stretchability of GNM and the range of elongation for GNM being extremely compliant remain nearly unchanged, while the effective stiffness of GNM in the second deformation stage decreases modestly (Fig. 5.3H). For a given L_C/W_R ratio, as W_R decreases (Figs. 5.3I-K), similar trend as shown in Figs. 5.3E-G is found. These parametric studies show that a suitably patterned GNM can be made extremely compliant up to about 20% elongation and then remain highly compliant up to about

50% elongation (with an effective stiffness more than one order of magnitude lower than that of pristine graphene).

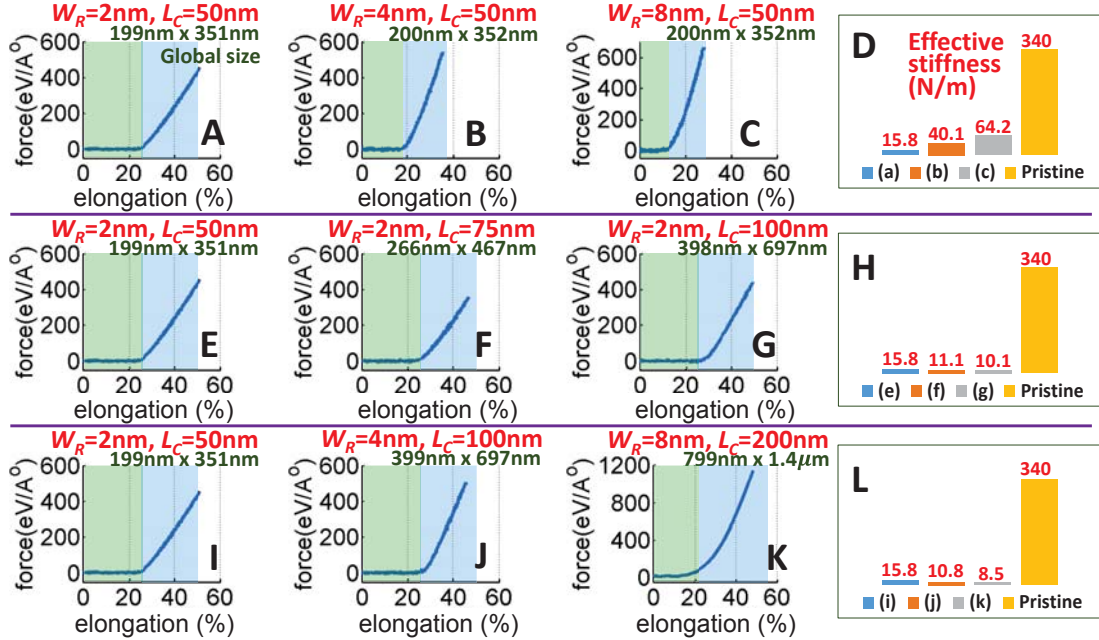


Figure 5.3 Effect of pattern geometry of GNM on the deformation behavior and stretchability of GNM. (A-C): Resultant force in GNM as a function of applied elongation for varying W_R (2 nm, 4 nm and 8 nm) with a fixed $L_C = 50$ nm; (E-G): Varying L_C (50 nm, 75 nm and 100 nm) with a fixed $W_R = 2$ nm; (I-K): W_R (2 nm, 4 nm and 8 nm) with a fixed ratio $L_C/W_R = 25$. (D), (H), and (L): Comparing the corresponding effective stiffness of the GNM in highly compliant stage (shaded in light blue) with that of pristine graphene. Total number of carbon atoms in the corresponding graphene network: (a) 353,552; (b) 671,536; (c) 981, 040; (f) 479,408; (g) 815,408; (j) 1,041,584; (k) 4,158,272 (simulation done by CG of 2nd order given the GNM in micron size).

The significantly enhanced stretchability and ultra-high compliance of suitably patterned structures, such as GNM and other materials (198, 219-222), find their origin in the deformation mechanism of bending and twisting, instead of pure stretching, to accommodate elongation. Such a deformation mechanism is essentially geometric, and thus independent of length scale. As suggested from the results of present study, GNM of size of microns (or even larger scale) can be made extremely compliant and highly stretchable under the same deformation mechanism. The advances in graphene

patterning with nanoscale precision (17, 125, 223-225) further allow applying GNMs as structural components to enable high biaxial stretchability of the overall functional structure. For example, for biological applications (198), these GNMs can be attached onto the surface of biological tissues. The high stretchability and compliance of GNM can potentially accommodate the large deformation in biological tissues while keeping the electronic devices functioning. As a demonstration of the concept, Fig. 5.4A depicts a possible design with biaxial stretchability, in which biaxial tensile loads would be mainly accommodated by the elongation of GNMs along their armchair direction, while the elongation of the GNMs along other directions would be minimal (198, 222). Nonetheless, to close the loop, we also study the tensile behavior of GNM under elongation along its zigzag direction (Fig. 5.4B). It is shown that the GNM as in Fig. 5.2 demonstrates the same two deformation stages when elongates along zigzag direction: being extremely compliant with nearly zero stiffness up to about 10% elongation and then being highly compliant with an effective stiffness of 15.7 N/m up to ~28% elongation. Given the hexagonal lattice symmetry of the GNM, it is expected the tensile behaviors of the GNM along its armchair and zigzag directions (as shown in Fig. 5.4B) set the upper and lower limits of the GNM under elongation in any arbitrary in-plane direction. As the elongation of the GNM structural elements along non-armchair directions would be minimal, it is reasonable to predict that structural designs such as Fig. 5.4A can enable a percolating graphene network that remains extremely compliant and highly stretchable under large elongation.

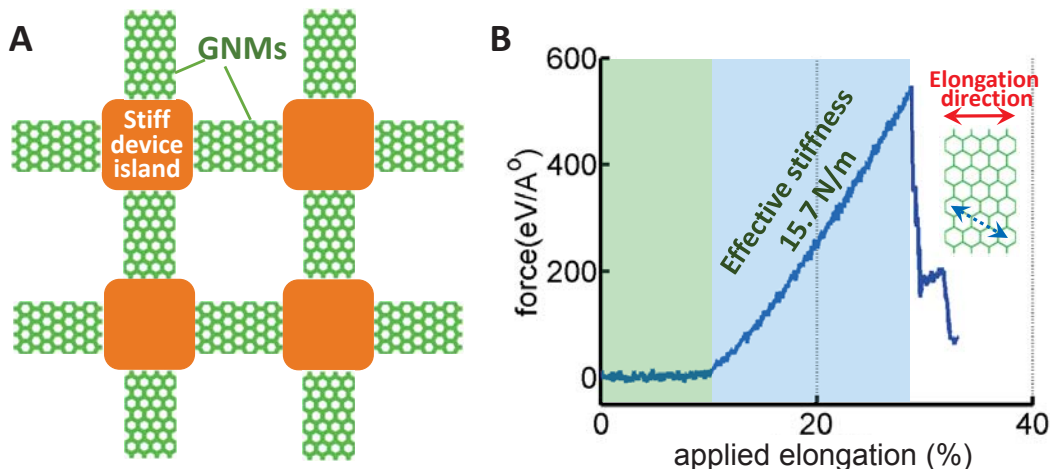


Figure 5.4 (A) A possible design of a biaxially stretchable functional structure with stiff device islands (hosting device components) interconnected via GNMs. Applied tension can be largely accommodated by the extremely compliant GNMs elongating along their armchair directions, with minimal elongation along other directions. (B) Tensile behavior of the GNM in Fig. 5.2 under elongation along its zigzag direction, which shows the similar two deformation stages. Dashed arrow shows armchair direction, which has 30° rotation from zigzag direction.

In conclusion, we demonstrate a feasible solution that holds promise to address the challenge of interfacing intrinsically ultra-stiff graphene with highly compliant biological tissues and elastomers: by suitably patterning graphene, the resulting GNM can be made extremely compliant with nearly zero stiffness up to ~20% elongation and then remain highly compliant up to ~50% elongation (with an effective stiffness more than one order of magnitude lower than and a stretchability more than twice higher than that of pristine graphene). Such extremely compliant and highly stretchable GNMs can be used to enable biaxial stretchability of functional structures. The robustness of the deformation behaviors of GNMs against the width of the graphene nanoribbon building blocks (as shown in Fig. 5.3) could be further leveraged to explore other desirable electronic properties (e.g., tunable bandgap) of GNMs. We therefore call for further experimental studies to fully exploit these fertile opportunities.

5.2. Incorporating cellulose: Attaining stronger and tougher materials

The quest of both strength and toughness is perpetual in advanced material design; unfortunately, these two mechanical properties are generally *mutually exclusive* (226). While strength measures a *stress* denoting a material's resistance to irreversible deformation, toughness characterizes a material's resistance to fracture and thus measures the *energy* needed to cause fracture. Toughness requires a material's ability of dissipating local high stress, e.g. by enduring deformation. Consequently, hard materials tend to be brittle (less tough); lower strength materials, which can deform more readily, tend to be tougher. For example, for metals and alloys, their toughness is usually inversely proportional to their strength. As a result, in practice, the design of strong and tough materials is inevitably a compromise.

Despite the consensus on mutual exclusiveness of strength and toughness, a significant gap exists between engineering practice and scientific considerations. For applications as large as nuclear reactor vessels and as small as cardiovascular stents, catastrophic failure of their structural materials is never acceptable. Therefore it is not unusual that materials used in most safety-critical engineering structures are rarely super strong materials without appropriate fracture resistance, but *rather materials with comparatively low in strength but high in toughness*. Acknowledging the necessary compromise between strength and toughness, one would expect that research on advanced material design would be focused on achieving an optimum combination of these two properties. Unfortunately, a great deal of research efforts in materials science are still too focused on pursuing higher strength, with rather limited corresponding

regard for toughness. One example is the enthusiasm sparked by the discovery of graphene and carbon nanotube, which exhibit remarkably high strength. However, it still remains uncertain how such a strong material can be incorporated with bulk materials to benefit from its high strength without sacrificing toughness.

Aiming to shed new insight on the long-sought strategy addressing the conflict of strength versus toughness, we first combine systematic atomistic modeling and complementary experiments to decipher the fundamental science underpinning the anomalous scaling law of strength and toughness revealed from our pilot study of cellulose-based nanopaper. We then employ such fundamental understanding and design strategy to hybridize graphene oxide and cellulose to obtain strong and tough fiber. This study potentially opens up fertile opportunities toward a new class of materials with both exceptional mechanical properties and other highly desirable features (e.g., environmentally sustainable, multi-functional) conferred by their constituent building blocks.

5.2.1. Anomalous scaling law of strength and toughness of cellulose nanopaper

5.2.1.1. Motivation

There have been tremendous efforts recently to develop materials with higher strength using smaller material structures. For example, by decreasing the grain size of metals, dislocation motions (thus plasticity) are more restricted, leading to a higher strength (227-232). On the other hand, such treatments also minimize possible mechanisms (e.g., crack-tip blunting) to relieve local high stress, resulting in lower toughness. The atomic scale origins of high strength of a material, e.g., strong directional bonding and

limited dislocation mobility, are also essentially the roots for brittleness of the material. In short, the well-recognized scaling law of “The smaller, the stronger” comes at a price of sacrificing toughness (Fig. 5.5).

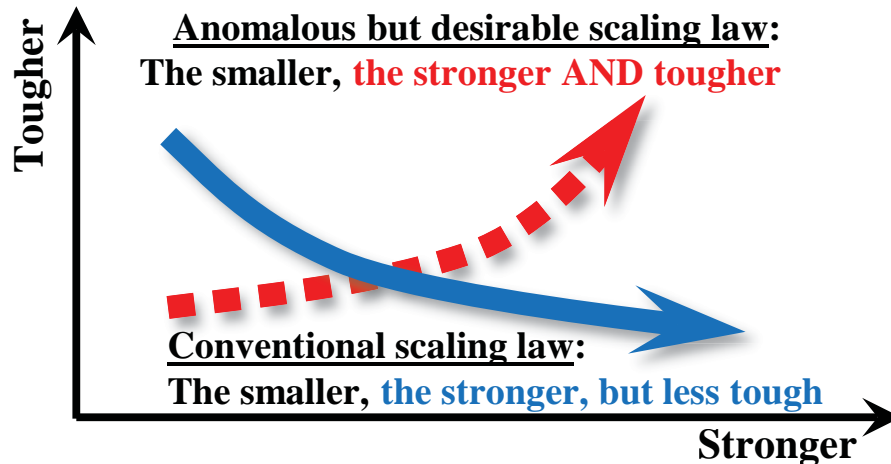


Figure 5.5. An anomalous but desirable scaling law of mechanical properties requires defeating the conventional conflict between strength and toughness.

The prevailing toughening mechanisms can be categorized into two types: intrinsic and extrinsic. Intrinsic toughening operates ahead of a crack tip to suppress its propagation. It is primarily related to plasticity and thus the primary source of fracture toughness in ductile materials. Recent progress involves introducing high-density nano-twin boundaries in metals to achieve high strength and toughness (233-237). Intrinsic toughening mechanisms are essentially ineffective with brittle materials, e.g., ceramics, which invariably must rely on extrinsic toughening (238). Extrinsic toughening act mainly behind the crack tip to effectively reduce the crack-driving force by microstructural mechanisms, e.g., crack bridging and meandering and crack surface sliding (239-241). A counter-intuitive but successful example is the development of bulk metallic glass (BMG)-based composites, in which a crystalline dendrite second phase is introduced into the BMG matrix to promote the formation of multiple shear

bands, leading to a strong and also tough material (231, 239, 242, 243). Intrinsic and extrinsic toughening mechanisms are also found to be effective in natural materials (e.g., bones and nacs), which often involve the hierarchical structure and/or a “brick-and-mortar” hybrid microstructure of the material (244-247). Nature-inspired toughening mechanisms are also employed to synthesize biomimetic structural materials. Nonetheless, so far, there exists only rather limited success in attaining both strength and toughness, which often involve material-specific, complicated (e.g., growing high density nanotwins) or expensive (e.g., BMG-dendrite composites) synthesis processes and thus are hardly applicable to other materials. A general and feasible mechanism to address the conflict between strength and toughness still remains elusive.

Aiming to shed insight on the long-sought strategy addressing the conflict of strength and toughness, we rationally design cellulose-based nanopaper and investigate the dependence of their mechanical properties on constituent cellulose fiber size. Surprisingly, we find that both the strength and toughness of the nanopaper increase simultaneously (40 and 130 times, respectively) as the size of the constituent cellulose building blocks decreases (from a mean diameter of 27 μm to 11 nm). These stimulating results suggest the promising potential toward a new and highly desirable scaling law: The smaller, the stronger AND the tougher (Fig. 5.5). While the increasing strength as the diameter of cellulose fiber decreases can be attributed to reduced intrinsic defect size and the dependence is well captured by a continuum fracture mechanics model, our atomistic simulations reveal that facile formation and re-formation of strong hydrogen bonding among cellulose chains is the key to the simultaneously increasing

toughness. These mechanistic findings that underpin the highly desirable scaling law of mechanical properties suggest a fundamental bottom-up material design strategy generally applicable to other material building blocks as well, and therefore open up abundant opportunities toward a novel class of engineering materials that are both strong and tough.

5.2.1.2. Cellulose nanopaper: The smaller, the stronger AND the tougher

Cellulose is the most abundant biopolymer on Earth and has long been used as the sustainable building block for conventional paper. Cellulose has appealing mechanical properties, with specific modulus ($\sim 100 \text{ GPa}/(\text{g}/\text{cm}^3)$) and specific strength ($\sim 4 \text{ GPa}/(\text{g}/\text{cm}^3)$) higher than most metals and composites, and many ceramics, making it as a promising building block for functional and structural materials (248). Wood fibers are the main natural source of cellulose and have an intrinsically hierarchical structure (Fig. 5.6A). A 20~50 μm thick native wood fiber comprises thousands of nanofibrillated cellulose (NFC) fibers (5-50 nm in diameter), each of which can be disintegrated into finer elementary fibrils consisting of cellulose molecular chains (248-257). Cellulose molecule is a linear chain of ringed glucose molecules, with a repeat unit (Fig. 5.6B) comprising two anhydroglucose rings ($\text{C}_6\text{H}_{10}\text{O}_5$) linked through C-O-C covalent bond. Rich hydroxyl groups in cellulose molecule (six in each repeat unit) enable facile formation of hydrogen bonds, both intra-chain and inter-chain (Fig. 5.6A). While the intra-chain hydrogen bonding stabilizes the linkage and results in the linear configuration of the cellulose chain, inter-chain hydrogen bonding among neighboring

cellulose molecules plays a pivotal role in the deformation and failure behaviors of cellulose-based materials.

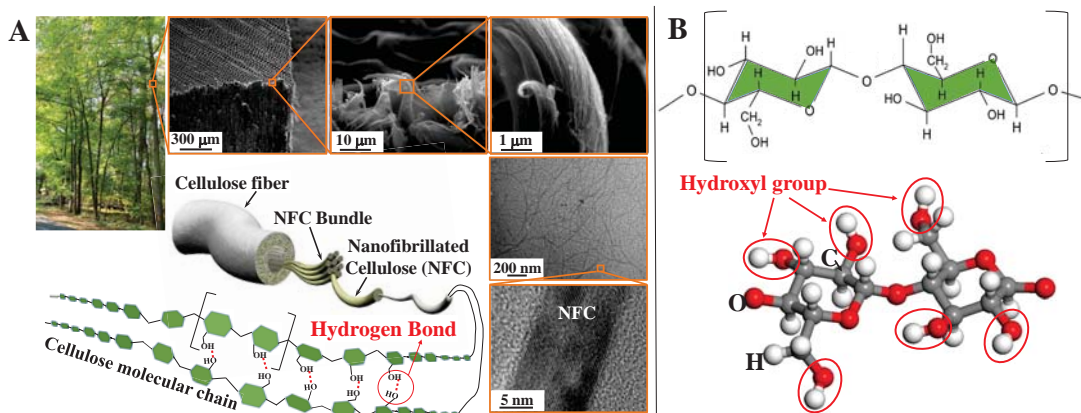


Figure 5.6. (A) Hierarchical structure of wood fibers and the characteristic of cellulose fibrils. Note the rich inter-chain hydrogen bonds among neighboring cellulose molecular chains. (B) Atomic structure of a cellulose chain repeat unit. Note the six hydroxyl groups (red circles) in each repeat unit.

In this study, cellulose fibers of different mean diameters (27 μm (native fiber), 28 nm, and 11 nm, respectively) are isolated from wood cell walls using a top-down approach and characterized (258). Cellulose nanopaper is made of a highly entangled random network of NFC fibers (Fig. 5.7A). Regular paper made of 27 μm native cellulose fibers with the same mass per area as the nanopaper is also fabricated as the control. The mechanical properties of both the cellulose nanopaper and regular paper are measured according to ASTM Standard D638 (details in (258)). Figure 5.7B shows the typical tensile stress-strain curves of cellulose nanopaper made of fibers of mean diameters of 11 nm and 28 nm, and that of regular paper made of fibers of mean diameter of 27 μm, respectively. Five samples of each mean fiber diameter are tested and the resulting stress-strain curves are consistent. The stress-strain curve of cellulose nanopaper made of 20 nm fibers in Ref. (259) is also plotted in Fig. 5.7B.

Table 5.2 lists the mechanical properties of the cellulose nanopaper and regular paper measured from the stress-strain curves: ultimate tensile strength (measured by the maximum stress that the paper can sustain before fracture), toughness (work to fracture, measured by the area under a stress-strain curve), and tensile strain at fracture, for mean fiber diameter of 11 nm, 20 nm, 28 nm, and 27 μm , respectively. The mean value and standard deviation of each property for each mean fiber diameter are calculated from the measurement of five samples.

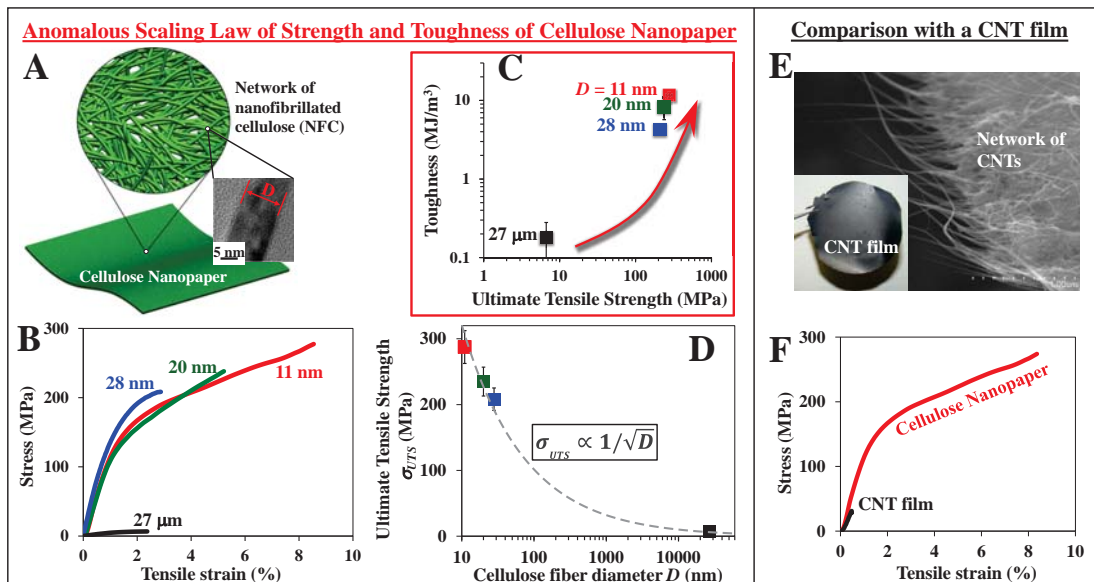


Figure 5.7. An anomalous scaling law of strength and toughness of cellulose nanopaper. (A) Schematic of cellulose nanopaper, made of a random network of NFC fibers. Inset shows the HRTEM image of a ~ 11 nm NFC fiber. (B) Stress-strain curves of cellulose paper made of cellulose fibers of various mean diameters. As the cellulose fiber diameter decreases from μm scale to nm scale, both tensile strength and ductility of the cellulose paper increases significantly, leading to an anomalous scaling law shown in (C): The smaller, the stronger AND the tougher. (D) further reveals that the ultimate tensile strength scales inversely with the square root of cellulose fiber diameter. (E) Optical (inset) and SEM images of a CNT film made of network of CNTs. (F) Lack of inter-CNT hydrogen bonds, the CNT film has a much lower tensile strength and toughness than the cellulose nanopaper, although the constituent CNT bundles and NFC fibers have comparable diameter (11 nm).

Figure 5.7C shows the ultimate tensile strength and toughness of the cellulose nanopaper and regular paper for four different mean diameters of cellulose fibers.

Surprisingly, as cellulose fiber diameter decreases, both the ultimate tensile strength and toughness of the cellulose paper increase dramatically. As the mean fiber diameter decreases from 27 μm to 11 nm, the ultimate tensile strength increases more than 40 times from 6.7 MPa (regular paper) to 275.2 MPa (11 nm nanopaper), the toughness increases nearly 130 times from 0.13 MJ/m³ (regular paper) to 11.68 MJ/m³ (11 nm nanopaper). Further measurements of the fracture toughness (resistance to crack propagation) of the cellulose paper reveals the similar trend: the fracture toughness increases more than 10 times (from 143.3 J/m² to 1481.4 J/m²) as the mean cellulose fiber diameter decreases from 27 μm to 11 nm (258). The increased toughness is a result of increased ultimate tensile strength and failure strain with decreasing fiber diameters, as evident in Fig. 5.7B. In other words, by tuning the constituent fiber diameter, we demonstrate an anomalous scaling law of mechanical properties of cellulose nanopaper: The smaller, the stronger and the tougher. There is no tradeoff between tensile strength and toughness, a highly desirable feature in advanced material design.

Table 5.2. Mechanical properties for paper made from cellulose fibers with different diameters

Mean Fiber Diameter (nm)	Ultimate Tensile Strength (MPa)	Toughness (MJ/m ³)	Tensile Strain at Fracture (%)	Density (g/cm ³)	Specific Strength (MPa/g/cm ³)
11	275.2±25	16.9±1	8.5±0.5	1.2	229.2±21
20 ⁽²⁵⁹⁾	235.0±21	7.26±2.6	5.2±1.2	/	/
28	208.3±17	4.3±0.2	2.9±0.1	1.2	173.6±14
27,000	6.7±0.7	0.13±0.1	2.4±0.1	0.8	8.3±0.9

Figure 5.7C shows the tensile strength of cellulose paper as a function of the mean fiber diameter, and clearly depicts the scaling law of “The smaller, the stronger”, which can be attributed to the reduced intrinsic defect size in constituent cellulose fibers as their diameter decreases, as justified below.

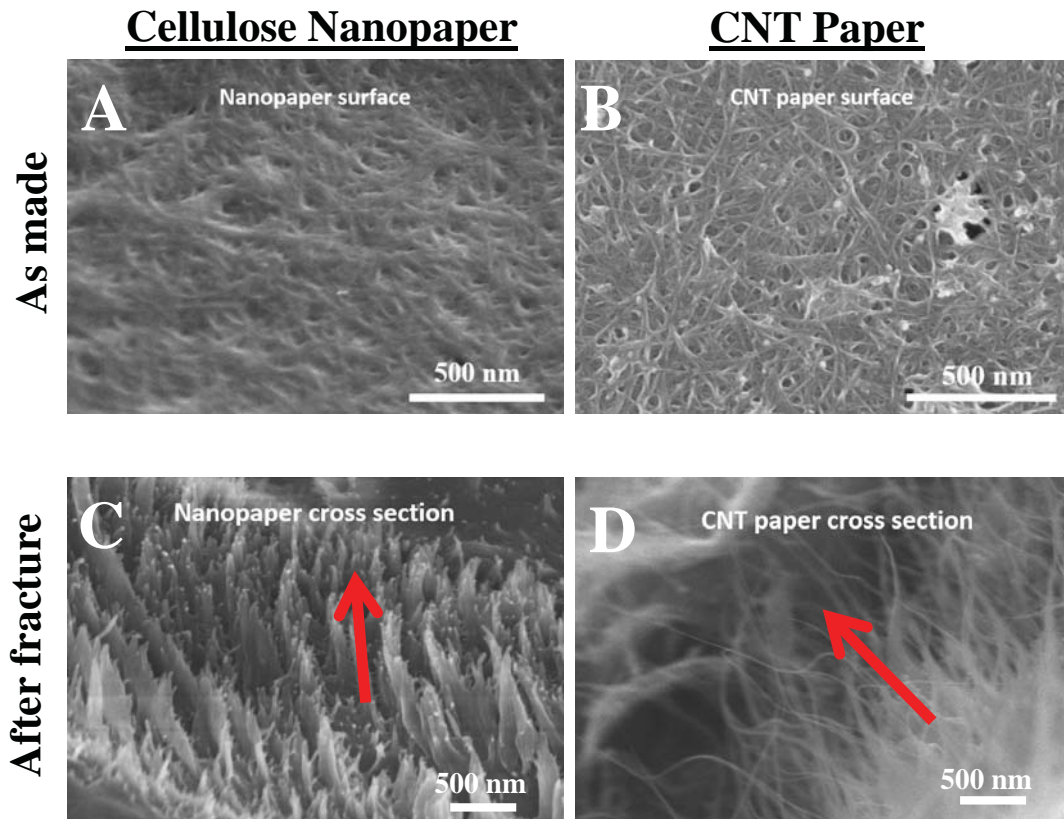


Figure 5.8. SEM images of (A) the surface of the as-made cellulose nanopaper (with a mean diameter of NFC fibers of 28 nm) and (B) the surface of the as-made CNT paper, both showing random distribution of constituent fibers. (C and D) SEM images of the cross-section of failure of the cellulose nanopaper and CNT paper, respectively, after the tensile tests. In both C and D, it is evident that the initially random network of constituent fibers aligns along the tensile loading direction indicated by the arrows.

Under tension, the initially entangled random cellulose fiber network deflects and twists to align parallel to the tensile direction. As the tensile load increases, the straightened cellulose fibers begin to fracture, resulting in an overall failure of the paper. This failure mechanism is supported by the SEM observation of the fractured

cross section of test samples, showing the NFC fibers are aligned with the tensile loading direction at failure (Fig. 5.8). In this sense, the failure stress of an individual cellulose fiber gives a reasonable estimate of the overall tensile strength of nanopaper. A theoretical fracture mechanics model (258) predicts that the ultimate tensile strength of the cellulose nanopaper $\sigma_{UTS} \propto 1/\sqrt{D}$, with D being the mean fiber diameter. Figure 5.7D demonstrates excellent agreement between such a theoretical prediction and experimental measurement (from two independent sources: present study and Ref. (259)) of the dependence of σ_{UTS} of cellulose nanopaper and regular paper on constituent fiber diameter over three orders of magnitude, and thus offers strong evidence of the above mechanistic understanding of the scaling law of tensile strength of cellulose nanopaper.

To further shed insight on the anomalous scaling law of strength and toughness of the cellulose nanopaper, we also fabricate single-walled CNT (SWCNT) films with a thickness of 20 μm using the same filtration and drying method as in cellulose nanopaper fabrication. The mean diameter of the constituent SWCNT bundles is 11 nm, comparable to that of the NFC fibers in our strongest and toughest cellulose nanopaper. Tensile test of the SWCNT films is executed under the same conditions as for the cellulose nanopaper. The fractured cross-section of the SWCNT film after the tensile test is examined with SEM (Fig. 5.7E). The initially random network of SWCNTs aligns parallel to the loading direction prior to fracture, suggesting the similar deformation/failure mechanism as that of the cellulose nanopaper (Fig. 5.8). By contrast, the comparison of the stress-strain curves of the SWCNT film and cellulose nanopaper reveals significant difference. Despite of the exceptional mechanical

properties of individual SWCNTs (e.g., with a tensile strength of ~ 100 GPa), the SWCNT film yields a tensile strength of 31 MPa, and a toughness of 0.06 MJ/m^3 , consistent with the data reported in literature (260) but drastically lower (9 times and 195 times, respectively) than those of our cellulose nanopaper made of 11 nm NFC fibers.

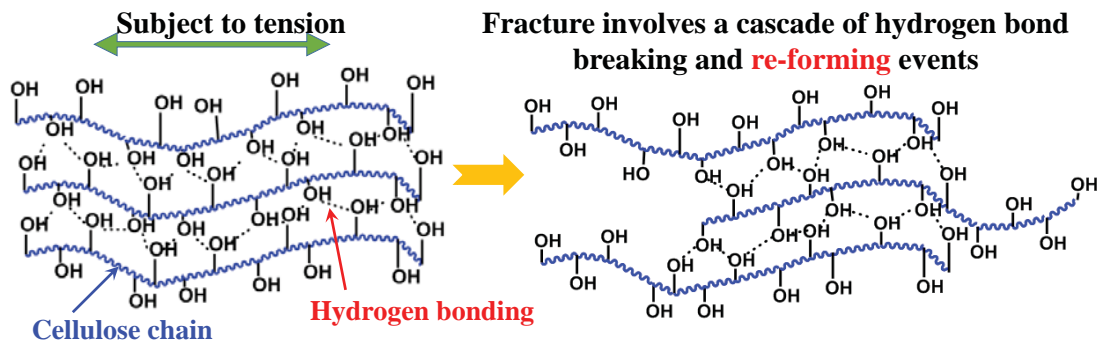


Figure 5.9. Envisioned molecular-level toughening mechanism of cellulose nanopaper: Failure involves a cascade of hydrogen bond forming, breaking and re-forming events, which dissipate a significant amount of energy, thus lead to much enhanced fracture toughness of cellulose nanopaper.

Based on the above results, we envision the following mechanistic understanding on the exceptional mechanical properties and anomalous scaling law of cellulose nanopaper: while the increase in tensile strength of cellulose nanopaper is attributed to reduced defect size as the constituent NFC fiber size decreases (the smaller, the stronger); the simultaneous increase in toughness essentially results from the significant increase of strong hydrogen bonding among NFC fibers as their diameter decreases (and thus their surface area increases). Figure 5.9 further clarifies the envisioned molecular-level toughening mechanism of cellulose nanopaper. Under tension, the initially entangled NFC network deflects and twists to align parallel to the tensile direction. As the load increases, the straightened NFC fibers begin to slide

relatively to each other, and the pulling-off and fracture of such fibers eventually lead to the overall failure of the nanopaper. Unlike covalent bonding, hydrogen bonding between hydroxyl groups readily re-forms after bond breaking due to inter-fiber sliding. If a cellulose fiber fractures under tension, the fractured segments remain bonded to neighboring fibers. In other words, mechanical failure of nanopaper involves both fiber fracture and a cascade of hydrogen bond breaking and re-forming events (as illustrated in Fig. 5.9), which dissipate a significant amount of energy, and thus result in much enhanced fracture toughness. By contrast, a SWCNT film lacks such a mechanism. Bonding between SWCNTs in the film is essentially van der Waals (vdW) forces, which are much weaker than the hydrogen bonding between hydroxyl groups in the cellulose nanopaper. Therefore, pulling out a SWCNT from the film dissipates much less energy than pulling out a NFC fiber from the cellulose nanopaper, which explains the significantly lower toughness and tensile strength of the SWCNT film compared with the cellulose nanopaper. To confirm the above envisioned mechanistic understanding, we then carry out atomistic modeling to simulate the key deformation and failure process in both cellulose nanopaper and SWCNT films.

5.2.1.3. Mechanistic understanding of the anomalous scaling law of cellulose nanopaper: A molecular dynamics study

Figure 5.10 illustrates the hydrogen bond breaking and re-forming process by a model that is representative of the molecular-level deformation events in a cellulose nanopaper under tension. A cellulose bundle contains seven cellulose chains (each with

4 repeat units) that are packed in a pattern as in cellulose crystal so that one cellulose chain is completely surrounded by other six chains (Fig. 5.10A).

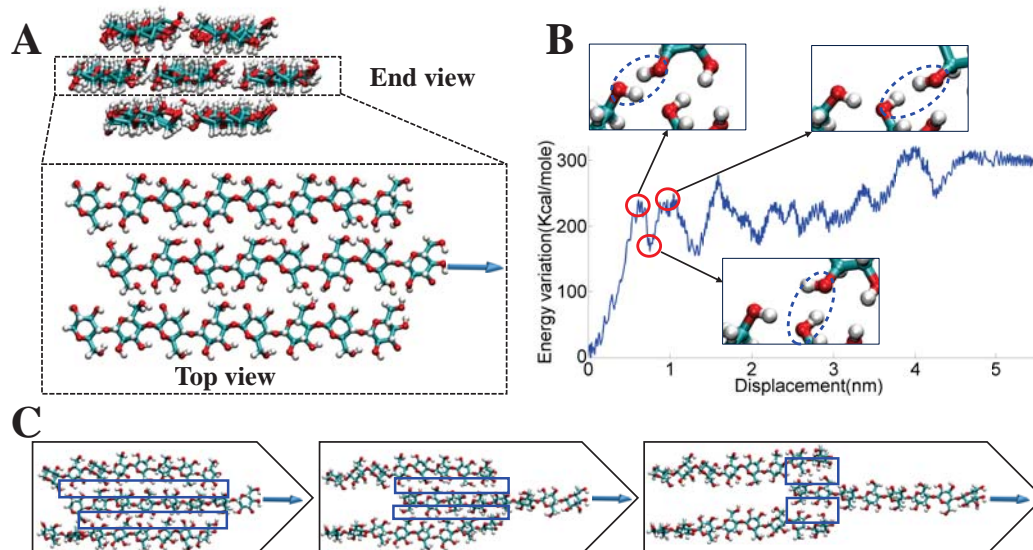


Figure 5.10. Atomistic simulations to demonstrate the hydrogen bond breaking and re-forming events among cellulose molecular chains. (A) Simulation model of a cellulose bundle contains seven cellulose molecular chains. Top view only shows the middle three chains for visual clarity. (B) Variation of total potential energy as a function of the sliding displacement of the center cellulose chain out of the bundle. Insets clearly show the hydrogen bond breaking and re-forming events (dotted circles), each of which dissipates energy. (C) illustrates relative cellulose chain sliding, during which a series of hydrogen bond breaking and re-forming events happen when neighboring hydroxyl groups come close to each other. The boxed region shows the evolution of newly formed hydrogen bonding region during pulling-out process. Only middle three chains are shown for visual clarity.

We simulate the pulling out of the center chain from the bundle by applying a constant velocity on the right end of the center chain. Figure 5.10B plots the variation of the total potential energy of the simulation model as a function of the pulling-out displacement, which clearly shows a zigzag fluctuation profile. The insets in Fig. 5.10B reveal that the zigzag energy fluctuation captures the hydrogen bond breaking and re-forming events: the potential energy ramps up to a local maximum (e.g., first peak in Fig. 5.10B) as the hydrogen bond stretches to the most, followed by a sudden drop of the potential energy to a local minimum (the first trough), which corresponds to the

hydrogen bond with constant velocity on the right end of the breaking and hydroxyl groups relocating to a new bonding site. The potential energy then ramps up again and reaches next local maximum, indicating the newly formed hydrogen bond stretches to the most. The above events repeat until the center chain is completely pulled out of the bundle. Figure 5.10C illustrates relative cellulose chain sliding, during which a series of hydrogen bond breaking and re-forming events happen when neighboring hydroxyl groups come close to each other. The boxed region shows the evolution of newly formed hydrogen bonding region during the pulling-out process. We believe that the combination of collective strength of massive hydrogen bonds and the repeated energy dissipation that is needed to completely separate two cellulose bundle surface (after a major series of hydrogen bond breaking and re-forming events) renders the anomalous scaling law of the mechanical properties of cellulose nanopaper, which is further supported by molecular dynamics simulation of the fiber-scale deformation process in cellulose nanopaper and SWCNT films, as detailed below.

The deformation of cellulose nanopaper (or a SWCNT film) under tension is accommodated by the relative sliding between neighboring NFC fibers (or CNT bundles). Such a relative sliding can be decomposed into two sliding modes: parallel sliding and perpendicular sliding. Note that the surface area in direct contact in two neighboring fibers (e.g., within the range of effective hydrogen bonding formation or vdW interaction) is often only a small portion of the whole fiber surface. Under such a consideration, Fig. 5.11A shows the simulation model of the two surface areas in direct contact for parallel sliding between two NFC fibers (Fig. 5.12), each of which consists of an array of 6 by 3 cellulose chains, with 7 and 14 repeat units (i.e., 7.7 nm and 15.4

nm) in each chain, and that between two SWCNT bundles, each of which consists of 3 (15, 0) SWCNTs, with length of 7.8 nm and 15.7 nm, respectively.

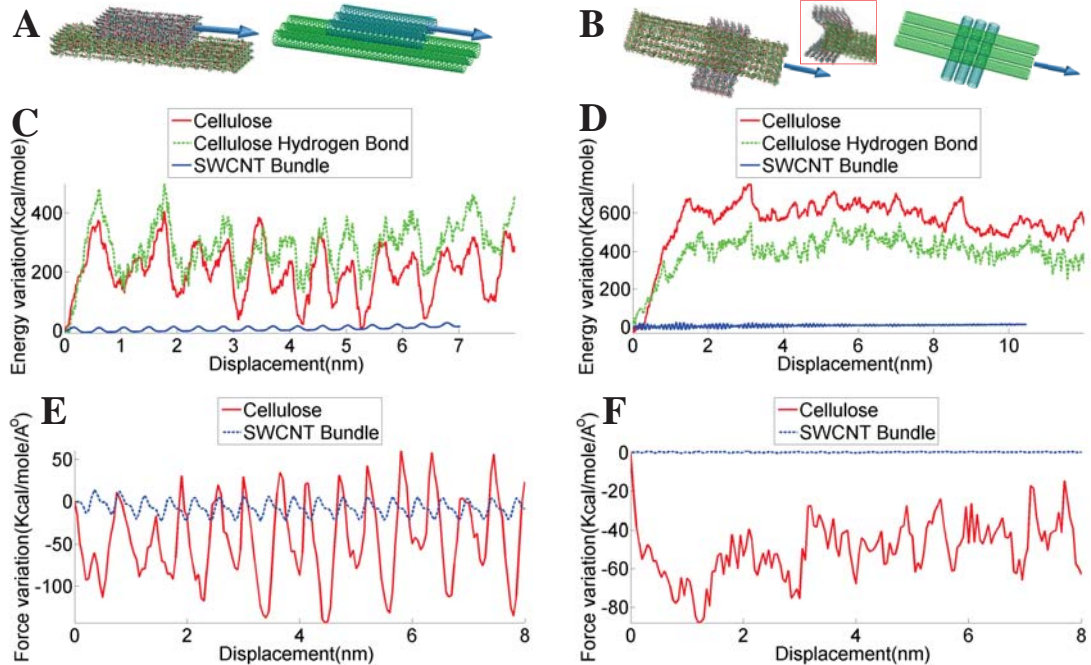


Figure 5.11. (A) Simulation models of the two surface areas in direct contact for parallel sliding between two NFC fibers (top panel) and that between two SWCNT bundles (bottom panel). (C) Variation of total potential energy as a function of relative displacement of parallel sliding between two NFC fibers (green) and that between two SWCNT bundles (blue). The contribution from hydrogen bonds between NFC fibers (red) is included for comparison. (E) The evolution of resistant force during parallel sliding of two neighboring NFC fibers (red) and two neighboring SWCNT bundles (blue). (B), (D) and (F): The results for the case of perpendicular sliding, in correspondence to A., C. and E., respectively.

Figure 5.11B shows the corresponding simulations models for perpendicular sliding between two NFC fibers and that between two SWCNT bundles. Figure 5.11C plots the variation of total potential energy as a function of relative displacement of parallel sliding between two NFC fibers and that between two SWCNT bundles. For the case of NFC fibers, zigzag fluctuation of potential energy is of substantial amplitude. Each peak in the curve corresponds to an energy barrier that the external load needs to overcome (i.e., work done by the load) to drive the relative sliding between neighboring

NFC fibers. The variation of total hydrogen bonding energy is also plotted in Fig. 5.11C for comparison, which matches well with that of the total potential energy in terms of both peak location and amplitude, offering strong evidence for the cascade of events of hydrogen bond breaking and re-forming during the sliding process and the dominant role of hydrogen bonding in the toughening mechanism of cellulose nanopaper. In other words, the sum of all the work associated with the repeated breaking and re-forming of strong hydrogen bonds among neighboring NFC fibers before final failure essentially dominates the toughness of the cellulose nanopaper. Therefore, the scaling law of “The smaller, the tougher” can be readily understood by the fact that the contact area between neighboring NFC fibers (thus the total number of hydrogen bonds) increases significantly as the diameter of NFC fibers decreases.

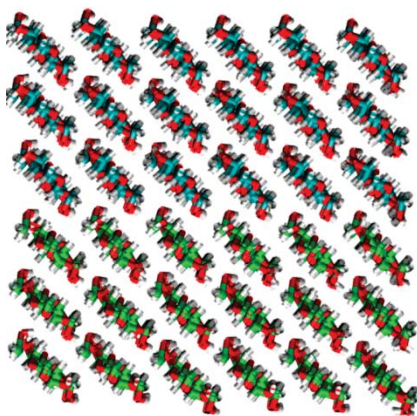


Figure 5.12. Cross-section view of the interface between two neighboring NFCs in Fig. 5.11. The contact surface is along (110) plane of the I β cellulose nanocrystal structure.

By contrast, for the case of SWCNT bundles, the potential energy variation is of much smaller amplitude. The regular wavy profile (with a period of ~ 4.38 Å) suggests that the energy variation corresponds to the periodic shift of atomic stacking (with a period of 4.26 Å) between the two neighboring SWCNT bundle. Parallel sliding between

neighboring SWCNT bundles dissipates much less energy than that between two NFC fibers.

Figure 5.11D plots the variation of the total potential energy as a function of relative displacement of perpendicular sliding between two NFC fibers and that between two SWCNT bundles. In perpendicular sliding mode, the difference between the two cases becomes even more drastic. For the case of NFC fibers, there is first a significant increase in the total potential energy, followed by the zigzag nature of the energy fluctuation similar to that in parallel sliding mode. The initial significant increase in total potential energy results from the severe bending of the bottom NFC fiber (see inset of Fig. 5.11B). Such a severe bending further confirms the strong hydrogen bonding between the two NFC fibers, a feature not existing in the SWCNT bundle case, where both SWCNT bundles remain nearly undeformed during sliding process. The severe bending of NFC fibers before perpendicular sliding occurs also contributes additional external work required to completely separate two perpendicular NFC fibers. The collective effect of these deformation features at individual NFC fiber scale leads to significant enhancement of both fracture strain and toughness of the cellulose nanopaper. On the other hand, for the case of SWCNT bundles, the variation of total potential energy is nearly negligible, which can be attributed to further reduced contact area and even weaker vdW interaction in lack of commensurate stacking between two perpendicular SWCNTs.

Figure 5.11E and 5.11F plot the evolution of resistant force when two neighboring NFC fibers (and two neighboring SWCNT bundles) slide in parallel and perpendicularly to

each other, respectively. In both sliding modes, the magnitude of resistant force in NFC fiber case is substantially higher than that in the SWCNT case, shedding light on molecular scale understanding of the huge difference in tensile strength between cellulose nanopaper and SWCNT films.

The full atomistic simulations uses the ReaxFF potential (261) as implemented in the LAMMPS (Large-scale Atomic/Molecular Massively Parallel Simulator) (79) simulation package, developed for carbon-carbon interactions and hydrocarbon oxidation. ReaxFF force field was developed via first principle and is also able to account for various non-bonded interactions including an explicit energy expression for hydrogen bonds. The simulations were subjected to a canonical ensemble, carried out at a temperature of 5K, for the purpose of suppressing thermal noise to clearly reveal the fine feature of the hydrogen bond stick-slip event. The time step is set to 0.5 femtoseconds (fs). The energy data points were sampled on every 200 time steps while the force data points were sampled on every 1000 time steps. For simulations in Fig. 5.10, the carbon atoms on the very left end (in the side view) of the six surrounding NFC chains are confined to only have the degree of freedom perpendicular to the pulling direction of the central NFC chain, the pulling of which is enabled by pulling the carbon atom with a velocity of 0.001 \AA/fs along the pulling direction is applied. For Fig. 5.11A, the pulling is applied to the ends of the longer NFC fiber (or SWCNT bundle) while the ends of the shorter NFC fiber (or SWCNT bundle) are hold still. For Fig. 5.11B, the pulling is applied to the ends of the longer NFC fiber (or SWCNT bundle). The force is calculated by summing up the force component along the sliding direction of all of the atoms in the shorter NFC fiber (or SWCNT bundle).

For simulations in Fig. 5.11, a half I β cellulose nanocrystal structure (consisting 18 cellulose chains) is used for each of the top and the bottom NFCs. The contact surface is along (110) plane (Fig. 5.12).

5.2.1.4. Concluding remarks

We rationally design and fabricate cellulose nanopaper by tuning the diameter of constituent cellulose fibers, which allows for the first-of-its-kind investigation of the size dependence of mechanical properties of cellulose nanopaper. Surprisingly, we find that both the ultimate tensile strength and toughness of the cellulose nanopaper increase significantly as the constituent cellulose fiber diameter decreases, suggesting an anomalous but highly desirable scaling law of mechanical properties: The smaller, the stronger and the tougher. The increase in tensile strength of cellulose nanopaper is attributed to reduced intrinsic defect size as the constituent cellulose fiber size decreases. A fracture mechanics model predicts that the tensile strength of cellulose nanopaper inversely scales with the square root of cellulose fiber diameter, in excellent agreement with experimental measurement over three orders of magnitude of fiber diameter. The simultaneous increase in toughness essentially results from the significant increase of strong hydrogen bonding among cellulose fibers as their diameter decreases. Further atomistic simulations reveal the key mechanism underlying this unconventional scaling law of mechanical properties: rich hydroxyl groups along cellulose molecular chains allow for facile formation and re-formation of strong hydrogen bonding among neighboring molecular chains, which in turn dictate significantly enhanced resistance force and energy dissipation during inter-cellulose

fiber sliding, and thus lead to both high tensile strength and toughness of the cellulose nanopaper. Such mechanistic understanding is further supported by control experiment, in which films made of SWCNT bundles of diameter comparable to that of cellulose fibers are shown to have drastically lower tensile strength and toughness, essentially due to rather weak vdW type interactions in lieu of strong hydrogen bonding among building blocks.

The findings from the present study shed fundamental insight on the long-sought strategy addressing the conflict of strength versus toughness in engineering material design by envisioning a bottom-up design strategy to achieve both high strength and toughness that is generally applicable for a wide range of other material building blocks. The opportunities are abundant and multi-faceted. There exist a wide variety of other biodegradable cellulose fibers and man-made fibers, with rich features in morphology, length, topology, crystallinity, and surface groups that can be further leveraged to enable both strong and tough cellulose based materials under the same bottom-up design strategy (262-266). It is well established that functional groups can be introduced to the surface and ends of CNTs (267-269). Properly functionalized CNTs (e.g., with carboxyl groups) can enable strong inter-CNT bonding and smaller CNT bundle size, holding promise toward strong and tough CNT films, another long-sought solution in nanocarbon-based materials. The fundamental bottom-up strategy can essentially go beyond one-dimensional (1D) building blocks (tubes, wires, filaments) toward two-dimensional (2D) building blocks (e.g., atomic layers of graphene oxide (GO), boron nitride and molybdenum disulfide) and 1D/2D hybrids. As a demonstration, in next section, we show that hybrid microfibers containing well

aligned and mixed 2D GO sheets and 1D NFC fibers are both much stronger and tougher than the microfibers made of pure GO sheets or NFC fibers, due to synergistic enhancement of bonding between GO and NFC fibers (270).

5.2.2. Hybridizing cellulose and graphene oxide toward strong and tough fibers

5.2.2.1. Motivation

Strong synthetic fibers such as carbon fibers play an important role in a range of applications from aircraft to wind turbine blades. However, these fibers are expensive and demonstrate limited performance. Nanofibrillated cellulose (NFC), derived mainly from wood, is an inexhaustible one-dimensional (1D) material with a diameter in the nanoscale and a length in the microscale (271). This material has been explored as a possible building block for high strength composites due to its impressive mechanical properties with an elastic modulus of approximately 140 GPa (248, 272). In addition, NFC possesses high specific area and strong interacting surface hydroxyls, and thus it can act as an excellent reinforcement/binder (273-276). Meanwhile, chemically exfoliated two-dimensional (2D) graphene oxide (GO) nanosheets demonstrate excellent mechanical properties, a high aspect ratio, and good processibility, making it another attractive building block to produce strong macroscale fibers (277, 278). There are a large amount of hydroxyl and epoxide functional groups on the GO nanosheet basal planes as well as carboxyl groups located at the edges that provide strong bonding sites and allow the GO nanosheets to be well-dispersed in water (279). Transforming 2D GO nanosheets into strong and highly ordered microfibers is a promising feat (278, 280-284). Efforts have been made to improve the mechanical properties of GO-based

microfibers by chemical cross-linking and polymer coating as well as through giant GO nanosheets (285-287). The best performing GO microfibers exhibit a tensile strength of 442 MPa and an elastic modulus of 47 GPa respectively (283, 284). The performance needs to be further improved, especially the mechanical strength (288).

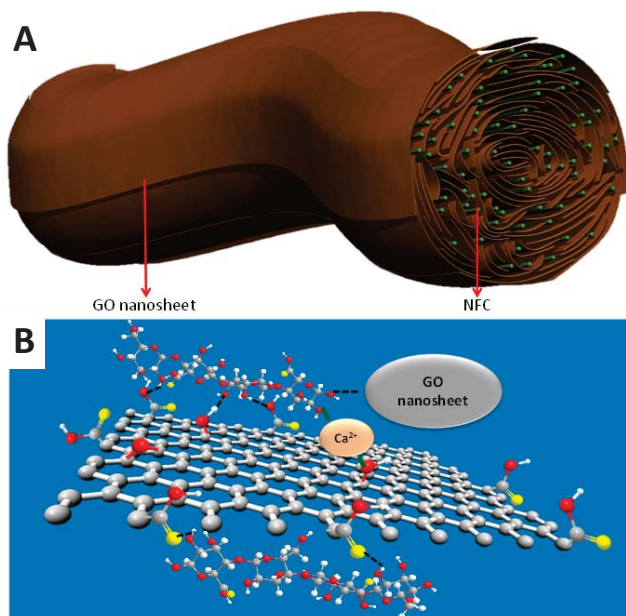


Figure 5.13. (A) Schematic of a GO-NFC hybrid microfiber consisting of aligned GO nanosheets and NFC chains along the microfiber direction. The synergistic interaction between NFC and GO leads to greatly improved mechanical strength, elastic modulus and toughness. (B) Structural representation of how metal ion (Ca^{2+}) infiltration further increases the bonding between building blocks in the hybrid microfiber.

Here we design and investigate microsized fibers by hybridizing GO and NFC. Great synergistic interactions between GO and NFC are identified, which led to noticeable improvements in the mechanical properties of these microfibers compared to microfibers made solely from one of the two building blocks. The underlying hypothesis is that, NFC enhances the bonding between the GO nanosheets which is similar to how larger GO nanosheets create a bridge between the neighboring NFC chains. Molecular dynamics simulations clearly verify such a hypothesis and

demonstrate that this synergistic interaction can enhance both the tensile strength and toughness of the microfibers. The synergistic interaction between 1D NFC and 2D GO revealed in this study is also applicable to other material building blocks facilitating a new design strategy to create a wide range of mechanically strong microfibers. Figure 5.13 shows the structure of the GO-NFC hybrid microfibers produced in this study. In the hybrid microfiber, the GO nanosheets and NFC chains align along the direction of the microfiber. Metal ions (Ca^{2+}) link the NFC and GO nanosheets together to further enhance the tensile strength of the hybrid microfiber.

5.2.2.2. Strong and tough fibers made from graphene oxide and cellulose

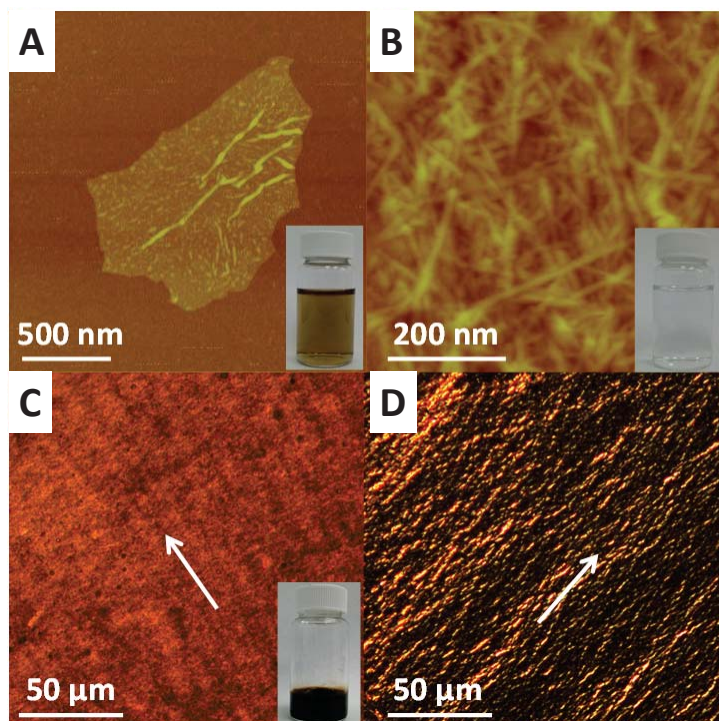


Figure 5.14. (A) AFM image of a GO nanosheet; inset is an optical image of the GO nanosheet solution. (B) AFM image of NFC; inset is an optical image of the NFC solution. (C) Polarized optical microscopy image of the GO-NFC liquid crystal solution showing a typical nematic LC phase; inset is an optical image of the GO-NFC solution used for wet spinning. (D) Polarized optical microscopy image of the GO-NFC solution after drying which shows clear alignment.

The GO nanosheets employed in this study were made using the Hummer's method (289). The lateral size of the GO nanosheet is approximately 1.5 μm as shown in Fig. 5.14A. Characterization of the GO nanosheets by atomic force microscopy (AFM) demonstrated that the average size of the sheets is 1.2 μm . The prepared GO demonstrated good solubility in water (Fig. 5.14A). The diameter of the NFC is approximately 10 nm and the length is 100-400 nm (Fig. 5.14B). TEMPO-oxidized nanocellulose has the unique property to self-assemble and form a chiral nematic phase at an appropriate concentration (290, 291). In our study, the NFC solution forms weak birefringence at a concentration of 1% indicating the onset of ordering (270).

Besides the excellent mechanical properties of the individual building blocks themselves, the alignment and interaction between the building blocks are crucial to achieve superior mechanical properties (292). Alignment is a proven strategy to achieve high strength nanocomposites by providing the maximum packing density with the minimum amount of defects for crack formation and propagation (293). An LCs spinning solution has been proven to create strong and well-aligned fibers (285). Both concentrated NFC and GO suspensions can self-assemble into ordered liquid crystal arrangements (294, 295). Here, we made a nematic LCs spinning solution consisting of GO and NFC (weight ratio of 1:1) at a concentration of 1.1 wt% (Figs. 5.14C-D). When GO and NFC are uniformly mixed together, the solution yields a uniform parallel Schlieren texture that is distinct from pure GO since the width of the aligned bands is thinner than the GO liquid crystals (Fig. 5.14C) (270). After drying, there is substantial alignment depicted in Fig. 5.14D which supports the nematic phase of the spinning solution.

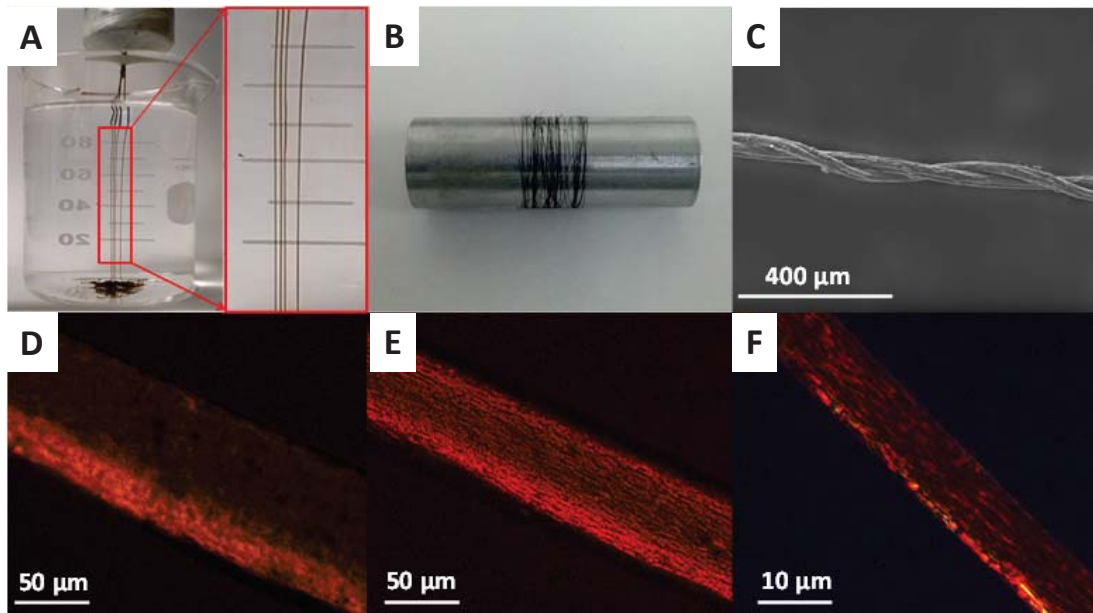


Figure 5.15. (A) Wet spinning process where 4 hybrid microfibers are spun at once. (B) Optical image of fibers from the 1 mL spinning solution wrapped around a 15 cm diameter steel stick. (C) SEM image of two hybrid microfibers twisted together. (D) POM image of a hybrid microfiber after extrusion from a syringe. (E) POM image of a hybrid microfiber that has dried in air for 10 s. (F) POM image of a hybrid microfiber under tension after drying completely in air.

The mechanically strong hybrid microfibers are made by extruding the GO-NFC spinning solution directly into a coagulation of ethanol. A skin is induced by ethanol on the extrudate when the spinning solution is extruded into ethanol and gel microfiber forms. Note that a solvent exchange from water to ethanol occurs in the coagulation bath (266). After the gel fiber is pulled out of the bath, the ethanol evaporates to form a dry hybrid microfiber. Figure 5.15A shows four hybrid microfibers that are made simultaneously by extruding the spinning solution into ethanol. From 1 mL of spinning solution, fibers that are tens of meters long can be produced (Fig. 5.15B). Diameters between 10-40 μm can be created and tuned by changing the syringe needles. The hybrid microfibers are strong and flexible and they can be readily twisted into yarn by hand (Fig. 5.15C).

In order to improve fiber alignment and strength, the hybrid microfibers are dried under tension causing the building blocks to align along the fiber direction. During the drying process, the fiber diameter dramatically decreases from $\sim 80 \mu\text{m}$ to $\sim 10 \mu\text{m}$ while the fiber alignment increases illustrated in the POM, which is a well-known method for fiber alignment evaluation (Figs. 5.15D-F) (296, 297). When the well-aligned hybrid microfiber is set parallel to the polarizer, only a dark image is obtained (270). A vivid fiber appears when the hybrid microfiber is rotated to an angle of 45° with respect to the polarizer (Fig. 5.15F). The differences in texture between Figs. 5.15D-F illustrate the enhanced alignment within the fiber as the drying process progresses.

Figure 5.16A exhibits the typical stress-strain curves for tensile testing GO microfibers, NFC microfibers, and GO-NFC hybrid microfibers. The average ultimate tensile strength (UTS) and elastic modulus of the GO-NFC hybrid microfibers was $274.6 \pm 22.4 \text{ MPa}$ and $20.6 \pm 0.9 \text{ GPa}$, respectively, which are higher than both the NFC microfibers ($139.1 \pm 28.7 \text{ MPa}$, $15.5 \pm 4.5 \text{ GPa}$) as well as the GO microfibers ($84.0 \pm 2.8 \text{ MPa}$, $2.3 \pm 2 \text{ GPa}$) in our study. Even though the mechanical performance of our GO-NFC hybrid microfiber is not superior to the literature, the synergistic effect of improving the mechanical properties of fibers is clearly demonstrated (270).

To improve the mechanical properties of our GO-NFC hybrid microfibers, we utilize metal ions (Ca^{2+}) to introduce ionic bonding between the GO and the NFC by taking advantage of the oxygen and carboxylate groups from these two building blocks. We infiltrate the hybrid microfibers in a 10 wt% CaCl_2 water solution in order to further improve the strength of the fibers. During the infiltration process, the fibers rewet and

swell. Ca^{2+} infiltrates within the fibers and forms ionic bonds with the building blocks after the drying process is complete. Figure 5.16B depicts the typical stress-strain curves when tensile testing GO microfibers, NFC microfibers, and GO-NFC hybrid microfibers after metal ion infiltration. After infiltration, the elastic modulus and the UST of the GO microfibers increase to 9.7 GPa and 96.3 MPa, respectively. The NFC microfibers reach even higher elastic modulus (20.7 GPa) and UST (272 MPa) values. The infiltrated GO-NFC hybrid microfibers possess an elastic modulus of 31.6 ± 2.5 GPa and a UTS of 416.6 ± 25.8 MPa. Our best wet-spun infiltrated GO-NFC hybrid microfibers exhibit an elastic modulus of 34.1 GPa, a UTS of 442.4 MPa, and a tensile failure strain of 2.0%.

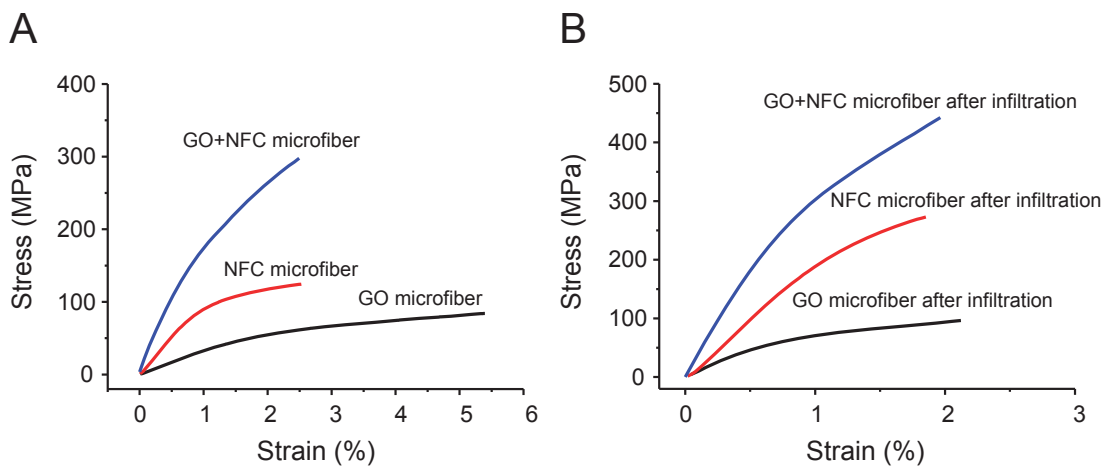


Figure 5.16. Typical stress-strain curves of tensile testing GO microfibers, NFC microfibers, and GO-NFC hybrid microfibers before (A) and after (B) metal ion infiltration.

Based on elastic modulus, our infiltrated GO-NFC hybrid microfibers surpass pure NFC microfibers fabricated with longer lengths and higher aspect ratios (22.5 GPa (266) and 23.6 GPa (298)), LC GO microfibers (about 7.7 GPa) (278), stretched Ca^{2+} infiltrated GO microfibers (6.3 GPa; after chemical reduction, 11.2 GPa) (285), and GO microfibers coagulated from chitosan (22.6 GPa). However, our infiltrated GO-

NFC hybrid microfibers are inferior in elastic modulus to the GO microfibers formed using large GO sheets (47 GPa) (283, 284). Our infiltrated GO-NFC hybrid microfibers possess a high toughness of 4.9 MJ/m³. The tensile strength of the infiltrated GO-NFC hybrid microfibers in this work is higher than wet spun NFC microfibers (275 MPa (266), 402 MPa (298)), LC GO microfibers (about 102 MPa) (278), stretched Ca²⁺ infiltrated GO microfibers (364 MPa) (285), hydrothermally reduced GO microfibers (180 MPa, after annealed at 800 °C: 420 MPa) (299), microfibers prepared from GO nanoribbons (39.3 MPa, after 1050 °C treatment: 383 MPa) (280), and GO microfibers formed using large GO sheets (214 MPa) (284). Comparable tensile strength to our infiltrated hybrid microfiber is exhibited by the GO microfibers prepared from very large GO sheets coagulated from chitosan (442 MPa; the average diameter of the GO sheet is 37 μm (283)). The very large GO sheet size is a basis of better mechanical properties for GO fibers. Our GO nanosheets have an average diameter of ~1.2 μm, which is much smaller than the sheets used by Jalili et al. in their studies (283). We expect that future studies using larger GO sheets will allow us to create even stronger GO-NFC hybrid microfibers.

Infiltrated GO-NFC hybrid microfibers exhibit a much higher elastic modulus and tensile strength compared to GO-only or NFC-only microfibers. To understand the synergistic effect between the GO nanosheets and the NFC, we examine the structural characteristics of different types of fibers since we expect the inter-sheet bonding to have a considerable effect on the fiber morphology.

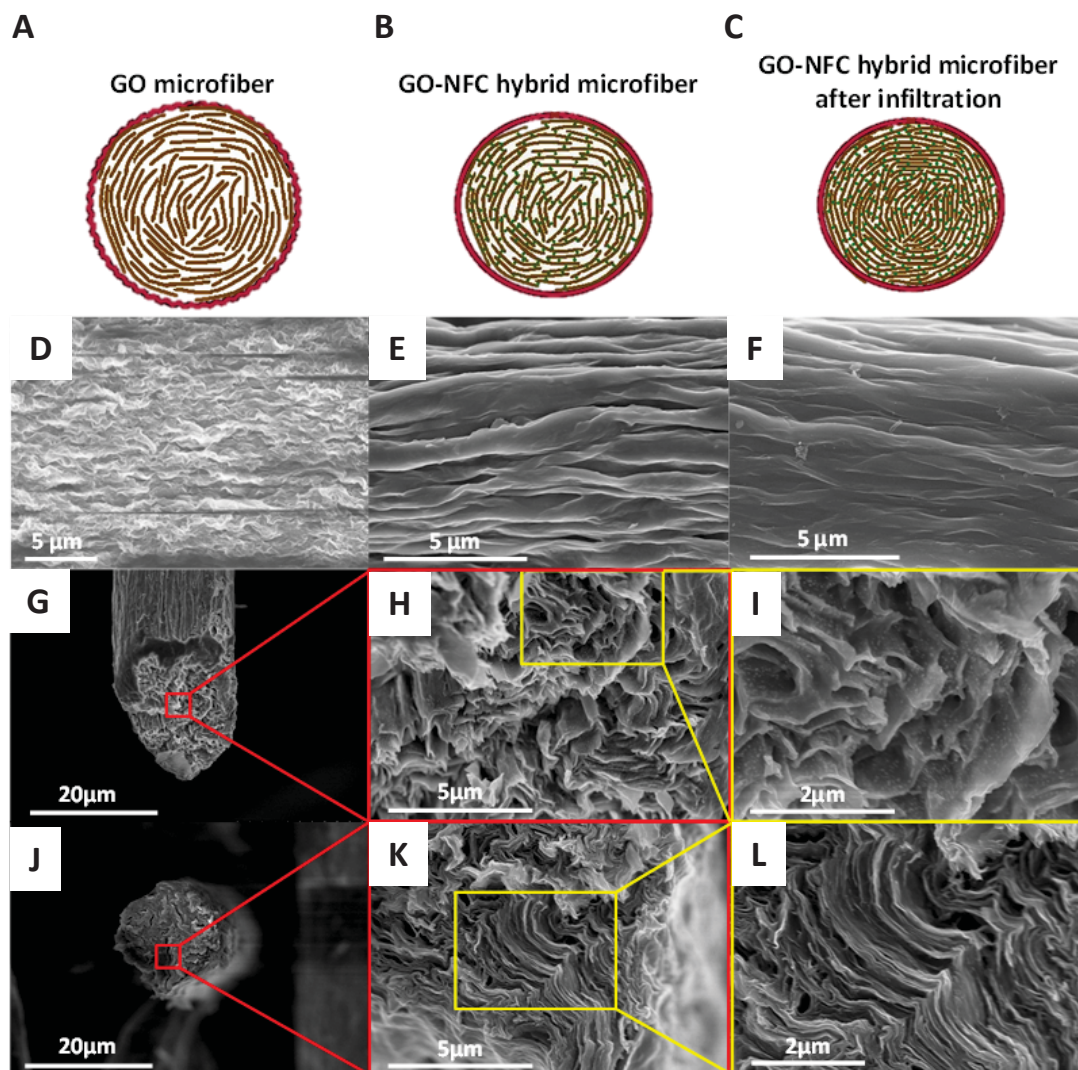


Figure 5.17. Schematics depicting the cross section. (A): GO microfiber. (B): GO-NFC hybrid microfiber. (C): GO-NFC hybrid microfiber after infiltration. The GO microfiber shows a corrugated rough surface and loose GO nanosheet packing. When NFC is added, the GO-NFC hybrid microfiber possesses a smoother surface and a denser building block packing. After infiltration in the 10 wt% CaCl_2 solution, the fiber surface is even smoother and possesses an even denser building block packing compared to the GO-NFC hybrid microfiber. SEM images of the surface morphology. (D): Porous GO microfiber. (E) GO-NFC hybrid microfiber. (F): GO-NFC hybrid microfiber after metal ion infiltration from the CaCl_2 solution. After NFC is added, the surface becomes dense and smooth but after infiltration, the fiber becomes exceptionally dense and smooth. SEM images displaying the cross section of GO-NFC hybrid microfiber. (G-I): Before CaCl_2 infiltration. (J-L): After CaCl_2 infiltration.

After the drying process under tension, the GO-NFC hybrid microfibers demonstrate improved mechanical performance due to the alignment of the NFC along the fiber direction as well as the circularity of the fiber cross section. The addition of the NFC

within the fiber yields a smoother surface and a higher packing density for the non-infiltrated GO-NFC hybrid microfibers. However, due to the infiltration of metal ions, there are further improvements in surface smoothness and packing density for the hybrid microfibers. These conclusions are evident and verified in the schematics shown in Figs. 5.17A-C as well as the characterizations performed using scanning electron microscopy (SEM) (Figs. 5.17D-F). The well-ordered, densely-stacked GO nanosheets in the middle of the fiber cross-section signify good alignment throughout the fiber (Figs. 5.17G-I). We find that metal ion infiltration results in more densely-packed and well-ordered GO nanosheets within the resulting GO-NFC hybrid microfibers (Figs. 5.17J-L). The prior observations suggest that the surface smoothness and packing density are strongly dependent upon the bonding between the GO nanosheets. This directly correlates to enhanced mechanical performance of the resulting GO-NFC hybrid microfibers since the inter-sheet sliding is the dominant microscopic deformation and failure mechanism of these fibers under tension. In other words, when the inter-sheet bonding density is increased, the surface of the fiber will be smoother, there will be a higher packing density, and the GO-NFC hybrid microfibers will be stronger and tougher.

5.2.2.3. Deformation and failure mechanism: A molecular dynamics study

To validate the above hypothesis and gain mechanistic insight into the strength of the GO-NFC hybrid microfibers, we perform systematic molecular dynamics modeling to reveal the fundamental deformation and failure mechanisms of the three types of microfibers fabricated in this study. Given the ultra-strong GO sheets, the tensile failure

of the GO microfibers stemmed from the inter-GO-sheet sliding, instead of the individual GO sheets fracturing. In a pure GO microfiber, hydrogen bonding can form between neighboring GO sheets only when one hydroxyl group from one GO sheet comes in close contact with another hydroxyl group (or oxygen functional group) from another GO sheet (i.e., $-\text{OH}$ to $-\text{OH}$ or $-\text{OH}$ to $-\text{O}-$, Fig. 5.18A). Conversely, in a GO-NFC hybrid microfiber, the abundant hydroxyl groups in NFC can significantly increase the number of hydrogen bonds between the neighboring GO sheets due to the availability of $-\text{O}-$ to $-\text{O}-$ bonding (Fig. 5.18B). Due to the nature of hydrogen bonding, the inter-GO-sheet sliding involves a cascade of formation, breaking, and reformation of hydrogen bonding (Figs. 5.18C-D). Therefore, the hydrogen bond density plays an important role in the mechanical properties of these microfibers (e.g, tensile strength and toughness). To yield quantitative evidence of the effect of hydrogen bond density, we carry out molecular dynamics modeling to simulate the representative inter-GO-sheet sliding events leading up to the tensile failure of a GO microfiber (Fig. 5.18C) and a GO-NFC hybrid microfiber (Fig. 5.18D). Figure 5.18E plots the force needed to drive the inter-GO-sheet sliding as a function of sliding displacement for both fibers. The fluctuation of the two curves reflects the breaking and reformation of the hydrogen bonds as the sliding proceeds. It is evident that significantly increasing the amount of hydrogen bonds from the NFC molecular chains sandwiched in between GO sheets lead to a nearly twofold increase of the peak force that drives the inter-GO-sheet sliding compared to the pure GO sheets.

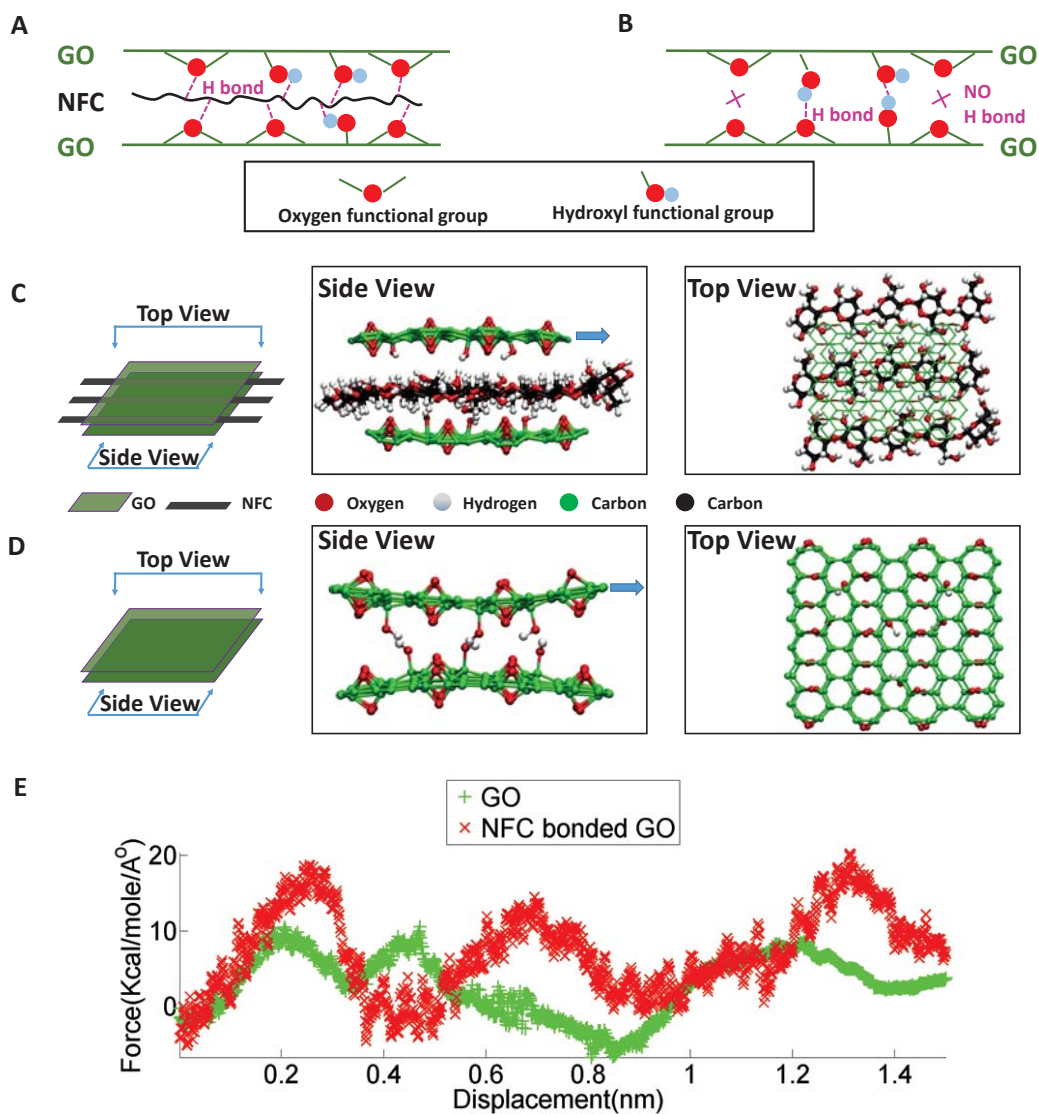


Figure 5.18. (A-B) Schematics showing the role of NFC by providing additional bonding options between GO sheets. (C-D) Molecular dynamics models for GO sheets with and without NFC. Insets show typical equilibrium structural configurations from different perspectives before the top sheet slides. (E) Comparison of the sliding force as a function of sliding displacement between the two cases (i.e. with and without NFC).

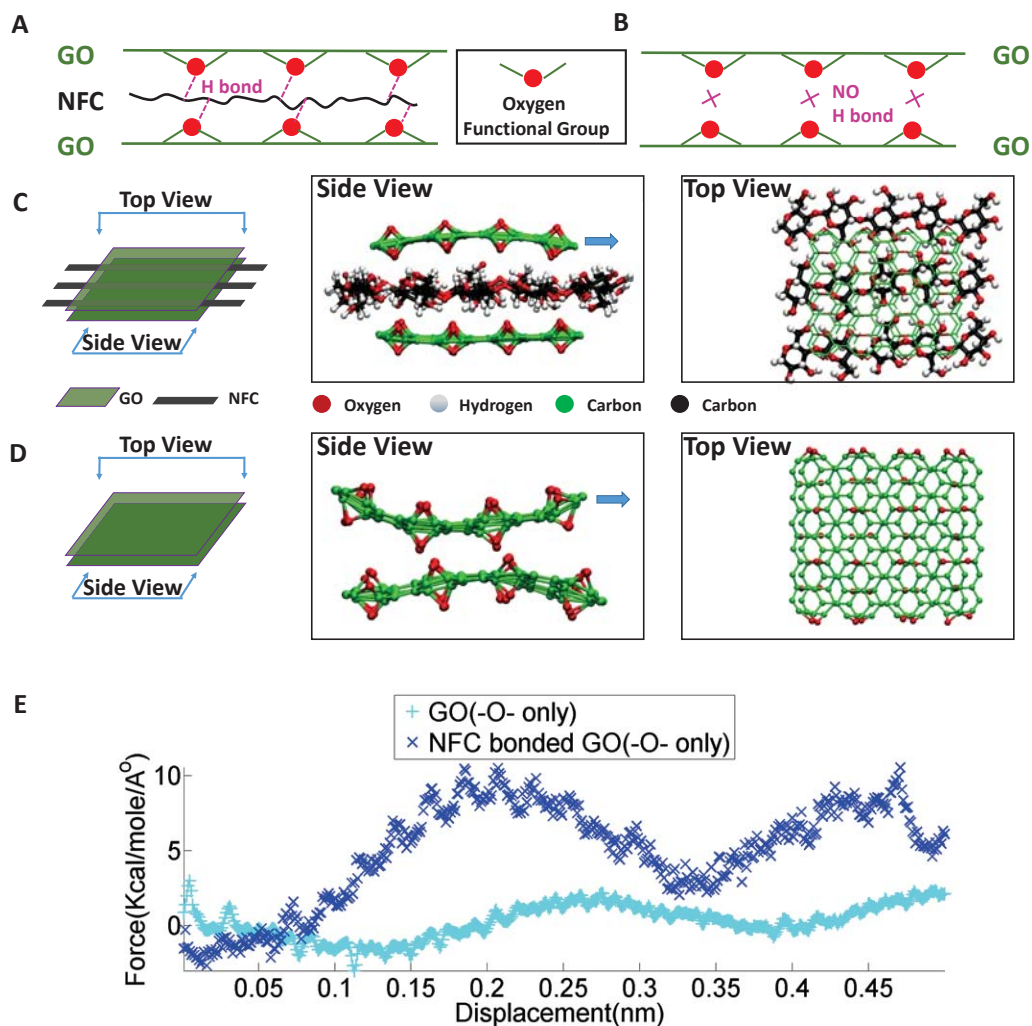


Figure 5.19. (A-B) Schematics show the role NFC plays in providing additional bonding options between the GO sheets (-O- only). (C-D) Molecular dynamics models for GO sheets (-O- only) with and without NFC. Insets show typical equilibrium structural configurations from different perspectives before the top sheet slides. (E) Comparison of the sliding force as a function of sliding displacement between the two cases (i.e. with and without NFC).

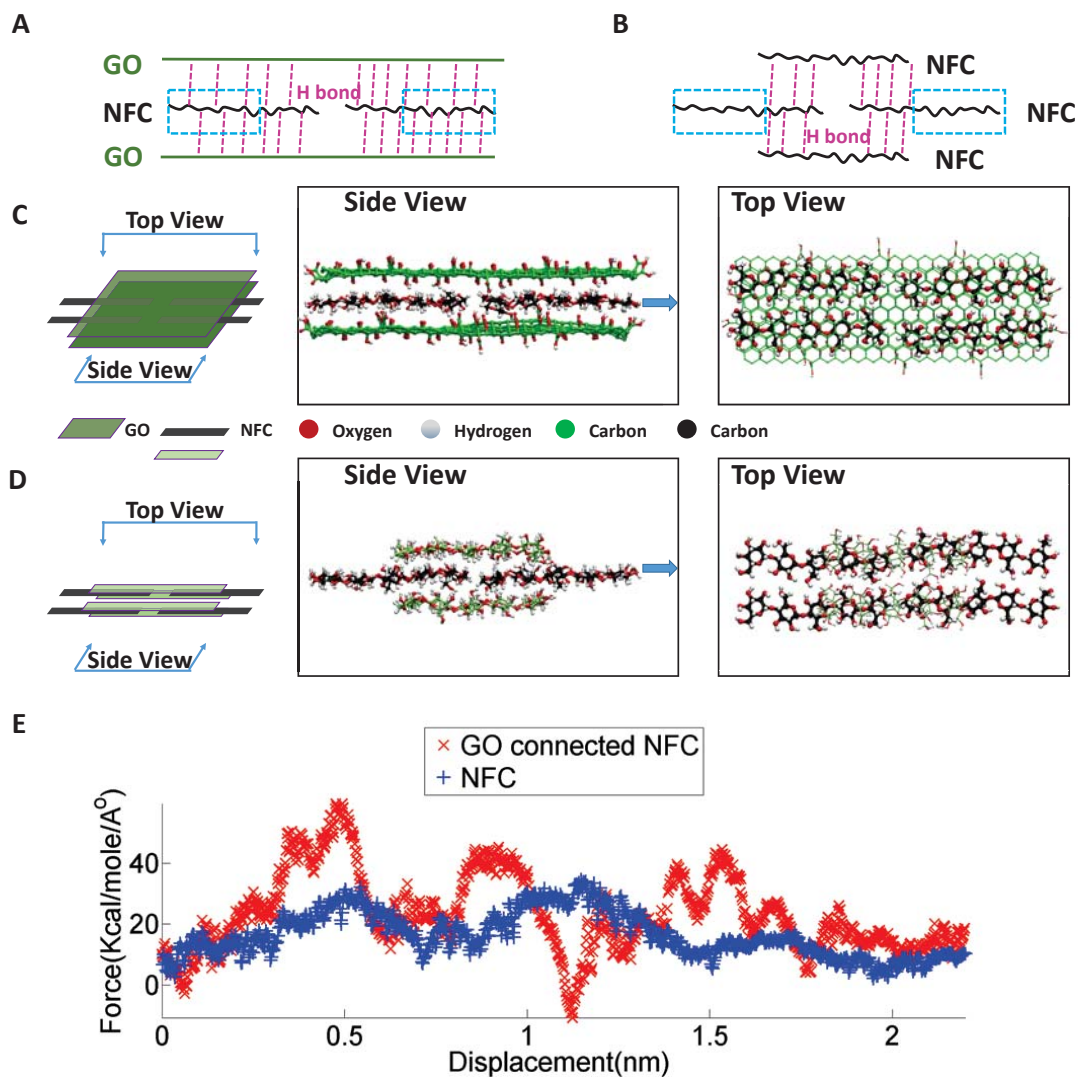


Figure 5.20. (A-B) Schematics demonstrate the role that GO plays by providing additional bonding sites (dashed boxes) between the NFC chains. (C-D) Molecular dynamics models for NFC chains with and without GO nanosheets. Insets show typical equilibrium structural configurations from different perspectives before the right NFC chains slide out. (E) Comparison of the sliding force as a function of sliding displacement between the above two cases.

This increase in peak force which causes hydrogen bond breaking offers a mechanistic understanding of the enhanced tensile strength of the GO-NFC hybrid microfibers relative to the GO microfibers at the atomic-scale. The area underneath the curves in Fig. 5.18E denotes the fracture energy (i.e. the work done by the sliding force) needed to drive the inter-GO-sheet sliding. The increased fracture energy due to NFC providing

a higher hydrogen bond density, as shown in Fig. 5.18E, explains the enhanced fracture toughness exhibited by our GO-NFC hybrid microfibers. Additional simulations (Fig. 5.19) show that such enhancements in the peak force to drive inter-sheet sliding and the associated fracture energy in a GO-NFC hybrid microfiber is even more significant when compared with a GO microfiber in the case of GO nanosheets without hydroxyl groups. The results also suggest that a smoother surface morphology of GO sheets in a GO-NFC hybrid microfiber can facilitate more facile formation of inter-sheet hydrogen bonds via NFC which leads to a microfiber with higher tensile strength and fracture toughness. This agrees with our experimental observations of the GO-NFC hybrid microfiber after CaCl_2 infiltration (Fig. 5.17).

The enhanced mechanical properties of the GO-NFC hybrid microfibers compared to the NFC microfibers can be understood as follows. In our samples, the length of the NFC chains is smaller than the feature size of the GO nanosheets. As a result, in the GO-NFC hybrid microfibers, a GO sheet (2D) can link several NFC chains (1D) together via hydrogen bonding, in both the aligned microfiber direction and in the transverse direction, providing extra bonding sites between NFC chains over a long distance (Figs. 5.20A and C). By contrast, in the NFC microfibers, a rather small length of NFC chains can be linked together via other NFC chains (Figs. 5.20B and D). To further clarify the quantitative effect of the GO sheets, we carry out molecular dynamics simulations of inter-NFC-sliding in these two cases, as illustrated in Figs. 5.20C-D. As shown in Fig. 5.20E, the existence of GO sheets linking together the neighboring NFC chains can effectively increase both the peak force to drive the inter-NFC sliding as well as the associated fracture energy relative to the case of pure NFC

microfibers. These molecular dynamics simulation results offer a mechanistic understanding of the enhanced mechanical properties of the GO-NFC hybrid microfibers compared to the NFC microfibers (Fig. 5.16).

The full atomistic simulations used the ReaxFF potential (261) as implemented in the LAMMPS (Large-scale Atomic/Molecular Massively Parallel Simulator) (79) simulation package, developed for carbon-carbon interactions and hydrocarbon oxidation. A first-principles-based ReaxFF force field was developed and able to account for various non-bonded interactions including an explicit expression for hydrogen bonds (300). For simulations in Fig. 5.18, the carbon atoms on the left and right end of the GO sheet were confined to only have the degree of freedom along the sliding direction. The vertical separation distance between left ends or right ends was fixed to be 0.7 nm (about the typical inter-layer distance between GO sheets) for Fig. 5.18C and 0.8 nm for Fig. 5.18D. The system was equilibrated at 300K in NVT before a constant translational velocity of 0.0002 Å/fs was assigned to the right end of the top GO sheet. The left end of the bottom GO sheet was held in position. The force was calculated by summing up the force components along the sliding direction of all the atoms in the top GO sheet. The simulations in Fig. 5.19 uses the same setup as that in Fig. 5.18. For simulations in Fig. 5.20, the carbon atoms on the sinistral of the left NFC chains were fixed in motion while the carbon atoms on the dextral of the right NFC chains were confined to only have the degree of freedom along the sliding direction. The system was equilibrated at 300K in NVT before a constant translational velocity of 0.0004 Å/fs was assigned to the right end of the dextral NFC chains. The force was calculated by summing up the force components along the sliding direction of all the

atoms in the two dextral NFC chains. In all simulations, the time step was 0.25 fs to ensure the stability of the simulations.

5.2.2.4. Concluding remarks

Well-aligned, strong microfibers were successfully fabricated by wet spinning a liquid crystal solution consisting of 2D GO nanosheets with 1D NFC. The major finding lies in that the well-aligned hybrid microfibers are much stronger than the microfibers composed of 1D NFC or 2D GO alone. Molecular dynamics simulations revealed that the synergetic interaction between the GO and NFC is the key to the enhanced mechanical performance since the introduction of NFC provides extra bonding options between the GO nanosheets similar to the way larger GO nanosheets can bridge neighboring NFC chains. After infiltrating Ca^{2+} within the GO-NFC hybrid microfibers, improvements in mechanical performance were exhibited, specifically fibers with a UTS and an elastic modulus of 442.4 MPa and 34.1 GPa, respectively. This high strength can be explained by the superior alignment within the fiber and by the increase in bonding density. Note that the infiltrated GO-NFC microfibers are also lightweight in nature. The low cost, earth-abundant building blocks used in this study satisfy the economic requirement to produce mechanically strong fibers for potential commercial use. We expect that further studies using high quality building materials, e.g. larger GO nanosheets, an improved fabrication process, and infiltration of other metal ions may enable us to create even stiffer, stronger, and tougher microfibers. Additionally, the mechanistic finding of the synergetic interactions between 2D and 1D

building blocks can be potentially applicable to design high performance microfibers composed of other materials.

5.3. Chapter summary

In this chapter, we have discussed how the graphene-based structures can be engineered to be 1) extreme compliant and high stretchable, and 2) both strong and tough.

Graphene is intrinsically ultra-stiff in its plane. Its huge mechanical mismatch when interfacing with ultra-compliant biological tissues and elastomers (7-9 orders of magnitude difference in stiffness) poses significant challenge in its application to functional devices such as epidermal electronics and sensing prosthesis. We offer a feasible and promising solution to this significant challenge by suitably patterning graphene into a nanomesh. Through systematic coarse-grained simulations, we show that graphene nanomesh can be made extremely compliant with nearly zero stiffness up to about 20% elongation and then remain highly compliant up to about 50% elongation.

The quest for both strength and toughness is perpetual in advanced material design; unfortunately, these two mechanical properties are generally mutually exclusive. So far there exists only limited success of attaining both strength and toughness, which often needs material-specific, complicated or expensive synthesis processes and thus can hardly be applicable to other materials. A general mechanism to address the conflict between strength and toughness still remains elusive. We report a first-of-its-kind study of the dependence of strength and toughness of cellulose nanopaper on the size of the constituent cellulose fibers. We reveal an anomalous but highly desirable scaling law

of the mechanical properties of cellulose nanopaper: The smaller, the stronger AND the tougher. Further fundamental mechanistic studies reveal that reduced intrinsic defect size and facile (re)formation of strong hydrogen bonding among cellulose molecular chains are the underlying key to this new scaling law of mechanical properties. These mechanistic findings are generally applicable to other material building blocks, therefore open up abundant opportunities to utilize the fundamental bottom-up strategy to design a new class of functional materials that are both strong and tough.

High performance microfibers such as carbon fibers are widely used in aircraft and wind turbine blades. We have designed well-aligned, strong microfibers by hybridizing two-dimensional (2D) graphene oxide (GO) nanosheets and one-dimensional (1D) nanofibrillated cellulose (NFC) that have the potential to supersede carbon fibers due to their low cost. These well-aligned hybrid microfibers are much stronger AND tougher than microfibers made of 1D NFC or 2D GO alone. Molecular dynamics simulations reveal the synergistic effect between GO and NFC: the bonding between neighboring GO nanosheets is enhanced by NFC. Additionally, a GO nanosheet can bridge several NFC chains together, providing extra bonding sites between NFC chains over a long distance.

Chapter 6: Conclusions and Outlook

6.1. Summary and concluding remarks

This dissertation covers several aspects on strain engineering of graphene nanostructures. We have studied the programmable formation of wrinkles in graphene, which can potentially offer guidance for the design of graphene-based electronics. We have demonstrated hydrogenation assisted manipulation of graphene's morphology, a feasible and robust approach to enabling the formation of unconventional carbon nanostructures. We have presented a comprehensive investigation to the on-demand design of pseudomagnetic field in graphene via strain engineering. We have provided a pioneering study on the engineering design of the strength, toughness, compliance, stretchability of graphene-based unconventional nanomaterials. Here I briefly summarize the main conclusions in the previous chapters.

Research finding and scientific contribution 1: Wrinkles in graphene with desirable morphology have practical significance for electronic applications. We carry out systematic molecular dynamics study on the wrinkling instability of 1) graphene bilayer intercalated by nanoparticles (NPs) and 2) graphene single layer on substrate-supported nanoparticles. In the first case, a critical dispersion distance of the NPs as a function of the NP size can be determined below which neighboring NPs evolve to form a bundle through the formation of tunneling wrinkles. In the second case, a critical NP dispersion distance for the onset of tunneling wrinkle instability of graphene is determined as a function of the NP size. Results from the present study offer further insights into the formation of desirable wrinkles in graphene nanostructures (i.e., graphene deposited on

a substrate with engineered protrusions), and thus can potentially enable novel design of graphene-based electronics.

Research finding and scientific contribution 2: Hydrogenation of graphene leads to local bond distortion of each hydrogenated carbon atoms, in order to release the strain energy in its planar form. Therefore, programmable hydrogenation of graphene can open up new pathways to controlling the morphology of graphene and therefore enable the exploration of graphene-based unconventional nanomaterials. We demonstrate hydrogenation assisted graphene origami (HAGO), a feasible and robust approach to enabling the formation of unconventional carbon nanostructures, through systematic molecular dynamics simulations. We show that single-sided hydrogenation can cause the scrolling of graphene. If a proper size of the graphene is hydrogenated in one side, the graphene can completely scroll up in to a carbon nanoscroll (CNS) that remains stable at room temperature. A unique and desirable feature of HAGO-enabled nanostructures is the programmable tunability of their morphology via an external electric field. In particular, we demonstrate reversible opening and closing of a HAGO-enabled graphene nanocage, a mechanism that is crucial to achieve molecular mass uptake, storage and release. HAGO holds promise to enable an array of carbon nanostructures of desirable functionalities by design. As an example, we demonstrate HAGO-enabled high-density hydrogen storage with a weighted percentage exceeding the ultimate goal of US Department of Energy.

Research finding and scientific contribution 3: Recent experiments reveal that a scanning tunneling microscopy (STM) probe tip can generate a highly localized strain

field in a graphene drumhead, which in turn leads to a pseudomagnetic field in the graphene that can effectively confine charge carriers in a way similar to a spatially confined quantum dot (QD). We carry out systematic molecular dynamics and coarse-grained simulations to reveal the effect of the STM tip size and graphene drumhead size as well as the influence from the back-gate voltage and the tip location on the induced strain field and corresponding pseudomagnetic field. These results can offer guidance for design of reversible and on-demand formation of graphene QDs in nanoelectronics. We have further demonstrated two new approaches to generating large pseudomagnetic fields with uniform distributions in a planar graphene sheet over a large area. We achieve this by patterning the planar graphene geometry and graphene-based hetero-structures with a shape function to engineer a desired strain gradient. Our method is geometrical, opening up new fertile opportunities of strain engineering of electronic properties of 2D materials in general.

Research finding and scientific contribution 4: Graphene is intrinsically ultra-stiff in its plane. Its huge mechanical mismatch when interfacing with ultra-compliant biological tissues and elastomers poses significant challenge in its application to functional devices such as epidermal electronics and sensing prosthesis. We offer a feasible and promising solution to this significant challenge by suitably patterning graphene into a nanomesh. Through systematic coarse-grained simulations, we show that graphene nanomesh can be made extremely compliant with nearly zero stiffness up to about 20% elongation and then remain highly compliant up to about 50% elongation. We have also revealed the anomalous scaling law of strength and toughness of nanopaper made from cellulose: the smaller, the stronger AND the tougher. The

understanding of such surprising findings have led us to design strong and tough graphene oxide fibers (GO) by incorporating nanofibrillated cellulose (NFC). We find that the synergistic effect between GO and NFC is the key: the bonding between neighboring GO nanosheets is enhanced by NFC. Additionally, a GO nanosheet can bridge several NFC chains together, providing extra bonding sites between NFC chains over a long distance. There are abundant opportunities to use the fundamental bottom-up strategy to design a novel class of functional materials that are both strong and tough.

6.2. Outlook and future work

The surge of interest in graphene, as epitomized by the Nobel Prize in Physics in 2010, is largely attributed to its exceptional capability to accommodate an array of remarkable electronic, mechanical and chemical properties. Extra-large surface-to-volume ratio renders graphene a highly flexible morphology, giving rise to intriguing observations such as ripples, wrinkles and folds as well as the potential to transform into other novel carbon nanostructures. This dissertation ushers in several mechanisms to actively manipulate the graphene morphology and properties and therefore enable the material design principle that delivers desirable mechanical and electronic functionalities of graphene and its derivatives. Beyond the work in this dissertation, the following topics remain interesting to explore in future work.

1. Engineering electronic properties of substrate-supported graphene by designing substrate surface feature

Graphene has strong tendency to conform to substrate corrugations, offering potentials to program morphological strain by patterning of substrate surface feature. Since

graphene's exceptional electronic properties are strongly tied to its morphology and strain, tremendous efforts have been directed on organized formation of wrinkles, ripples, bumps and bubbles in macroscopic graphene sheets when transferred onto substrates with protrusions, but a systematic designing diagram is still missing. The purpose of this research is to systematically study how the patterning of substrate surface feature (e.g., cylindrical pillars, pyramids, etc.) affects the strain distribution in graphene membrane, therefore guiding the design of graphene-based electronics. Highly stretchable substrate can also be employed.

2. Strain engineering of emerging two dimensional materials

Two dimensional (2D) materials, such as monolayer MoS₂, h-BN, Phosphorene, Silicene, Germanene, are emerging as graphene's analogues for their particular properties of interests. For example, first principle studies have shown that strain can tune the electronic properties of phosphorene. The investigation of the mechanical and electronic properties of those structures are promising to offer new understanding and discovery of intriguing phenomenon, while they are current barely explored to its full potential. To this end, this research focuses on the interplay between nanomechanics, electron physics and chemistry. Computational method such as density functional theory will be employed to offer quantum mechanics insights on the exploration of mechanical, thermal, electronic, optical properties of those 2D materials and how mechanical strains affect those properties.

Bibliography

1. A. Geim, K. Novoselov, The rise of graphene. *Nature Materials* **6**, 183-191 (2007).
2. K. Novoselov *et al.*, Electric field effect in atomically thin carbon films. *Science* **306**, 666-669 (2004).
3. Y. Zhang, Y. Tan, H. Stormer, P. Kim, Experimental observation of the quantum Hall effect and Berry's phase in graphene. *Nature* **438**, 201-204 (2005).
4. J. Meyer *et al.*, The structure of suspended graphene sheets. *Nature* **446**, 60-63 (2007).
5. X. Li *et al.*, Large-area synthesis of high-quality and uniform graphene films on copper foils. *Science* **324**, 1312-1314 (2009).
6. P. Sutter, J. Flege, E. Sutter, Epitaxial graphene on ruthenium. *Nature Materials* **7**, 406-411 (2008).
7. K. Kim *et al.*, Large-scale pattern growth of graphene films for stretchable transparent electrodes. *Nature* **457**, 706-710 (2009).
8. A. Reina *et al.*, Large area, few-layer graphene films on arbitrary substrates by chemical vapor deposition. *Nano Letters* **9**, 30-35 (2009).
9. G. Eda, G. Fanchini, M. Chhowalla, Large-area ultrathin films of reduced graphene oxide as a transparent and flexible electronic material. *Nature Nanotechnology* **3**, 270-274 (2008).
10. C. Berger *et al.*, Electronic confinement and coherence in patterned epitaxial graphene. *Science* **312**, 1191-1196 (2006).
11. Y. Hao *et al.*, The role of surface oxygen in the growth of large single-crystal graphene on copper. *Science* **342**, 720-723 (2013).
12. J. Lee *et al.*, Wafer-scale growth of single-crystal monolayer graphene on reusable hydrogen-terminated germanium. *Science* **344**, 286-289 (2014).
13. C. Lee, X. Wei, J. Kysar, J. Hone, Measurement of the elastic properties and intrinsic strength of monolayer graphene. *Science* **321**, 385-388 (2008).
14. Q. Lu, W. Gao, R. Huang, Atomistic simulation and continuum modeling of graphene nanoribbons under uniaxial tension. *Modelling and Simulation in Materials Science and Engineering* **19**, 054006 (2011).
15. W. Bao *et al.*, Controlled ripple texturing of suspended graphene and ultrathin graphite membranes. *Nature Nanotechnology* **4**, 562-566 (2009).
16. V. Barone, O. Hod, G. Scuseria, Electronic structure and stability of semiconducting graphene nanoribbons. *Nano Letters* **6**, 2748-2754 (2006).
17. L. Tapasztó, G. Dobrik, P. Lambin, L. Biro, Tailoring the atomic structure of graphene nanoribbons by scanning tunnelling microscope lithography. *Nature Nanotechnology* **3**, 397-401 (2008).
18. M. Han, B. Ozyilmaz, Y. Zhang, P. Kim, Energy band-gap engineering of graphene nanoribbons. *Physical Review Letters* **98**, 206805 (2007).
19. Y. Zhang *et al.*, Direct observation of a widely tunable bandgap in bilayer graphene. *Nature* **459**, 820-823 (2009).

20. K. Novoselov *et al.*, Two-dimensional gas of massless Dirac fermions in graphene. *Nature* **438**, 197-200 (2005).
21. S. Morozov *et al.*, Two-dimensional electron and hole gases at the surface of graphite. *Physical Review B* **72**, 201401(R) (2005).
22. J. Chen, C. Jang, S. Xiao, M. Ishigami, M. Fuhrer, Intrinsic and extrinsic performance limits of graphene devices on SiO₂. *Nature Nanotechnology* **3**, 206-209 (2008).
23. F. Guinea, B. Horovitz, P. Le Doussal, Gauge field induced by ripples in graphene. *Physical Review B* **77**, 205421 (2008).
24. F. Guinea, M. Katsnelson, M. Vozmediano, Midgap states and charge inhomogeneities in corrugated graphene. *Physical Review B* **77**, 075422 (2008).
25. A. de Parga *et al.*, Periodically rippled graphene: Growth and spatially resolved electronic structure. *Physical Review Letters* **100**, 056807 (2008).
26. E. Kim, A. Castro Neto, Graphene as an electronic membrane. *Epl* **84**, 57007 (2008).
27. M. Katsnelson, A. Geim, Electron scattering on microscopic corrugations in graphene. *Philosophical Transactions of the Royal Society a-Mathematical Physical and Engineering Sciences* **366**, 195-204 (2008).
28. S. Morozov *et al.*, Giant intrinsic carrier mobilities in graphene and its bilayer. *Physical Review Letters* **100**, 016602 (2008).
29. A. Fasolino, J. Los, M. Katsnelson, Intrinsic ripples in graphene. *Nature Materials* **6**, 858-861 (2007).
30. D. Elias *et al.*, Control of graphene's properties by reversible hydrogenation: Evidence for graphane. *Science* **323**, 610-613 (2009).
31. S. Koenig, N. Boddeti, M. Dunn, J. Bunch, Ultrastrong adhesion of graphene membranes. *Nature Nanotechnology* **6**, 543-546 (2011).
32. W. Cullen *et al.*, High-fidelity conformation of graphene to SiO₂ topographic features. *Physical Review Letters* **105**, 215504 (2010).
33. E. Stolyarova *et al.*, High-resolution scanning tunneling microscopy imaging of mesoscopic graphene sheets on an insulating surface. *Proceedings of the National Academy of Sciences of the United States of America* **104**, 9209-9212 (2007).
34. U. Stoberl, U. Wurstbauer, W. Wegscheider, D. Weiss, J. Eroms, Morphology and flexibility of graphene and few-layer graphene on various substrates. *Applied Physics Letters* **93**, 051906 (2008).
35. F. Tikhonenko, D. Horsell, R. Gorbachev, A. Savchenko, Weak localization in graphene flakes. *Physical Review Letters* **100**, 056802 (2008).
36. V. Geringer *et al.*, Intrinsic and extrinsic corrugation of monolayer graphene deposited on SiO₂. *Physical Review Letters* **102**, 076102 (2009).
37. S. Scharfenberg *et al.*, Probing the mechanical properties of graphene using a corrugated elastic substrate. *Applied Physics Letters* **98**, 091908 (2011).
38. M. Yamamoto *et al.*, "The princess and the pea" at the nanoscale: Wrinkling and delamination of graphene on nanoparticles. *Physical Review X* **2**, 041018 (2012).
39. M. Zaeri, S. Ziaei-Rad, Elastic properties of carbon nanoscrolls. *Rsc Advances* **4**, 22995-23001 (2014).

40. L. Viculis, J. Mack, R. Kaner, A chemical route to carbon nanoscrolls. *Science* **299**, 1361-1361 (2003).
41. G. Mpourmpakis, E. Tylianakis, G. Froudakis, Carbon nanoscrolls: A promising material for hydrogen storage. *Nano Letters* **7**, 1893-1897 (2007).
42. X. Shi, N. Pugno, Y. Cheng, H. Gao, Gigahertz breathing oscillators based on carbon nanoscrolls. *Applied Physics Letters* **95**, 163113 (2009).
43. Z. Zhang, T. Li, Ultrafast nano-oscillators based on interlayer-bridged carbon nanoscrolls. *Nanoscale Research Letters* **6**, 470 (2011).
44. X. Shi, N. Pugno, H. Gao, Constitutive behavior of pressurized carbon nanoscrolls. *International Journal of Fracture* **171**, 163-168 (2011).
45. X. Shi, Y. Cheng, N. Pugno, H. Gao, A translational nanoactuator based on carbon nanoscrolls on substrates. *Applied Physics Letters* **96**, 053115 (2010).
46. F. Zeng *et al.*, Supercapacitors based on high-quality graphene scrolls. *Nanoscale* **4**, 3997-4001 (2012).
47. X. Shi, Y. Cheng, N. Pugno, H. Gao, Tunable water channels with carbon nanoscrolls. *Small* **6**, 739-744 (2010).
48. X. Xie *et al.*, Controlled fabrication of high-quality carbon nanoscrolls from monolayer graphene. *Nano Letters* **9**, 2565-2570 (2009).
49. Z. Zhang, T. Li, Carbon nanotube initiated formation of carbon nanoscrolls. *Applied Physics Letters* **97**, 081909 (2010).
50. M. Yan *et al.*, Nanowire templated semihollow bicontinuous graphene scrolls: Designed construction, Mechanism, and Enhanced Energy Storage Performance. *Journal of the American Chemical Society* **135**, 18176-18182 (2013).
51. D. Berman, S. Deshmukh, S. Sankaranarayanan, A. Erdemir, A. Sumant, Macroscale superlubricity enabled by graphene nanoscroll formation. *Science* **348**, 1118-1122 (2015).
52. J. Sofo, A. Chaudhari, G. Barber, Graphane: A two-dimensional hydrocarbon. *Physical Review B* **75**, 153401 (2007).
53. A. Castro Neto, F. Guinea, N. Peres, K. Novoselov, A. Geim, The electronic properties of graphene. *Reviews of Modern Physics* **81**, 109-162 (2009).
54. L. Ponomarenko *et al.*, Chaotic dirac billiard in graphene quantum dots. *Science* **320**, 356-358 (2008).
55. K. Ritter, J. Lyding, The influence of edge structure on the electronic properties of graphene quantum dots and nanoribbons. *Nature Materials* **8**, 235-242 (2009).
56. D. Pan, J. Zhang, Z. Li, M. Wu, Hydrothermal route for cutting graphene sheets into blue-luminescent graphene quantum dots. *Advanced Materials* **22**, 734-738 (2010).
57. X. Yan, X. Cui, L. Li, Synthesis of large, stable colloidal graphene quantum dots with tunable size. *Journal of the American Chemical Society* **132**, 5944-5945 (2010).
58. J. Lu, P. Yeo, C. Gan, P. Wu, K. Loh, Transforming C-60 molecules into graphene quantum dots. *Nature Nanotechnology* **6**, 247-252 (2011).
59. J. Bai, X. Zhong, S. Jiang, Y. Huang, X. Duan, Graphene nanomesh. *Nature Nanotechnology* **5**, 190-194 (2010).

60. J. Bai, X. Duan, Y. Huang, Rational fabrication of graphene nanoribbons using a nanowire etch mask. *Nano Letters* **9**, 2083-2087 (2009).
61. L. Jiao, L. Zhang, X. Wang, G. Diankov, H. Dai, Narrow graphene nanoribbons from carbon nanotubes. *Nature* **458**, 877-880 (2009).
62. X. Duan, Assembled semiconductor nanowire thin films for high-performance flexible macroelectronics. *Mrs Bulletin* **32**, 134-141 (2007).
63. W. Lu, C. Lieber, Nanoelectronics from the bottom up. *Nature Materials* **6**, 841-850 (2007).
64. A. Sinitskii, J. Tour, Patterning graphene through the self-assembled templates: Toward periodic two-dimensional graphene nanostructures with semiconductor properties. *Journal of the American Chemical Society* **132**, 14730-14732 (2010).
65. N. Safron, A. Brewer, M. Arnold, Semiconducting two-dimensional graphene nanoconstriction arrays. *Small* **7**, 492-498 (2011).
66. Q. Cheng *et al.*, Supramolecular self-assembly induced graphene oxide based hydrogels and organogels. *Langmuir* **28**, 3005-3010 (2012).
67. S. Zu, B. Han, Aqueous dispersion of graphene sheets stabilized by pluronic copolymers: Formation of supramolecular hydrogel. *Journal of Physical Chemistry C* **113**, 13651-13657 (2009).
68. H. Bai, C. Li, X. Wang, G. Shi, On the gelation of graphene oxide. *Journal of Physical Chemistry C* **115**, 5545-5551 (2011).
69. J. Liu, G. Chen, M. Jiang, Supramolecular hybrid hydrogels from noncovalently functionalized graphene with block copolymers. *Macromolecules* **44**, 7682-7691 (2011).
70. Y. Xu, Q. Wu, Y. Sun, H. Bai, G. Shi, Three-dimensional self-assembly of graphene oxide and dna into multifunctional hydrogels. *Acs Nano* **4**, 7358-7362 (2010).
71. R. Liu *et al.*, Tough and highly stretchable graphene oxide/polyacrylamide nanocomposite hydrogels. *Journal of Materials Chemistry* **22**, 14160-14167 (2012).
72. J. Hicks *et al.*, A wide-bandgap metal-semiconductor-metal nanostructure made entirely from graphene. *Nature Physics* **9**, 49-54 (2013).
73. Y. Guo, W. Guo, Electronic and field emission properties of wrinkled graphene. *Journal of Physical Chemistry C* **117**, 692-696 (2013).
74. J. Zang *et al.*, Multifunctionality and control of the crumpling and unfolding of large-area graphene. *Nature Materials* **12**, 321-325 (2013).
75. Y. Wang *et al.*, Super-elastic graphene ripples for flexible strain sensors. *Acs Nano* **5**, 3645-3650 (2011).
76. T. Li, Extrinsic morphology of graphene. *Modelling and Simulation in Materials Science and Engineering* **19**, 054005 (2011).
77. J. K. Lee, K. B. Smith, C. M. Hayner, H. H. Kung, Silicon nanoparticles-graphene paper composites for Li ion battery anodes. *Chemical Communications* **46**, 2025-2027 (2010).
78. S. Stuart, A. Tutein, J. Harrison, A reactive potential for hydrocarbons with intermolecular interactions. *Journal of Chemical Physics* **112**, 6472-6486 (2000).

79. S. Plimpton, Fast parallel algorithms for short-range molecular-dynamics. *Journal of Computational Physics* **117**, 1-19 (1995).
80. N. N. Klimov *et al.*, Electromechanical properties of graphene drumheads. *Science* **336**, 1557-1561 (2012).
81. S. Zhu, J. Galginitis, T. Li, Critical dispersion distance of silicon nanoparticles intercalated between graphene layers. *Journal of Nanomaterials* **2012**, 375289 (2012).
82. K. Kim *et al.*, Multiply folded graphene. *Physical Review B* **83**, 245433 (2011).
83. N. Patra, B. Wang, P. Kral, Nanodroplet activated and guided folding of graphene nanostructures. *Nano Letters* **9**, 3766-3771 (2009).
84. Z. Zhang, B. Liu, K. Hwang, H. Gao, Surface-adsorption-induced bending behaviors of graphene nanoribbons. *Applied Physics Letters* **98**, 121909 (2011).
85. R. Xu, Y. Wang, B. Liu, D. Fang, Mechanics interpretation on the bending stiffness and wrinkled pattern of graphene. *Journal of Applied Mechanics-Transactions of the Asme* **80**, 040910 (2013).
86. N. Boddeti *et al.*, Mechanics of adhered, pressurized graphene blisters. *Journal of Applied Mechanics-Transactions of the Asme* **80**, 040909 (2013).
87. S. Zhu, T. Li, Hydrogenation enabled scrolling of graphene. *Journal of Physics D-Applied Physics* **46**, 075301 (2013).
88. D. Yu, F. Liu, Synthesis of carbon nanotubes by rolling up patterned graphene nanoribbons using selective atomic adsorption. *Nano Letters* **7**, 3046-3050 (2007).
89. X. Shi, N. Pugno, H. Gao, Tunable core size of carbon nanoscrolls. *Journal of Computational and Theoretical Nanoscience* **7**, 517-521 (2010).
90. S. Braga *et al.*, Structure and dynamics of carbon nanoscrolls. *Nano Letters* **4**, 881-884 (2004).
91. B. Martins, D. Galvao, Curved graphene nanoribbons: Structure and dynamics of carbon nanobelts. *Nanotechnology* **21**, 075710 (2010).
92. H. Yan, Y. Sun, L. He, J. Nie, M. Chan, Observation of Landau-level-like quantization at 77 K along a strained-induced graphene ridge. *Physical Review B* **85**, 035422 (2012).
93. Z. Zhang, T. Li, Graphene morphology regulated by nanowires patterned in parallel on a substrate surface. *Journal of Applied Physics* **107**, 103519 (2010).
94. Z. Zhang, T. Li, A molecular mechanics study of morphologic interaction between graphene and Si nanowires on a SiO₂ substrate. *Journal of Nanomaterials* **2011**, 374018 (2011).
95. T. Li, Z. Zhang, Snap-through instability of graphene on substrates. *Nanoscale Research Letters* **5**, 169-173 (2010).
96. T. Li, Z. Zhang, Substrate-regulated morphology of graphene. *Journal of Physics D-Applied Physics* **43**, 075303 (2010).
97. Z. Aitken, R. Huang, Effects of mismatch strain and substrate surface corrugation on morphology of supported monolayer graphene. *Journal of Applied Physics* **107**, 123531 (2010).
98. S. Zhu, T. Li, Wrinkling instability of graphene on substrate-supported nanoparticles. *Journal of Applied Mechanics* **81**, 061008 (2014).

99. L. Jiang *et al.*, A cohesive law for carbon nanotube/polymer interfaces based on the van der Waals force. *Journal of the Mechanics and Physics of Solids* **54**, 2436-2452 (2006).
100. Z. Zong, C. Chen, M. Dokmeci, K. Wan, Direct measurement of graphene adhesion on silicon surface by intercalation of nanoparticles. *Journal of Applied Physics* **107**, 026104 (2010).
101. H. Tomori *et al.*, Introducing nonuniform strain to graphene using dielectric nanopillars. *Applied Physics Express* **4**, 075102 (2011).
102. G. Li *et al.*, Adhesion of graphene sheet on nano-patterned substrates with nanopillar array. *Journal of Applied Physics* **113**, 244303 (2013).
103. M. Neek-Amal, L. Covaci, F. Peeters, Nanoengineered nonuniform strain in graphene using nanopillars. *Physical Review B* **86**, 041405(R) (2012).
104. Y. Xu, H. Bai, G. Lu, C. Li, G. Shi, Flexible graphene films via the filtration of water-soluble noncovalent functionalized graphene sheets. *Journal of the American Chemical Society* **130**, 5856–5857 (2008).
105. S. Ryu *et al.*, Reversible basal plane hydrogenation of graphene. *Nano Letters* **8**, 4597-4602 (2008).
106. X. Wang, S. Tabakman, H. Dai, Atomic layer deposition of metal oxides on pristine and functionalized graphene. *Journal of the American Chemical Society* **130**, 8152–8153 (2008).
107. D. Boukhvalov, M. Katsnelson, Chemical functionalization of graphene with defects. *Nano Letters* **8**, 4373-4379 (2008).
108. D. Boukhvalov, M. Katsnelson, A. Lichtenstein, Hydrogen on graphene: Electronic structure, total energy, structural distortions and magnetism from first-principles calculations. *Physical Review B* **77**, 035427 (2008).
109. R. Balog *et al.*, Bandgap opening in graphene induced by patterned hydrogen adsorption. *Nature Materials* **9**, 315-319 (2010).
110. P. Sessi, J. Guest, M. Bode, N. Guisinger, Patterning graphene at the nanometer scale via hydrogen desorption. *Nano Letters* **9**, 4343-4347 (2009).
111. H. Xiang, E. Kan, S. Wei, X. Gong, M. Whangbo, Thermodynamically stable single-side hydrogenated graphene. *Physical Review B* **82**, 165425 (2010).
112. B. Pujari, S. Gusarov, M. Brett, A. Kovalenko, Single-side-hydrogenated graphene: Density functional theory predictions. *Physical Review B* **84**, 041402(R) (2011).
113. J. Zhou *et al.*, Ferromagnetism in semihydrogenated graphene sheet. *Nano Letters* **9**, 3867-3870 (2009).
114. Z. Sun *et al.*, Towards hybrid superlattices in graphene. *Nature Communications* **2**, 559 (2011).
115. V. Coluci, S. Braga, R. Baughman, D. Galvao, Prediction of the hydrogen storage capacity of carbon nanoscrolls. *Physical Review B* **75**, 125404 (2007).
116. C. Reddy, Q. Cheng, V. Shenoy, Y. Zhang, Interfacial properties and morphologies of graphene-graphane composite sheets. *Journal of Applied Physics* **109**, 054314 (2011).
117. V. Shenoy, C. Reddy, A. Ramasubramaniam, Y. Zhang, Edge-stress-induced warping of graphene sheets and nanoribbons. *Physical Review Letters* **101**, 245501 (2008).

118. C. Reddy, Y. Zhang, V. Shenoy, Patterned graphone-a novel template for molecular packing. *Nanotechnology* **23**, 165303 (2012).
119. J. Siegel, Materials chemistry Carbon origami. *Nature* **486**, 327-328 (2012).
120. J. Feng *et al.*, Patterning of graphene. *Nanoscale* **4**, 4883-4899 (2012).
121. J. Qi, J. Huang, J. Feng, D. Shi, J. Li, The possibility of chemically inert, graphene-based all-carbon electronic devices with 0.8 eV gap. *Acs Nano* **5**, 3475-3482 (2011).
122. D. Bell, M. Lemme, L. Stern, J. RWilliams, C. Marcus, Precision cutting and patterning of graphene with helium ions. *Nanotechnology* **20**, 455301 (2009).
123. L. Ci *et al.*, Controlled nanocutting of graphene. *Nano Research* **1**, 116-122 (2008).
124. L. Ci *et al.*, Graphene shape control by multistage cutting and transfer. *Advanced Materials* **21**, 4487-4491 (2009).
125. M. Fischbein, M. Drndic, Electron beam nanosculpting of suspended graphene sheets. *Applied Physics Letters* **93**, 113107 (2008).
126. G. Whitesides, Nanoscience, nanotechnology, and chemistry. *Small* **1**, 172-179 (2005).
127. H. Chen, D. Sun, X. Gong, Z. Liu, Self-assembled water molecules as a functional valve for a high-pressure nanocontainer. *Angewandte Chemie-International Edition* **52**, 1973-1976 (2013).
128. O. Pupysheva, A. Farajian, B. Yakobson, Fullerene nanocage capacity for hydrogen storage. *Nano Letters* **8**, 767-774 (2008).
129. Y. Chen *et al.*, Aerosol synthesis of cargo-filled graphene nanosacks. *Nano Letters* **12**, 1996-2002 (2012).
130. Y. Chen *et al.*, Encapsulation of particle ensembles in graphene nanosacks as a new route to multifunctional materials. *Acs Nano* **7**, 3744-3753 (2013).
131. R. Fernandes, D. Gracias, Self-folding polymeric containers for encapsulation and delivery of drugs. *Advanced Drug Delivery Reviews* **64**, 1579-1589 (2012).
132. DOE.
(http://www1.eere.energy.gov/hydrogenandfuelcells/storage/pdfs/targets_onboard_hydro_storage.pdf, 2009).
133. L. Chernozatonskii, P. Sorokin, Nanoengineering structures on graphene with adsorbed hydrogen "lines". *Journal of Physical Chemistry C* **114**, 3225-3229 (2010).
134. H. Zhang, Y. Miyamoto, A. Rubio, Laser-induced preferential dehydrogenation of graphane. *Physical Review B* **85**, 201409(R) (2012).
135. J. Zhou, Q. Sun, How to fabricate a semihydrogenated graphene sheet? A promising strategy explored. *Applied Physics Letters* **101**, 073114 (2012).
136. K. Tada, S. Furuya, K. Watanabe, Ab initio study of hydrogen adsorption to single-walled carbon nanotubes. *Physical Review B* **63**, 155405 (2001).
137. P. Ruffieux *et al.*, Hydrogen adsorption on sp(2)-bonded carbon: Influence of the local curvature. *Physical Review B* **66**, 245416 (2002).
138. C. Lui, L. Liu, K. Mak, G. Flynn, T. Heinz, Ultraflat graphene. *Nature* **462**, 339-341 (2009).
139. M. Ishigami, J. Chen, W. Cullen, M. Fuhrer, E. Williams, Atomic structure of graphene on SiO₂. *Nano Letters* **7**, 1643-1648 (2007).

140. E. Santos, E. Kaxiras, Electric-field dependence of the effective dielectric constant in graphene. *Nano Letters* **13**, 898-902 (2013).
141. E. Santos, Magnetoelectric effect in functionalized few-layer graphene. *Physical Review B* **87**, 155440 (2013).
142. Y. Gogotsi *et al.*, Tailoring of nanoscale porosity in carbide-derived carbons for hydrogen storage. *Journal of the American Chemical Society* **127**, 16006-16007 (2005).
143. G. Yushin, R. Dash, J. Jagiello, J. Fischer, Y. Gogotsi, Carbide-derived carbons: Effect of pore size on hydrogen uptake and heat of adsorption. *Advanced Functional Materials* **16**, 2288-2293 (2006).
144. K. Novoselov *et al.*, Two-dimensional atomic crystals. *Proceedings of the National Academy of Sciences of the United States of America* **102**, 10451-10453 (2005).
145. K. Bolotin *et al.*, Ultrahigh electron mobility in suspended graphene. *Solid State Communications* **146**, 351-355 (2008).
146. M. Fogler, F. Guinea, M. Katsnelson, Pseudomagnetic fields and ballistic transport in a suspended graphene sheet. *Physical Review Letters* **101**, 226804 (2008).
147. F. Guinea, M. Katsnelson, A. Geim, Energy gaps and a zero-field quantum Hall effect in graphene by strain engineering. *Nature Physics* **6**, 30-33 (2010).
148. N. Levy *et al.*, Strain-induced pseudo-magnetic fields greater than 300 tesla in graphene nanobubbles. *Science* **329**, 544-547 (2010).
149. K. Kim, Y. Blanter, K. Ahn, Interplay between real and pseudomagnetic field in graphene with strain. *Physical Review B* **84**, 081401(R) (2011).
150. G. Wakker, R. Tiwari, M. Blaauboer, Localization and circulating currents in curved graphene devices. *Physical Review B* **84**, 195427 (2011).
151. F. Guinea, A. Geim, M. Katsnelson, K. Novoselov, Generating quantizing pseudomagnetic fields by bending graphene ribbons. *Physical Review B* **81**, 035408 (2010).
152. T. Wehling, A. Balatsky, A. Tselik, M. Katsnelson, A. Lichtenstein, Midgap states in corrugated graphene: Ab initio calculations and effective field theory. *Epl* **84**, 17003 (2008).
153. M. Gibertini, A. Tomadin, M. Polini, A. Fasolino, M. Katsnelson, Electron density distribution and screening in rippled graphene sheets. *Physical Review B* **81**, 125437 (2010).
154. S. Jung *et al.*, Evolution of microscopic localization in graphene in a magnetic field from scattering resonances to quantum dots. *Nature Physics* **7**, 245-251 (2011).
155. A. Luican, G. Li, E. Andrei, Quantized Landau level spectrum and its density dependence in graphene. *Physical Review B* **83**, 041405(R) (2011).
156. J. A. Stroscio, E. W. Hudson, S. R. Blankenship, R. J. Celotta, A. P. Fein, Facility for nanoscience research: An overview. *SPIE Proceedings* **4608**, 112 (2002).
157. G. Rutter *et al.*, Microscopic polarization in bilayer graphene. *Nature Physics* **7**, 649-655 (2011).

158. B. LeRoy, J. Kong, V. Pahilwani, C. Dekker, S. Lemay, Three-terminal scanning tunneling spectroscopy of suspended carbon nanotubes. *Physical Review B* **72**, 075413 (2005).
159. L. Kouwenhoven, D. Austing, S. Tarucha, Few-electron quantum dots. *Reports on Progress in Physics* **64**, 701-736 (2001).
160. A. Rappe, C. Casewit, K. Colwell, W. Goddard, W. Skiff, UFF, A full periodic-table force-field for molecular mechanics and molecular-dynamics simulations. *Journal of the American Chemical Society* **114**, 10024-10035 (1992).
161. M. Katsnelson, K. Novoselov, A. Geim, Chiral tunnelling and the Klein paradox in graphene. *Nature Physics* **2**, 620-625 (2006).
162. J. Guttinger *et al.*, Electron-hole crossover in graphene quantum dots. *Physical Review Letters* **103**, 046810 (2009).
163. P. Xu, S. Barber, M. Ackerman, J. Schoelz, P. Thibado, Role of bias voltage and tunneling current in the perpendicular displacements of freestanding graphene via scanning tunneling microscopy. *Journal of Vacuum Science & Technology B* **31**, 04D103 (2013).
164. R. Zan *et al.*, Scanning tunnelling microscopy of suspended graphene. *Nanoscale* **4**, 3065-3068 (2012).
165. P. Xu *et al.*, Atomic control of strain in freestanding graphene. *Physical Review B* **85**, 121406(R) (2012).
166. F. Eder *et al.*, Probing from both sides: Reshaping the graphene landscape via face-to-face dual-probe microscopy. *Nano Letters* **13**, 1934-1940 (2013).
167. S. Zhu, Y. Huang, T. Li, Extremely compliant and highly stretchable patterned graphene. *Applied Physics Letters* **104**, 173103 (2014).
168. Y. Guo, N. Karasawa, W. Goddard, Prediction of fullerene packing in C60 and C70 crystals. *Nature* **351**, 464-467 (1991).
169. F. de Juan, J. Manes, M. Vozmediano, Gauge fields from strain in graphene. *Physical Review B* **87**, 165131 (2013).
170. J. Sloan, A. Sanjuan, Z. Wang, C. Horvath, S. Barraza-Lopez, Strain gauge fields for rippled graphene membranes under central mechanical load: An approach beyond first-order continuum elasticity. *Physical Review B* **87**, 155436 (2013).
171. A. Pantano, D. Parks, M. Boyce, Mechanics of deformation of single- and multi-wall carbon nanotubes. *Journal of the Mechanics and Physics of Solids* **52**, 789-821 (2004).
172. A. Hemmasizadeh, M. Mahzoon, E. Hadi, R. Khandan, A method for developing the equivalent continuum model of a single layer graphene sheet. *Thin Solid Films* **516**, 7636-7640 (2008).
173. D. Guo *et al.*, Observation of Landau levels in potassium-intercalated graphite under a zero magnetic field. *Nature Communications* **3**, 1068 (2012).
174. S. Zhu *et al.*, Pseudomagnetic fields in a locally strained graphene drumhead. *Physical Review B* **90**, 075426 (2014).
175. Z. Qi *et al.*, Pseudomagnetic fields in graphene nanobubbles of constrained geometry: A molecular dynamics study. *Physical Review B* **90**, 125419 (2014).

176. M. Neek-Amal, L. Covaci, K. Shakouri, F. Peeters, Electronic structure of a hexagonal graphene flake subjected to triaxial stress. *Physical Review B* **88**, 115428 (2013).
177. M. Vozmediano, M. Katsnelson, F. Guinea, Gauge fields in graphene. *Physics Reports-Review Section of Physics Letters* **496**, 109-148 (2010).
178. Z. Zeng *et al.*, Fabrication of graphene nanomesh by using an anodic aluminum oxide membrane as a template. *Advanced Materials* **24**, 4138-4142 (2012).
179. X. Liang *et al.*, Formation of bandgap and subbands in graphene nanomeshes with sub-10 nm ribbon width fabricated via nanoimprint lithography. *Nano Letters* **10**, 2454-2460 (2010).
180. M. Wang *et al.*, CVD growth of large area smooth-edged graphene nanomesh by nanosphere lithography. *Scientific Reports* **3**, 1238 (2013).
181. S. Zhu, T. Li, Hydrogenation-assisted graphene origami and its application in programmable molecular mass uptake, storage, and release. *Acs Nano* **8**, 2864-2872 (2014).
182. L. Zhang, X. Wang, Atomistic insights into the nanohelix of hydrogenated graphene: Formation, characterization and application. *Physical Chemistry Chemical Physics* **16**, 2981-2988 (2014).
183. J. Baringhaus *et al.*, Exceptional ballistic transport in epitaxial graphene nanoribbons. *Nature* **506**, 349-354 (2014).
184. L. Liu *et al.*, Heteroepitaxial growth of two-dimensional hexagonal boron nitride templated by graphene edges. *Science* **343**, 163-167 (2014).
185. Y. Gao *et al.*, Toward single-layer uniform hexagonal boron nitride-graphene patchworks with zigzag linking edges. *Nano Letters* **13**, 3439-3443 (2013).
186. G. Han *et al.*, Continuous growth of hexagonal graphene and boron nitride in-plane heterostructures by atmospheric pressure chemical vapor deposition. *Acs Nano* **7**, 10129-10138 (2013).
187. P. Sutter, R. Cortes, J. Lahiri, E. Sutter, Interface formation in monolayer graphene-boron nitride heterostructures. *Nano Letters* **12**, 4869-4874 (2012).
188. H. Garza, E. Kievit, G. Schneider, U. Staufer, Controlled, reversible, and nondestructive generation of uniaxial extreme strains (> 10%) in graphene. *Nano Letters* **14**, 4107-4113 (2014).
189. J. Soler *et al.*, The SIESTA method for ab initio order-N materials simulation. *Journal of Physics-Condensed Matter* **14**, 2745-2779 (2002).
190. Q. Peng, W. Ji, S. De, Mechanical properties of the hexagonal boron nitride monolayer: Ab initio study. *Computational Materials Science* **56**, 11-17 (2012).
191. E. Cadelano, P. Palla, S. Giordano, L. Colombo, Elastic properties of hydrogenated graphene. *Physical Review B* **82**, 235414 (2010).
192. E. Munoz, A. Singh, M. Ribas, E. Penev, B. Yakobson, The ultimate diamond slab: GraphAne versus graphEne. *Diamond and Related Materials* **19**, 368-373 (2010).
193. Q. Pei, Y. Zhang, V. Shenoy, A molecular dynamics study of the mechanical properties of hydrogen functionalized graphene. *Carbon* **48**, 898-904 (2010).
194. J. Tersoff, New empirical-approach for the structure and energy of covalent systems. *Physical Review B* **37**, 6991-7000 (1988).

195. A. Kinaci, J. Haskins, C. Sevik, T. Cagin, Thermal conductivity of BN-C nanostructures. *Physical Review B* **86**, 115410 (2012).
196. S. Lacour, J. Jones, S. Wagner, T. Li, Z. Suo, Stretchable interconnects for elastic electronic surfaces. *Proceedings of the Ieee* **93**, 1459-1467 (2005).
197. S. Wagner *et al.*, Electronic skin: Architecture and components. *Physica E-Low-Dimensional Systems & Nanostructures* **25**, 326-334 (2004).
198. D. Kim *et al.*, Epidermal electronics. *Science* **333**, 838-843 (2011).
199. S. Park *et al.*, Printed assemblies of inorganic light-emitting diodes for deformable and semitransparent displays. *Science* **325**, 977-981 (2009).
200. J. Viventi *et al.*, Flexible, foldable, actively multiplexed, high-density electrode array for mapping brain activity in vivo. *Nature Neuroscience* **14**, 1599-U1138 (2011).
201. S. Lee *et al.*, All graphene-based thin film transistors on flexible plastic substrates. *Nano Letters* **12**, 3472-3476 (2012).
202. Z. Chen *et al.*, Three-dimensional flexible and conductive interconnected graphene networks grown by chemical vapour deposition. *Nature Materials* **10**, 424-428 (2011).
203. S. Bae *et al.*, Roll-to-roll production of 30-inch graphene films for transparent electrodes. *Nature Nanotechnology* **5**, 574-578 (2010).
204. T. Georgiou *et al.*, Vertical field-effect transistor based on graphene-WS₂ heterostructures for flexible and transparent electronics. *Nature Nanotechnology* **8**, 100-103 (2013).
205. K. Novoselov *et al.*, A roadmap for graphene. *Nature* **490**, 192-200 (2012).
206. I. Meric *et al.*, Current saturation in zero-bandgap, topgated graphene field-effect transistors. *Nature Nanotechnology* **3**, 654-659 (2008).
207. Y. Son, M. Cohen, S. Louie, Energy gaps in graphene nanoribbons. *Physical Review Letters* **97**, 216803 (2006).
208. F. Sols, F. Guinea, A. Neto, Coulomb blockade in graphene nanoribbons. *Physical Review Letters* **99**, 166803 (2007).
209. X. Li, X. Wang, L. Zhang, S. Lee, H. Dai, Chemically derived, ultrasoft graphene nanoribbon semiconductors. *Science* **319**, 1229-1232 (2008).
210. R. Paul, S. Badhulika, N. Saucedo, A. Mulchandani, Graphene nanomesh as highly sensitive chemiresistor gas sensor. *Analytical Chemistry* **84**, 8171-8178 (2012).
211. G. Ning *et al.*, Chemical vapor deposition derived flexible graphene paper and its application as high performance anodes for lithium rechargeable batteries. *Journal of Materials Chemistry A* **1**, 408-414 (2013).
212. J. Liu *et al.*, Doped graphene nanohole arrays for flexible transparent conductors. *Applied Physics Letters* **99**, 023111 (2011).
213. X. Ye, L. Qi, Two-dimensionally patterned nanostructures based on monolayer colloidal crystals: Controllable fabrication, assembly, and applications. *Nano Today* **6**, 608-631 (2011).
214. S. Cranford, M. Buehler, Twisted and coiled ultralong multilayer graphene ribbons. *Modelling and Simulation in Materials Science and Engineering* **19**, 054003 (2011).

215. S. Cranford, D. Sen, M. Buehler, Meso-origami: Folding multilayer graphene sheets. *Applied Physics Letters* **95**, 123121 (2009).
216. J. Walther, R. Jaffe, T. Halicioglu, P. Koumoutsakos, Carbon nanotubes in water: Structural characteristics and energetics. *Journal of Physical Chemistry B* **105**, 9980-9987 (2001).
217. W. David *et al.*, Crystal-structure and bonding of ordered C60. *Nature* **353**, 147-149 (1991).
218. R. Tuzun, D. Noid, B. Sumpter, R. Merkle, Dynamics of fluid flow inside carbon nanotubes. *Nanotechnology* **7**, 241-246 (1996).
219. M. Tucker, T. Li, Strain deconcentration in thin films patterned with circular holes. *International Journal of Applied Mechanics* **1**, 557-568 (2009).
220. T. Li, Z. Suo, S. Lacour, S. Wagner, Compliant thin film patterns of stiff materials as platforms for stretchable electronics. *Journal of Materials Research* **20**, 3274-3277 (2005).
221. S. Lacour, D. Chan, S. Wagner, T. Li, Z. Suo, Mechanisms of reversible stretchability of thin metal films on elastomeric substrates. *Applied Physics Letters* **88**, 204103 (2006).
222. J. Rogers, T. Someya, Y. Huang, Materials and mechanics for stretchable electronics. *Science* **327**, 1603-1607 (2010).
223. B. Song *et al.*, Atomic-scale electron-beam sculpting of near-defect-free graphene nanostructures. *Nano Letters* **11**, 2247-2250 (2011).
224. Q. Xu *et al.*, Controllable atomic scale patterning of freestanding monolayer graphene at elevated temperature. *Acs Nano* **7**, 1566-1572 (2013).
225. M. Lemme *et al.*, Etching of graphene devices with a helium ion beam. *Acs Nano* **3**, 2674-2676 (2009).
226. R. O. Ritchie, The conflicts between strength and toughness. *Nature Materials* **10**, 817-822 (2011).
227. K. Lu, L. Lu, S. Suresh, Strengthening materials by engineering coherent internal boundaries at the nanoscale. *Science* **324**, 349-352 (2009).
228. L. Lu, X. Chen, X. Huang, K. Lu, Revealing the maximum strength in nanotwinned copper. *Science* **323**, 607-610 (2009).
229. L. Lu, Y. Shen, X. Chen, L. Qian, K. Lu, Ultrahigh strength and high electrical conductivity in copper. *Science* **304**, 422-426 (2004).
230. T. Zhu, J. Li, Ultra-strength materials. *Progress in Materials Science* **55**, 710-757 (2010).
231. J. Greer, J. De Hosson, Plasticity in small-sized metallic systems: Intrinsic versus extrinsic size effect. *Progress in Materials Science* **56**, 654-724 (2011).
232. C. Deng, F. Sansoz, Near-ideal strength in gold nanowires achieved through microstructural design. *Acs Nano* **3**, 3001-3008 (2009).
233. O. Anderoglu *et al.*, Epitaxial nanotwinned Cu films with high strength and high conductivity. *Applied Physics Letters* **93**, 083108 (2008).
234. A. Cao, Y. Wei, S. Mao, Deformation mechanisms of face-centered-cubic metal nanowires with twin boundaries. *Applied Physics Letters* **90**, 151909 (2007).
235. M. Dao, L. Lu, Y. Shen, S. Suresh, Strength, strain-rate sensitivity and ductility of copper with nanoscale twins. *Acta Materialia* **54**, 5421-5432 (2006).

236. D. Jang, X. Li, H. Gao, J. Greer, Deformation mechanisms in nanotwinned metal nanopillars. *Nature Nanotechnology* **7**, 594-601 (2012).
237. X. Li, Y. Wei, L. Lu, K. Lu, H. Gao, Dislocation nucleation governed softening and maximum strength in nano-twinned metals. *Nature* **464**, 877-880 (2010).
238. A. Evans, Perspective on the development of high-toughness ceramics. *Journal of the American Ceramic Society* **73**, 187-206 (1990).
239. M. Launey *et al.*, Fracture toughness and crack-resistance curve behavior in metallic glass-matrix composites. *Applied Physics Letters* **94**, 241910 (2009).
240. R. Ritchie, Mechanisms of fatigue crack-propagation in metals, ceramics and composites - role of crack tip shielding. *Materials Science and Engineering a-Structural Materials Properties Microstructure and Processing* **103**, 15-28 (1988).
241. D. Vashishth, Rising crack-growth-resistance behavior in cortical bone: implications for toughness measurements. *Journal of Biomechanics* **37**, 943-946 (2004).
242. R. Conner, W. Johnson, N. Paton, W. Nix, Shear bands and cracking of metallic glass plates in bending. *Journal of Applied Physics* **94**, 904-911 (2003).
243. M. Demetriou *et al.*, A damage-tolerant glass. *Nature Materials* **10**, 123-128 (2011).
244. K. Koester, J. Ager, R. Ritchie, The true toughness of human cortical bone measured with realistically short cracks. *Nature Materials* **7**, 672-677 (2008).
245. M. Launey *et al.*, On the mechanistic origins of toughness in bone. *Annual Review of Materials Research, Vol 40* **40**, 25-53 (2010).
246. R. Nalla, J. Kinney, R. Ritchie, Mechanistic fracture criteria for the failure of human cortical bone. *Nature Materials* **2**, 164-168 (2003).
247. H. Gupta *et al.*, Nanoscale deformation mechanisms in bone. *Nano Letters* **5**, 2108-2111 (2005).
248. R. Moon, A. Martini, J. Nairn, J. Simonsen, J. Youngblood, Cellulose nanomaterials review: Structure, properties and nanocomposites. *Chemical Society Reviews* **40**, 3941-3994 (2011).
249. D. Klemm *et al.*, Nanocelluloses: A new family of nature-based materials. *Angewandte Chemie-International Edition* **50**, 5438-5466 (2011).
250. D. Klemm, B. Heublein, H. Fink, A. Bohn, Cellulose: Fascinating biopolymer and sustainable raw material. *Angewandte Chemie-International Edition* **44**, 3358-3393 (2005).
251. H. Khalil, A. Bhat, A. Yusra, Green composites from sustainable cellulose nanofibrils: A review. *Carbohydrate Polymers* **87**, 963-979 (2012).
252. G. Chinga-Carrasco, Cellulose fibres, nanofibrils and microfibrils: The morphological sequence of MFC components from a plant physiology and fibre technology point of view. *Nanoscale Research Letters* **6**, 417 (2011).
253. N. Lavoine, I. Desloges, A. Dufresne, J. Bras, Microfibrillated cellulose - Its barrier properties and applications in cellulosic materials: A review. *Carbohydrate Polymers* **90**, 735-764 (2012).
254. A. Isogai, T. Saito, H. Fukuzumi, TEMPO-oxidized cellulose nanofibers. *Nanoscale* **3**, 71-85 (2011).

255. M. Samir, F. Alloin, A. Dufresne, Review of recent research into cellulosic whiskers, their properties and their application in nanocomposite field. *Biomacromolecules* **6**, 612-626 (2005).
256. H. Zhu *et al.*, Tin anode for sodium-ion batteries using natural wood fiber as a mechanical buffer and electrolyte reservoir. *Nano Letters* **13**, 3093-3100 (2013).
257. Z. Fang *et al.*, Novel nanostructured paper with ultrahigh transparency and ultrahigh haze for solar cells. *Nano Letters* **14**, 765-773 (2014).
258. H. Zhu *et al.*, Anomalous scaling law of strength and toughness of cellulose nanopaper. *Proceedings of the National Academy of Sciences* **112**, 8971–8976 (2015).
259. H. Sehaqui, M. Allais, Q. Zhou, L. Berglund, Wood cellulose biocomposites with fibrous structures at micro- and nanoscale. *Composites Science and Technology* **71**, 382-387 (2011).
260. T. Sreekumar *et al.*, Single-wall carbon nanotube films. *Chemistry of Materials* **15**, 175-178 (2003).
261. T. Mattsson *et al.*, First-principles and classical molecular dynamics simulation of shocked polymers. *Physical Review B* **81**, 054103 (2010).
262. S. Eichhorn *et al.*, Review: Current international research into cellulose nanofibres and nanocomposites. *Journal of Materials Science* **45**, 1-33 (2010).
263. S. Fernandes *et al.*, Novel transparent nanocomposite films based on chitosan and bacterial cellulose. *Green Chemistry* **11**, 2023-2029 (2009).
264. J. Juntaro *et al.*, Creating hierarchical structures in renewable composites by attaching bacterial cellulose onto sisal fibers. *Advanced Materials* **20**, 3122-3126 (2008).
265. H. Yano *et al.*, Optically transparent composites reinforced with networks of bacterial nanofibers. *Advanced Materials* **17**, 153–155 (2005).
266. A. Walther, J. Timonen, I. Diez, A. Laukkanen, O. Ikkala, Multifunctional high-performance biofibers based on wet-extrusion of renewable native cellulose nanofibrils. *Advanced Materials* **23**, 2924–2928 (2011).
267. A. Felten, C. Bittencourt, J. Pireaux, G. Van Lier, J. Charlier, Radio-frequency plasma functionalization of carbon nanotubes surface O-2, NH3, and CF4 treatments. *Journal of Applied Physics* **98**, 074308 (2005).
268. L. Hu, D. Hecht, G. Gruner, Carbon nanotube thin films: Fabrication, properties, and applications. *Chemical Reviews* **110**, 5790-5844 (2010).
269. W. Yuan *et al.*, Wrapping carbon nanotubes in pyrene-containing poly(phenylacetylene) chains: Solubility, stability, light emission, and surface photovoltaic properties. *Macromolecules* **39**, 8011-8020 (2006).
270. Y. Li *et al.*, Hybridizing wood cellulose and graphene oxide toward high-performance fibers. *Npg Asia Materials* **7**, e150 (2015).
271. I. Siro, D. Plackett, Microfibrillated cellulose and new nanocomposite materials: A review. *Cellulose* **17**, 459-494 (2010).
272. Y. Y. Li *et al.*, Strong transparent magnetic nanopaper prepared by immobilization of Fe3O4 nanoparticles in a nanofibrillated cellulose network. *Journal of Materials Chemistry A* **1**, 15278-15283 (2013).

273. C. N. Wu, T. Saito, S. Fujisawa, H. Fukuzumi, A. Isogai, Ultrastrong and high gas-barrier nanocellulose/clay-layered composites. *Biomacromolecules* **13**, 1927-1932 (2012).
274. C. J. Zhou, R. Chu, R. Wu, Q. L. Wu, Electrospun polyethylene oxide/cellulose nanocrystal composite nanofibrous mats with homogeneous and heterogeneous microstructures. *Biomacromolecules* **12**, 2617-2625 (2011).
275. J. Fox *et al.*, High-Strength, healable, supramolecular polymer nanocomposites. *Journal of the American Chemical Society* **134**, 5362-5368 (2012).
276. A. J. Uddin, J. Araki, Y. Gotoh, Toward "strong" green nanocomposites: polyvinyl alcohol reinforced with extremely oriented cellulose whiskers. *Biomacromolecules* **12**, 617-624 (2011).
277. D. Li, M. B. Muller, S. Gilje, R. B. Kaner, G. G. Wallace, Processable aqueous dispersions of graphene nanosheets. *Nature Nanotechnology* **3**, 101-105 (2008).
278. Z. Xu, C. Gao, Graphene chiral liquid crystals and macroscopic assembled fibres. *Nature Communications* **2**, 571 (2011).
279. S. Stankovich *et al.*, Graphene-based composite materials. *Nature* **442**, 282-286 (2006).
280. C. S. Xiang *et al.*, Graphene nanoribbons as an advanced precursor for making carbon fiber. *Acs Nano* **7**, 1628-1637 (2013).
281. E. Y. Jang *et al.*, Fibers of reduced graphene oxide nanoribbons. *Nanotechnology* **23**, 235601 (2012).
282. Z. S. Tian *et al.*, Self-assembled free-standing graphene oxide fibers. *Acs Applied Materials & Interfaces* **5**, 1489-1493 (2013).
283. R. Jalili *et al.*, Scalable one-step wet-spinning of graphene fibers and yarns from liquid crystalline dispersions of graphene oxide: Towards multifunctional textiles. *Advanced Functional Materials* **23**, 5345-5354 (2013).
284. C. S. Xiang *et al.*, Large flake graphene oxide fibers with unconventional 100% knot efficiency and highly aligned small flake graphene oxide fibers. *Advanced Materials* **25**, 4592-4597 (2013).
285. Z. Xu, H. Y. Sun, X. L. Zhao, C. Gao, Ultrastrong fibers assembled from giant graphene oxide sheets. *Advanced Materials* **25**, 188-193 (2013).
286. L. Kou, C. Gao, Bioinspired design and macroscopic assembly of poly(vinyl alcohol)-coated graphene into kilometers-long fibers. *Nanoscale* **5**, 4370-4378 (2013).
287. X. Z. Hu, Z. Xu, C. Gao, Multifunctional, supramolecular, continuous artificial nacre fibres. *Scientific Reports* **2**, 767 (2012).
288. H. P. Cong, X. C. Ren, P. Wang, S. H. Yu, Wet-spinning assembly of continuous, neat, and macroscopic graphene fibers. *Scientific Reports* **2**, 613 (2012).
289. D. C. Marcano *et al.*, Improved synthesis of graphene oxide. *Acs Nano* **4**, 4806-4814 (2010).
290. J. Araki, M. Wada, S. Kuga, T. Okano, Birefringent glassy phase of a cellulose microcrystal suspension. *Langmuir* **16**, 2413-2415 (2000).
291. F. Jiang, Y. L. Hsieh, Chemically and mechanically isolated nanocellulose and their self-assembled structures. *Carbohydrate Polymers* **95**, 32-40 (2013).

292. H. G. Chae, S. Kumar, Materials science - Making strong fibers. *Science* **319**, 908-909 (2008).
293. X. M. Sun, T. Chen, Z. B. Yang, H. S. Peng, The alignment of carbon nanotubes: An effective route to extend their excellent properties to macroscopic scale. *Accounts of Chemical Research* **46**, 539-549 (2013).
294. Y. Habibi, L. A. Lucia, O. J. Rojas, Cellulose nanocrystals: Chemistry, self-assembly, and applications. *Chemical Reviews* **110**, 3479-3500 (2010).
295. R. Jalili *et al.*, Organic solvent-based graphene oxide liquid crystals: A facile route toward the next generation of self-assembled layer-by-layer multifunctional 3d architectures. *Acs Nano* **7**, 3981-3990 (2013).
296. Z. Lin, Q. Q. Deng, X. Y. Liu, D. W. Yang, Engineered large spider eggcase silk protein for strong artificial fibers. *Advanced Materials* **25**, 1216-1220 (2013).
297. S. J. Zhang, K. K. K. Koziol, I. A. Kinloch, A. H. Windle, Macroscopic fibers of well-aligned carbon nanotubes by wet spinning. *Small* **4**, 1217-1222 (2008).
298. S. Iwamoto, A. Isogai, T. Iwata, Structure and mechanical properties of wet-spun fibers made from natural cellulose nanofibers. *Biomacromolecules* **12**, 831-836 (2011).
299. Z. L. Dong *et al.*, Facile fabrication of light, flexible and multifunctional graphene fibers. *Advanced Materials* **24**, 1856-1861 (2012).
300. O. Compton *et al.*, Tuning the mechanical properties of graphene oxide paper and its associated polymer nanocomposites by controlling cooperative intersheet hydrogen bonding. *Acs Nano* **6**, 2008-2019 (2012).